UNIVERSIDADE DE LISBOA
INSTITUTO SUPERIOR TÉCNICO

Study of solar modulation effects on cosmic ray fluxes measured by the AMS experiment

Miguel Reis Orcinha

Supervisor: Doctor Fernando José de Carvalho Barão

Thesis approved in public session to obtain the PhD Degree in
Physics

Jury final classification: **Pass with Distinction**

2023

UNIVERSIDADE DE LISBOA
INSTITUTO SUPERIOR TÉCNICO

Study of solar modulation effects on cosmic ray fluxes measured by the AMS experiment

Miguel Reis Orcinha

Supervisor: Doctor Fernando José de Carvalho Barão

Thesis approved in public session to obtain the PhD Degree in
Physics

Jury final classification: **Pass with Distinction**

Jury

Chairperson: Doctor Luís Paulo da Mota Capitão Lemos Alves, Instituto Superior Técnico, Universidade de Lisboa.
Members of the committee:
Doctor Laurent Derome, UFR PhITEM (Physique, Ingénierie, Terre, Environnement, Mécanique) department, Grenoble Alpes University, France
Doctor Mário João Martins Pimenta, Instituto Superior Técnico, Universidade de Lisboa
Doctor Nicola Tomassetti, Università degli Studi di Perugia, Italy
Doctor Fernando José de Carvalho Barão, Instituto Superior Técnico, Universidade de Lisboa

Funding Institution:
Grant SFRH/BD/104462/2014 from FCT - Fundação para a Ciência e a Tecnologia

2023

Em memória de Francisco dos Reis Agostinho.

Resumo

Ao atravessarem o sistema solar os raios cósmicos deparam-se com um fluxo de plasma magnetizado altamente condutor que emana do Sol, conhecido como Vento Solar, que transporta o turbulento campo magnético solar e com o qual estes interagem. Devido à atividade solar, a heliosfera está sujeita a variações de curta e longa duração que se refletem no fluxo de raios cósmicos na forma de variabilidade temporal, especialmente a baixas energias (até cerca de 50 GeV), na proximidade da Terra. Esta variabilidade da intensidade de raios cósmicos na heliosfera é conhecida como Modulação Solar dos Raios Cósmicos Galácticos.

O Espectrómetro Magnético de Partículas Alfa (AMS-02) é um detetor de raios cósmicos de alta precisão instalado na Estação Espacial Internacional (ISS) que observa continuamente o fluxo de raios cósmicos e as suas variações no tempo, posicionando-se como uma plataforma única para estudar Modulação Solar.

Nesta tese caracterizou-se de forma introdutória os raios cósmicos e relevou-se AMS enquanto o detetor usado para os observar e estudar. Estudou-se a estimativa do fluxo de raios cósmicos em grande detalhe enquanto se analisou o desempenho dos diferentes sub-detetores envolvidos. Descreveu-se o processo através do qual se utilizou a grande precisão de AMS e dos seus sub-detetores para identificar as astro-partículas que esta deteta e como foi estimado o fluxo resolvido em tempo com uma resolução de 27 dias (conhecida como rotação solar Bartel).

Foi introduzido o processo físico da Modulação Solar e apresentou-se uma revisão da equação de transporte de Parker e as suas ligações ao campo magnético solar através dos parâmetros de propagação.

Utilizando técnicas modernas de análise de frequências, caracterizou-se o fluxo de protões resolvido no tempo, quer no domínio do tempo quer das frequências, e correlacionou-se o mesmo com as diferentes periodicidades temporais presentes no Ciclo de Atividade Solar. Usando um modelo do transporte de raios cósmicos na heliosfera, em combinação com uma grande coleção de dados experimentais, mostrou-se evidência de um atraso temporal de 8 meses entre as observações do ciclo de atividade solar e o fluxo de raios cósmicos medido no espaço. Este resultado permite prever o fluxo de raios cósmicos na Terra através da observação da atividade solar.

Palavras-Chave

AMS-02, Física de raios cósmicos, Periodicidades no fluxo de raios cósmicos, Modulação Solar, Análise de atraso temporal

Abstract

As cosmic rays traverse through the solar system they are faced with an outward flow of highly-conductive magnetized plasma known as the Solar Wind. Embedded in this wind is the turbulent Heliospheric Magnetic Field with which cosmic rays interact, significantly changing both their energy and trajectory. Due to solar activity, the heliosphere is subjected to both short and long-term changes which reflect as temporal variations on the cosmic-ray flux, specially at lower energies (up to 50 GeV). These temporal variations of cosmic ray intensity in the heliosphere are known as the Solar Modulation of Galactic Cosmic Rays.

AMS-02, the Alpha Magnetic Spectrometer is a high-precision state-of-the-art cosmic-ray detector installed in the International Space Station, continuously monitoring the cosmic-ray flux as it changes with time positioning it as a unique platform to study Solar Modulation.

In this thesis we will begin by briefly exploring the history of the discovery of cosmic rays and showcase AMS as the detector used to observe them. After, we characterize the estimation of a cosmic-ray flux in detail as we study the performance of the different AMS detectors involved. Finally we describe the process by which we use AMS' high-precision detectors to identify the cosmic-ray particles arriving at the detector and how we estimated the 27-day (known as Bartel solar rotation) time-resolved cosmic-ray proton flux.

We will then introduce the physical process that is Solar Modulation and present an overview of Parker's transport equation and its connections to the solar magnetic field through the different propagation parameters.

Utilizing modern frequency-analysis techniques we characterized the time-resolved proton flux, in both time and frequency domains, as we correlated it to the different temporal periodicities present in the Solar Activity Cycle.

Using a data-driven model of cosmic-ray transport in the heliosphere, in combination with a large collection of data, we showed evidence of an eight-month time-lag between observations of solar activity and measurements of cosmic-ray fluxes in space. This result enables us to forecast the cosmic ray flux on Earth well in advance by monitoring solar activity.

Keywords

AMS-02, Cosmic-ray Physics, Periodicities in the Cosmic-Ray Flux, Solar Modulation, Time-Lag Analysis

Acknowledgments

I would like to begin by thanking my thesis supervisor Prof. Fernando Barão for the mentoring throughout the decade we've known each other. When he first started mentoring me, during my MSc degree, he always made sure I felt welcome at the lab and in the group. Ever since I've known him he's always been open to sharing his wealth of knowledge and to humbly listen to the questions and challenges his students present him. Both in his field and in the university he is known for always having his door open to both students and colleagues. In his office you will always find the same openness and enthusiasm for discussing and solving even the most challenging problems in physics, regardless of the topic. He introduced me to his Computation Physics course as a teaching assistant even as a MSc student and was always the first to support every position I've every applied for. He's an incredible teacher and friend. It has been a pleasure to work with him both as a student and as a colleague.

I would like to thank Laurent Derome for his support in my work and for extending a helping hand whenever I needed it. He generously hosted me in LSPC and gave me complete access to his code, his data and his knowledge, from the very beginning. His support proved invaluable and was fundamental to all the work done in this thesis related to the estimation of the proton flux in AMS. Thank you Laurent.

For the short time I've known Nicola Tomassetti he's always shown himself to be an incredibly curious and enthusiastic person. His friendly demeanour and passion for physics made his company incredibly easy to enjoy and I miss working with him very much. He was always open to discussion and I've learned a lot from him. I can't wait for your return to Lisbon. All of the work done on the time-delay topic was done in direct collaboration with Nicola Tomassetti.

In no particular order, to Gonçalo, Inês, Mário, Carolina, Rui, João, Catarina and Gonçalo, my lifelong friends who have always shown me nothing but absolute support. They have helped more times than I can count and have never let me face any of life's challenges alone. They are truly the best friends any person could ever hope for. Thank you all.

I would like to thank my mother, Ana Maria Vieira dos Reis for being a source of constant support and love. She has supported me and my sisters in every single one of our endeavours and always made sure that we never needed anything or missed any opportunity life threw at us, even to her personal detriment. Ana Reis is by far the most brilliant loving and kind person I've had the pleasure of knowing and can't help but being thankful for being her son. She is the embodiment of the person I can only wish to become.

My sisters, Catarina and Beatriz, two beautiful human beings. Each in their own way, they have both stood by me all my life and helped me reach every goal I've put my mind to. They have supported me in every path my life took and never shied away from being honest whenever I was facing the wrong way. For your infinite patience, for your loving support and, mostly for putting up with me, thank you.

To my grandfather, Francisco dos Reis Agostinho and to whom this work is dedicated, I would like to thank with all my heart for the great life advice, for the opportunity to study for as long as I needed to and for all of his other contributions not only to myself but to my country. Nothing brought him greater joy than seeing his children and grandchildren succeed, pursue their passion for knowledge and follow their curiosity. He was a kind and loving man. Thank you.

Contents

List of Figures

List of Tables

List of Publications

Direct Contribution

- N. Tomassetti, F. Barao, B. Bertucci, E. Fiandrini, M. Orcinha, “Numerical modeling of cosmic-ray transport in the heliopshere and interpretation of proton and helium fluxes in Solar Cycle 24”, Advances in Space Research 64 (2019) 2477-2489, doi: 10.1016/j.asr.2019.06.025
- M. Orcinha, N. Tomassetti, F. Barão and B. Bertucci, “Observation of a time lag in solar modulation of cosmic rays in the heliosphere”, J. Phys.: Conf. Ser. 1181 (2019) 012013, doi: 10.1088/1742-6596/1181/1/012013
  26th Extended European Cosmic Ray Symposium and 35th Russian Cosmic Ray Conference, Barnaul - Belokurikha - Altai Mountains, Russia, July 6 - 10, (2018)
- N. Tomassetti, F. Barao, B. Bertucci, E. Fiandrini, J. L. Figueiredo, J. B. Lousada, M. Orcinha, “Testing Diffusion of Cosmic Rays in the Heliosphere with Proton and Helium Data from AMS”, Phys. Rev. Lett. 121 (2018) 251104, doi: 10.1103/PhysRevLett.121.251104
- N. Tomassetti, M. Orcinha, F. Barao, B. Bertucci, “Evidence for a Time Lag in Solar modulation of galactic cosmic rays”, ApJL, 849 (2017) L32, doi: 10.3847/2041-8213/aa9373

Indirect Contribution

- M. Aguilar et al. (AMS Collaboration), “Properties of Daily Helium Fluxes”, Phys. Rev. Lett. 128 (2021) 231102, doi: 10.1103/PhysRevLett.128.231102
- M. Aguilar et al. (AMS Collaboration), “Periodicities in the Daily Proton Fluxes from 2011 to 2019 Measured by the Alpha Magnetic Spectrometer on the International Space Station from 1 to 100 GV”, Phys. Rev. Lett. 127 (2021) 271102, doi: 10.1103/PhysRevLett.127.271102
- M. Aguilar et al. (AMS Collaboration), “Properties of a New Group of Cosmic Nuclei: Results from the Alpha Magnetic Spectrometer on Sodium, Aluminum, and Nitrogen”, Phys. Rev. Lett. 127 (2021) 021101, doi: 10.1103/PhysRevLett.127.021101
- M. Aguilar et al. (AMS Collaboration), “Properties of Heavy Secondary Fluorine Cosmic Rays: Results from the Alpha Magnetic Spectrometer”, Phys. Rev. Lett. 126 (2021) 081102, doi: 10.1103/PhysRevLett.126.081102
- M. Aguilar et al. (AMS Collaboration), “Properties of Iron Primary Cosmic Rays: Results from the Alpha Magnetic Spectrometer”, Phys. Rev. Lett. 126 (2021) 041104, doi: 10.1103/PhysRevLett.126.041104
- M. Aguilar et al. (AMS Collaboration), “The Alpha Magnetic Spectrometer (AMS) on the international space station: Part II – Results from the first seven years”, Phys. Rept. 894 (2020) 1-116, doi: 10.1016/j.physrep.2020.09.003

- M. Aguilar et. al. (AMS Collaboration), “Properties of Neon, Magnesium, and Silicon Primary Cosmic Rays Results from the Alpha Magnetic Spectrometer”, Phys. Rev. Lett. 124 (2020) 211102, doi: 10.1103/PhysRevLett.124.211102
- M. Aguilar et. al. (AMS Collaboration), “Properties of Cosmic Helium Isotopes Measured by the Alpha Magnetic Spectrometer”, Phys. Rev. Lett. 123 (2019) 181102, doi: 10.1103/PhysRevLett.123.181102
- M. Aguilar et. al. (AMS Collaboration), “Towards Understanding the Origin of Cosmic-Ray Electrons”, Phys. Rev. Lett. 122 (2019) 101101, doi: 10.1103/PhysRevLett.122.101101
- M. Aguilar et. al. (AMS Collaboration), “Towards Understanding the Origin of Cosmic-Ray Positrons”, Phys. Rev. Lett. 122 (2019) 041102, doi: 10.1103/PhysRevLett.122.041102
- M. Aguilar et. al. (AMS Collaboration), “Precision Measurement of Cosmic-Ray Nitrogen and its Primary and Secondary Components with the Alpha Magnetic Spectrometer on the International Space Station”, Phys. Rev. Lett. 121 (2018) 051103, doi: 10.1103/PhysRevLett.121.051103
- M. Aguilar et. al. (AMS Collaboration), “Observation of Complex Time Structures in the Cosmic-Ray Electron and Positron Fluxes with the Alpha Magnetic Spectrometer on the International Space Station”, Phys. Rev. Lett. 121 (2018) 051102, doi: 10.1103/PhysRevLett.121.051102
- M. Aguilar et. al. (AMS Collaboration), “Observation of Fine Time Structures in the Cosmic Proton and Helium Fluxes with the Alpha Magnetic Spectrometer on the International Space Station”, Phys. Rev. Lett. 121 (2018) 051101, doi: 10.1103/PhysRevLett.121.051101
- M. Aguilar et. al. (AMS Collaboration), “Observation of New Properties of Secondary Cosmic Rays Lithium, Beryllium, and Boron by the Alpha Magnetic Spectrometer on the International Space Station”, Phys. Rev. Lett. 120 (2018) 021101, doi: 10.1103/PhysRevLett.120.021101
- M. Aguilar et. al. (AMS Collaboration), “Observation of the Identical Rigidity Dependence of He, C, and O Cosmic Rays at High Rigidities by the Alpha Magnetic Spectrometer on the International Space Station”, Phys. Rev. Lett. 120 (2017) 021101, doi: 10.1103/PhysRevLett.119.251101
- M. Aguilar et. al. (AMS Collaboration), “Precision Measurement of the Boron to Carbon Flux Ratio in Cosmic Rays from 1.9 GV to 2.6 TV with the Alpha Magnetic Spectrometer on the International Space Station”, Phys. Rev. Lett. 117 (2016) 231102, doi: 10.1103/PhysRevLett.117.231102
- M. Aguilar et al. (AMS Collaboration), “Antiproton Flux, Antiproton-to-Proton Flux Ratio, and Properties of Elementary Particle Fluxes in Primary Cosmic Rays Measured with the Alpha Magnetic Spectrometer on the International Space Station”, Phys. Rev. Lett. 117 (2016) 091103, doi: 10.1103/PhysRevLett.117.091103
- M. Aguilar et al. (AMS Collaboration), “Precision Measurement of the Helium Flux in Primary Cosmic Rays of Rigidities 1.9 GV to 3 TV with the Alpha Magnetic Spectrometer on the International Space Station”, Phys. Rev. Lett. 115 (2015) 211101, doi: 10.1103/PhysRevLett.115.211101

- M. Aguilar et al. (AMS Collaboration), “Precision Measurement of the Proton Flux in Primary Cosmic Rays from Rigidity 1 GV to 1.8 TV with the Alpha Magnetic Spectrometer on the International Space Station”, Phys. Rev. Lett. 114 (2015) 171103, doi: 10.1103/PhysRevLett.114.171103

Abbreviations

ACC Anti-Coincidence Counter
ACR Anomalous Cosmic Rays
AMS Alpha Magnetic Spectrometer
AMS-02 Alpha Magnetic Spectrometer
CME Coronal Mass Ejection
ECAL Electromagnetic Calorimeter
GCR Galactic Cosmic Rays
HCS Heliospheric Current Sheet
HMF Heliospheric Magnetic Field
IMF Interplanetary Magnetic Field
ISS International Space Station
LIS Local Interstellar Spectrum
LISM Local Interstellar Medium
MHD Magnetohydrodynamics
NASA National Aeronautics and Space Administration
pdf probability density function
cdf cumulative distribution function
PDG Particle Data Group
PMT Photomultiplier Tube
QLT Quasi-Linear Theory
RICH Ring-Imaging Cherenkov Detector
SEP Solar Energetic Particle
TAS Tracker Alignment System
ToF Time-of-Flight System
TRD Transition Radiation Detector
TRK Silicon Tracker
RTI Real Time Information
MLE Maximum Likelihood Estimation
AIC Akaike Information Criteria
BIC Bayesian Information Criteria
TTCS Tracker Thermal Control System
SST Surface Sea Temperature
FT Fast Trigger
HT High Threshold
SHT Super High Threshold
SDE Stochastic Differential Equations

Preface

This document pertains to the work done during the course of the PhD of Miguel Reis Orcinha and was specially prepared to obtain the PhD degree in Physics.

The work was done in the context of the AMS Collaboration of which the author is a member. As the title suggests, it has the overall goal of studying cosmic-ray variability due to solar modulation within the context of the AMS experiment. The thesis is split into seven chapters and one appendix.

The first chapter, titled *Cosmic Rays*, will present a brief introduction to cosmic rays, their origin, the observed spectrum at Earth and their history.

The second chapter, titled *Solar Modulation of Galactic Cosmic Rays*, will discuss the process by which solar activity modulates the galactic cosmic rays as they traverse the solar system, granting a theoretical standing which will be used to interpret time-variability of the proton flux measured by AMS. It will also introduce the Parker transport equation which models the different processes the Galactic cosmic-ray endures as it is transported through the solar system.

The third chapter, titled *The Alpha Magnetic Spectrometer*, briefly discusses the AMS-02 detector and the different sub-detectors that compose it, emphasizing the physical quantity they observe and their measurement principle. We discussed the space environment in which AMS is inserted and the effect that has on the cosmic rays

The forth chapter, titled *Measurement of the Proton Flux*, describes the process of estimating the Bartel rotation time-resolved proton flux as measured by AMS-02, the characterization of the AMS-02 detector and the sub-detectors involved in the analyses as well as presenting the results in comparison to the Proton Flux published by the AMS collaboration.

The fifth chapter, titled *Variability of the AMS-02 Proton Flux*, interprets the time-resolved cosmic-ray flux as a time-series which can be analysed in both time and frequency domains. It develops tools to study and compares the results directly to solar activity and other heliospheric observables.

The sixth chapter, titled *Interpretation of results under Solar Modulation*, describes the different solar observables that will serve as proxies for solar activity and presents some of the numerical approaches that can be taken to solve Parker's transport equation. It will model propagation parameters in terms of solar observables and will show a time-delay between the solar activity cycle and the attenuation of the cosmic-ray flux.

The seventh chapter, titled *Conclusions and Prospects*, summarizes the conclusions and results presented in this work and proposes some future work for some of the topics.

The appendix, titled *Algorithms and Code*, aims to emphasize the technical work required for the analyses done during the course of this work. The development of computational platforms and tools is often overlooked and this chapter aims to discuss some of the design choices and the performance of the tools so they can be implemented by the scientific community.

1

Cosmic Rays

The Particle Data Group (PDG) offers a definition of cosmic ray as all the cosmic radiation incident at the top of the terrestrial atmosphere, which includes all stable charged particles and nuclei with lifetimes of order 10^6 years or longer[1]. These particles carry energies starting at about 1 MeV, up to 10^{20} eV and are comprised of protons, fully ionized nuclei and isotopes, antiprotons, electrons, positrons, among others, the most abundant of which are the protons.

Beginning with a brief historic introduction, this chapter will give an overview of the cosmic ray spectrum, cosmic-ray relative abundance and some mechanisms responsible for their arrival at Earth.

1.1 Brief History of Cosmic Rays

In 1909, the dominant theory towards ambient radiation was that ionizing radiation would come from rocks and soil. To test this theory, Theodor Wulf[2] measured the rate of ionization at the bottom and at the top of the Eiffel tower (300 m), using a series of electroscopes of his own design. He expected an exponential decrease in the rate of ionization measured as he got farther from the ground but this decrease was only of about half of that measured at the surface, contradicting his expectations.

Victor Francis Hess took the next big step by taking electroscopes in balloon flights. Even though he was not the first to do so[3], he was the first one with the interpretation that lead to the discovering of cosmic rays.

Hess, in 1912, showed, from his balloon flights, that as the altitude increased, the radiation decreased until it reached a minimum, starting to increase again rapidly above 1400 m, as can be seen in Figure 1.1[4]. This was a major breakthrough since it proved that the ionizing radiation's origin could not be terrestrial, it had to come from above. He also found that the radiation had hourly variations but he did not find a reduction of the radiation's intensity during the night or during a Solar eclipse, thus concluding that the origin of the radiation could not be the Sun, it had to come from outside the Solar System.

This discovery of the natural source of high-energy particles coming from outside the Solar System won him the Nobel Prize in Physics in 1936, which he divided equally with C. D. Anderson for his discovery of the positron.[4]

Hess' discoveries were corroborated by later balloon experiments such as those made by Kolhörster[6]. The term *cosmic ray* was coined by Robert Millikan in the 1920's[7]. In 1927, J. Clay discovered the geomagnetic effect by measuring a variation of cosmic ray intensity with latitude[8].

In 1930, Bruno Rossi predicted a difference between the intensity of cosmic rays arriving

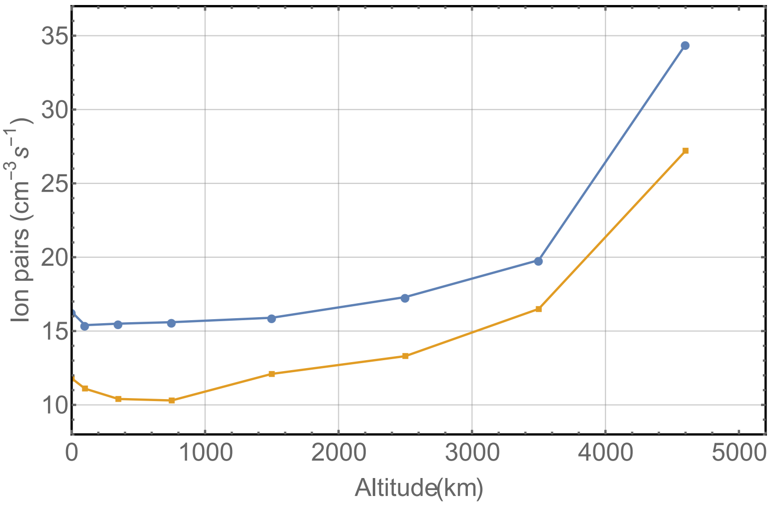

Figure 1.1: Some of Hess's 1912 balloon electroscope observations[5].

from the east and the west, depending on the charge of the primary particles, the East-West Effect[9]. His prediction was later proven right by several experiments[10, 11, 12].

After deriving the differential cross-section of the scattering of positrons by electrons (the Bhabha scattering), Homi Bhabha, alongside Walter Heitler, published in 1937 an article describing how cosmic rays interact with the upper atmosphere to produce particles observed at ground level[13]. They explained cosmic ray shower formation as a cascade production of γ-rays and positron-electron pairs. This discovery was fundamental towards the study of high energy cosmic rays since by studying these air shower, it is possible to use the atmosphere as part of a large detector system (detection principle used in Pierre-Auger Observatory and other experiments).

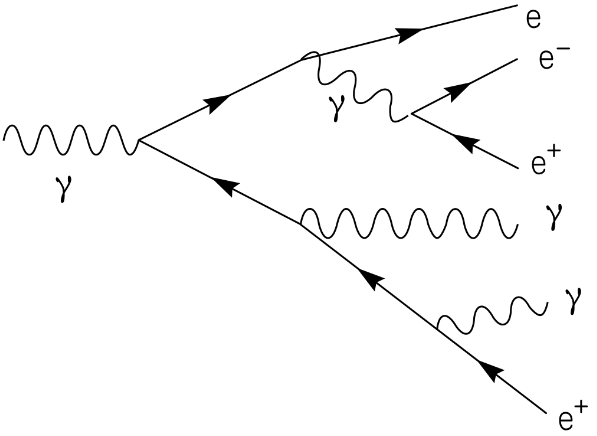

Figure 1.2: Schematic view of the beginning of an electromagnetic shower.

Further study of cosmic rays lead to the discovery of several new particles among which were[14]:

- 1937 - Muon discovery by Neddermeyer (mistaken for a pion until proven wrong in 1947 by Conversi, Pancini and Piccioni)
- 1947 - Pion discovery by Lattes, Occhialini and Powell
- 1947 - Kaon discovered by Rochester and Butler

- 1951 - Λ discovered by Armenteros

In 1949, Enrico Fermi proposed a model explaining how cosmic particles could be accelerated up to relativistic speeds, allowing them to reach Earth[15]. This process is now known as Fermi acceleration.

As time went by, the study of cosmic rays developed from ground-based studies to balloon experiments and, lastly, to upper atmosphere and spacial detectors. The discovery of this cosmic radiation together with an appropriate interpretation, allows for a deeper understanding of the Universe and the physical phenomena that govern it.

1.2 The Cosmic-ray Spectrum

The intensity of primary nucleons in energy range from the GeV to 100 TeV is approximately described by the following power-law[1],

$$I_N(E) \approx 1.8 \times 10^4 \left(\frac{E}{1\,\mathrm{GeV}}\right)^{-\alpha} \left[\frac{\mathrm{nucleons}}{m^2\, s\, sr\, \mathrm{GeV}}\right], \tag{1.1}$$

where α is the differential spectral index of the cosmic ray flux and varies with energy. From ~ 30 GeV up to energies of about 10^{15} eV the differential spectral index is ~ 2.7. Below the 30 GeV the flux begins to be modulated by solar activity which is referred to Solar Modulation and will be heavily scrutinized in coming chapters. Near 10^{15} eV energies the power-law changes to become proportional to $E^{-3.1}$, steepening. At higher energies other structures emerge as can be seen in Figure 1.5[16].

The cosmic ray flux is usually written up in terms of magnetic rigidity, momentum, kinetic energy, energy-per-nucleon or energy-per-nucleus. The differential intensity of the cosmic-ray flux written in terms of magnetic rigidity usually takes the differential form

$$\varphi = \frac{\mathrm{d}^4 N}{\mathrm{d}t\, \mathrm{d}P\, \mathrm{d}\Omega\, \mathrm{d}S},$$

where N is the number of particles, t is time, P is the magnetic rigidity, Ω stands for the solid angle and S stands for the transverse area being crossed by the flux. Magnetic rigidity, or simply rigidity, relates to the gyroradius of a particle in a magnetic field and can be expressed as

$$P = \frac{p\, c}{Z\, e} = r_{\mathrm{L}}\, B,$$

where p is the relativistic particle's momentum, c the speed of light, $Z\, e$ is the electric charge of the particle expressed as a multiple of the electric charge of an electron. r_{L} is the Larmor radius while B is the magnetic field the particle is being transported through. Rigidity directly relates to aspects of the propagation of cosmic rays in the Galaxy so it is often used when studying cosmic rays.

A spectrum for different particles, as measured by the AMS-02[17, 18, 19, 20], ATIC[21], BESS[22], CREAM[23], CRN[24], HEAO[25], HESS[26], JACEE[27], PAMELA[28], RUNJOB[29], TRACER[30], VERITAS[31] experiments, is shown in Figure 1.3. Up to the TeV scale, $E \sim 10^{12} eV$, these cosmic rays can be directly detected outside of Earth's atmosphere. Above this energy direct detection becomes difficult due to the increased probability of the particles interacting with the Earth's atmosphere.

The composition and energy spectrum of nuclei can be interpreted using propagation models in which the sources are located within the Galaxy and these travel towards the Solar System by traversing through the Galactic magnetic field. The result of this propagation gives rise to a complex spectrum (detailed in Figure 1.3) that shows the average chemical composition, given by Table 1.1 and shown in Figure 1.4.

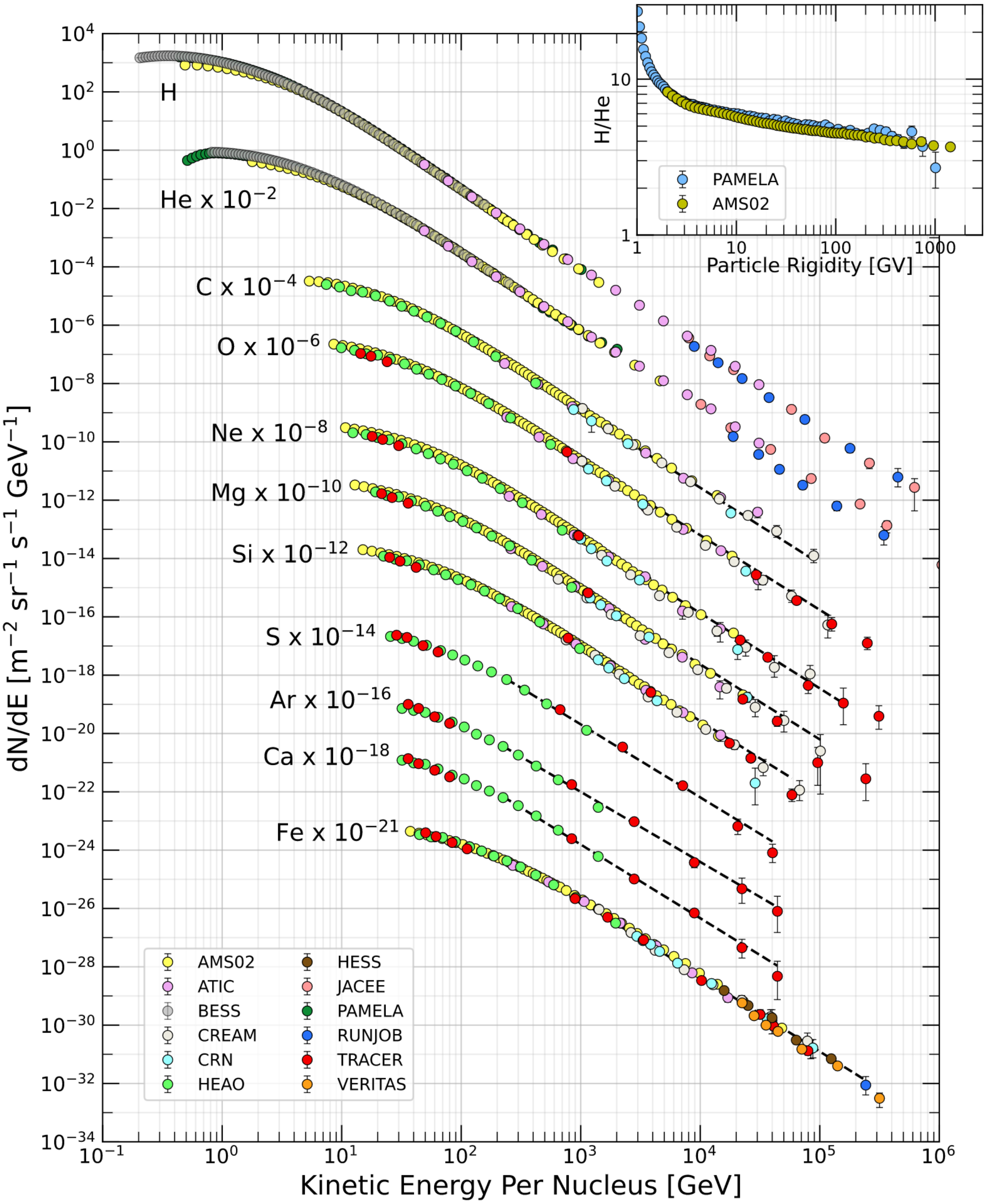

Figure 1.3: Fluxes of nuclei of the primary cosmic radiation in particles per energy-per-nucleus are plotted vs energy-per-nucleus using data from AMS-02[17, 18, 19, 20], ATIC[21], BESS[22], CREAM[23], CRN[24], HEAO[25], HESS[26], JACEE[27], PAMELA[28], RUNJOB[29], TRACER[30], VERITAS[31] experiments. The inset shows the H/He ratio as a function of rigidity[28, 18]. Figure taken from Figure 30.1 from Workman et al., (2022)[1].

In Figure 1.4 we can see the relative abundance of the different elements present in the cosmic-ray spectrum and in the solar system. Most primary nucleons arriving at Earth are free protons (74%) with about 70% of the rest being nucleons bound in helium nuclei, while other elements will contribute to a much lesser degree[1]. We see that the contribution of

Z	Element	F
1	H	550
2	He	34
3-5	Li-B	0.4
6-8	C-O	2.20
9-10	F-Ne	0.30
11-12	Na-Mg	0.22
13-14	Al-Si	0.19
15-16	P-S	0.03
17-18	Cl-Ar	0.01
19-20	K-Ca	0.02
21-25	Sc-Mn	0.05
26-28	Fe-Ni	0.12

Table 1.1: Relative abundances F of cosmic-ray nuclei at 10.6 GeV/nucleon normalized to oxygen ($\equiv 1$). Table taken from Workman et al., (2022)[1].

cosmic-rays to the so-called even-odd effect is attenuated when compared to the one present in the elemental abundances of the solar system. We also see that cosmic rays contribute greatly to the abundance of some rarer elements[1].

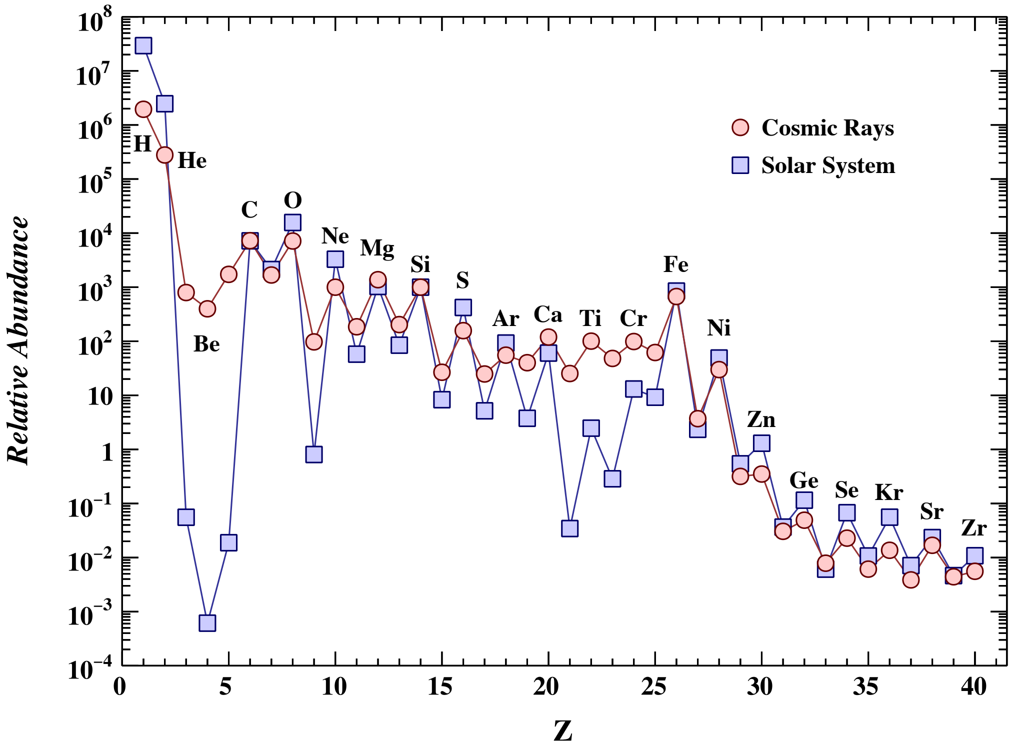

Figure 1.4: Cosmic ray elemental abundances of low-energy cosmic rays compared to abundances in present-day solar system material. Abundances are normalised to Si$=10^3$. Cosmic ray abundances are from AMS-02 (H,He)[18, 32], ACE/CRIS (Li-Ni)[33, 34], and TIGER/SuperTIGER (Cu-Zr)[35, 36]. Solar system abundances are from Table 6 of Lodders, Palme and Gail, ()[37]. Figure taken from Figure 30.2 from Workman et al., (2022)[1].

The spectrum from Figure 1.3 can be extended to higher energies (up to 10^{20} GeV) if the measurement of cosmic ray showers is taken into account as well (it is very difficult to directly measure particles with such high energies). In this case, the atmosphere is used as part of the detector. A very high energy cosmic ray will interact with the atmosphere and generate a shower of particles that will then be detected in the ground. By studying shower development in air, it's possible to estimate the energy and direction of the primary particle that generated the shower.

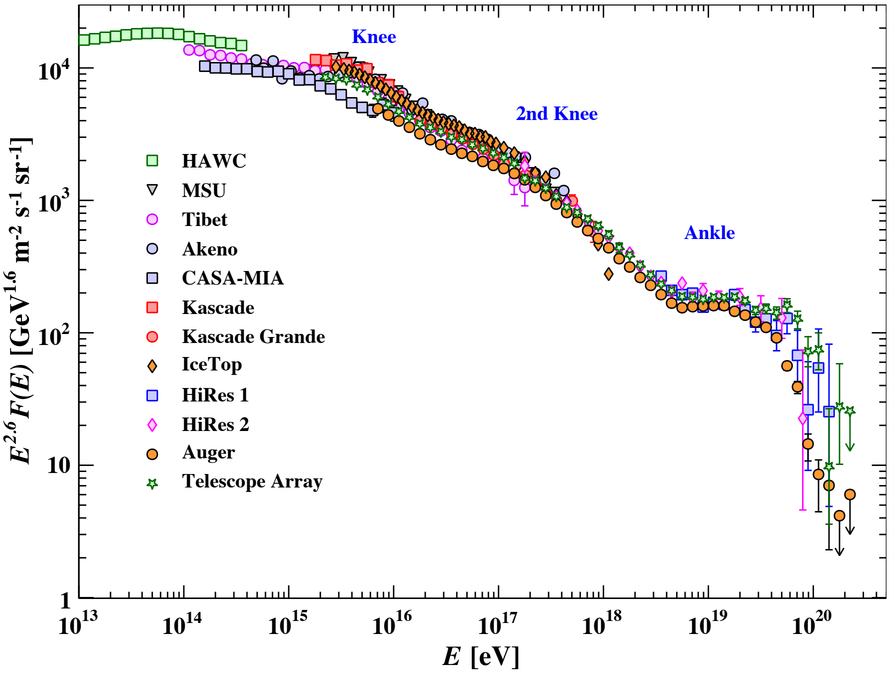

Figure 1.5: The all-particle spectrum as a function of energy-per-nucleus from air shower measurements. Figure taken from Figure 30.9 from Workman et al., (2022)[1].

Figure 1.5 shows the extended cosmic ray spectrum up to 10^{20} eV.

Observing this more complete spectrum reveals structures. Instead of having just one power law it is possible to identify two more powers law (with different indexes), each being separated by a knee, and having a so-called ankle at the end of the entire spectrum.

1.3 Detection of Cosmic Rays

As has been shown, there is great interest in the study of cosmic rays by the scientific community. In order to do so, a plethora of cosmic-rays detectors were developed to study the different particles and with different degrees of precision and duration. While this chapter mostly focuses on charged cosmic-rays, there is deep scientific interest in exploring all physics channels when it comes to Galactic cosmic rays.

Comic-ray experiments can be largely separated into neutral and charged particle detectors. With the main purpose of studying neutral cosmic rays, such as γ rays and neutrinos, both satellite and ground-based experiments were developed: Satellite - COBE, EGRET, WMAP, Planck, ROSAT, Fermi, AGILE, Chandra, INTEGRAL, Hubble Space Telescope, James Webb Telescope, etc.; Ground-based - ARGO-YBJ, HAWC, H.E.S.S., MAGIC, IceCube, Tibet ASgamma, LHAASO and others. For studying charged cosmic rays several balloon, satellite and non-magnetic, calorimeter experiments were developed: Balloon - ATIC, BESS, CAPRICE/WiZard, CREAM; Satellite - CRIS, HEAO, PAMELA; Non-magnetic, Calorimeter - CALET, ISS-CREAM, DAMPE and more[38].

To tackle the difficult task of detecting very high energy cosmic rays some ground-based and innovative air-borne experiments are used[38]:

- Balloon & Satellite: EUSO-SPB and POEMMA;

- Ground-based: Pierre Auger Observatory, H.E.S.S., LHAASO, KASCADE-Grande, TA, CTA and others.

The AMS-02 detector remains as the first long duration, large acceptance, magnetic spectrometer in space. It is capable of measuring sign and magnitude of electric charge, velocity, momentum and rigidity of any charged particle it detects. Its is also equipped with a transition radiation detector which contributes to the separation of hadrons from leptons and an electromagnetic calorimeter which not only extends the detection range beyond the silicon tracker's capabilities but also provides an additional trigger for AMS. With all these tools AMS is capable of detecting elementary particles, nuclei and anti-nuclei directly in space[38]. With its extremely long exposure time, it is capable of being a monitor for time-variability of the cosmic-ray flux and is able to measure the flux of rare elements with unprecedented detail.

We will be covering this experiment extensively in the coming chapters in the context of estimating the time-resolved primary proton flux.

1.4 Comic-ray origin

Cosmic rays can be divided into three categories, depending on their origin: Galactic Cosmic Rays (GCR), Solar Energetic Particle (SEP) and Anomalous Cosmic Rays (ACR).

GCR are the most typical cosmic rays, being comprised of $\sim$ 90% protons, 9% alpha particles and 1% electrons, these extend to energies up to 10^{20} eV. They are accelerated by supernovae remnants[39] in a process called Fermi Acceleration. A star, upon turning supernova, will leave behind remnants, capable of lasting up to thousands of years. According to the supernovae remnants cosmic ray hypothesis, particles are accelerated by the shock front of the supernova and then further accelerated by the magnetic fields[16, 40, 41, 42].

SEP, as their name tells, are particles originating from the Sun. They mostly consist of protons, electrons and helium ions with energy ranging from a few keV up to GeV. They can originate from energization at a Solar flare site or by shock waves associated with coronal mass ejections.

ACR arise mainly from neutral interstellar atoms which are swept into the heliosphere by the motion of the solar system through the interstellar medium[43]. These particles then become singly ionized (in stark contrast to GCR's) either by photo-ionization by Solar UV photons or by charge exchange collisions with Solar wind protons and are accelerated by the solar wind termination shock[44]. This process is pictorially shown in Figure 1.6.

Galactic cosmic rays can be further split into two categories according to their provenance: primary and secondary. While primary cosmic ray are accelerated by astrophysical sources such as supernovae remnants, the latter is produced by interactions of primaries with the interstellar gas[16].

These primaries are bi-products of stellar nucleosynthesis. The study the origin of cosmic rays such as antiprotons and positrons is still up for debate and constitutes one of the objectives of the AMS-02 experiment. The AMS-02 experiment and its measurements will be the focus of upcoming chapters.

It is interesting to note that the Larmor radii of Galactic cosmic-rays varies from 10^5km at the lowest energies and up to 10^{-1} pc near 10^{15}eV[41]. This means directional information on the sources of these cosmic rays is completely lost and for a directional analysis one would be required to use either γ rays or very high energy energies. Additionally, these Larmor radii confine cosmic rays to have been accelerated in galactic sites up to the knee energy. Above the knee these cosmic rays are likely being accelerated outside the Galaxy since above 10^{18}eV the Larmor radii is of the order of the kilo-parsec and no directional correlation has been found with Galactic disc[41].

The location of these features in the flux changes between primaries and secondaries and between hadrons and leptons. In a result recently published by the AMS collaboration[45]

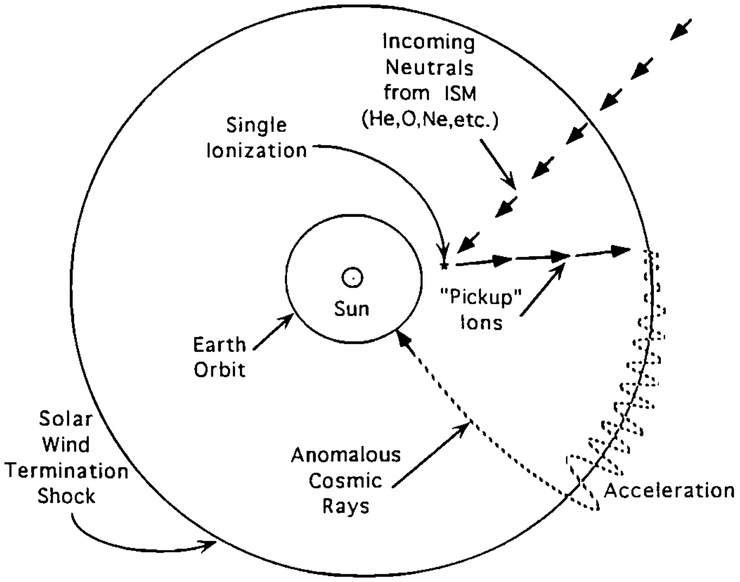

Figure 1.6: The origin of anomalous cosmic rays. Figure taken from Figure 4 of Mewaldt, Cummings and Stone, (1994)[44].

on the properties of secondary cosmic rays Lithium, Beryllium and Boron the fluxes were compared to each other and to primary cosmic-ray fluxes such as Helium, Carbon and Oxygen. The comparison can be seen in Figure 1.7. This result not only shows a hardening of both primary and secondary fluxes but also a clear spectral index difference between the two. The differences found in these spectral indexes between primary and secondary cosmic-ray fluxes and the grouping found between the two origins means that these can be used to better understand the mechanisms behind the production of secondaries and the propagation of cosmic-rays in the Galaxy. The secondary fluxes can be computed from the primary spectra, interaction cross-sections and interstellar gas densities and then compared to data to constrain the different models used[16].

Another interesting topic to study lies in the origin of positrons and antiprotons. Both have been measured by AMS-02[46, 47, 48]. The fluxes for these particles can be largely explained by secondary production but whether a fraction of this production is of primary origin (such as dark matter annihilation or decay[49]) remains a question of interest[46, 47, 48, 1, 16, 40, 49].

Other cosmic-rays such as nuclei isotopes[50] and searches for anti-matter[51, 46] are also of great interest to the astrophysical community since they provide information on the sources, acceleration and propagation of cosmic rays. Depending on the choice of the flux ratios (such as B/C or ^{3}He/^{4}He), one can be sensitive to different aspects of the propagation and processes since different secondary particles can be produced from different channels and thus probe them differently. For example, while ^{3}He is produced from the fragmentation of ^{4}He with the interstellar medium, Li, Be and B are produced from multiple fragmentation channels of several nuclei[52, 53].

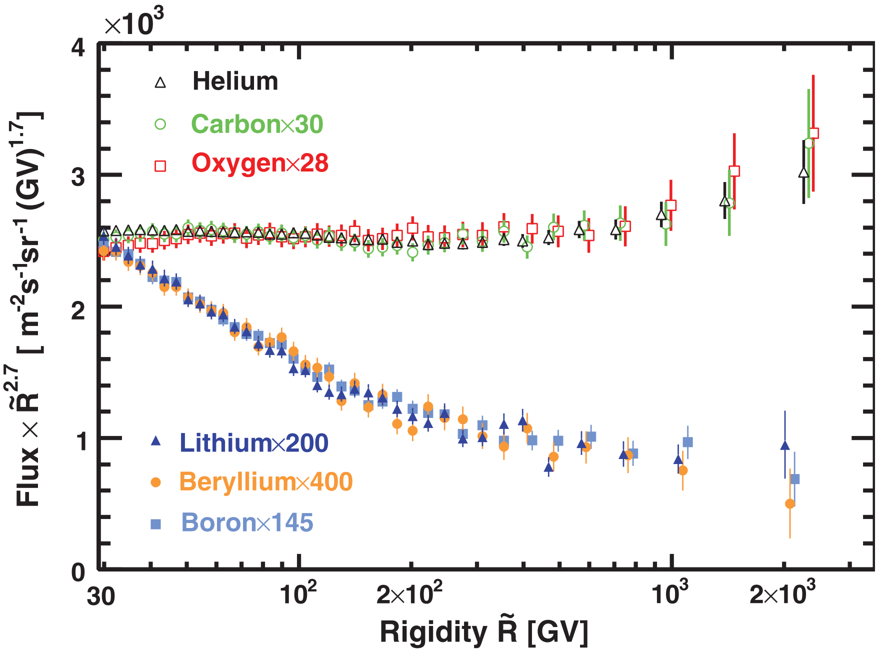

Figure 1.7: Comparison of the secondary cosmic ray fluxes with the AMS primary cosmic ray fluxes multiplied by $\tilde{R}^{2.7}$ with their total error as a function of rigidity above 30 GV. For display purposes only, the C, O, Li, Be, and B fluxes were rescaled as indicated. For clarity, the He, O, Li, and B data points above 400 GV are displaced horizontally. As seen, the three secondary fluxes have an identical rigidity dependence above 30 GV, as do the three primary fluxes above 60 GV. The rigidity dependences of primary cosmic rays fluxes and of secondary cosmic rays fluxes are distinctly different. Figure taken from Figure 4 from Aguilar et al., (2018)[45].

1.5 Low-energy cosmic-ray flux under the influence of the Sun

Most particles that reach Earth's upper atmosphere come from outside the Solar System and are modulated by the expanding magnetized plasma generated by the Sun. This plasma decelerates and partially excludes the lower energy Galactic cosmic rays[1]. Solar activity is also known to be anti-correlated with the intensity of cosmic rays at low energies as well, the Forbush decrease phenomenon.

After passing through the Solar plasma, these Galactic cosmic rays have to overcome another barrier, the geomagnetic field. This magnetic field will cut out any low energy radiation. These two phenomena combined give any cosmic ray on the GeV energy range a dependency on both time and space.

This topic will be studied in great detail throughout this work.

2

Solar Modulation of Galactic Cosmic Rays

As cosmic rays travel towards the solar system they are faced with an outward flow of magnetized plasma known as **Solar Wind**. Embedded in this wind is the turbulent Heliospheric Magnetic Field (HMF) with which cosmic rays interact, leading to significant variations in their energy and direction, depending on their position inside the heliosphere. Due to solar activity, the heliosphere is subject to both short and long-term changes which reflect as temporal variations on the cosmic ray flux. These temporal variations of cosmic ray intensity in the heliosphere are identified as **Solar Modulation of Galactic Cosmic Rays** [54].

Some of these phenomena are periodical but the most notorious is the 11-year **Solar Activity Cycle**, connected to the reversal of the solar magnetic dipole. The interaction between the solar activity cycle and these periodic changes in the cosmic ray flux will be the main focus of this chapter.

In this chapter we will overview the history of solar modulation and work through the physical processes which are responsible for the modulation of the cosmic-ray flux by the solar activity cycle.

2.1 Origins of the Solar Wind

In 1951, by observing the tails of comets (as seen in Figure 2.1), Biermann and Schlüter [55, 56] suggested that their shape was not due to the pressure of solar radiation on the molecules in the comet's tail but rather by a gas streaming outwardly from the Sun. His suggestion was that this gas was flowing radially in all directions from the Sun and had to have velocities ranging from 500 to 1500 km/s. This phenomenon is known today as solar wind and it plays a fundamental role in understanding solar modulation. It permeates the entire solar system creating the heliosphere.

In 1958, Parker tried to understand the consequences of having this outward stream of hot gas coming from the Sun. In his famous article [58], he showed that there should be no hydrostatic equilibrium solution for the solar wind and thus tried to estimate what sort of steady expansion could be expected from the solar corona.

He started by assuming that the temperature distribution was modelled by a function of only distance, $T(r)$ and then deduced the consequences of this expanding corona by having the following equation of motion (both assuming a spherical corona and that it is a hot enough so that the gas is fully ionized, thus ensuing a gas pressure given by $2NkT$),

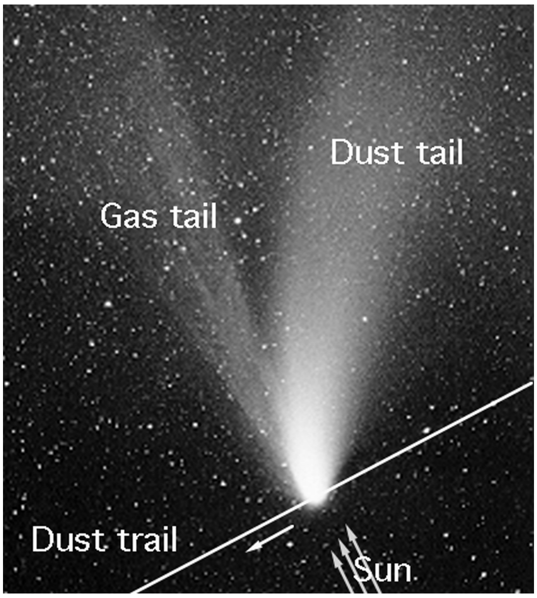

Figure 2.1: Comet trail and tail, evidence of the existence of a solar wind. Image taken from [57].

$$NMv\frac{\mathrm{d}v}{\mathrm{d}r} = -\frac{\mathrm{d}}{\mathrm{d}r}(2NkT) - GNMM_{\odot} \tag{2.1}$$

and the following equation of continuity,

$$\frac{\mathrm{d}}{\mathrm{d}r}\left(r^2Nv\right) = 0. \tag{2.2}$$

Parker then derived the expansion velocity of a spherically symmetric and isothermal solar corona, as can be seen in figure 2.2.

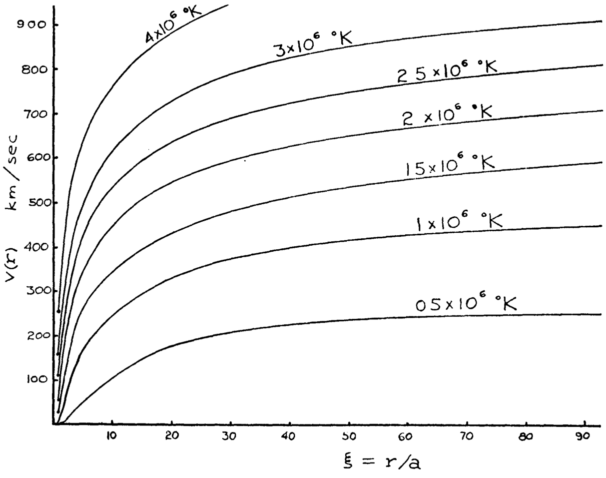

Figure 2.2: Spherically symmetric hydrodynamic expansion velocity of an isothermal solar corona, with a = 10^{11} cm. Image taken from Parker, (1958)[58].

2.2 Parker Spiral Magnetic Field

Parker then hypothesised that if there were no field-free regions in the Sun from which the gas could be emitted, the stream of outward flowing fully-ionized gas, according to the Alfvén's *frozen-flux* theorem [59], should carry the magnetic field force lines. This entails that if there is a region defined by a radius $r = b$, around the Sun, after which the ejected gas shows a completely spherical symmetry, the magnetic field lines should have the same structure. This sort of HMF geometry gives rise to the commonly known Parker Spiral Field.

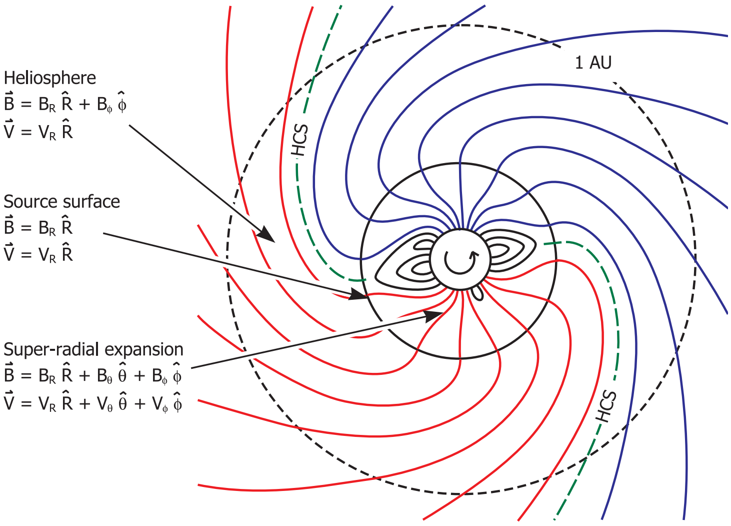

Figure 2.3: Sketch of the steady-state solar magnetic field in the ecliptic plane. It shows the spacial region bounding the solar corona, the general shape of the magnetic field as it interacts with plasma flow, turning into the spiral field we have expected from Parker and showing the Heliospheric Current Sheet (HCS) structure. The solar magnetic field lines is represented in the figure by red (blue) lines below (above) the HCS. Image taken from Owens and Forsyth, (2013)[60].

Assuming a constant spherically symmetric outward velocity V_w for the Solar wind, its shape should be (as seen from a reference frame co-rotating with the Sun at a frequency of ω),

$$v_r = V_w, \;\; v_\theta = 0, \;\; v_\phi = \omega(r - b)\sin\theta, \tag{2.3}$$

thus having the streamline given by

$$\frac{r}{b} - 1 - \ln\left(\frac{r}{b}\right) = \frac{V_w}{b\omega}(\phi - \phi_0). \tag{2.4}$$

Introducing the coronal magnetic field after the reorganization, one can derive the Parker Spiral Magnetic Field (shown in Figure 2.4),

$$\begin{aligned} B_r(r,\theta,\phi) &= B(\theta,\phi_0)\left(\frac{b}{r}\right)^2 \\ B_\theta(r,\theta,\phi) &= 0 \\ B_\phi(r,\theta,\phi) &= B(\theta,\phi_0)\left(\frac{\omega}{V_w}\right)(r-b)\left(\frac{b}{r}\right)^2 \sin\theta. \end{aligned} \tag{2.5}$$

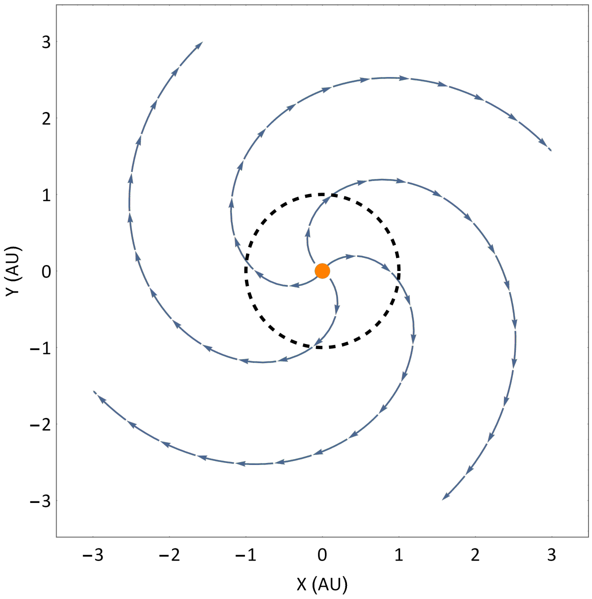

Figure 2.4: Projection onto the Solar equatorial plane of the lines of the force of the magnetic field. Dashed line is $r = 1\,\mathrm{AU}$, Earth's orbit around the Sun.

2.3 The Heliospheric Magnetic Field

We now begin to see the crucial role of solar wind as the agent behind both the existence of the heliosphere and the shape of the magnetic field inside of it since it will carry the magnetic field lines all across the solar system.

Even though the idea of a constant solar wind speed is only an approximation, the first measurements of the mean interplanetary magnetic field at Earth's orbit, made by Ness, Scearce and Seek, (1964)[61] showed rapid fluctuations ($\Delta B \sim B$). Despite that, they were able to estimate a mean field of $B \sim 0.6 \times 10^{-4}$ Gauss inclined to the expected spiral angle ($\psi = \arctan(r\omega/V_w)$) of $30 - 45°$ [62].

After Parker's original work [63, 58], there have been numerous developments. In the current understanding of the heliosphere, the plasma keeps expanding until its outward pressure equalizes with the Local Interstellar Medium (LISM)'s pressure and it becomes a boundary called the **heliopause**. Before this frontier, another boundary can be defined, the **Termination Shock**. It is the point after which the solar wind slows down and becomes subsonic [64]. Spacecrafts were sent across the Solar system to evaluate the behaviour of the heliosphere and the solar wind. Voyager 1, in 2004, and Voyager 2, in 2007, traversed the Termination Shock[65].

A recent picture of the heliosphere is drawn by Dialynas et al., (2017)[65] in which they show the different probe results and a full overview of the current understanding is made (as can be seen in Figure 2.5).

It is important to note how the influence of the LISM flow in the shape of the heliopause, as is shown figure 2.5.

Even though the heliosphere displays a complex shape on its furthest regions, close to Earth ($r := 1\,\mathrm{AU} = 149\,597\,871\,\mathrm{km}$), the radial solar wind (even if it has variable speed) is usually a good start when it comes to the analysis of the magnetic field[60].

The main solar magnetic field component is the dipole created from a major Magnetohydrodynamics (MHD) dynamo[60]. This magnetic dipole inverts its polarity with a periodicity of about 11 years, changing the entire spacial environment inside the solar system. A direct correlation was found between the solar activity cycle and the angle of the solar magnetic dipole with the rotation axis (known as tilt angle and henceforth shown as α) and the number of observed

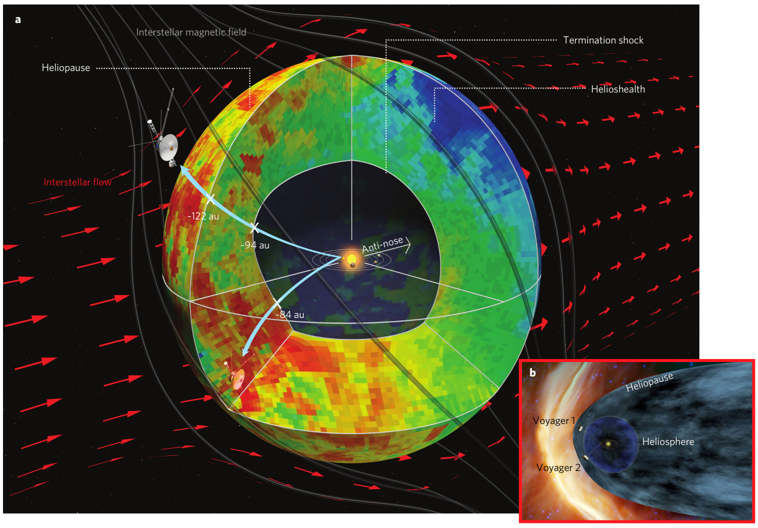

Figure 2.5: (a) Gross shape and basic properties of the global heliosphere in three dimensions based on both remote ENA and in situ ion measurements from Cassini/INCA and LECP/V1 and V2, respectively. (b) A magnetosphere-like configuration including an elongated heliotail (http://voyager.jpl.nasa.gov/mission/), widely adopted as one of two possibilities put forward by Parker in 1961[63]. Figure taken from Dialynas et al., (2017)[65].

sunspots was found (as can be seen in figure 2.6).

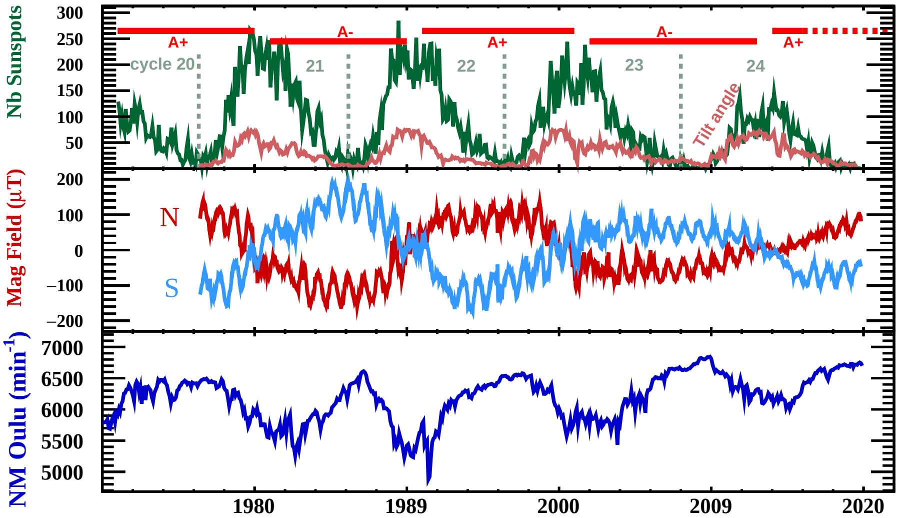

Figure 2.6: Comparison between neutron monitor counts, Sunspot number and tilt angle.

The existence of sunspots has been known since at least the fourth century B.C. These can be as large as 20000 km and have temperatures of 3000-4500 K, contrasting with the surrounding 5780 K. They are caused by intense magnetic activity which inhibits convection, thus allowing it to cool down [66]. These sunspots usually appear in pairs of opposing polarities but can also take place under other configurations. Figure 2.7 shows these sunspots in dark. As the Sun gets closer to flipping its magnetic dipole, the more twisted the magnetic field lines become, creating more areas of instability and Solar sunspots start to emerge in its surface.

With the increase in solar activity and magnetic field instability, prominences and their rupture become more frequent. These ruptures originate Coronal Mass Ejection (CME) which in turn will give rise to a decrease in the observed galactic cosmic ray, a process first observed in 1937 by Forbush, (1937)[68] and later named **Forbush decrease** [68].

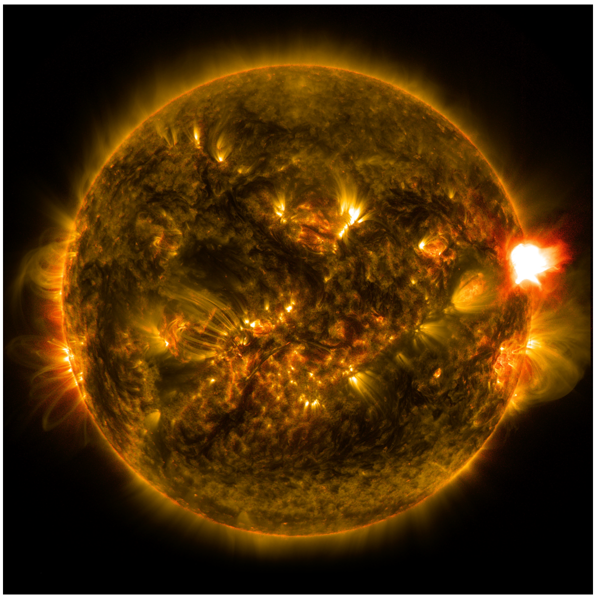

Figure 2.7: Photo of the sun displaying solar activity, magnetic loops, sunspots and a solar flare of M-class on the right side, from Jan. 12, 2015. The image blends two wavelengths of light – 171 and 304 angstroms – as captured by NASA's Solar Dynamics Observatory. Figure taken from NASA/SDO, (2014)[67].

During the course of the solar activity cycle the direction of the dipole changes and the angle it makes relative to the rotation axis goes from its measurable minimum at $\sim 10°$ to its observable maximum[69] at $\sim 70°$, by which time the organization of the magnetic field starts degrading and after a time it will start going from the maximum to the minimum but this time with an inverted polarity. The complete phenomenon of the reversal is a rather complex one and the estimation of the *moment* of reversal [70] can be constructed based on several solar observations such as the crossing of reversal of the radial magnetic field for the nothern and southern solar hemispheres or the reversal of the axial direction of the estimated dipole. In Figure 2.8 we can see a comparison between different solar observables from the middle of 2010 up to early 2014, at which time the reversal occurred. The graph showcases some of the different solar observables relevant to the reversal and some of the different reversal criteria which can be applied to determine its occurrence. Notably, on (c)Figure 2.8 we can see the radial component for the southern hemisphere nearly invert and increase for a time while the northern component reversed late 2012, decreased and nearly reversed back in early 2014. These observations showcase the complexity of the phenomenon and the need for direct usage of solar variables to tie cosmic-ray propagation models to the heliospheric environment directly.

These events all have major significance to the modelling of the Sun's magnetic field. Sunspots and CME's can create large fluctuations in the magnetic field and even if the frequency of their appearance is correlated with the solar activity cycle, they are not periodical in nature, as seen in Figure 2.6.

Apart from the 11-year cycle and its effect on the change in the flux, the 26-day rotation of the Sun is also responsible for variations in the magnetic field as a consequence of the tilt angle (α).

The fact that the Sun's magnetic field is mainly a dipole implies the existence of a plane that separates the two major magnetic domains, perpendicular to the dipole direction. This plane is called the Heliospheric Current Sheet (HCS).

By assuming that the magnetic field is reasonably stable across several Solar rotation periods it is possible to describe the topology of this magnetic field. The wind will flow

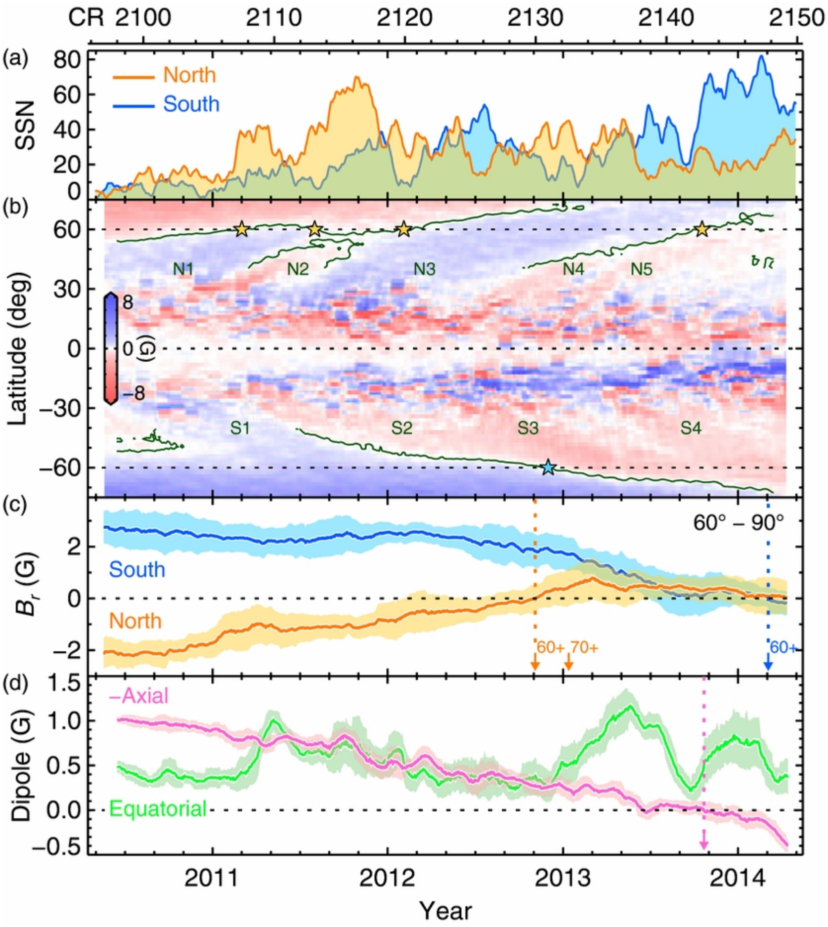

Figure 2.8: Magnetic field evolution. (a) SIDC hemispheric sunspot number (SSN). (b) Time-latitude diagram of zonally averaged Br. Contours indicate polarity inversion; their intersections with horizontal dotted lines indicate reversals at ±60° (star symbols). Here and after, N1-N5 and S1-S4 mark individual flux surges in the northern and southern hemispheres. (c) Mean Br above 60° as polar fields. (d) Global axial and equatorial dipole. The axial component is multiplied by -1 for better comparison. Averaging window is 30 days for (a) and (d). Vertical dotted lines and arrows mark the reversal times of polar fields above the denoted latitudes (c), and axial dipole (d). Image taken from Sun et al., (2015)[70].

continuously and propagate the magnetic field lines according to the Solar dipole configuration by the time of leaving the corona. The field lines will flow outward continuously and create a peculiar shape, Parker described this phenomenon as a ballerina skirt.

Any point in the Sun's surface is transported through the heliosphere by the Solar wind according to the following equations written in the Sun's coordinate system (one where the rotation axis is aligned with the Z direction),

$$\begin{aligned} r(t) &= V_w t + r_0, \\ \theta(t) &= \theta(t=0), \\ \phi(t) &= -\omega t + \phi_0, \end{aligned} \tag{2.6}$$

where V_w is the Solar wind speed and ω is the Sun's angular frequency for rotation.

In the case of a null tilt angle ($\alpha = 0$), all the points in the HCS are at the same $\theta = \theta_{\text{HCS}} = \pi/2$. The fact that there is a non-zero tilt angle demands that $\theta_0 = \theta_{\text{HCS}} = f(\phi_0)$. In all calculations that follow, the usage of θ' refers to the angle shown in figure 2.9, which relates to the angle of the point in spherical coordinates as $\theta' = \frac{\pi}{2} - \theta_{\text{HCS}}$.

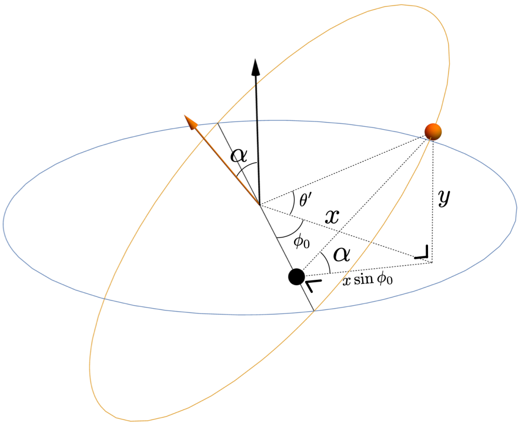

Figure 2.9: Diagram depicting the coordinates of the HCS in the Sun's coordinate system. The blue line represents the Solar system plane and the orange is the HCS plane at the Sun's surface. Black arrow represents solar rotation axis and the orange arrow the magnetic dipole direction.

Refering to figure 2.9, we can start by calculating the spherical coordinates of a point that lies in the HCS plane with respect to the Sun's coordinate system,

$$\begin{aligned} \tan\theta' &= \frac{y}{x} \\ \frac{y}{x\sin\phi_0} &= \tan\alpha \end{aligned} \tag{2.7}$$

which in turn leads to,

$$\tan\theta' = \tan\alpha\sin\phi_0 \Rightarrow \tan\left(\frac{\pi}{2} - \theta_{\text{HCS}}\right) = \tan\alpha\sin\phi_0 \tag{2.8}$$

The only substitution left is to parametrize ϕ_0 as a function of r and ϕ, so we can propagate it across space. This is done by making use of expression 2.6,

$$\phi_0 = \phi - \frac{\omega(r-b)}{v_w}, \tag{2.9}$$

which when inserted into 2.8 gives us $\theta_{\text{HCS}}(r,\phi)$,

$$\theta_{\text{HCS}} = \frac{\pi}{2} - \arctan\left[\tan\alpha\sin\left(\phi - \frac{\omega(r-b)}{v_w}\right)\right]. \tag{2.10}$$

The surface defined by sweeping ϕ and r can be seen in Figure 2.10.

Now that we know how the HCS behaves we can derive the full Parker magnetic field from Equation 2.5 by including the wavy neutral current sheet,

$$\vec{B}(r,\theta,\phi) = \frac{\pm B_0 r_0^2}{r^2}\left(\vec{e}_r - \frac{(r-b)\omega}{v_w}\sin\theta\,\vec{e}_\phi\right)[1 - 2H(\theta - \theta_{\text{HCS}})], \tag{2.11}$$

where $B_0 r_0^2$ is a constant which comes from the definition of the magnetic field and H is the Heaviside step function. The ± sign is there to characterize the Solar cycle modelled as being a positive, with fields lines coming out from the northern hemisphere or negative.

Now we have a picture of the solar wind and how it propagates the magnetic field through the heliosphere. The next step is understanding how charged particles interact with this magnetic field.

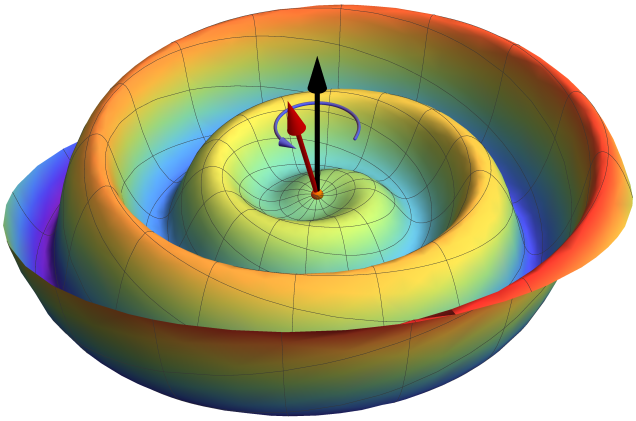

Figure 2.10: Artistic depiction of the Heliospheric Current Sheet. The black arrow indicates the axis of Solar rotation, the red arrow indicates the magnetic dipole direction and the purple arrow indicates solar rotation.

2.4 Parker's Transport Equation

Parker's contribution to the field of solar modulation did not stop at the modelization of the spiral solar wind and consequent magnetic field, he also helped understand the transport mechanisms cosmic rays face when they traverse the solar system. The cosmic ray transport equation through the solar system is known as Parker's Transport Equation due to the famous paper Parker, (1965)[71] in which derived it. It was later on more rigorously obtained by Gleeson and Axford, (1967)[72] which in the same paper derived an approximate solution so called Force-Field Approximation which will be discussed in detail in 6.2.

This section will now proceed to derive Parker's transport equation explaining the different steps and approximations as well as giving some insight on the different ingredients.

2.4.1 Transport in a magnetic field

When charged particles pass through a magnetic field they interact with the field lines, shifting their trajectories and changing their energies. The motion of the particle in the magnetic field is characterized by the circular motion around a central point (known as **guiding centre**) and the movement of that point. The radius of the circular motion is known as gyroradius and is defined as

$$r_g = \frac{P}{Bq}, \; P = \frac{pc}{Ze}, \tag{2.12}$$

where P is known as magnetic rigidity, p is the momentum of the particle, c is the speed of light, Z is the charge of the particle in electron charge units and e is the unitary charge of the electron.

This gyroradius is an essential tool in understanding the effect of the magnetic field on the particle since irregularities smaller than it do not affect the particle in a measurable way but, if the dimension of the irregularities is of the order of the gyroradius, the particle will begin a **random walk** process called diffusion[73].

2.4.2 Particle Density

The transport equation is the equation of motion of the isotropic differential density of cosmic rays through phase space[54].

We can start by considering an infinitesimal volume box $\mathrm{d}^3r = r^2 \sin\theta \,\mathrm{d}r\,\mathrm{d}\theta\,\mathrm{d}\phi$ containing $N = n\,\mathrm{d}^3r$ cosmic rays inside. We also wish to characterize this density in a given interval of kinetic energy per nucleon $(T, T + dT)$, so we define the differential density, U_T, such that all particles inside the volume are also in the same kinetic energy interval,

$$\begin{aligned} \mathrm{d}N &= U_T \ \mathrm{d}^3r \ \mathrm{d}T = U_T \, r^2 \sin\theta \ \mathrm{d}r \ \mathrm{d}\theta \ \mathrm{d}\phi \ \mathrm{d}T \\ &= U_P \ \mathrm{d}^3r \ \mathrm{d}P \\ &= U_p \ \mathrm{d}^3r \ \mathrm{d}p \end{aligned} \tag{2.13}$$

As we can see, this differential density can be defined as a function of rigidity or momentum as well (U_p, U_P), with the appropriate transformations ($U_P = (\beta c/A)U_T$, where c is the speed of light, $\beta = v/c$ and A is the atomic number).

This definition of differential density assumes an isotropic distribution of particles since when an interval of kinetic energy (or momentum) is chosen it implies an integration over all directions. Cosmic ray detectors do not measure differential densities, they measure differential intensities, so we must see how many of the particles in our volume will go through an infinitesimal area dA at any given time (as depicted in figure 2.11).

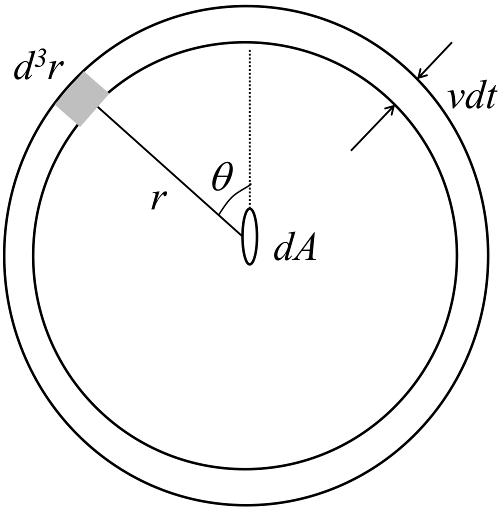

Figure 2.11: Intensity of particles going through the ring. Taken from Moraal, (2011)[54].

The number of particles that go through the detector at some given time were moving towards the detector at a speed of v at a time prior to the detection (grey area in figure 2.11). This number is given by replacing the term dr by $v\,\mathrm{d}t$ in Equation 2.13,

$$\mathrm{d}n' = U_T \ \mathrm{d}^3r \ \mathrm{d}T = U_T \, r^2 \sin\theta \, v \, \mathrm{d}t \ \mathrm{d}\theta \ \mathrm{d}\phi \ \mathrm{d}T \,. \tag{2.14}$$

Since these particles are moving in all directions, the fraction of them that will actually go through the detector is $\mathrm{d}A\,|\cos\theta|/4\pi r^2$, making the total number of particles from the previously mentioned volume that cross the detector in a time interval dt be,

$$\mathrm{d}n'' = \mathrm{d}n' \left(\frac{\mathrm{d}A\,|\cos\theta|}{4\pi r^2}\right) = U_T \left(\frac{\mathrm{d}A\,|\cos\theta|}{4\pi r^2}\right) r^2 \sin\theta \, v \, \mathrm{d}t \ \mathrm{d}\theta \ \mathrm{d}\phi \ \mathrm{d}T \,. \tag{2.15}$$

Integrating Equation 2.15 over θ and ϕ, we get that the number of particles passing through the detector per unit of area, per unit of time, per unit of kinetic energy interval. Since it's common practice to refer not to the total number of particles but rather those coming from one steradian of solid angle[54] we will divide the integral by 4π, giving rise to the following expression

$$j_T = \iint \frac{\mathrm{d}n''}{4\pi} \, \mathrm{d}\theta \, \mathrm{d}\phi = \frac{v\,U_T}{8\pi} = \left(\frac{A}{8\pi Ze}\right) U_P \,. \tag{2.16}$$

This quantity has the dimension of particles/m^2/s/sr/GeV/nucleon is commonly labelled the **differential flux of cosmic rays** crossing a detector. Similarly, one can see that $j_p = vU_p/8\pi$ and $j_P = vU_P/8\pi$. These fluxes relate to each other through the identity $U_T\,\mathrm{d}T = U_p\,\mathrm{d}p = U_P\,\mathrm{d}P$.

Since it is common practice to think in terms of the particle distribution function rather than in terms of differential density U, the number of particles can be more robustly described by a distribution in $\vec{r}$ and $\vec{p}$, written as $\mathrm{d}n = F(\vec{r},\vec{p},t)\ \mathrm{d}^3r\ \mathrm{d}^3p$. To note the difference between F and U_p, one can examine their definitions

$$\begin{aligned} F &= \frac{\mathrm{d}n}{\mathrm{d}^3r\,\mathrm{d}^3p} \\ U_p &= \frac{\mathrm{d}n}{\mathrm{d}^3r\,\mathrm{d}p} \end{aligned} \tag{2.17}$$

and note that one can be derived from the other.

The particles coming from the volume cell in Figure 2.11 is then

$$\begin{aligned} \mathrm{d}n &= \mathrm{d}^3p\,\mathrm{d}^3r\int_\Omega F(\vec{r},\vec{p},t)\,\mathrm{d}\Omega \\ &= p^2\,\mathrm{d}p\,\mathrm{d}^3r\int_\Omega F(\vec{r},\vec{p},t)\,\mathrm{d}\Omega \end{aligned} \tag{2.18}$$

but since U_p obeys Equation 2.17, one can easily see that

$$U_p = p^2\int_\Omega F(\vec{r},\vec{p},t)\,\mathrm{d}\Omega$$

From that, we can define our directional average of the distribution function as,

$$f(\vec{r},p,t) = \frac{\int_\Omega F(\vec{r},\vec{p},t)\,\mathrm{d}\Omega}{\int_\Omega \mathrm{d}\Omega} = \frac{1}{4\pi}\int_\Omega F(\vec{r},\vec{p},t)\,\mathrm{d}\Omega\,. \tag{2.19}$$

Finally, we arrived at a robust and useful definition of our cosmic ray distribution as an isotropic distribution of cosmic rays in the interval $\vec{r}+\mathrm{d}\vec{r}$ and $p+\mathrm{d}p$ which crosses our detector with an intensity of

$$j_T = \frac{A}{8\pi}U_p = \frac{A}{2}p^2 f \tag{2.20}$$

2.4.3 Cosmic-Ray Transport Equation

We can start constructing the Parker transport equation using continuity:

$$\frac{\mathrm{d}N}{\mathrm{d}t} = -\oint \vec{S}\cdot\frac{\mathrm{d}\vec{A}}{\mathrm{d}t} + Q, \tag{2.21}$$

which, according to the divergence theorem, $\oint \vec{S}\cdot\mathrm{d}\vec{A} = \int(\nabla\cdot\vec{S})\,\mathrm{d}\tau$, where $\mathrm{d}\tau$ is the volume element within the surface $\oint \mathrm{d}\vec{a}$. Using $N = \int n\,\mathrm{d}\tau$, we can write out the differential form of the equation as,

$$\frac{\partial f}{\partial t} + \nabla\cdot\vec{S} = q', \tag{2.22}$$

where q' is the source/sink function per unit of volume.

The physics of a propagation phenomenon can be express in terms of a given flux $\vec{S}$ [54]. In this case, the flux is split into a diffusive flux due to the scattering of the particles over the irregularities of the HMF and a radial convective flux due to the solar wind $\vec{S}_c = n\vec{V}$ [54, 74].

2.4.4 Particle Diffusion and Drifts

As charged cosmic rays traverse the solar system they encounter a magnetized plasma and their trajectories are changed as they attach themselves to the magnetic field lines carried by the solar wind. This propagation process is usually modelled as having two major components, a (mostly) smooth transport of the guiding centre, as the particle gyrotates following the background magnetic field, and a diffusive process in which the before mentioned trajectory is abruptly changed by irregularities in the magnetic field lines.

Particle motion can then be understood as a superposition of a gyrorotation of the particle and a stochastic motion of the guiding centre, which follows the magnetic field lines, showing the diffuse nature of this transport mechanism [75]. The relation between the gyroradius of the particle and the irregularities in the background magnetic field line will dictate the general motion of the particle. Highly energetic particles (when compared to the magnetic field) will travel mostly unaffected by the magnetic field, a feature we will recover later in the cosmic ray fluxes. Figure 2.12 shows some of the scattering processes a particle suffers while travelling through a magnetic field.

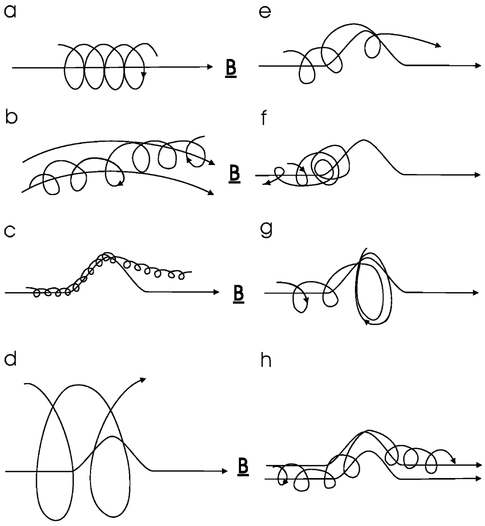

Figure 2.12: Different motions of a charged particle in a magnetic field. Taken from Moraal.

This diffusion is split into components parallel and perpendicular to the magnetic field lines. Diffusion parallel to the background magnetic field is studied under the so-called quasi-linear theory of scattering, which holds true for weak fluctuations ($\frac{\Delta B^2}{B^2} \ll 1$) and allows to write the parallel diffusion coefficient as a function of the rigidity spectrum of ΔB^2. This theory goes back to the paper of Jokipii in which he studied how the fluctuations in the magnetic field affects particle motion and offered insight on this mechanism for propagation of particles in the solar system. The process of perpendicular diffusion is still a big topic in the field and is now understood as a combination of field line random walk, backscattering from parallel diffusion and a transfer of particles across field lines due to the magnetic field's perpendicular complexity and scale [76]. Recent developments in the field include Matthaeus et al., Bieber, Matthaeus and Shalchi. Further details can be seen in Salchi.

With this understanding and using Fick's law we can write the diffusive flux as

$$\vec{S}_d = k_{\parallel} \nabla n_{\parallel} + k_{\perp} \nabla n_{\perp} \tag{2.23}$$

where both k's represent the diffusion coefficients parallel and perpendicular to underlying magnetic field lines. Under normal conditions, in the solar magnetic plasma, $k_{\perp} \ll k_{\parallel}$ [73]. This is called the weak-scattering limit. The upper limit for the diffusion coefficients happens when $k_\perp = k_\parallel$, in which case the fluctuations in the field are so high that they become as large as the background value, making the notion of a well-ordered background disappear and the diffusion process becomes isotropic since the diffusion tensor becomes scalar[54].

So far we've seen how small-scale changes in the magnetic field are responsible for perturbing the trajectories of cosmic rays. Another important transport mechanism is the organized drift motion that charged particles suffer due to large-scale structures in the magnetic field. These are known as the gradient and curvature drifts. It is possible to describe the drifts of particles, under the weak-scattering condition, using the following general expression, as given by Jokipii and Levy,

$$\langle \vec{v}_d \rangle = \frac{\beta P}{3} \nabla \times \frac{\vec{B}}{B^2}, \tag{2.24}$$

giving rise to a flux of the form,

$$\vec{S}_d = \frac{\beta P}{3B^2} \vec{B} \times \nabla n. \tag{2.25}$$

For the Parker field (Equation 2.5), the drift velocity is shown to be [79],

$$\langle \vec{v}_d \rangle = \frac{2pv(r-b)}{\pm B_0 r_0^2 3q(1+\Gamma^2)^2} [1 - 2H(\theta - \theta_{\mathrm{HCS}})] \left[-\frac{\Gamma}{\tan\theta} \vec{e}_r + (2+\Gamma^2)\Gamma \vec{e}_\theta + \frac{\Gamma^2}{\tan\theta} \vec{e}_\phi \right], \tag{2.26}$$

where $\Gamma = (r-b)\omega \sin\theta / V_w$, q is the charge, p the momentum and v the velocity.

The drift motion of particles in a magnetic field can be included into the diffusion formalist presented in the beginning of this section by writing it as an antisymmetric element of the cosmic ray diffusion tensor in the following way

$$\mathbf{k} = k_{ij} = \begin{pmatrix} k_\parallel & 0 & 0 \\ 0 & k_\perp & -k_T \\ 0 & k_T & k_\perp \end{pmatrix}, \tag{2.27}$$

where $k_T = \beta P/(3B)$, thus contracting the drift flux and the anisotropic diffusion into a single term, $-\mathbf{k} \cdot \nabla n$. This treatment of the drift effect is completely equivalent to direct usage of equation 2.24. This formalism was first used by Jokipii and Levy, (1977)[78].

We can now simply write our flux as,

$$\vec{S} = \vec{V} n - \mathbf{k} \cdot \nabla n, \tag{2.28}$$

with $\vec{V} n$ as the simple convective drift of the Solar wind.

This leads us to $\partial n/\partial t + \nabla \cdot (\vec{V} n - \mathbf{k} \cdot \nabla n) = q'$ or, equivalently, $\partial f/\partial t + \nabla \cdot (\vec{V} f - \mathbf{k} \cdot \nabla f) = q$.

After taking this result into consideration and combining it with both the divergence of the flux in momentum space and the adiabatic cooling (this due to the fact that particles ride with the fields in the wind and that these fields expand due to the positive divergence of the wind speed at a rate of change of momentum of $\langle \dot{p} \rangle / p = -(1/3) \nabla \cdot \vec{V}$) Parker reached the final form of the transport equation,

$$\frac{\partial f}{\partial t} + \nabla \cdot (\vec{V} f - \mathbf{k} \cdot \nabla f) - \frac{1}{3p^2} (\nabla \cdot \vec{V}) \frac{\partial}{\partial p} (p^3 f) = q, \tag{2.29}$$

which has the simplest form (and the one we will be using further on)

$$\frac{\partial f}{\partial t} + \nabla \cdot (\vec{V} f - \mathbf{k} \cdot \nabla f) - \frac{1}{3} (\nabla \cdot \vec{V}) \frac{\partial f}{\partial \ln p} = q. \tag{2.30}$$

As a final remark, the existence of a neutral current sheet, a discontinuity in the magnetic field, generates a drift of particles that follow it if they get close enough that their gyroradius intersects it, as depicted in figure 2.13. This drift is parallel to the surface and perpendicular to the magnetic field. Our calculation assumes that the HCS is locally flat enough to use the approximation of the drift over a flat surface, as was done by Burger, Moraal and Webb, (1985)[80]. Our expression for this drift then becomes,

$$\left\langle \vec{V}_d \right\rangle = \frac{2pv(r-b)}{\pm B_0 r_0^2 3q(1+\Gamma^2)} \delta(\theta - \theta_{\mathrm{HCS}})(\Gamma \vec{e}_r + \vec{e}_\phi), \tag{2.31}$$

where $\Gamma = (r-b)\omega \sin\theta / V_w$, q is the charge, p the momentum and v the velocity. Burger [81] introduced a parametrization that requires a calculation of the normal to the HCS at every point and the distance to it, which can be quite cumbersome. We shall use the first one in our simulations.

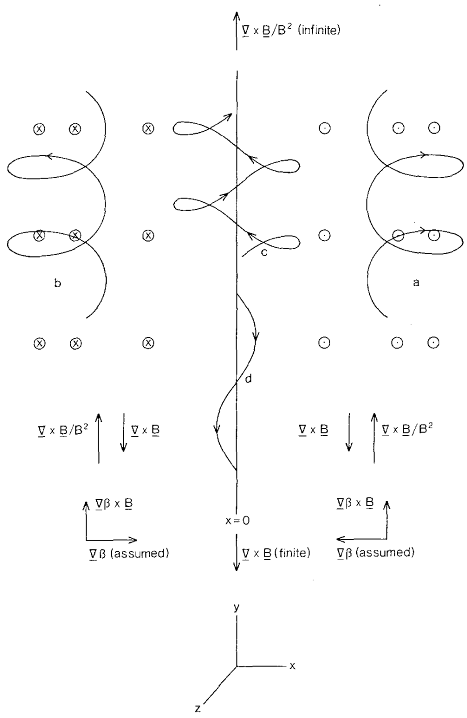

Figure 2.13: Trajectories of positively charged particles in and near a neutral plane. Image taken from Burger, Moraal and Webb, (1985)[80].

Lastly, another approach was suggested by Potgieter and Moraal, (1985)[82]. In their paper they studied the 2D model (r and θ) and, due to simetry, the study was only done in $0 < \theta < \pi/2$. He suggested that a transition function could be created so that it was simpler to compute the numerical model near the HCS. This function introduces a drift so that the nothern hemisphere of the heliosphere is defined not with a wavy bottom (due to the HCS) but instead with a flat surface. The required drift velocity had the form

$$\left\langle \vec{V}_d \right\rangle = \frac{K_T \sin\Psi}{r} \left[-\left(2\cos^2\Psi \cot\theta + \frac{\dot{\mathrm{f}}}{\mathrm{f}} \right) \vec{e}_r + 2(\cos^2\Psi + 1)\vec{e}_\theta - \left(2\sin^2\Psi \cot\theta + \frac{\dot{\mathrm{f}}}{\mathrm{f}} \right) \vec{e}_\phi \right], \tag{2.32}$$

where $\Psi = \arctan(r\omega/V_w)$, known as the Parker spiral angle, the f, the smoothing function, is defined as

$$f(\theta) = \frac{1}{\alpha} \arctan\left[\left(1 - \frac{2\theta}{\pi} \right) \tan\alpha \right],$$

and α is

$$\alpha = \arccos\left(\frac{\pi}{2\theta_{1/2}} - 1 \right).$$

This method was not used in this work but, for completeness sake, had to be mentioned.

2.4.5 Solar Magnetic Field & Drift motion

Expanding equation 2.30 in 3 dimensions gives

$$\begin{aligned}
\frac{\partial f}{\partial t} &= k_{rr}\frac{\partial^2 f}{\partial r^2} + \frac{k_{\theta\theta}}{r^2}\frac{\partial^2 f}{\partial \theta^2} + \frac{k_{\phi\phi}}{r^2\sin^2\theta}\frac{\partial^2 f}{\partial \phi^2} \\
&+ \frac{k_{\theta r}+k_{r\theta}}{r}\frac{\partial^2 f}{\partial r\partial\theta} + \frac{k_{\phi r}+k_{r\phi}}{r\sin\theta}\frac{\partial^2 f}{\partial r\partial\phi} + \frac{k_{\phi\theta}+k_{\theta\phi}}{r^2\sin\theta}\frac{\partial^2 f}{\partial\theta\partial\phi} \\
&+ \left(\frac{2k_{rr}}{r} + \frac{\cot\theta k_{\theta r}}{r} + \frac{1}{r\sin\theta}\frac{\partial k_{\phi r}}{\partial\phi} + \frac{1}{r}\frac{\partial k_{\theta r}}{\partial\theta} + \frac{\partial k_{rr}}{\partial r}\right)\frac{\partial f}{\partial r} \\
&+ \left(\frac{k_{r\theta}}{r^2} + \frac{\cot\theta k_{\theta\theta}}{r^2} + \frac{1}{r^2\sin\theta}\frac{\partial k_{\phi\theta}}{\partial\phi} + \frac{1}{r^2}\frac{\partial k_{\theta\theta}}{\partial\theta} + \frac{1}{r}\frac{\partial k_{r\theta}}{\partial r}\right)\frac{\partial f}{\partial\theta} \\
&+ \left(\frac{k_{r\phi}}{r^2\sin\theta} + \frac{1}{r^2\sin^2\theta}\frac{\partial k_{\phi\phi}}{\partial\phi} + \frac{1}{r^2\sin\theta}\frac{\partial k_{\theta\phi}}{\partial\theta} + \frac{1}{r\sin\theta}\frac{\partial k_{r\phi}}{\partial r}\right)\frac{\partial f}{\partial\phi} \\
&- \left(V_{wr}\frac{\partial f}{\partial r} + \frac{V_{w\theta}}{r}\frac{\partial f}{\partial\theta} + \frac{V_{w\phi}}{r\sin\theta}\frac{\partial f}{\partial\phi}\right) \\
&+ \frac{1}{3}\left(\frac{2}{r}V_{wr} + \frac{\cos\theta}{r\sin\theta}V_{w\theta} + \frac{1}{r\sin\theta}\frac{\partial V_{w\phi}}{\partial\phi} + \frac{1}{r}\frac{\partial V_{w\theta}}{\partial\theta} + \frac{\partial V_{wr}}{\partial r}\right)\frac{\partial f}{\partial\ln p}
\end{aligned} \tag{2.33}$$

If only the r and θ directions are considered and the Parker model for the magnetic field (i.e. radial Solar wind and dipole magnetic field) is assumed we get,

$$\begin{aligned}
\frac{\partial f}{\partial t} &= k_{rr}\frac{\partial^2 f}{\partial r^2} + \frac{k_{\theta\theta}}{r^2}\frac{\partial^2 f}{\partial\theta^2} \\
&+ \left(\frac{2k_{rr}}{r} + \frac{\cot\theta k_{\theta r}}{r} + \frac{1}{r}\frac{\partial k_{\theta r}}{\partial\theta} + \frac{\partial k_{rr}}{\partial r}\right)\frac{\partial f}{\partial r} \\
&+ \left(\frac{k_{r\theta}}{r^2} + \frac{\cot\theta k_{\theta\theta}}{r^2} + \frac{1}{r^2}\frac{\partial k_{\theta\theta}}{\partial\theta} + \frac{1}{r}\frac{\partial k_{r\theta}}{\partial r}\right)\frac{\partial f}{\partial\theta} \\
&- V_{wr}\frac{\partial f}{\partial r} + \frac{2V_{wr}}{3r}\frac{\partial f}{\partial\ln p}
\end{aligned} \tag{2.34}$$

From equation 2.24 we can see that,

$$\begin{aligned}
(\nabla\cdot k_T)_r &= \frac{1}{r}\frac{\partial k_{\theta r}}{\partial\theta} + \frac{\cot\theta}{r}k_{\theta r} = V_{gr}, \\
(\nabla\cdot k_T)_\theta &= \frac{\partial k_{r\theta}}{\partial r} + \frac{k_{r\theta}}{r} + \frac{1}{r\sin\theta}\frac{\partial k_{\phi\theta}}{\partial\phi} = V_{g\theta}, \\
(\nabla\cdot k_T)_\phi &= \frac{1}{r}\frac{\partial k_{\theta\phi}}{\partial\theta} = V_{g\phi},
\end{aligned} \tag{2.35}$$

which makes equation 2.34 become,

$$\begin{aligned}
\frac{\partial f}{\partial t} &= k_{rr}\frac{\partial^2 f}{\partial r^2} + \frac{k_{\theta\theta}}{r^2}\frac{\partial^2 f}{\partial\theta^2} + \left(\frac{2k_{rr}}{r} + \frac{\partial k_{rr}}{\partial r} - V_{wr} + V_{gr}\right)\frac{\partial f}{\partial r} \\
&+ \left(\frac{\cot\theta k_{\theta\theta}}{r} + V_{g\theta}\right)\frac{1}{r}\frac{\partial f}{\partial\theta} + \frac{2V_{wr}}{3r}\frac{\partial f}{\partial\ln p}.
\end{aligned} \tag{2.36}$$

These drift velocities were calculated in 2.26. In Figure 2.14 we can see the typical direction of particle drift motion for the Parker solar magnetic field. During the positive polarity ($A > 0$), positive particles will suffer a drift motion from the polar regions and towards the equatorial plane, where they will begin to be affected by the HCS structure which will provide an additional drift which radially moves outwards towards from the Sun. During negative polarities ($A < 0$) particles will suffer the complete opposite drift motion, equatorially towards

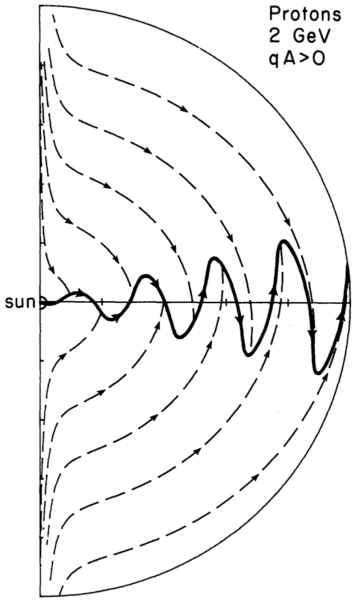

Figure 2.14: Meridional projection of the drift trajectories (including convection with the solar wind) for 2 GeV protons with qA $>$ 0. Image taken from Jokipii and Davila, (1981)[83].

the sun and elsewhere towards the polar regions. Both effects will be mirrored for particles of the opposite charge, creating a charge sign dependent phenomenon for particles and their anti-particles. This effect was observed by AMS in the time-resolved positron-to-electron flux ratio published in Aguilar et al., (2018)[47] (see Figure 2.15). Additionally, the graph also highlights the dependence on particle energy.

Since the diffusion tensor was defined in terms of the parallel and perpendicular directions to the magnetic field lines, the coordinate transformation from the spherical referential to the magnetic field referential has to be calculated. As can be seen in equation 2.11, the magnetic field has no θ component. This simplifies the problem since we can start by defining the θ direction as $\vec{e}_{\perp\theta}$, making $\vec{e}_{\|} = \frac{\vec{B}}{B}$ and the third as perpendicular to the other two,

$$\begin{aligned} \vec{e}_{\|} &= \cos\Psi\vec{e}_r - \sin\Psi\vec{e}_\phi \\ \vec{e}_{\perp\theta} &= \vec{e}_\theta \\ \vec{e}_{\perp r} &= \vec{e}_{\|} \times \vec{e}_{\perp\theta}. \end{aligned} \tag{2.37}$$

This gives out the following change of coordinates between the two systems,

$$\begin{pmatrix} k_{\mathrm{rr}} & k_{\mathrm{r}\theta} & k_{\mathrm{r}\phi} \\ k_{\theta\mathrm{r}} & k_{\theta\theta} & k_{\theta\phi} \\ k_{\phi\mathrm{r}} & k_{\phi\theta} & k_{\phi\phi} \end{pmatrix} = \begin{pmatrix} k_{\|}\cos^2\Psi + k_{\perp\mathrm{r}}\sin^2\Psi & -k_{\mathrm{T}}\sin\Psi & (k_{\perp\mathrm{r}} - k_{\|})\cos\Psi\sin\Psi \\ k_{\mathrm{T}}\sin\Psi & k_{\perp\theta} & k_{\mathrm{T}}\cos\Psi \\ (k_{\perp\mathrm{r}} - k_{\|})\cos\Psi\sin\Psi & -k_{\mathrm{T}}\cos\Psi & k_{\|}\sin^2\Psi + k_{\perp\mathrm{r}}\cos^2\Psi, \end{pmatrix} \tag{2.38}$$

where $\tan\Psi = \frac{\omega(r-b)\sin\theta}{V_w}$. This transformation was the same used in Burger et al., (2008)[84].

The coefficient chosen in this work was the one used by Pei et al., (2010)[85]. Even though there is still constant debate over the general form of the diffusion coefficient, one of the most used as a benchmark [83, 86, 87] (which comes from Quasi-Linear Theory (QLT) of plasma) is

$$k_{\|} = k_0 \beta P \frac{B_\odot}{B}, \tag{2.39}$$

where $B_\odot$ is the Solar magnetic field measured near Earth.

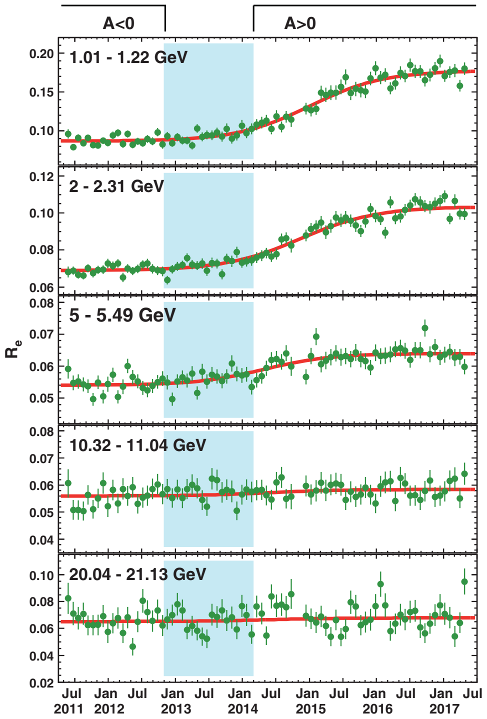

Figure 2.15: The ratio Re of the positron flux to the electron flux as a function of time as measured by AMS. The polarity of the heliospheric magnetic field is denoted by A $<$ 0 and A $>$ 0. The period without well-defined polarity is marked by the shaded area. Image taken from Aguilar et al., (2018)[47].

For the perpendicular diffusion coefficient, a common choice is $k_\perp/k_\parallel = 0.1$. Ways to determine the appropriate diffusion coefficient usually envolve the study of turbulence models based on spacecraft measurements [88, 89], which is out of the scope of this work.

Some times the following simpler version is used [54, 90],

$$k_\parallel = k_0 \beta P. \tag{2.40}$$

Several approaches can be taken to solve this very complex transport equation. The most common methodologies involve the Force-Field approximation which we will detail later and the finite-difference numerical scheme. A review of some of these methods can be found in Orcinha, (2014)[91]. In recent years the solving of transport equations through the stochastic differential method have been gaining traction[92] as solving scheme codes have become publicly available. We will be using a modified version of the SOLARPROP[92] code base in order to study the cosmic-ray proton flux.

3

The Alpha Magnetic Spectrometer

The AMS (as shown in figure 3.1) is a state-of-the-art particle physics detector mounted on the ISS. It was built, tested and is being operated by an international collaboration of 56 institutions from 16 countries, under the sponsorship of the United States Department of Energy. It was installed in the ISS by National Aeronautics and Space Administration (NASA) in 2011 and is designed to operate during the remainder of the station's lifetime.

Figure 3.1: Photograph of the AMS-02 detector on the International Space Station. Figure taken from AMS-02 Collaboration, (2014)[93]

3.1 Brief History

AMS-02 is the second iteration of the Alpha Magnetic Spectrometer, a detector proposed by the group led by Samuel Ting in 1995. Under Professor Ting's direction, the prototype, AMS-01, was built and made a 2 day flight in orbit in June 1998.

Through its results, AMS-01 proved the success of its magnetic spectrometer design in a space environment and was a fundamental step towards the building of the AMS-02. One of its scientific results was that it was able to establish an upper limit of 1.1×10^{-6} for the antihelium to helium flux ratio[94].

In 16 May of 2011, the Space Shuttle Endeavour carried AMS-02 into space, in the flight STS-134. AMS-02 was installed 3 days later, beginning its data acquisition and, counting over 205 billion events up to July 2022.

3.1.1 Physics Goals

The AMS experiment has several goals: the detailed measurement of the cosmic ray spectrum, the search for cosmological antimatter and the indirect search for dark matter signals. It is also able to detect γ-rays using its electromagnetic calorimeter and its Silicon Tracker.

3.2 Sub-Detectors

The AMS-02 detector is composed of several sub-detectors and sub-systems (as seen in figure 3.2). As a whole, it's designed to make independent measurements of several physical properties (electric charge, rigidity, velocity and energy) in order to identify the particle species and be able to precisely measure the cosmic ray spectrum.

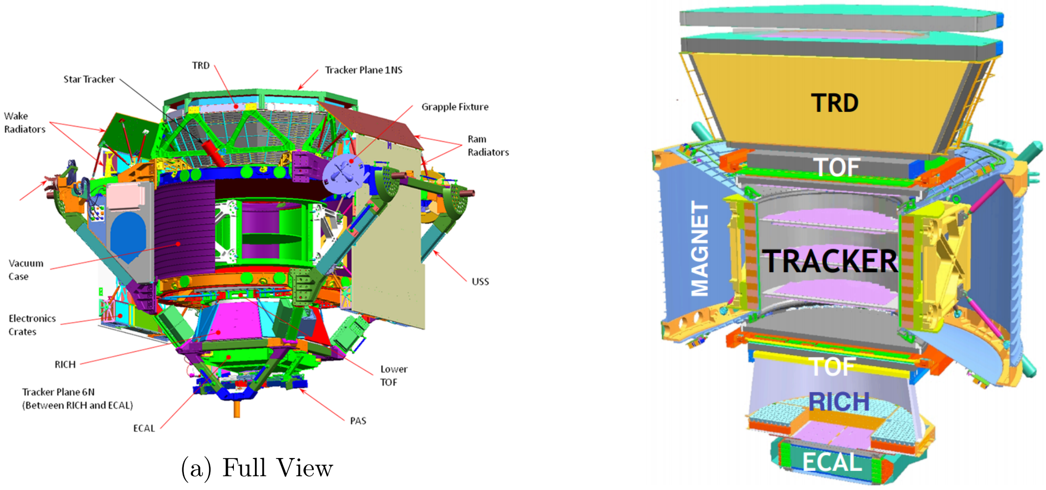

(a) Full View

(b) Detailed View

Figure 3.2: Detailed schematic representation of the AMS-02 detector. Figures taken from AMS-02 Collaboration, (2014)[93] and Ting, (2010)[95].

The AMS detector (see Figure 3.2) is, fundamentally, a magnetic spectrometer, it uses a central permanent magnet to bend the trajectory of charged particles which cross it in order to measure their rigidity ($P = p/Z$) by interpolating the particle's trajectory using a silicon tracker which is spread through the detector and within the magnet itself.

The detector is also equipped with a ToF detector which consists of 4 orthogonal planes of ToF counters which, at a fixed distance measure particle velocity and, due to their sensitivity, provide the main trigger on AMS. They are also complementarily used in tracking the particle's trajectory. The Transition Radiation Detector (TRD) is located at the top of AMS and provides a measurement which helps distinguish between leptons and hadrons and is also capable of providing a rough estimation of particle direction and position in AMS. Bellow the magnet lies the Ring-Imaging Cherenkov Detector (RICH) detector which offers both charge and velocity measurement capabilities in AMS. It offers both a complementary measurement of charge and also a more precise velocity measurement which extends the velocity measurement range of AMS. This instrument is fundamental in extending the range and improving mass and velocity separation capabilities of AMS.

At the bottom of the detector, the Electromagnetic Calorimeter (ECAL) is capable of identifying and separating hadronic and electromagnetic showers and thus identify the particle which collided with it. Same as the TRD, but with more sensitivity, it is capable of making an estimation of particle direction and position but to a much lesser degree than the Tracker. It is also an alternative trigger in AMS. Both ECAL and TRD are great tools for rejection and provide complementary measurements to the rest of the detector.

AMS offers great identification capabilities from 1 GV up to a few TeV. Other experiments have successfully used calorimeters[96, 97, 98] in space in order to achieve TeV-scale measurements but, without a magnet, they will forego charge sign measurement and will only be capable of measuring both particles and their respective anti-particles together.

3.2.1 Silicon Tracker & Permanent Magnet

In the centre of the detector lies a Neodymium-Iron-Boron permanent magnet. This magnet surrounds most of the Silicon Tracker (TRK) making possible rigidity measurement. It is fundamental in AMS since it is the only sub-detector to allow for a direct electric charge sign measurement (particles of different electric charge signs bend in opposite directions). This capability is paramount in AMS's contribution to understanding antimatter and dark matter in the Universe.

The TRK (seen in Figure 3.3) consists of 9 layers, L1-L9, made up of 2264 double-sided silicon sensors split into 192 ladders and it is responsible for measuring the particle's rigidity, charge and energy loss.

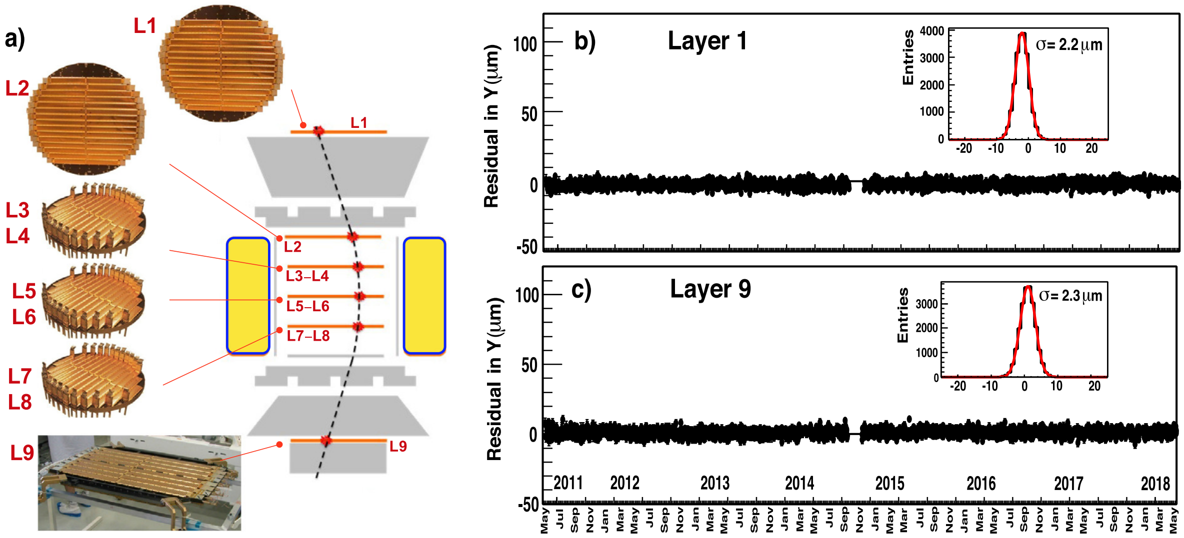

Figure 3.3: (a) The 9 layers of the AMS silicon tracker and their locations within the detector. The alignment stability of (b) Layer 1 and (c) Layer 9 over seven years. Figure taken from Figure 4 of Aguilar et al., (2021)[38].

It is also equipped with a Tracker Alignment System (TAS) which consists of 20 IR laser beams which are used to periodically calibrate the individual tracker planes in order to keep track of TRK's mechanical deformations due to temperature changes with micron level accuracy (ISS has an orbital period of $\sim$ 93 minutes, changing rapidly from daylight to darkness depending on the orbit). The L1 and L9 planes are aligned every 2 minutes using cosmic ray protons. The tracker is capable of providing a spatial resolution of 5-10 μm in the bending direction and about 13-20 in the non-bending direction[38].

Due to this level of precision and calibration, the tracker is capable of holding 2-3μm plane alignment, as can be seen in Figure 3.3. This level of temporal stability enables time-variability studies as the ones presented in the later chapters of this work.

By making use of the hits from each plane, the TRK is able to measure rigidity by estimating the curvature in the particle's trajectory inside AMS's permanent magnetic field. It is also possible to interpolate the particle's trajectory, allowing for a precise estimation of the particle's entry point in the different sub-detectors (RICH depends on this estimation in order to make its own) in order to characterize their performance. The magnetic field map was estimated to a great degree of precision in order to accurately infer the particle's trajectory from the hits on the TRK planes.

As we will later discuss, the tracker is capable of having a high degree of precision in both charge and rigidity measurements. Figure 3.4 shows TRK rigidity resolution for test beam events at 400 GV and rigidity measurement consistence performance between L1 to L8 tracks and L2 to L9 tracks.

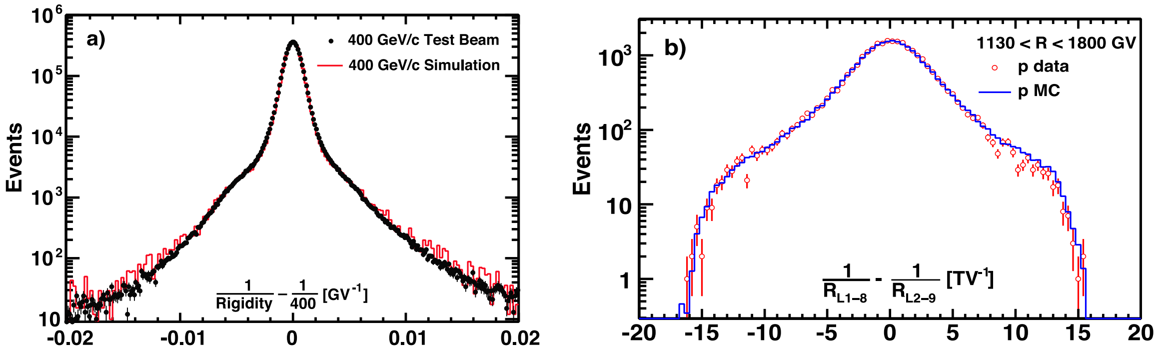

Figure 3.4: (a) Comparison between data and the Monte Carlo simulation of the inverse rigidity measured by the tracker for 400 GV test beam protons. As seen, the agreement between the data and the Monte Carlo simulation extends over five orders of magnitude. (b) The difference of the inverse rigidities measured with the upper (Layers L1–L8) and the lower (Layers L2–L9) parts of the tracker for the cosmic ray proton data collected on the ISS and for the Monte Carlo simulation in the rigidity range [1130-1800]GV. Figure taken from Figure 9 of Aguilar et al., (2021)[38].

As previously stated, the tracker is also capable of measuring energy loss as a particle traverses each of the planes. Combined with a velocity measurement, this provides a charge measurement for each of this planes which can be used to estimate particle charge. The inner TRK charge, l2-L8 is one of the main charge measurements used in this analysis (see Figure 3.5. Combined with the ToF charge measurement, it offers an incredible degree of precision at this analysis' rigidities.

3.2.2 Anti-Coincidence Counter

The Anti-Coincidence Counter is a system built around the inside of AMS's magnet in order to reject particles which would transverse the detector from the side. These particles would interfere with the detection of other particles.

It is comprised of 16 curved scintillating panels whose sole purpose is to detect events resulting from particles crossing the detector sideways or to help reject particles that interacted inside the detector and displaying erratic trajectories after collision (see Figure 3.6).

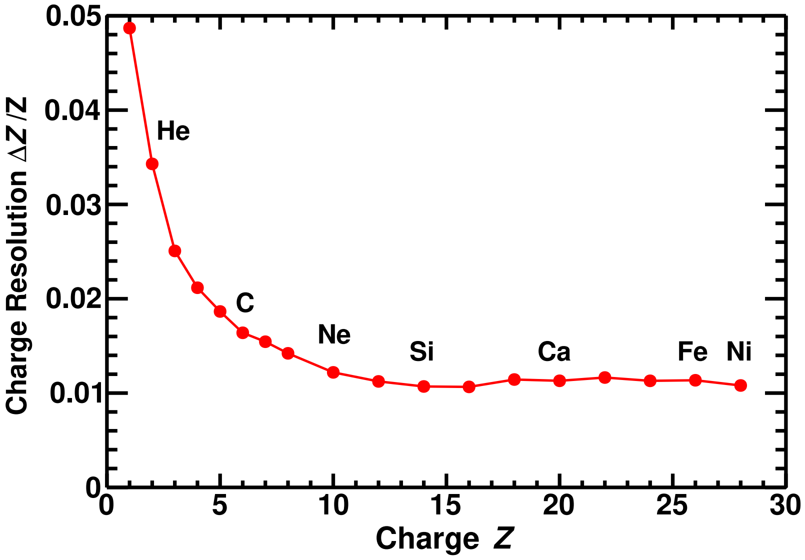

Figure 3.5: The inner tracker (layers L2–L8 combined) charge resolution $\Delta Z/Z$. The solid line is to guide the eye. Figure taken from Figure 15 of Aguilar et al., (2021)[38].

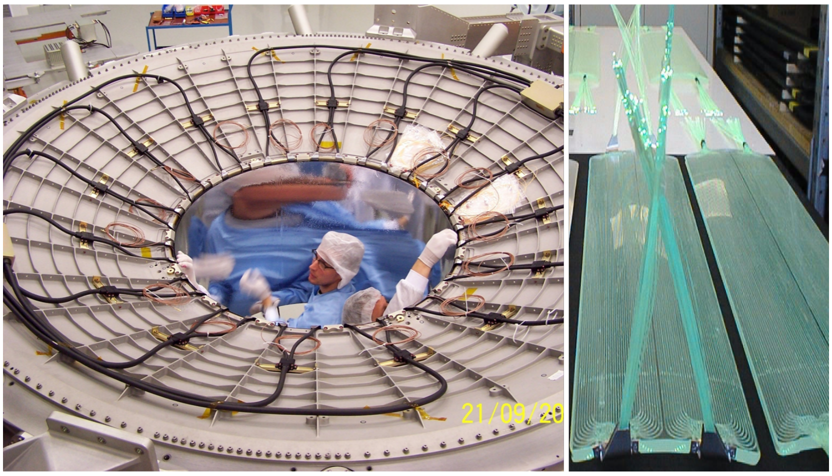

Figure 3.6: Photograph of the Anti-Coincidence Counters being installed. Image taken from *AMS-02 Website*.

3.2.3 Ring-Imaging Cherenkov Detector

The RICH (seen in Figure 3.7) is a sub-detector of AMS capable of measuring both velocity and charge of the traversing cosmic ray by making use of the Cherenkov radiation phenomenon. It allows for the best velocity measurement of AMS.

The RICH detector in Alpha Magnetic Spectrometer (AMS-02) consists of a matrix of Photomultiplier Tube (PMT) surrounded by a conic mirror surface, closed off by a dual radiator at the top made of a sodium fluoride central square section ($n = 1.33$ and thickness 0.5 cm), surrounded by Aerogel ($n = 1.05$ and thickness 2.5 cm), as can be seen in figure 3.8. This radiator configuration was chosen to increase ring acceptance since it allows for wider rings near the centre of the detector, where the hole in the PMT matrix due to the ECAL lies.

The detector is built in such a way that fast enough particles that traverse the radiator will create a ring of photoelectrons in the PMT matrix below, which will then serve to estimate the Cherenkov angle. The mirror helps increase ring acceptance by reflecting back onto the matrix any rings that would be too close to the sides to have the full ring inside the detector.

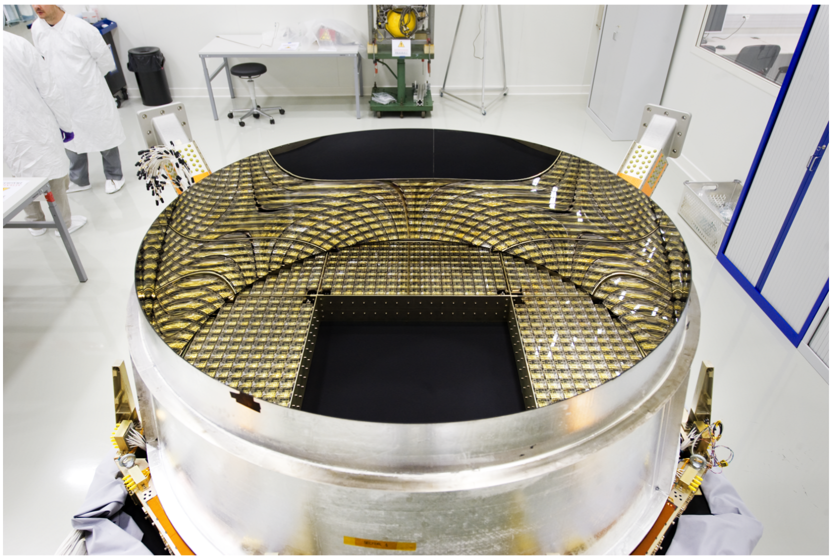

Figure 3.7: View of the RICH detector assembled into AMS experiment at CERN. Image taken from *Cern Document Server*.

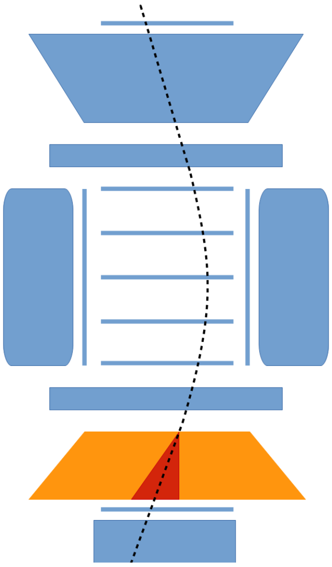

Figure 3.8: Diagram depicting the geometry of the RICH sub-detector in the AMS-02 overall scheme.

3.2.4 Transition Radiation Detector

The TRD (seen in Figure 3.9) is a sub-detector specialized in particle identification. When a charged particle crosses a boundary between two media with different dielectric constants, it emits photons. This radiation is known as transition radiation and is on the X-ray range.

At high energies, photon production is highly dependent on the Lorentz factor, γ. Due to its mass being $\sim$ 1836 times that of an electron, a proton with kinetic energy 1TeV, would behave like a 0.5 GeV electron in terms of transition radiation. This differentiation is the core of TRD's detection principle.

The TRD is constituted of several of these interfaces together with several straws with a thin wire in the centre and filled with a $Xe - CO_2$ mixture which will then ionize as the particle goes through. The electron/positron case will have a greater component of X-rays.

Figure 3.9: Pre-integration of the transition radiation detector (TRD) onto the AMS experiment. Image taken from *Cern Document Server*.

The TRD then makes use of a likelihood function which takes into account the contribution of each tube fired by the particle making the geometric average of the different probabilities estimated from each tube ($\mathcal{L} = \sqrt[n]{\prod_{i=0}^{n} P_i}$). This likelihood estimator is then used to estimate the probability (seen in Figure 3.10) of a particle being of a given species.

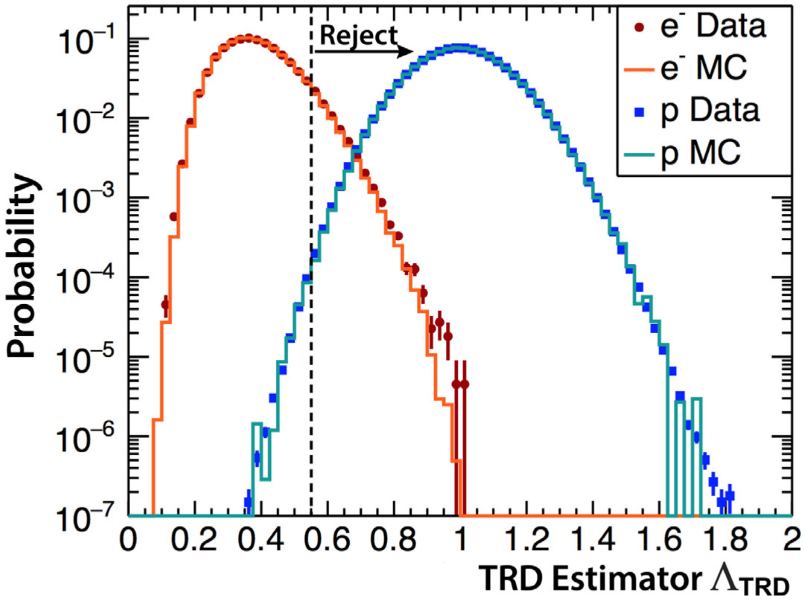

Figure 3.10: The Δ_{TRD} distributions for cosmic ray protons (blue) and electrons (red) in the rigidity range 10–100GV together with the Monte Carlo simulation. As seen, the simulation describes the data over six orders of magnitude. The vertical dashed line shows the position of the cut corresponding to 90% efficiency of the electron signal. By tightening this cut (i.e. moving the dashed line to the left) we can achieve better purity of the electron signal with the corresponding reduction of the signal efficiency. Figure taken from [38]

3.2.5 Time-Of-Flight Detector

The ToF (seen in Figure 3.11) is a detector designed to measure the of impact of a given particle with all 4 planes. From these times the velocity can be calculated. It also plays a fundamental role as a key integrand of the AMS trigger system, as will be discussed in section 3.3.

It is composed of 4 planes of scintillation counters, 2 above and 2 below the magnet, containing 8-10 scintillator paddles (8,8,10,8 from top to bottom) with PMT's on both sides. Each ToF plane consists of paddles aligned along the x and y coordinates, respectively, as depicted in figure 3.11.

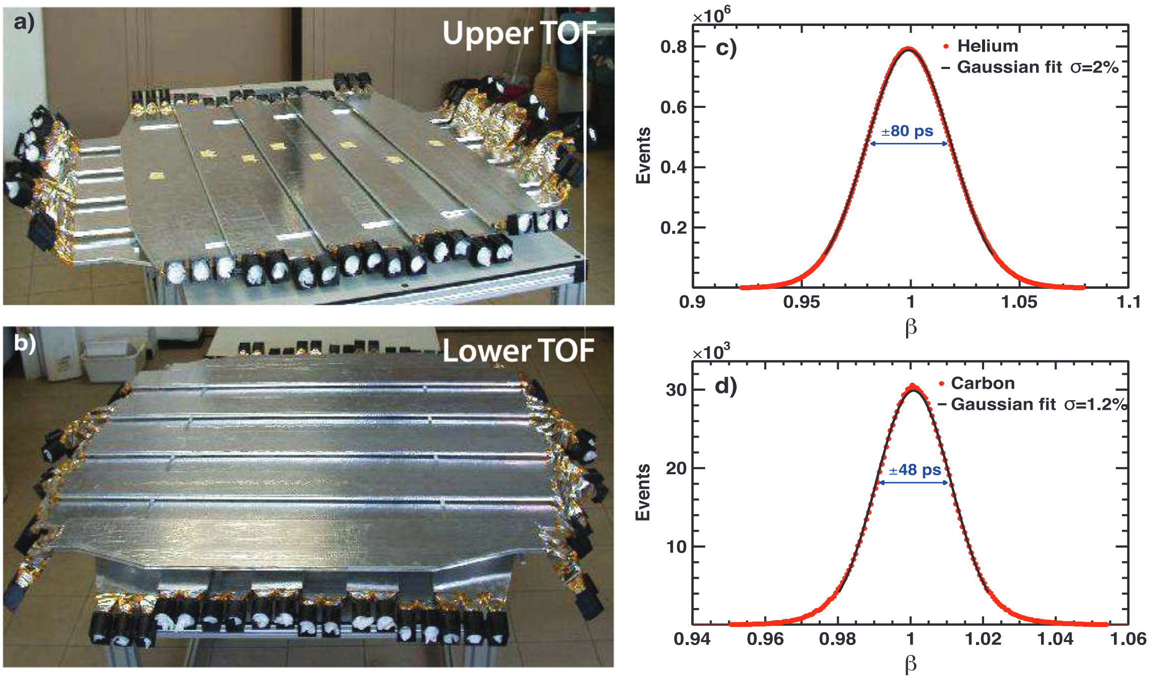

Figure 3.11: (a) The upper TOF counters. (b) The lower TOF counters. The measured TOF velocity distribution for (c) $Z = 2$ (He) and (d) $Z = 6$ (C) nuclei with rigidity > 20 GV. The solid black lines are Gaussian fits with standard deviations of $\sigma = 2\%$ for helium and $\sigma = 1.2\%$ for carbon. This corresponds to TOF time resolution of 80ps and 48ps, respectively. Figure taken from Figure 20 of Aguilar et al., (2021)[38].

From the different scintillator signals the ToF is capable of making a precise charge measurement from each ToF counter (see Figure 3.12) and these are used, in combination with TRK charge, as the charge selectors for the analyses presented in this work.

3.2.6 Electromagnetic Calorimeter

At the bottom of AMS-02 lies ECAL. The ECAL consists of a series of 9 super-layers, each with a thickness of 18.5 mm and composed of 11 grooved, 1 mm thick lead foils interleaved with layers of 1 mm diameter scintillating fibbers, glued together with epoxy resin.

The detector's imaging capability is obtained by stacking super-layers with fibres, alternatively parallel to the x-axis (4 layers) and y-axis (5 layers). The detector has an average density of 6.9 g/cm^3 for a total weight of 496 kg.

As the cosmic ray passes through ECAL, it creates a shower of particles whose shape is related to the nature of the primary particle (electromagnetic shower for fermions and hadronic shower for hadrons). ECAL is then able to reconstruct a 3D shower profile at 18 different depths, thus identifying the species and direction of the incident particle. The sum

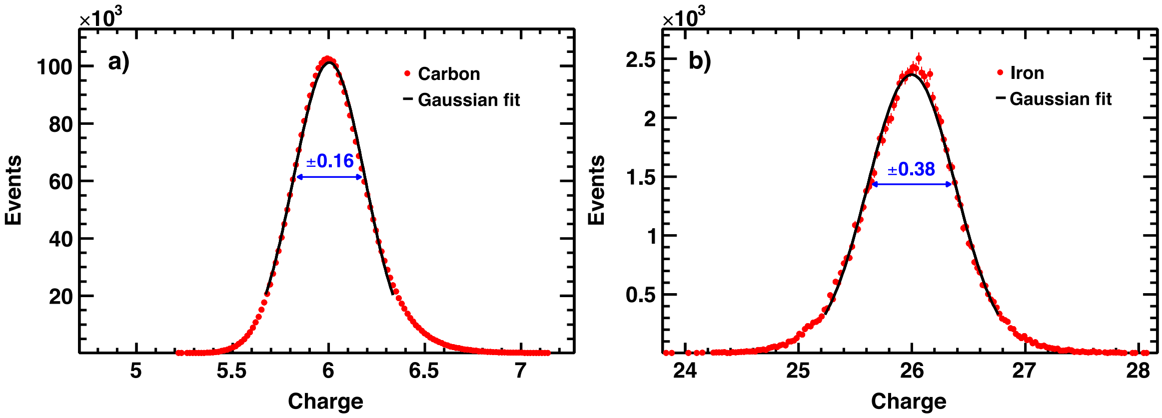

Figure 3.12: Distribution of the TOF charge Z for (a) carbon (Z = 6) and (b) iron (Z = 26) nuclei for a single TOF counter. The solid black lines are Gaussian fits with standard deviations of 0.16 and 0.38 charge units, respectively. Figure taken from Figure 22 of Aguilar et al., (2021)[38].

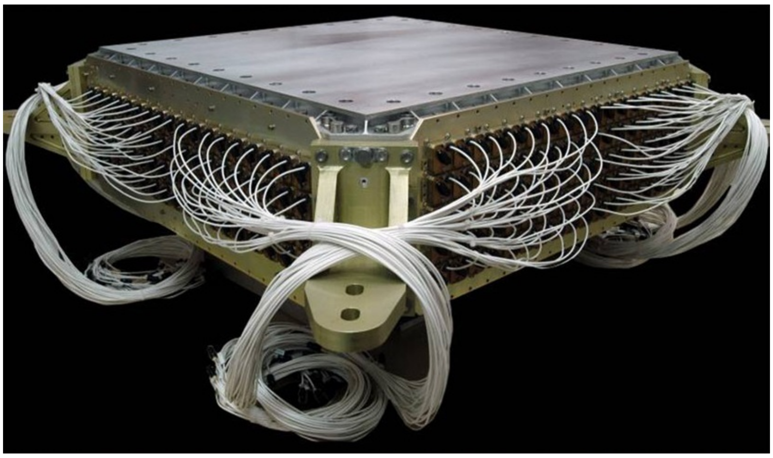

Figure 3.13: Photograph of the Electromagnetic Calorimeter. Figure taken from Figure 25 of Aguilar et al., (2021)[38].

of all layer signals in ECAL is proportional to the particle's deposited energy. It also allows for the AMS γ-ray measurement.

3.3 Trigger Logic, Livetime & Exposure time

After understanding the different sub-detectors that constitute the AMS-02 experiment, we can begin looking at some of its key systems such as the trigger system and its importance for the measurement of the cosmic ray flux and the estimation of exposure time.

3.3.1 Trigger Logic

The main goal of the AMS-02's trigger is to enable the recording of events crossing the instrument's fiducial volume while rejecting all others. When AMS-02 triggers on a given event, the acquisition system shifts into a *busy* state in which it will no longer record new events, this is called dead-time [99]. In order to handle the high event rates AMS encounters, the trigger is composed of two stages, Fast Trigger (FT) and level-1 trigger. The FT has the goal of contributing to dead-time as little as possible and is composed of signals from both ToF and ECAL detectors.

Through the combination of these FT's the following general FT signals are constructed:

- **FTC**: Coincidence of 3 out of 4 of the ToF plane hits within a window of 240 ns with a signal height larger than 50% of a Z=1 particle signal, namely High Threshold (HT).
- **FTE**: Energy deposition in ECAL greater than that of a charged particle with 1 GeV of energy.
- **FTZ**: Coincidence of all 4 ToF planes within a window of 640 ns and with a pulse height of 3.5 times that of a Z=1 particle signal, namely Super High Threshold (SHT).

The activation of FT will then enable the evaluation of the level-1 trigger which is comprised of several sub-triggers which combine signals from ToF, ECAL and the Anti-Coincidence Counter (ACC) to form the following combinations, with respective bit masks:

Table 3.1: LVL1 Sub-triggers

0	**Unbiased charged**	(0x00)	3/4 ToF hits, presc. factor ~ 100
1	**Single charged**	(0x02)	4/4 ToF hits, $N_{Acc} = 0$
2	**Normal Ions**	(0x04)	4/4 ToF hits, $N_{Acc} < 5$ SHT
3	**Slow Ions**	(0x08)	4/4 ToF hits, SHT gate=640ns
4	**Electrons**	(0x10)	4/4 ToF hits, ECALF&
5	**Photons**	(0x20)	ECALA&
6	**Unbiased EM**	(0x40)	ECALF||, presc. factor ~ 1000

3.3.2 Livetime & Geomagnetic Field

The evaluation of these triggers enables the accurate recording of the signals from the different detectors but introduces a dead-time. When estimating any result from the AMS-02 rate we have to correct for this factor by introducing *Livetime*, the fraction of time in each second that AMS was available for data taking. For a fixed dead-time, increasing event rate will decrease livetime, as can be seen in Figure 3.14.

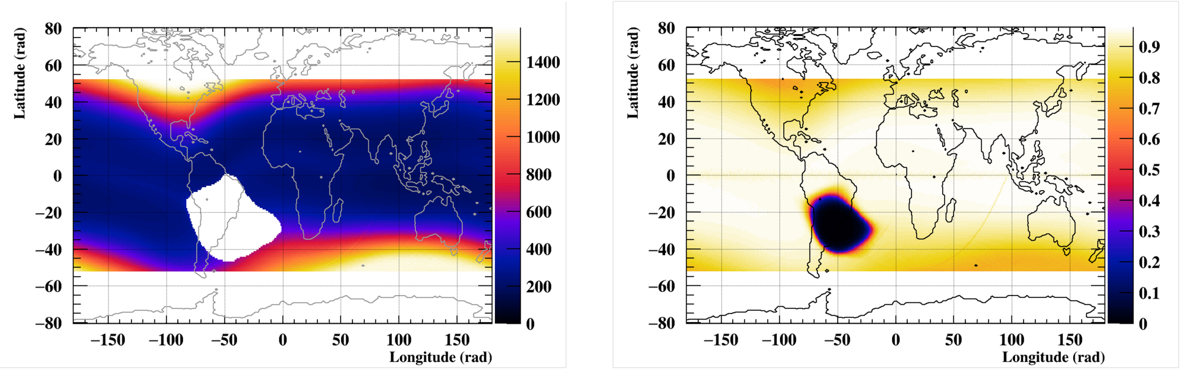

(a) Trigger rate [Hz]

(b) Livetime

Figure 3.14: AMS-02's average trigger rate (left) and livetime (right) for 2015 as a function of ISS orbital position.

3.3.3 Geomagnetic Field

As it orbits the Earth on the ISS, about once every 90 minutes, the AMS detector is exposed to a magnetic field that varies depending on its latitude, longitude and altitude. This magnetic field traps low-energy charged particles which can be detected in AMS, introducing a background in all low-energy flux measurements[100, 101, 102]. These particles can be so abundant at times that the detector itself saturates and exposure time can no longer be estimated as livetime drops down drastically, as can be seen in when comparing Figure 3.15 with Figure 3.14.

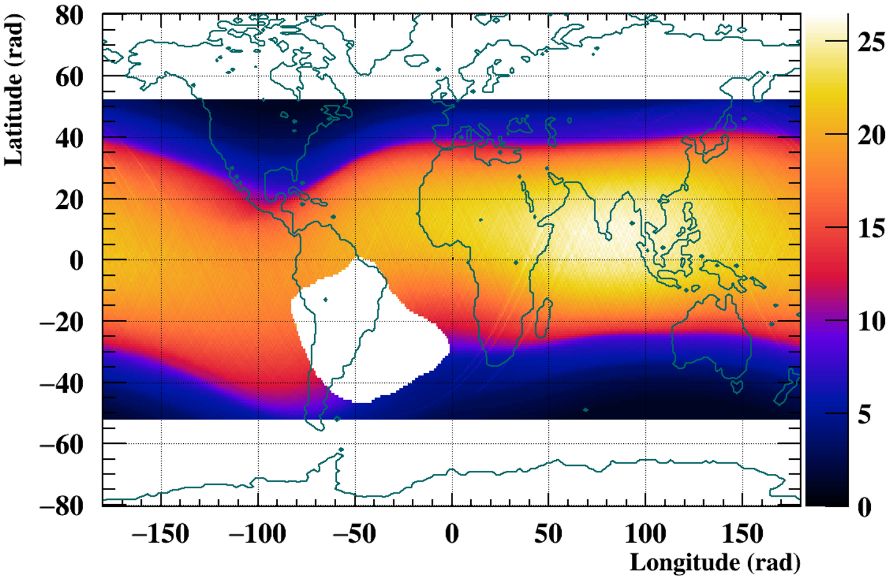

Figure 3.15: AMS-02's average geomagnetic cutoff (GV) for 2015 as a function of ISS orbital position.

In order to remove this contamination of secondaries, the AMS collaboration estimated the minimum rigidity a charged particle needs to have in order to be considered unaffected by Earth's magnetic field and thus a primary cosmic ray, for every second of AMS's data taking. This rigidity is known as the *Geomagnetic Cutoff Rigidity*.

This cutoff rigidity is determined by backtracing particles that would arrive at the detector for every second of ISS's orbit, for both positive and negatively charged particles and for different maximum angular apertures. The temporal granularity adopted was 1 s since it offered a good compromise between computational time, the accuracy of the models used to parametrize the magnetic field and the spacial variation of the magnetic field during ISS's 90 minute orbits. This data is stored in a *Real Time Information* (RTI) object which is accessible during offline analysis. This object contains the minimum rigidity that a cosmic ray needs to have in order to be a primary primary, within certain fiducial acceptances of the detector for both positive and negative particles.

In order to filter out these secondary events, we need to accept only particles whose rigidity measurement is greater than the geomagnetic cutoff rigidity for the second in which that particle was measured. This introduces a very interesting effect in the exposure time in which it becomes dependent on measured rigidity instead of a constant value. This was studied in great detail by Barão et al., (2011)[103] which presented their results in an internal AMS collaboration presentation.

4

Measurement of the Proton Flux

This chapter will be dedicated to the estimation of the Bartel solar rotation (27-day) time-resolved proton flux measured by AMS with the goal of being able to characterize it and interpret it under solar modulation models (see chapter 5).

Through this chapter we will work through the process of estimating the proton cosmic-ray flux and correcting it by the different efficiencies and detector effects involved. The efficiencies associated with the different sub-detectors and measurement cuts used will be characterized and used to correct the measured proton rates.

We will briefly characterize the space environment surrounding the ISS and its consequences on cosmic rays observed by AMS. We will briefly explain AMS' data structure and will lay out the selection scheme and framework used to analyse and select these events.

Some physical context will be given to emphasize the requirements of this physical result and the challenges posed by the measurement of a time-dependent physical quantity in a varying space environment and how to decouple the two effects through the estimation of time-dependent corrections.

The flux was estimated from 11 June 2011 to 14 November 2019, corresponding to the Bartel number 2427 up to 2541, producing a total of 115 time bins, with the exclusion of Bartel rotations 2472 and 2473[1] during which AMS was performing detector studies.

4.1 Estimation of cosmic-ray flux

When we talk about galactic cosmic-ray flux φ we are discussing a differential continuous physical observation of charged particles arriving at Earth coming from galactic sources. We are expecting to see a dependence on magnetic rigidity P, which is due to source emission/acceleration spectra and interstellar propagation effects (see chapter 1) and a dependence with time which comes from Solar Modulation effects (see chapter 2). In these studies we will not consider a dependence with oncoming direction.

As was previously discussed in chapter 1, the cosmic-ray flux comes in the form of

$$\varphi_0(t, P_0) = \frac{\mathrm{d}^4 N(t, P_0)}{\mathrm{d}t\,\mathrm{d}P_0\,\mathrm{d}\Omega\,\mathrm{d}A_\perp}\,,$$

---

[1] Taken from `https://izw1.caltech.edu/ACE/ASC/DATA/bartels/Bartels2004-2023.pdf`

where P_0 is the *true* rigidity of the incoming cosmic-ray (in opposition to the measured rigidity which we will henceforth denote as P) φ_0 is the incoming cosmic-ray isotropic flux on our detector, N is the number of particles traversing our detector, t is time, Ω is a abbreviation for every cosmic-ray direction contained inside the detectors geometrical aperture, thus defining a solid angle (measured in steradians) and $A_\perp$ is the transverse area of our detector, in relation to a given incoming direction.

We then expect that the distribution of the number of particles detected at each rigidity will generally have the following form,

$$\frac{\mathrm{d}^2 N_{\text{detected}}}{\mathrm{d}P_0\,\mathrm{d}t}(t, P_0) = \int\limits_A \iint\limits_\Omega \varphi_0(t, P_0)\,\mathrm{d}\Omega\,\mathrm{d}A_\perp\ . \tag{4.1}$$

If we consider some transfer function $K(t, P_0, P)$ that accounts for both instrumental and environmental effects we can update our expression to become

$$\frac{\mathrm{d}^2 N_{\text{detected}}}{\mathrm{d}P\,\mathrm{d}t}(t, P) = \int_0^\infty \int\limits_A \iint\limits_\Omega \varphi_0(t, P_0)\,K(t, P_0, P, \Omega, A)\,\mathrm{d}\Omega\,\mathrm{d}A_\perp\,\mathrm{d}P_0\,, \tag{4.2}$$

where, as mentioned before, P_0 represents the incoming cosmic-ray's true rigidity value and P its measured value. This transfer function can be factorized as

$$K(t, P_0, P, \Omega, A) = L(t)\,\varepsilon_{\text{cutoff}}(t, P_0)\,\varepsilon_{\text{geom}}(P_0, \Omega, A)\,\mathcal{P}(P \mid P_0)\,\varepsilon_{\text{sel}}(t, P_0)\,\varepsilon_{\text{trig}}(t, P_0)\,, \tag{4.3}$$

where:

- $L(t)$ is the livetime of the detector, defined as the fraction of time the detector is available to detect incoming particles (see subsection 3.3.2). This is a key component in the estimation of the exposure time since it determines for every second the fraction of time in that second that the detector was available to observe cosmic rays. The full calculation of exposure time is detailed in section 4.3;

- $\varepsilon_{\text{cutoff}}(t, P_0)$ represents the effects of the geomagnetic cutoff in the flux (see subsection 3.3.3). This factor will correct the exposure time by the fraction of time our detector was exposed to only primary particles and, notably, has a dependence on rigidity to reflect that for every second we are only exposed to primary cosmic-rays above a certain rigidity. For this correction in time to be accurate, we need to make sure that when selecting our events we also cut every event that is below the geomagnetic cutoff rigidity to completely remove secondary particles trapped in the geomagnetic field. In practice, it is a step function for every second that starts at the cutoff rigidity;

- $\varepsilon_{\text{geom}}(P_0, \Omega, A)$ is the geometrical efficiency of the detector and it determines, for every possible incoming direction and entry position if the particle trajectory is fully confined within the sensitive (fiducial) volume of our detector. Notably, this function is dependent on rigidity due to, in part, the existence of a magnetic field (see subsection 3.2.1) inside of the detector which changes particle direction within the sensitive volume of the detector depending on its magnetic rigidity (see subsection 4.4.1);

- $\mathcal{P}(P \mid P_0)$ is a transfer function known as migration probability (also known as migration matrix, when discretized into measurement bins, depending on normalization) and takes into account migration effects due to rigidity measurement uncertainty and bias (see subsection 4.4.9). It is a probability density function (pdf) on the variable P as it symbolizes measured rigidity distribution, as a function P_0;

- $\varepsilon_{\text{sel}}(t, P_0)$ represents selection efficiency (see subsection 4.4.1);

- $\varepsilon_{\text{trig}}(t, P_0)$ is the trigger efficiency of our detector for the particle being selected.

Since we are interested in turning the measurement of the cosmic-ray flux into a counting experiment, we can begin writing a binned version of Equation 4.2, both in time and rigidity, as:

$$
\begin{aligned}
&\int_{T_k^{\mathrm{L}}}^{T_k^{\mathrm{U}}} \int_{P_i^{\mathrm{L}}}^{P_i^{\mathrm{U}}} \frac{\mathrm{d}^2 N_{\text{detected}}}{\mathrm{d}P\,\mathrm{d}t}(t, P)\,\mathrm{d}P\,\mathrm{d}t = N_{\text{detected}}(t_k, P_i) = N(t_k, P_i) \\
&= \int_{T_k^{\mathrm{L}}}^{T_k^{\mathrm{U}}} \int_{P_i^{\mathrm{L}}}^{P_i^{\mathrm{U}}} \int_0^{\infty} \varphi_0(t, P_0) \int\limits_A \iint\limits_{\Omega} K(t, P_0, P, \Omega, A)\,\mathrm{d}\Omega\,\mathrm{d}A_\perp\,\mathrm{d}P_0\,\mathrm{d}P\,\mathrm{d}t \\
&= \int_{T_k^{\mathrm{L}}}^{T_k^{\mathrm{U}}} \int_{P_i^{\mathrm{L}}}^{P_i^{\mathrm{U}}} \int_0^{\infty} \varphi_0(t, P_0) \int\limits_A \iint\limits_{\Omega} L(t)\,\varepsilon_{\text{cutoff}}(t, P_0)\,\varepsilon_{\text{geom}}(P_0, \Omega, A)\,\mathcal{P}(P \mid P_0) \\
&\qquad\qquad \varepsilon_{\text{sel}}(t, P_0)\,\varepsilon_{\text{trig}}(t, P_0)\,\mathrm{d}\Omega\,\mathrm{d}A_\perp\,\mathrm{d}P_0\,\mathrm{d}P\,\mathrm{d}t\ ,
\end{aligned}
$$

where, from now on, we will use the notation of $N(t_k, P_i)$ for binned data (a bin in a histogram) and $N(t, P)$ for a continuous function as usual. The values T_k^{L}, T_k^{U}, P_i^{L}, P_i^{U} denote, respectively, lower and upper bin limits for both time and rigidity, circumscribing the measurement. Since we are interested in the Bartel proton flux we will denote the periods for a Bartel solar rotation as t_k to describe this 27 day rotation.

Although the migration matrix is a delicate matter that we will characterize in subsection 4.4.1, we will assume for now that it will be a simple one-to-one correction on measured rigidity, thus turning it into:

$$
\mathcal{P}(P \mid P_0) = \delta(P, P_0)\,g(P) \tag{4.4}
$$

and creating our final binned result of:

$$
\begin{aligned}
N(t_k, P_i) &= \int_{T_k^{\mathrm{L}}}^{T_k^{\mathrm{U}}} \int_{P_i^{\mathrm{L}}}^{P_i^{\mathrm{U}}} \int_0^{\infty} \varphi_0(t, P_0) \int\limits_A \iint\limits_{\Omega} L(t)\,\varepsilon_{\text{cutoff}}(t, P_0)\,\varepsilon_{\text{geom}}(P_0, \Omega, A)\,\mathcal{P}(P, P_0) \\
&\qquad \varepsilon_{\text{sel}}(t, P_0)\,\varepsilon_{\text{trig}}(t, P_0)\,\mathrm{d}\Omega\,\mathrm{d}A_\perp\,\mathrm{d}P_0\,\mathrm{d}P\,\mathrm{d}t \\
&= \int_{T_k^{\mathrm{L}}}^{T_k^{\mathrm{U}}} \int_{P_i^{\mathrm{L}}}^{P_i^{\mathrm{U}}} L(t)\,\varepsilon_{\text{cutoff}}(t, P)\,\varepsilon_0(t, P) \int\limits_A \iint\limits_{\Omega} \varepsilon_{\text{geom}}(P, \Omega, A)\,\varepsilon_{\text{sel}}(t, P) \\
&\qquad \varepsilon_{\text{trig}}(t, P)\,\mathrm{d}\Omega\,\mathrm{d}A_\perp\,\mathrm{d}P\,\mathrm{d}t \\
&= \int_{T_k^{\mathrm{L}}}^{T_k^{\mathrm{U}}} \int_{P_i^{\mathrm{L}}}^{P_i^{\mathrm{U}}} L(t)\,\varepsilon_{\text{cutoff}}(t, P)\,\varphi_0(t, P)\,Acc(t, P)\,\varepsilon_{\text{sel}}(t, P)\,\varepsilon_{\text{trig}}(t, P)\,\mathrm{d}P\,\mathrm{d}t\ ,
\end{aligned}
\tag{4.5}
$$

where we define our detector's acceptance $Acc(t, P)$ as the integration of the geometrical efficiency over the entire geometrical aperture of the detector.

If we consider these functions as slowly varying (or if the bins are sufficiently narrow) in any given bin, when compared to the flux, we can then finish our binned measurement of the number of cosmic-rays events by approximating it as:

$$
N(t_k, P_i) \approx \Delta T(t_k, P_i)\,\langle \varphi_0(t_k, P_i) \rangle\,Acc(t_k, P_i)\,\varepsilon_{\text{sel}}(t_k, P_i)\,\varepsilon_{\text{trig}}(t_k, P_i) \Delta P_i, \quad \text{with} \tag{4.6}
$$

$$
\Delta T(t_k, P_i) = \int_{T_k^{\mathrm{L}}}^{T_k^{\mathrm{U}}} \int_{P_i^{\mathrm{L}}}^{P_i^{\mathrm{U}}} L(t)\,\varepsilon_{\text{cutoff}}(t, P)\,\mathrm{d}t\,\mathrm{d}P\ , \tag{4.7}
$$

where we then note that $\Delta P_i = P_i^{\mathrm{U}} - P_i^{\mathrm{L}}$. This leads to our experimental estimation of the mean differential cosmic-ray flux in a given bin (t_k, P_i) as:

$$
\langle \varphi_0(t_k, P_i) \rangle \approx \frac{N(t_k, P_i)}{\Delta T(t_k, P_i)\,Acc(t_k, P_i)\,\varepsilon_{\text{sel}}(t_k, P_i)\,\varepsilon_{\text{trig}}(t_k, P_i) \Delta P_i}\ . \tag{4.8}
$$

This formulation of our flux estimation clarifies the observables we will need to estimate to correct the number of observed events for detector, selection and environmental effects. We will expand upon it later on section 4.4.

4.2 Proton Event Selection

This section will detail the specific criteria used to select protons from all events present in AMS data for the period of 11 June 2011 to 14 November 2019. Since this analysis intends to estimate a time-resolved proton flux, one of the major goals is the maximization of number of detected events. In order to keep statistics high we selected an appropriate geometrical configuration for the reconstructed tracks (Layer 1 and Inner Tracker) in order to increase acceptance. This resulted in a reduction of the upper rigidity range of the estimated flux due to the exclusion of layer 9, a key component in being able to determine curvature at energies higher than 100 GV.

The framework for selecting these proton events from all AMS events can be split into the following categories:

1. **Preselection cuts**
   This step is aimed at determining a sample of events which is mostly free from bad reconstructions and contains only observations done during appropriate detector and trigger setups. This selection is applied for each orbital second and uses information contained mostly in AMS' Real Time Information (RTI) database, thus determining whether a certain second (and all associated events) can be used for the flux estimation.

   - Mean difference between track alignment calibrations (Perugia and CIEMAT)
   - Position of ISS not over the South Atlantic Anomaly (SAA)
   - AMS Zenith Angle < 40 degrees
   - Geomagnetic Cutoff Rigidity derived from IGRF model [104, 105, 106]
   - Number of triggered events > 1
   - Number of particle reconstructions / number of triggered events $> 25\%$
   - Number of errors / number of events $> 10\%$
   - Event Rate > 1800 Hz

   Trigger Configuration
   We wish to select protons so we will be concerned with selecting charged particles using the ToF trigger. In order to do this we chose a trigger configuration that can be represented as the bit mask 0x1E, which is a combination of either of the following triggers (see subsection 3.3.1):

   - 0x02 - "Single charged" - 4/4 ToF hits, Anti-Coincidence Counters = 0
   - 0x04 - "Normal Ions" - 4/4 ToF hits, Anti-Coincidence Counters < 5, super high threshold
   - 0x08 - "Slow Ions" - 4/4 ToF hits, super high threshold, gate = $640ns$
   - 0x10 - "Electrons" - 4/4 ToF ECALF&

2. **Reconstruction, Identification and Selection**
   This selection seeks to first identify if the event is of the candidate track geometry required and then, based on this reconstructed trajectory, it seeks to associate the appropriate detector measurements.

   Tracker Detector

   - Track must have L1 + Inner geometry: hits used on reconstruction must include Layer 1 and Inner tracker

- Reconstructed track must include hits with at least 4 hits distributed between layers 2 to 8 with the following pattern:
  L2 and (L3 or L4) and (L5 or L6) and (L7 or L8)
- Only 1 reconstructed track per event
- Quality of inner track reconstruction in bending direction (Y):
  $\chi^2_{\text{Inner}}(Y)/n.d.f. < 10$
- Track has a XY hit on Layer 1
- Quality of full (L1+Inner) track reconstruction in bending direction (Y):
  $\chi^2_{\text{L1+Inner}}(Y)/n.d.f. < 10$

Time-of-Flight Detector

- 4 of 4 ToF planes with hits used in reconstruction
- Down-going relativistic particle: $\beta > 0.4$
- Match between ToF track and Tracker track

Geomagnetic Cutoff

- Reconstructed rigidity (Layer 1 + Inner geometry) above the maximum geomagnetic cutoff rigidity estimated for positive particles in the orbital second in question. A safety factor can be applied to the geomagnetic cutoff rigidity such that $P > S\, P_{cutoff}$. In this analysis we chose the safety factor to be 1 (see subsection 4.5.6).

3. **Fiducial Volume** Since we are interested in determining protons with rigidity up to 100 GV, we will require only the upper portion of the Tracker Detector, excluding the bottom layer (9) in order to increase geometrical aperture.

   - Reconstructed track must cross fiducial volume of layer 1 + inner geometry of the tracker and all planes of the ToF
   - Reconstructed track from hits in the Time-of-Flight detector must cross the fiducial volume of both layer 1 and the inner tracker
   - Reconstructed θ angle at top of the instrument must be within the angular opening used in geomagnetic cutoff estimation

4. **Charge Selection**
   During this step the events have already been tagged as good reconstructions of primary cosmic rays. The last step is to identify them as having a charge of $Z = 1$.

   - Track bending direction corresponding to a positively charged particle
   - Inner tracker charge measurement compatible with $Z = 1$: $0.7 < Z_{\text{Inner}} < 1.4$
   - Small root mean square of charge measurement spread: $Z_{RMS} < 0.4$
   - Layer 1 tracker charge measurement compatible with $Z = 1$: $0.6 < Z_{\text{L1}} < 1.9$
   - Upper ToF charge measurement compatible with $Z = 1$: $0.5 < Z_{\text{UTOF}} < 2.5$

4.2.1 AMS data and reduced trees

This selection was implemented on the *Nuc* analysis framework developed by Prof. Laurent Derome alongside other contributors. It follows a system in which events are first classified according to a set of selection criteria (also known as cuts) and then they are selected based on combinations of these cuts. This system allows for multiple analysis to be ran at once, making it ideal for this scenario in which several physical estimations have to be calculated simultaneously for a flux result to be produced (distribution of events, livetime, efficiencies, ...).

The structure for the analysis portion of the code is shown in Figure 4.1.

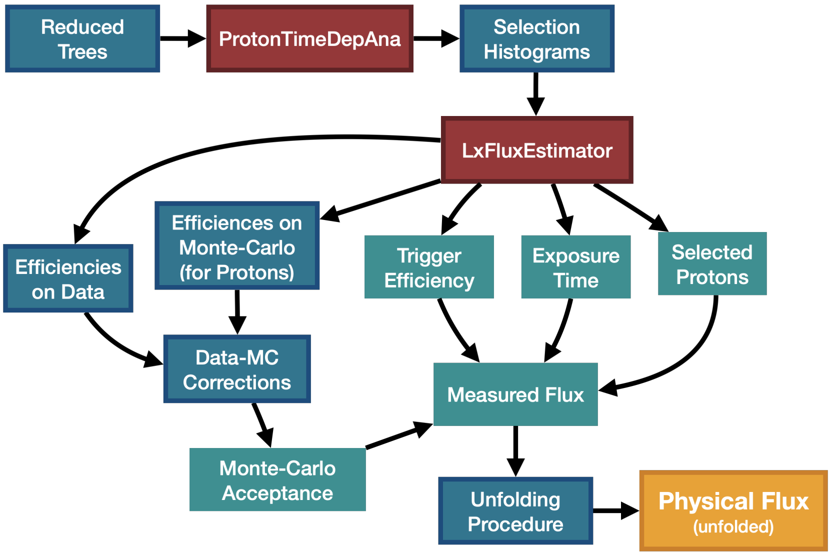

Figure 4.1: Diagram of the selection framework.

One final important note regards the data used. This selection was run on two batches of AMS data, each of a different time period and corresponding to different reprocessing of the data. The first period, from 3 June of 2011 to 12 October of 2017, corresponds to data reprocessed from raw AMS data into *pass6* while the second batch, from 12 October of 2017 to 14 November 2019, was reprocessed into the next iteration *pass7*. This next iteration changes the track reconstruction algorithm (improving upon it) and, given the importance of track reconstruction to the rest of the selection, changes some of the efficiencies. This will become apparent in the time-resolved efficiency estimations where a sudden change appears.

Additionally, this analysis was ran on reduced data trees instead of AMS's main software ntuples. These reduced trees vastly reduce the event size, allowing for increased flexibility of the analyses (allowing for different trees with different pre-selections) and a major speed-up in event classification and selection. Unfortunately, the data used for the early initial part of the analysis, at *Centre de Calcul de l'IN2P3/CNRS*, only contain the *pass6* portion of the data and corresponding Monte-Carlo version. In order to extend the analysis, AMS data (and Monte-Carlo data) had to be reproduced at CERN's computing centre in order to construct the reduced trees used in this analysis. The available space at CERN did not allow for a complete reconstruction of all data for the *pass7* extension period, despite our best efforts to reduce event size by removing unused branches and performing other optimizations. This resulted in lower exposure times (which will be apparent later on the time-resolved fluxes) for the later part of the period. One time period (Bartel rotation number 109) had to be removed due to low statistics.

From 29-Sep-2014 to 28-Nov-2014 Tracker Thermal Control System (TTCS) system was off and part of the tracker was off so the corresponding two bartel periods were also removed. Other variations of detector performance were observed.

4.3 Exposure time and Geomagnetic Cutoff

When aiming to calculate the proton flux we need to calculate the total amount of time that our experiment was available to detect cosmic rays. As was detailed in subsection 3.3.2, when AMS-02 triggers on a given particle, there is a dead time τ_D during which no particles can be recorded[99]. Since we will be using RTI to evaluate total exposure time fractionally, one second at a time, we need to reformulate Equation 4.7.

The determination of our exposure time is done by calculating the sum of the fractions of livetime of the detector for every second within a certain time period t_k, delimited by T_k^{L} and T_k^{U}.

As was delineated in Barão et al., Barão and Derome, (2011, 2011)[103, 107], the presence of secondary particles in our cosmic-ray flux due to the geomagnetic field (see subsection 3.3.3) needs to be addressed and the authors proposed that we construct a step function on rigidity above which we are guaranteed to only have primary particles. This rigidity is called the geomagnetic cutoff rigidity. This rigidity is estimated by reconstructing the trajectories of incoming cosmic-ray's at the top of the AMS detector for every orbital position (evaluated every second), for every measurable rigidity (up to a reasonable upper bound) and identifying if the incoming particle was primary or secondary, thus determining the rigidity above which every particle is a primary, as depicted in Figure 4.2. The particle is considered primary of secondary if it reaches 50 Earth's radii out from the top of AMS[108].

Figure 4.2: Step function of the effect of the geomagnetic cutoff rigidity.

This approach consists in constructing a step function $\varepsilon_{\text{cutoff}}(t, P)$ that is null below the geomagnetic cutoff rigidity for a given second and one above it after as shown by the following expression:

$$\varepsilon_{\text{cutoff}}(t, P) = \begin{cases} 0 & P \leq P_{\text{cutoff}}(t) \\ 1 & P > P_{\text{cutoff}}(t) \end{cases} \tag{4.9}$$

Our exposure time for a given period t_k for a given rigidity bin P_i becomes:

$$\Delta T(t_k, P_i) = \sum_{t=T_k^{\mathrm{L}}}^{T_k^{\mathrm{U}}} L(t)\, \varepsilon_{\text{cutoff}}(t, P_i) = \sum_{t=T_k^{\mathrm{L}}}^{T_k^{\mathrm{U}}} L(t) \begin{cases} 0 & P_i^L \leq P_{\text{cutoff}}(t) \\ 1 & P_i^L > P_{\text{cutoff}}(t) \end{cases} \tag{4.10}$$

The estimation of the exposure time histogram consist of, for every second on the analysis period, adding the livetime fraction of that second on every rigidity bin above the cutoff rigidity. The exposure time for a given Bartel period of this analysis can be seen in Figure 4.3. Given geomagnetic cutoff rigidity's variation with different orbital positions, implying a dependence with time, exposure time also varies between the different analysis periods. In Figure 4.57a and Figure 4.57b we can see the time profiles of the exposure time for this analysis.

In order to guarantee bin integrity (i.e. the entire bin width is available for measurements) on both the histograms of events and exposure time, the rigidity bin in which the cutoff rigidity falls is not be considered and only those higher than it are considered to be available. Filling the bin of an histogram with events represents the integration of the pdf over the bin's entire width. If only parts of the bins are available than this integration is done over a much narrower (and undetermined) interval which would make the results very hard to treat statistically. This is represented in Figure 4.4.

Since we are comparing the cutoff rigidity estimated for a given orbital second with the measured rigidity of all events that are detected within that second, we have to take into account rigidity measurement resolution. In AMS this is done by including a safety factor S which will increase the cutoff rigidity in the following manner:

$$P > S\, P_{\text{cutoff}}(t)$$

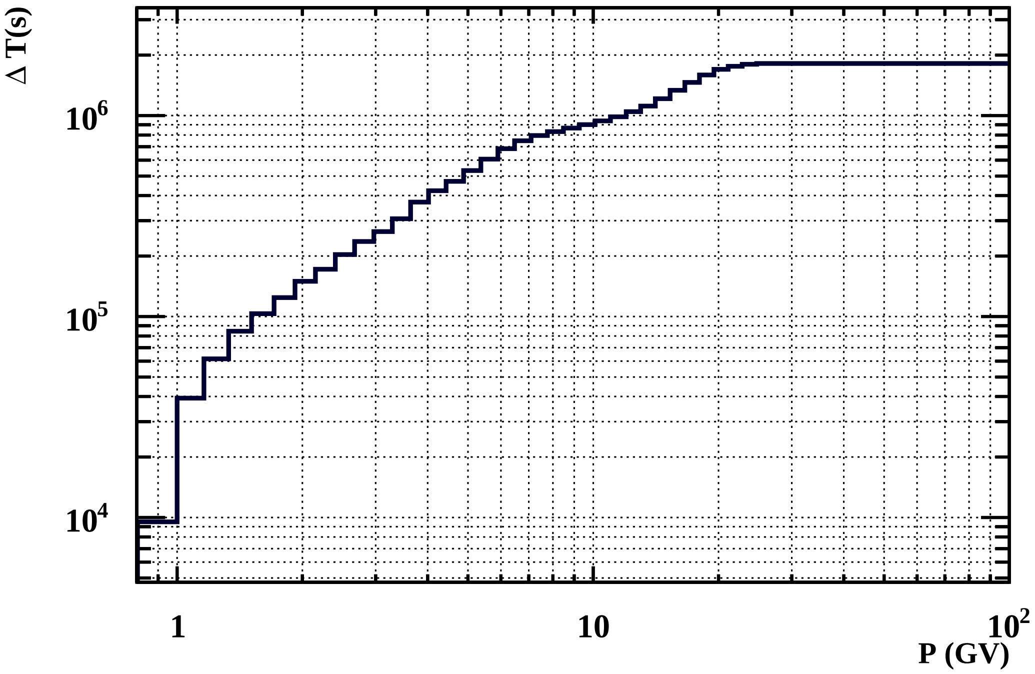

Figure 4.3: Total exposure time as a function of rigidity.

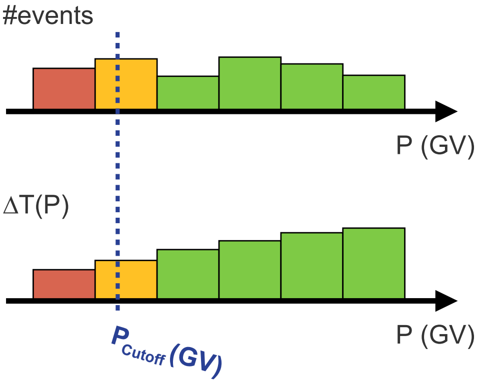

Figure 4.4: Preservation of bin integrity while using the rigidity cutoff. The green bins are considered available and both orange and red bins are considered as excluded when filling both event histograms (e.g. selected events) and exposure time.

.

This factor S acts as a safety measure against rigidity resolution but introduces variations to both exposure time and the number of events measured given that increasing it will reduce the number of orbital seconds that rigidity bins are exposed to. This safety factor can also be used to increase the purity of our sample but, in principle, it will reduce both the number of events and the exposure time linearly, keeping the rate unchanged. A discussion on the choice of this safety factor and on the systematic it introduces is discussed in subsection 4.5.6. Other effects such as the angular dependence of the acceptance or the considered distribution of directions of incoming particles may introduce errors in the estimation of the acceptance.

4.4 Selection Efficiency

In this section we will make use of the different categories stipulated in section 4.2 in order to define our major factors to correct for. Efficiency of a detector can be defined as the probability that a particle which passes through the detector is also seen by it [99]. During the process of event selection the cuts made are always a trade-off between purity of the sample and efficiency of the cut[109]. In order to correct for these inefficiencies we have to estimate them.

A common theme throughout these efficiency estimations will be purity. We will have the aim of estimating these efficiencies for proton only thus we have to select an especially pure sample of events in order to guaranty that we are correcting directly for the signal and not for the signal and background at the same time. We achieve this by increasing the purity through charge and mass cuts until the efficiency no longer varies significantly while maintaining a reasonable number of events. Additionally, we need to consider that the Monte-Carlo simulation will not contain any contamination and this might be reflected as small differences between efficiencies estimated in Data and in Monte-Carlo.

All of these efficiencies will be estimated for both physical events which we will henceforth call **Data** events and for Monte-Carlo events which we will call **MC** events.

These efficiencies will be estimated as *last cuts*[110, 111], implying that we consider that each cut is made on strictly independent variables, meaning that we can extract the efficiency using simple conditional probability:

$$\mathcal{P}(Selection) = \mathcal{P}((Selection \wedge Cut) \cap Cut) = \mathcal{P}(Selection \wedge Cut)\,\mathcal{P}(Cut)$$
$$\mathcal{P}(Cut) = \frac{\mathcal{P}(Selection)}{\mathcal{P}(Selection \wedge Cut)},$$

where, symbolically, $P(Selection \wedge Cut)$ simply means the probability of selecting an event that passes on the entire selection excluding Cut.

The effects of the selection can be seen on Figure 4.5.

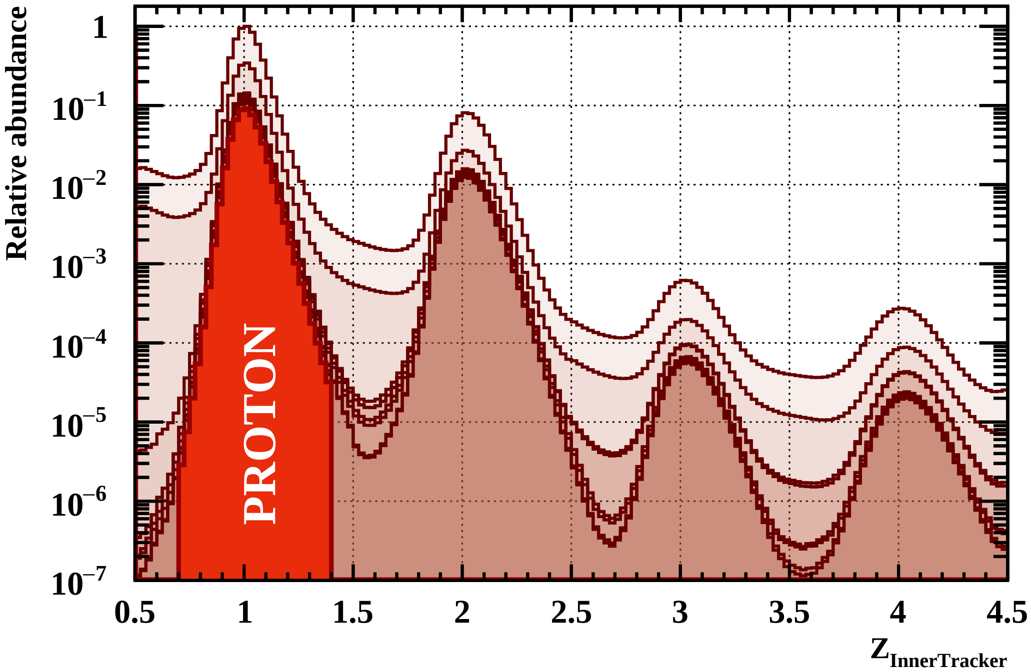

Figure 4.5: Effects of progressively applying selection cuts on the distribution of charge for events in one of the analysis periods.

We will divide these efficiencies into:

- Inner Tracker Reconstruction Efficiency;
- External Layer Pickup Efficiency;
- Time-of-Flight Charge Selection Efficiency;
- Time-of-Flight β Efficiency;
- Trigger Efficiency.

This approach requires that we understand every contribution to efficiency and correct for them individually while making sure that they are all strictly independent. Additionally, by inspecting Equation 4.8 we can see that we will also need to estimate detector acceptance.

4.4.1 Acceptance

Given that the detector contains a permanent magnet, as we've seen before, this acceptance should be dependent on particle rigidity, entry point and direction at the top of the detector, particle charge and others. If we try to estimate a *pure* acceptance that is completely independent from our event selection we would also need to correct it for the effects that our selection might have on it. Additionally, we would also need to take into account that our selection will not express itself perfectly in events of the Monte-Carlo simulation which we are using to calculate this acceptance and its correction to our selection. This process can be rather cumbersome.

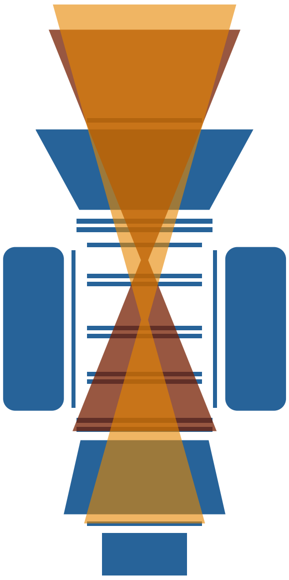

Figure 4.6: Diagram of the difference between acceptances result from L1+Inner track geometry (shaded in red) and L1+Inner+L9 geometry (shaded in orange).

4.4.1.1 Geometrical Acceptance

We will begin by elaborating on the construction of acceptance done in Equation 4.5

$$Acc(P_i) = \int\limits_A \iint\limits_\Omega \varepsilon_{\text{geom}}(P_i, \Omega, A)\, \mathrm{d}A_\perp\, \mathrm{d}\Omega \ ,$$

where the integration is done over the transverse area of the detector, for every possible cosmic-ray direction within the detector's solid angle aperture.

The process of estimating acceptance in Monte-Carlo starts with the generation of cosmic-rays from every direction (in fact, in the case of AMS-02 we only need to generate from the top). Given that AMS is not very sensitive to incoming direction and position of the cosmic-ray ($\varepsilon_{\text{geom}}(P_0, \Omega, A) \approx \varepsilon_{\text{geom}}(P_0)$), we can begin to establish a set of criteria for accepting or rejecting these cosmic-ray trajectories inside of the detector and create a geometric efficiency by writing the following expression:

$$N_{\text{sel}}^{\text{geom}}(P_i) = N_{\text{gen}}(P_i)\,\varepsilon_{\text{geom}}(P_i) = \frac{\int_{P_i^{\text{L}}}^{P_i^{\text{U}}} \varphi_{\text{gen}}^{\text{MC}} \varepsilon_{\text{geom}}(P_0)\,\mathrm{d}P_0}{\int_{P_i^{\text{L}}}^{P_i^{\text{U}}} \varphi_{\text{gen}}^{\text{MC}}\,\mathrm{d}P_0}\,,$$

where $N_{\text{sel}}^{\text{geom}}(P_i)$ is the number of selected events in a given rigidity bin P_i and $N_{\text{gen}}(P_i)$ is the number of selected events in that bin, giving us the following expression for the average value of geometric efficiency for a given rigidity bin:

$$\varepsilon_{\text{geom}}(P_i) = \frac{N_{\text{sel}}^{\text{geom}}(P_i)}{N_{\text{gen}}(P_i)}\,.$$

Acceptance then becomes:

$$Acc(P_i) = Acc_0\,\varepsilon_{\text{geom}}(P_i) = A_{\text{gen}}\,\Omega_{\text{gen}}\,\frac{N_{\text{sel}}^{\text{geom}}(P_i)}{N_{\text{gen}}(P_i)}\,,$$

where Acc_0 is the generated acceptance, A_{gen} is the surface area of generation and Ω_{gen} is the generation solid angle. In AMS' software chain the generation surface is the top plane of a $3.9m \times 3.9m \times 3.9m$ cube and cosmic rays are generated in every down-going direction (see Figure 4.7) with the following rigidity distribution:

$$\frac{\mathrm{d}N}{\mathrm{d}\log(P_0)} = \frac{\mathrm{d}N}{\mathrm{d}P_0}\frac{\mathrm{d}P_0}{\mathrm{d}\log(P_0)} = \frac{\mathrm{d}N}{\mathrm{d}P_0}\,P_0 = constant \implies \frac{\mathrm{d}N}{\mathrm{d}P_0} \propto \frac{1}{P_0}.$$

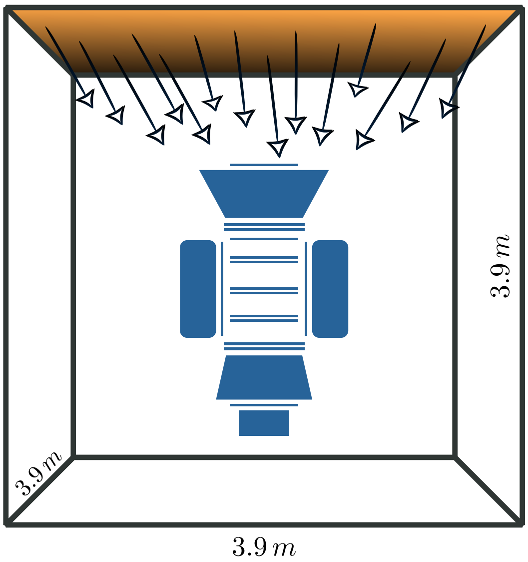

Figure 4.7: Diagram of AMS-02's Monte-Carlo generation surface.

When the need arises to change this generation flux one can re-weight the Monte-Carlo events instead of re-running the simulation for all of the events. This can be done during the selection process by attributing weights to each event according to its generated rigidity according to the following expressions:

$$N(P_i|\phi_{\text{gen}}) = \Delta\text{T} \int\limits_{P_i} \phi_{\text{gen}}(P_0)\,\text{Acc}(P_0)\,\text{d}P_0 \tag{4.11}$$

$$N(P_i|\phi_{\text{alt}}) = \Delta\text{T} \int\limits_{P_i} w(P_0)\,\phi_{\text{gen}}(P_0)\,\text{Acc}(P_0)\,\text{d}P_0\,, \quad \text{with} \quad w(P_0) = \frac{\phi_{\text{alt}}(P_0)}{\phi_{\text{gen}}(P_0)} \tag{4.12}$$

$$= \Delta\text{T} \int\limits_{P_i} \frac{\phi_{\text{alt}}(P_0)}{\phi_{\text{gen}}(P_0)} \phi_{\text{gen}}(P_0)\,\text{Acc}(P_0)\,\text{d}P_0 \tag{4.13}$$

$$= \Delta\text{T} \int\limits_{P_i} \phi_{\text{alt}}(P_0)\,\text{Acc}(P_0)\,\text{d}P_0\,. \tag{4.14}$$

This technique was used when producing the Monte-Carlo results for this for work. The generation fluxes and their respective first weights can be seen in Figure 4.8 for a given time period. This result also holds in the discretized case where histograms with number of events are used as long as the bins are very thin when compared to the variation of the flux.

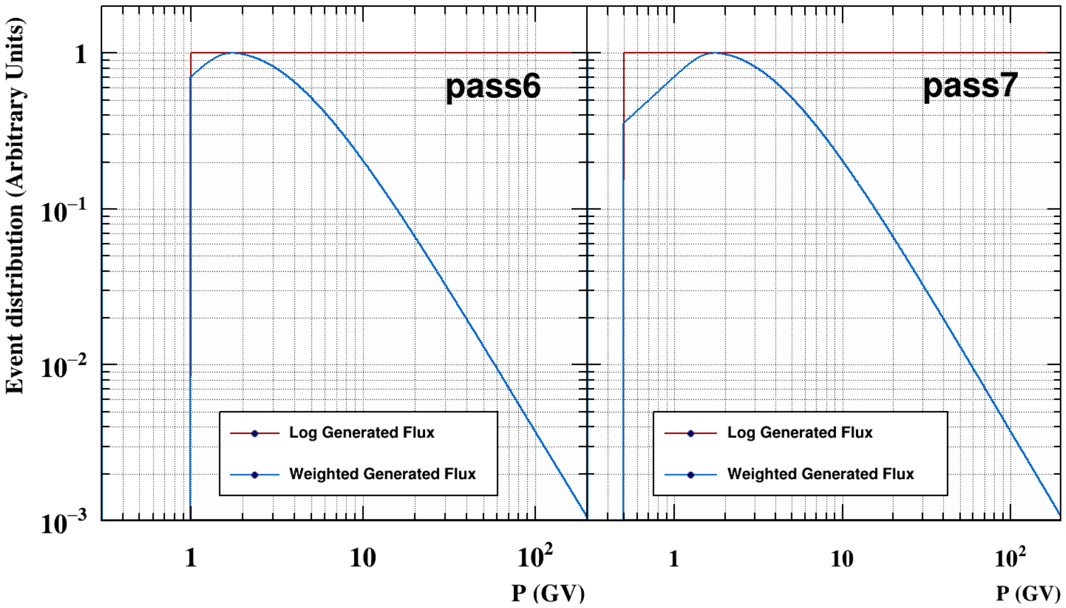

Figure 4.8: Generated event distributions for both analyses before and after weighting by a flux hint related to the bartel period in question.

There are some slight differences in the two generation ranges, one starting in 1 GV (*pass6*) and the other starting in 0.5 GV (*pass7*), the latter being more appropriate. This difference in generation range will become very important later when we tackle migration (see subsubsection 4.4.1.3). This generation range for the *pass6* period lead to some subtleties in how the first bin is treated when unfolding the flux.

4.4.1.2 Effective Acceptance: Geometrical Acceptance including efficiencies

Since we have not made any restricting considerations on what the selection of events needs to be and, by including fiducial cuts we inherently guarantee that this estimated acceptance is respected, we can simply incorporate the full event selection on this concept of an acceptance, generating an *Effective Acceptance* which for convenience will be referred to as $Acc(P_0)$ from now on and can be written as:

$$\begin{aligned} Acc(P_i) = Acc_0\,\frac{N_{\text{sel}}(P_i)}{N_{\text{gen}}(P_i)} &= Acc_0\,\frac{\int_{P_i^{\text{L}}}^{P_i^{\text{U}}}\int_0^{\infty}\varphi_{\text{gen}}^{\text{MC}}(P_0)\,\varepsilon_{\text{geom}}(P_0)\,\varepsilon_{\text{sel}}(P_0)\,\mathrm{d}P_0\,\mathrm{d}P}{\int_{P_i^{\text{L}}}^{P_i^{\text{U}}}\varphi_{\text{gen}}^{\text{MC}}(P_0)\,\mathrm{d}P_0} \\ &\approx Acc_0\,\frac{N_{\text{gen}}(P_i)\,\varepsilon_{\text{geom}}(P_i)\,\varepsilon_{\text{sel}}(P_i)}{N_{\text{gen}}(P_i)} = Acc_0\,\varepsilon_{\text{geom}}(P_i)\,\varepsilon_{\text{sel}}(P_i)\,. \end{aligned}$$

As mentioned before, these acceptances are fully estimated in the Monte-Carlo simulation which includes its efficiencies as well. If we correct this acceptance for slight differences in the Monte-Carlo efficiencies with Data-to-Monte-Carlo corrections $C_{\text{MC}}^{\text{Data}}(t_k, P_i)$ we can write the final form of Equation 4.8 as:

$$\langle\varphi_0(t_k, P_i)\rangle \approx \frac{N(t_k, P_i)}{\Delta T(t_k, P_i)\,Acc(t_k, P_i)\,C_{\text{MC}}^{\text{Data}}(t_k, P_i)\Delta P_i} \quad \text{with,} \tag{4.15}$$

$$C_{\text{MC}}^{\text{Data}}(t_k, P_i) = \frac{\varepsilon_{\text{sel}}^{\text{Data}}(P_i)}{\varepsilon_{\text{sel}}^{\text{MC}}(P_i)}\ , \tag{4.16}$$

where $\varepsilon_{\text{sel}}^{\text{Data}}(P)$ is the efficiency calculated using Data and $\varepsilon_{\text{sel}}^{\text{MC}}(P)$ is the same efficiency determined for the Monte-Carlo sample used.

This acceptance estimated for a given time slice can be seen in Figure 4.9.

The uncertainty of each acceptance bin is determined as the standard deviation of a Binomial process where the number of generated events in that bin is the number of trials.

Another detail that needs to be addressed is the presence of statistical fluctuations in the acceptance (see Figure 4.9c). These are not physically meaningful and need to be smoothed so that these statistical fluctuations are not transported to the final result. This will be a common theme on all efficiencies since some of them require pure proton samples, thus reducing available statistics. Additionally, due to varying conditions in the space environment and the natural degradation and variation of the detector, these efficiencies vary with time and, consequently, so will the respective regularizations and their critical parameters (such as nodes in the case of a spline regularization). In order to tackle this issue an automated spline regularization tool named *LxSmoother* was developed. A more detailed description of the algorithm is present in section A.1.

After this regularization tool is applied to acceptance we get the result presented in Figure 4.10.

Every estimated corrections for the rest of the work will be regularized using the same tool that was used for the acceptance and the final result presented will always be smoothed and the corresponding regularization systematic uncertainty applied to it. Another benefit from this spline regularization is in the translation of a result from one binning to another. This is particularly useful when rebinning is applied to efficiencies to tackle low statistics.

4.4.1.3 “Folded” Acceptance

Finally, the previous formulation of acceptance is not very dependent on the generation flux distribution since, in a given bin, both numerator and denominator are both *scaled* by the flux. If we wish to expand the concept of acceptance into including not only the effects of event selection but also bin migration we can consider expanding our migration model from Equation 4.4 into a bin-to-bin correction $g(P_i)$.

The simplest model for a bin-to-bin correction of a given migration would be to calculate the ratio of events that fell on a given bin of measured rigidity divided by the number of

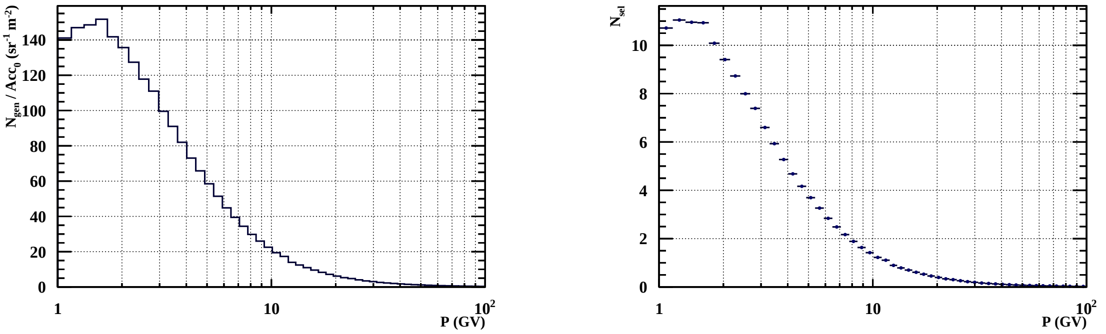

(a) Distribution of Monte-Carlo generated events, normalized to the generation acceptance.

(b) Distribution of Monte-Carlo selected events.

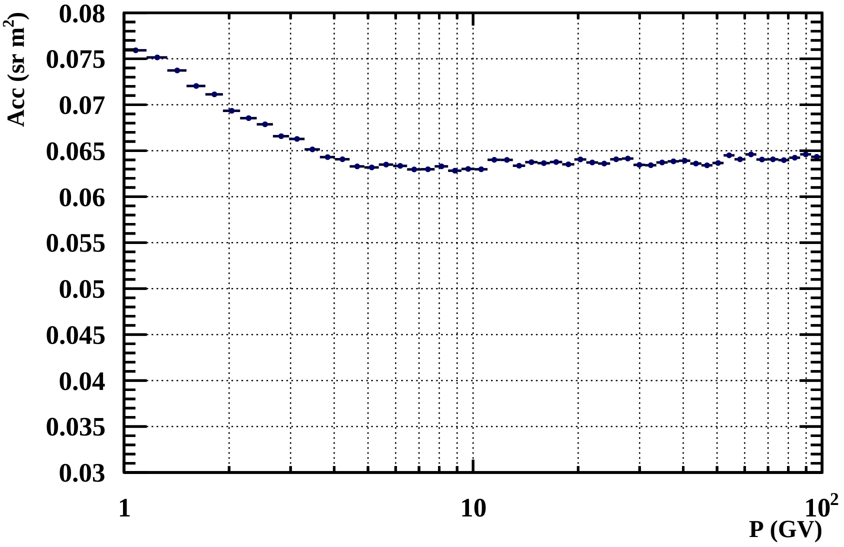

(c) Effective acceptance.

Figure 4.9: Plots of the effective acceptance for a given time bin.

generated events on that same interval but binned using the true (generated) rigidity:

$$\mathcal{P}(P \mid P_0) = \delta(P, P_0)\, g(P) \tag{4.17}$$

$$g(P_i) = \frac{\int_{P_i^{\mathrm{L}}}^{P_i^{\mathrm{U}}} \int_0^\infty \varphi_{\mathrm{gen}}^{\mathrm{MC}}(P_0)\, \mathcal{P}(P \mid P_0)\, \mathrm{d}P_0\, \mathrm{d}P}{\int_{P_i^{\mathrm{L}}}^{P_i^{\mathrm{U}}} \varphi_{\mathrm{gen}}^{\mathrm{MC}}(P_0)\, \mathrm{d}P_0}. \tag{4.18}$$

By incorporate this effect directly into the acceptance we get the *Folded Acceptance*:

$$Acc^{\mathrm{Fold}}(P_i) = Acc_0\, \frac{\int_{P_i^{\mathrm{L}}}^{P_i^{\mathrm{U}}} \int_0^\infty \varphi_{\mathrm{gen}}^{\mathrm{MC}}(P_0)\, \varepsilon_{\mathrm{geom}}(P_0)\, \varepsilon_{\mathrm{sel}}(P_0)\, \mathcal{P}(P \mid P_0)\, \mathrm{d}P_0\, \mathrm{d}P}{\int_{P_i^{\mathrm{L}}}^{P_i^{\mathrm{U}}} \varphi_{\mathrm{gen}}^{\mathrm{MC}}(P_0)\, \mathrm{d}P_0}. \tag{4.19}$$

In opposition to the *folded acceptance* we will name the previous acceptance, which contains the selection efficiency but not the migration effects, the *True Acceptance*. We can see a comparison between these two acceptances in Figure 4.11.

This *folded acceptance* is designed to correct for bin-to-bin migration effects and will explicitly depend on the shape of our Monte-Carlo generation flux which by design is supposed to mimic the proton flux we are trying to estimate. This creates a recursive problem in which we require some hint of the proton flux shape in order to experimentally estimate a proton

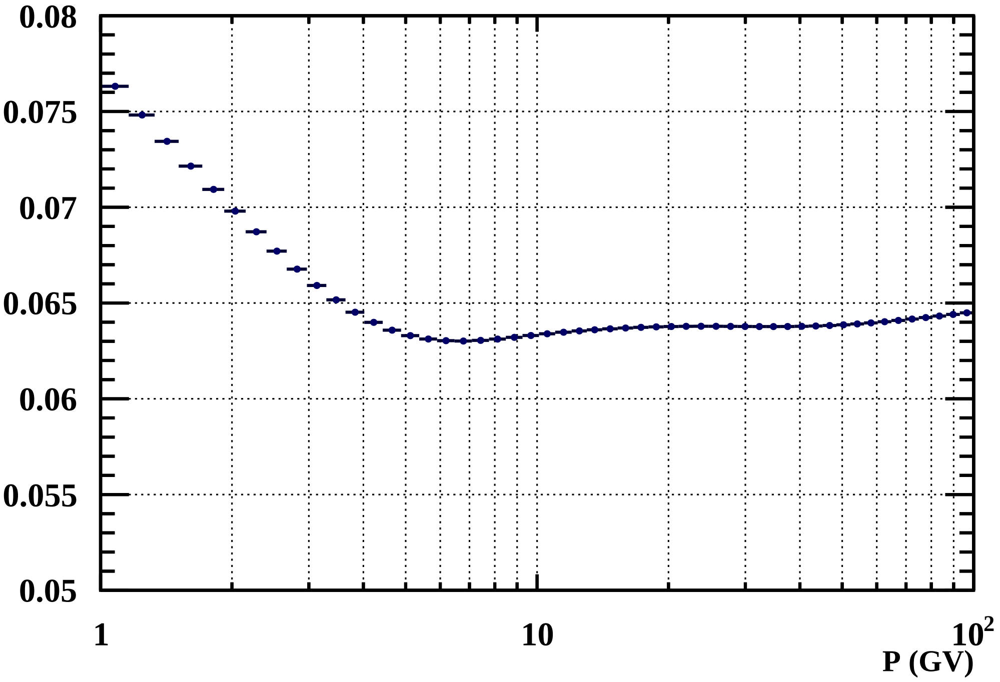

Figure 4.10: Smoothed effective acceptance for a given time bin.

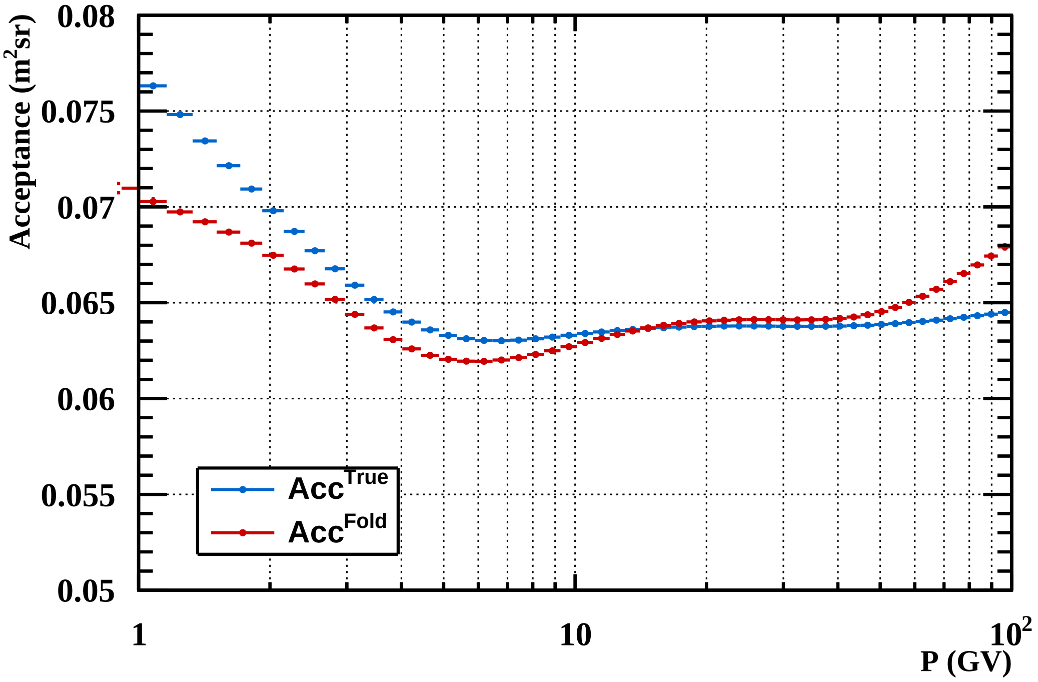

Figure 4.11: Comparison between *folded acceptance* and true acceptance.

flux that is independent of our experimental apparatus. Later in subsection 4.4.9 we will see how to tackle this issue.

In general, the more accurate we can get our generation flux, the more accurate will be any result related to these migration effects. Even if a result is independent of the generation flux, it should also evenly sample the rigidity range being studied with high enough statistics in order to minimize relative variance.

One final aspect (discussed in subsubsection 4.4.1.1) was raised due to the generation flux used for the *pass6* period. Due to the generation range used for the *pass6* Monte-Carlo trees, the first bin will be subjected to migrations which will reduce the number of events in it (same as other bins) but it will only get contributions from the bins with higher rigidities since there were no events events generated at rigidities lower than 1 GV which would contribute to this bin by migrating upwards in rigidity. This meant that the first bin of the *folded acceptance* was very underestimated and when applied to the rate results in an abnormal increase in the flux at the lowest rigidity. To correct for this we extrapolate the value of the first rigidity bin for the *folded acceptance* and reached a very satisfactory result as will be seen later.

4.4.2 Inner Tracker Reconstruction Efficiency

This efficiency aims to represent the probability that a given cosmic-ray traversing the detector has its trajectory accurately reconstructed.

Track reconstruction is an integral part of every aspect of proton detection in AMS. It allows for spacial matching of the signals from the different sub-detectors, it enables every fiducial cut, it consists of the only measurement of charge sign in AMS-02 and, since it is contained inside of the permanent magnet and includes most of the tracker planes, it is responsible for the measurement of the particle's magnetic rigidity, the variable with which we will be describing the flux.

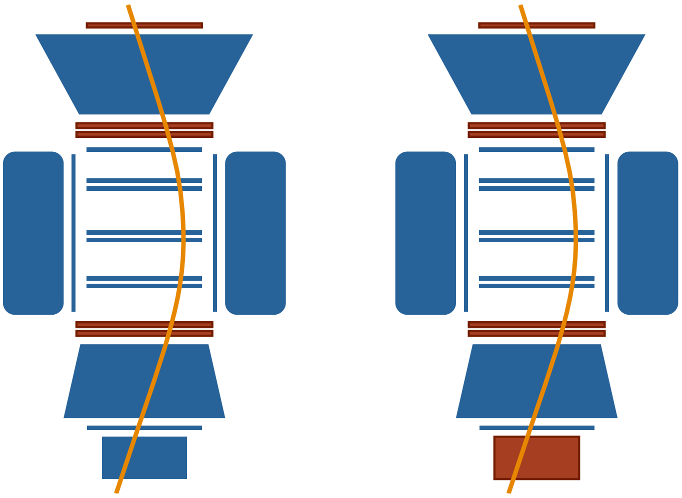

(a) Diagram of detectors used for inner reconstruction efficiency estimation using ToF β and geomagnetic cutoff.

(b) Diagram of detectors used for inner reconstruction efficiency estimation using ECAL energy.

Figure 4.12: Diagram of detectors used for inner reconstruction efficiency estimation.

An additional challenge in this estimation comes from the fact that we can no longer use measured rigidity as a describing variable for this efficiency, we will have to estimate rigidity from the measurements of other sub-detectors. We will be using particle velocity from ToF in the $0.8-3$GV interval, cutoff rigidity in the $3-7$GV interval and reconstructed energy from ECAL for $7-100$GV (see Figure 4.13).

As will be the case for all the following efficiencies, we have to modify our event selection with the goals of guaranteeing that the particle crosses the detector being evaluated (in this case the inner tracker) and that the particle is a proton. This new selection should guarantee our goals and remain as close as possible to the original selection on every other cut not being evaluated. A depiction of the detectors involved is in Figure 4.12. For the 3 rigidity ranges we

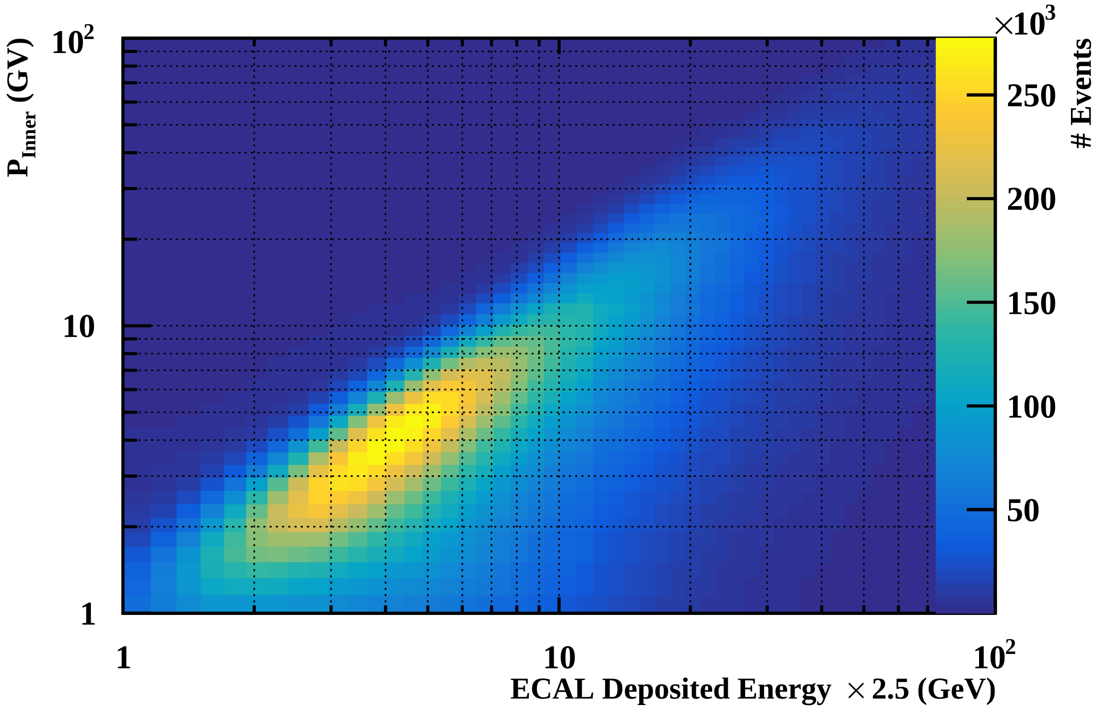

Figure 4.13: Distribution of inner rigidity as a function of deposited energy extracted from proton Data events of AMS-02.

will use very similar selections.

The selection used for the ToF portion is:

- **Denominator**
  - Preselection from proton flux selection
  - ToF cuts from proton flux selection minus track matching
  - Rigidity from β above geomagnetic cutoff rigidity
  - Tight ToF charge cuts on both upper and lower planes: $0.5 < Z_{\mathrm{UTOF}} < 1.2$ and $0.5 < Z_{\mathrm{LTOF}} < 1.2$
  - Unbiased charge cut on Layer 1 hit: $0.7 < Z_{L1}^{\mathrm{unb}} < 1.9$
  - Extrapolated track from ToF hits inside the fiducial volume of interest, including passing through the inner tracker
- **Numerator**
  - Same as Denominator
  - Reconstructed inner track must include hits with at least 4 hits distributed between layers 2 to 8 with the following pattern: L2 and (L3 or L4) and (L5 or L6) and (L7 or L8)
  - Only 1 reconstructed track per event
  - Quality of inner track reconstruction in bending direction (Y): $\chi^2_{\mathrm{Inner}}(Y)/n.d.f. < 10$
  - Match between ToF track and Tracker track
  - Inner tracker charge measurement compatible with $Z = 1$: $0.7 < Z_{\mathrm{Inner}} < 1.4$

The efficiencies estimated for this portion of the selection can be seen in Figure 4.14.

For the next portion of this efficiency we will need to estimate the efficiency for the region of $3-7$GV. We will use the cutoff rigidity as the most probable value of rigidity for every particle. We can use this approach since the efficiency varies very slowly (or if the bins are

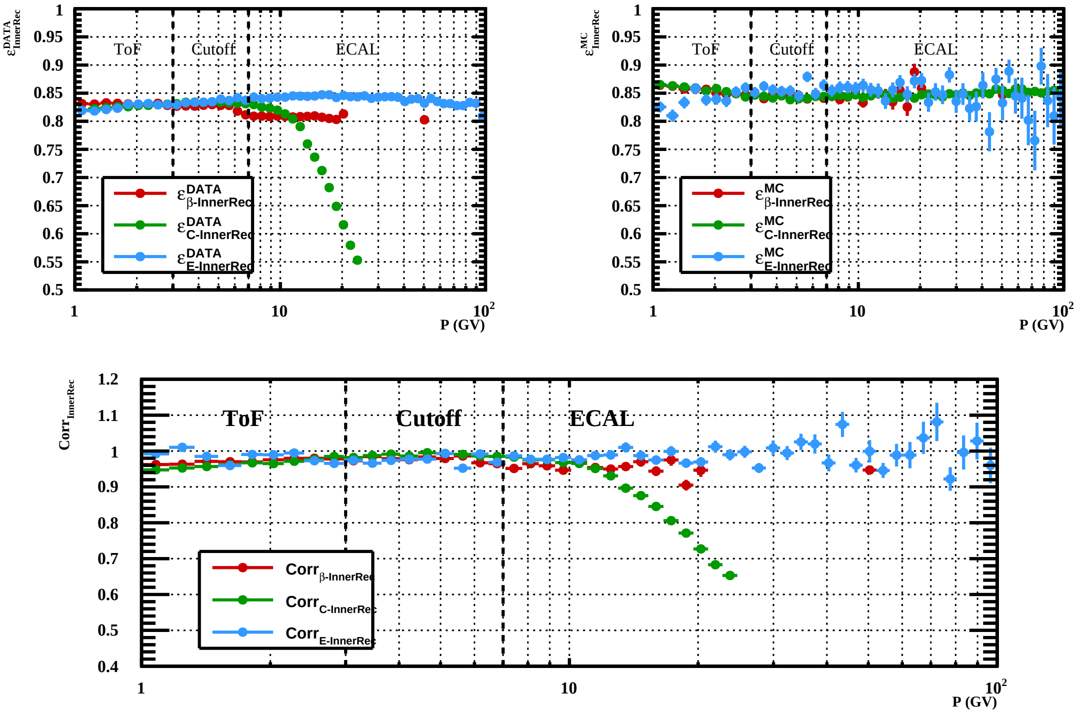

Figure 4.14: (Top left) Inner tracker reconstruction efficiency for Data. (Top right) Inner tracker reconstruction efficiency for Monte-Carlo. (Bottom) Inner tracker reconstruction correction for the different energy ranges.

sufficiently narrow), making it so that slight imprecisions in rigidity estimation will not affect the result greatly and given that the flux varies very rapidly with rigidity, in this range, we can estimate what the most likely measurement of rigidity will be for every second by doing the following calculation:

$$\langle R \rangle = \frac{\int_{R_{\text{cutoff}}}^{\infty} R\,\varphi_0(R)\,\mathrm{d}R}{\int_{R_{\text{cutoff}}}^{\infty} \varphi_0(R)\,\mathrm{d}R} ,$$

where, if we assume $\varphi_0 \propto R^{-2.7}$, we can see that we get that $\langle R \rangle \approx R_{\text{cutoff}}\, 1.7/0.7$.

The only selection difference between the geomagnetic cutoff rigidity portion and the ToF *beta* portion lies in the application of the rigidity cutoff cut only for ToF *beta*. Since we are using the geomagnetic cutoff rigidity to estimate rigidity the event is already assumed primary. The efficiencies estimated for this portion of the selection can be seen in Figure 4.14.

Finally, for the higher rigidity portion of the efficiency, in the $7 - 100$GV range, the only difference in the selection lies is in the inclusion of the ECAL in the fiducial volume requirements. The extrapolated track from the ToF hits needs to cross ECAL.

After these events are selected, rigidity is reconstructed from deposited energy based on an estimation based on the Monte-Carlo simulation of the detector (seen in Figure 4.13).

The ranges were chosen so that they lie inside each of the detectors accurate reconstruction range while still matching each other on the overlapping regions. The geomagnetic cutoff rigidity estimation bridges the gap between ToF's and ECAL's sensitivity ranges. This process is represented graphically in Figure 4.14

The correction of the inner tracker reconstruction efficiency can be seen in Figure 4.15.

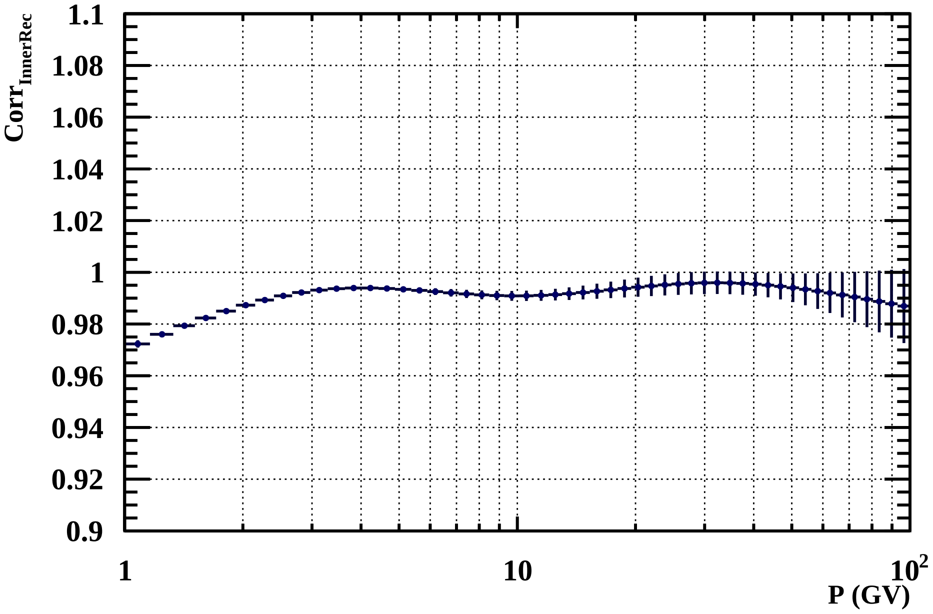

Figure 4.15: Inner tracker reconstruction correction for a given time slice.

4.4.3 External Layer Pickup Efficiency

This efficiency aims to encapsulate the probability that a *good* event that passes most of our selection and has a reconstructed track inside of the detector's layer 1 + inner tracker geometry acceptance will have a *good* hit on layer 1 and will have a *good* layer 1 + inner track reconstructed using said hit (see Figure 4.16).

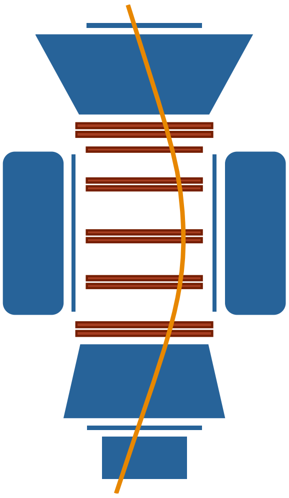

Figure 4.16: Diagram of detectors used for Layer 1 pickup efficiency.

We will follow a similar logic to that used in the inner tracker reconstruction efficiency. We will reconstruct our track using only inner tracker hits and then estimate the probability that an event that had a hit on layer 1 that is compatible with a proton ($|Z = 1|$) will have a layer 1 + inner track reconstructed. To do so we will use the following selection:

- **Denominator**
  - Preselection from proton flux selection

  - Rigidity from inner track above geomagnetic cutoff rigidity
  - Tracker, Time-of-Flight cuts from proton flux selection using only inner track reconstruction instead of layer 1 + inner geometry
  - Tight ToF charge cuts on both upper and lower planes: $0.5 < Z_{\text{UTOF}} < 1.2$ and $0.5 < Z_{\text{LTOF}} < 1.2$
  - Unbiased charge cut on Layer 1 hit: $0.7 < Z_{L1}^{\text{unb}} < 1.9$

- **Numerator**
  - Same as Denominator
  - Reconstructed inner track must include hits with at least 4 hits distributed between layers 2 to 8 with the following pattern: L2 and (L3 or L4) and (L5 or L6) and (L7 or L8)
  - Only 1 reconstructed track per event
  - Quality of inner track reconstruction in bending direction (Y): $\chi^2_{\text{Inner}}(Y)/n.d.f. < 10$
  - Match between ToF track and Tracker track
  - Inner tracker charge measurement compatible with $Z = 1$: $0.7 < Z_{\text{Inner}} < 1.4$

The correction for the tracker's layer 1 pickup efficiency can be seen in Figure 4.17.

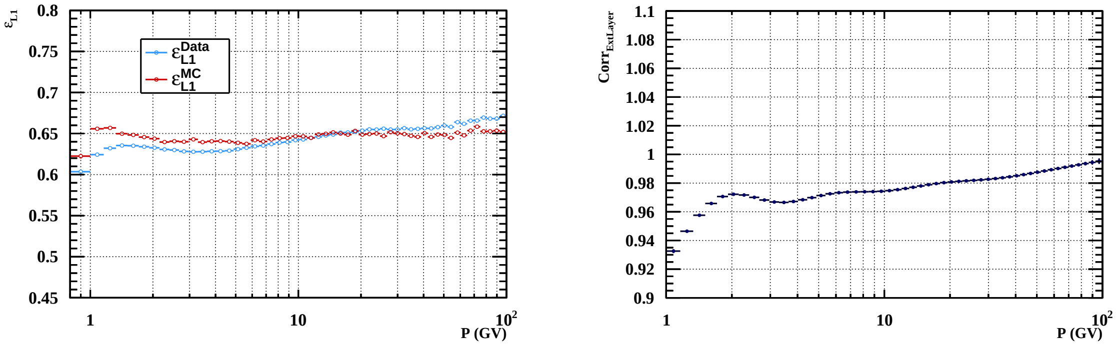

(a) Efficiency for Layer 1 pickup.

(b) Correction for Layer 1 pickup efficiency.

Figure 4.17: Corrections for Layer 1 pickup.

4.4.4 Time-of-Flight Charge Selection Efficiency

As we've done before, for this efficiency we isolate the variable (or cut) of interest, ToF charge measurement and then proceed to estimate the efficiency using the selection shown below.

- **Denominator**
  - Full selection from proton flux selection except for ToF charge cuts.
  - Tight Inner Tracker charge cuts: $0.8 < Z_{\text{Inner}} < 1.3$
  - Tight Layer 1 Tracker charge cuts: $0.7 < Z_{\text{L1}} < 1.5$

- **Numerator**
  - Full selection from proton flux selection
  - Tight Inner Tracker charge cuts: $0.8 < Z_{\text{Inner}} < 1.3$
  - Tight Layer 1 Tracker charge cuts: $0.7 < Z_{\text{L1}} < 1.5$

The results for this efficiency can be seen in Figure 4.18.

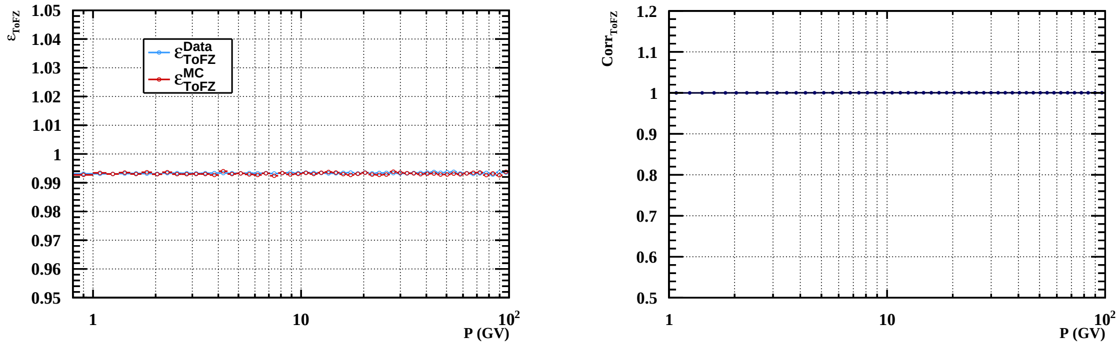

(a) Efficiency for ToF charge related cuts.

(b) Correction for ToF charge related cuts efficiency.

Figure 4.18: Corrections for ToF charge related cuts.

4.4.5 Time-of-Flight β Efficiency

This is one of the simplest efficiencies but its one that guarantees no only a quality measurement of velocity, included in other cuts, but guarantees that the particle is down-going. A positive particle moving down the detector will bend in the same direction as a negative particle moving up. The flux of particles coming from the bottom of the detector is very low due to amount of mass at the bottom of the detector but nonetheless they can be seen. The selection applied for this efficiency lies below.

- **Denominator**
  - Full selection from proton flux selection except for ToF β cuts.
- **Numerator**
  - Full selection from proton flux selection

The results for this efficiency can be seen in Figure 4.19.

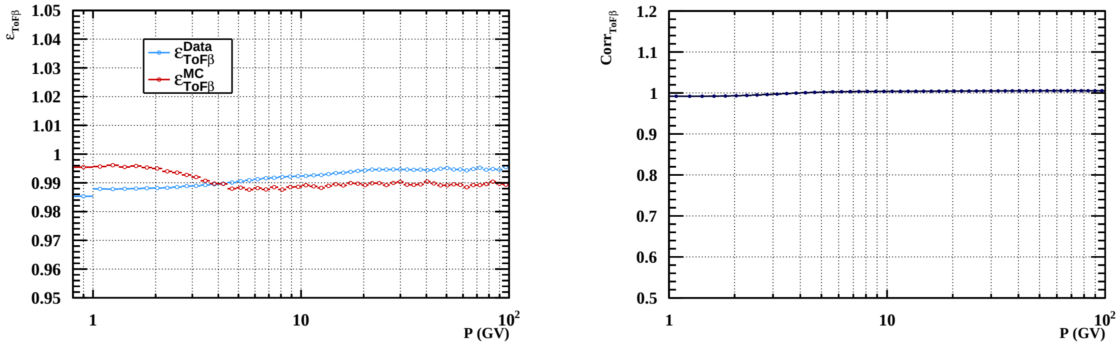

(a) Efficiency for ToF β related cuts.

(b) Correction for ToF β related cuts efficiency.

Figure 4.19: Corrections for ToF β related cuts.

4.4.6 Trigger Efficiency

The simplest way to calculate trigger efficiency would be to simply estimate the ratio between triggered events and the number of cosmic-rays arriving at our detector (see 4.20a). We will refer to these triggers as physical triggers and the rest as non-physical triggers since they include conditions such as a veto on the number of hits in the ACC, which might come from fragmentations inside the detector or other particles entering the detector from the side within our trigger time window, and other characteristics we might want to avoid. AMS-02 is subjected to a constantly varying space environment which directly affects both detector performance and the incoming flux. In order to estimate trigger efficiency AMS-02 is equipped with an unbiased trigger whose efficiency is nearly perfect and is subjected to a pre-scaling factor of 100 for the ToF-based unbiased trigger (see section 3.3). Additionally, AMS-02 only stores the non-physical portion of these unbiased triggers, leading to the following necessary construction in order to estimate trigger efficiency:

$$\begin{aligned}
N^{\text{phys}} &= \varepsilon_{trig}\, N_0 \\
N^{\overline{\text{phys}}} &= (1-\varepsilon_{trig})\, N_0 \\
N^{\overline{\text{phys}}}_{\text{unb}} &= \frac{N^{\overline{\text{phys}}}}{S} = (1-\varepsilon_{trig})\,\frac{N_0}{S} \implies N_0 = \frac{S\, N^{\overline{\text{phys}}}_{\text{unb}}}{(1-\varepsilon_{trig})} \\
\varepsilon_{trig} &= \frac{N^{\text{phys}}}{N^{\text{phys}} + S\, N^{\overline{\text{phys}}}_{\text{unb}}}\,,
\end{aligned}$$

where S is the pre-scaling factor which we consider to be 100. Diagrams of trigger events can be seen in Figure 4.20. This calculation is easy enough to tackle computationally by storing these unbiased non-physical triggers with a weight of 100.

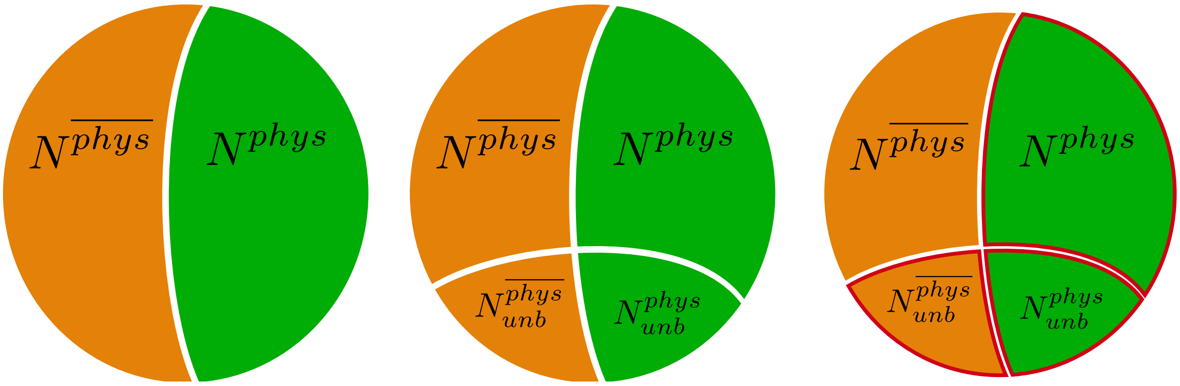

(a) Physical and non-physical trigger events.

(b) Physical and non-physical trigger events as sampled by the unbiased trigger. Physical events are presented in green and non-physical in orange.

(c) Events stored by AMS (highlighted in red). Physical events are presented in green and non-physical in orange.

Figure 4.20: Diagram of the different classifications of events as belonging to the physical trigger, non-physical trigger and unbiased trigger.

We can imagine that this pre-scaling mechanism stores the first non-physical trigger and counts the number of non-physical triggers observed until it reaches 100, then it stores that triggered event and starts counting to 100 again. In this manner, the total number of events in our sample can be considered an *ancillary statistic*[111] and we can simply treat our number of physical events N^{phys} as being distributed by a Binomial function,

$$\begin{aligned}
N^{\text{phys}} &\sim \mathit{Binomial}(p=\varepsilon_{trig},\, n = N^{\text{phys}} + S\, N^{\overline{\text{phys}}}_{\text{unb}}) \\
\varepsilon_{trig} &= \frac{N^{\text{phys}}}{N^{\text{phys}} + S\, N^{\overline{\text{phys}}}_{\text{unb}}} \quad \text{(from Maximum Likelihood Estimation (MLE))}
\end{aligned}$$

which makes efficiency uncertainty have the following expression:

$$\sigma_{\varepsilon_{trig}} = \frac{\sigma_{N^{\text{phys}}}}{N^{\text{phys}} + S\,N_{\text{unb}}^{\overline{\text{phys}}}} = \frac{\sqrt{\left(N^{\text{phys}} + S\,N^{\overline{\text{phys}}}\right)\,\varepsilon_{trig}\,(1-\varepsilon_{trig})}}{N^{\text{phys}} + S\,N_{\text{unb}}^{\overline{\text{phys}}}}\,, \tag{4.20}$$

where the standard deviation of the estimation of efficiency follows simply from the standard deviation of the number of observed physical triggers N^{phys}.

This estimation of uncertainty is based on the premise that our pre-scaling counter works in a fully deterministic way (i.e. if 100 non-physical events arrive at our detector it will always store 1 event). Since we are applying our event selection to these events and given that there are many types of particles arriving at the detector in any one moment, we cannot guarantee that the unbiased trigger is not triggering as well on particles which are not protons, thus increasing the pre-scaling counter, making the total number of selected proton triggers non-deterministic since we are interested in measuring 1 in every 100 non-physical protons and not 1 in every 100 non-physical general particles.

The triggering of the unbiased trigger is independent from our event selection (so long as the cosmic-ray particle triggering it is the same) so the probabilities are separable and we can consider that regardless of the probability of our selection, the probability of a given event (so long as it is a primary proton) triggering the unbiased pre-scaled trigger is always 1/100. The effects we could expect from these diverse particles include different particle inclinations and even different charged particles, creating different energy depositions on the ToF's scintillators, giving a different signal and thus changing the probability of triggering on that event. We can expect (and this has been shown by AMS) that differently charged particles will have different trigger efficiencies so we have to be careful when estimating this quantity for our particle of interest.

To solve this issue we can modify our distribution slightly by using the actual number of observed triggers (non scaled) as our *ancillary statistic* ($N_0 = N^{\text{phys}} + N_{\text{unb}}^{\overline{\text{phys}}}$). This results in a new approach in the efficiency uncertainty estimation which will follow. We begin by delineating our model for physical triggers as:

$$\begin{aligned}
N^{\text{phys}} &\sim \mathit{Binomial}(p = \varepsilon'_{trig},\, n = N^{\text{phys}} + N_{\text{unb}}^{\overline{\text{phys}}}) \\
\varepsilon'_{trig} &= \frac{N^{\text{phys}}}{N^{\text{phys}} + N_{\text{unb}}^{\overline{\text{phys}}}} \implies \frac{1}{\varepsilon'_{trig}} - 1 = \frac{N_{\text{unb}}^{\overline{\text{phys}}}}{N^{\text{phys}}} \\
\sigma_{\varepsilon'_{trig}} &= \frac{\sigma_{N^{\text{phys}}}}{N^{\text{phys}} + N_{\text{unb}}^{\overline{\text{phys}}}} = \frac{\sqrt{\left(N^{\text{phys}} + N_{\text{unb}}^{\overline{\text{phys}}}\right)\,\varepsilon'_{trig}\left(1-\varepsilon'_{trig}\right)}}{N^{\text{phys}} + N_{\text{unb}}^{\overline{\text{phys}}}}\,,
\end{aligned}$$

where the standard deviation of the estimation of efficiency follows simply from the standard deviation of the number of observed physical triggers N^{phys} but now for the new Binomial probability ε'_{trig}.

We can then construct our trigger efficiency ε_{trig} and relate it to the new Binomial probability in the following manner:

$$\begin{aligned}
\varepsilon_{trig} &= \frac{N^{\text{phys}}}{N^{\text{phys}} + S\,N_{\text{unb}}^{\overline{\text{phys}}}} \implies \frac{1}{\varepsilon_{trig}} - 1 = S\,\frac{N_{\text{unb}}^{\overline{\text{phys}}}}{N^{\text{phys}}} \\
\varepsilon_{trig} &= \frac{1}{1 + S\left(\frac{1}{\varepsilon'_{trig}-1}\right)}\,.
\end{aligned}$$

This formulation enables us to write our trigger efficiency uncertainty as:

$$\sigma_{\varepsilon_{trig}} = \left|\frac{\partial \varepsilon_{trig}}{\partial \varepsilon'_{trig}}\right| \sigma'_{\varepsilon_{trig}} = \frac{S}{\left(S-(S-1)\,\varepsilon'_{trig}\right)^2}\,\sigma'_{\varepsilon_{trig}} = S\,\frac{\sqrt{N^{\text{phys}}\,\overline{N^{\text{phys}}_{\text{unb}}}(N^{\text{phys}}+\overline{N^{\text{phys}}_{\text{unb}}})}}{(N^{\text{phys}}+S\,\overline{N^{\text{phys}}_{\text{unb}}})^2}\ . \tag{4.21}$$

In order to confirm this result a small toy Monte-Carlo simulation of these two models was created. In this toy Monte-Carlo we created both scenarios which we will call deterministic or random in regards to the pre-scaling counter behaviour. If we increase the counter every 100 non-physical triggers then we expect to have our initial distribution with $N_0 = N^{\text{phys}} + S\,\overline{N^{\text{phys}}_{\text{unb}}}$, as described by Equation 4.20, and if we increase the counter randomly whenever a non-physical trigger arrives with a uniform probability of 1/100 (since it is unbiased it should trigger uniformly for every particle species, including protons), we will consider that $N_0 = N^{\text{phys}} + \overline{N^{\text{phys}}_{\text{unb}}}$, as described by Equation 4.21. The results can be seen in Figure 4.21.

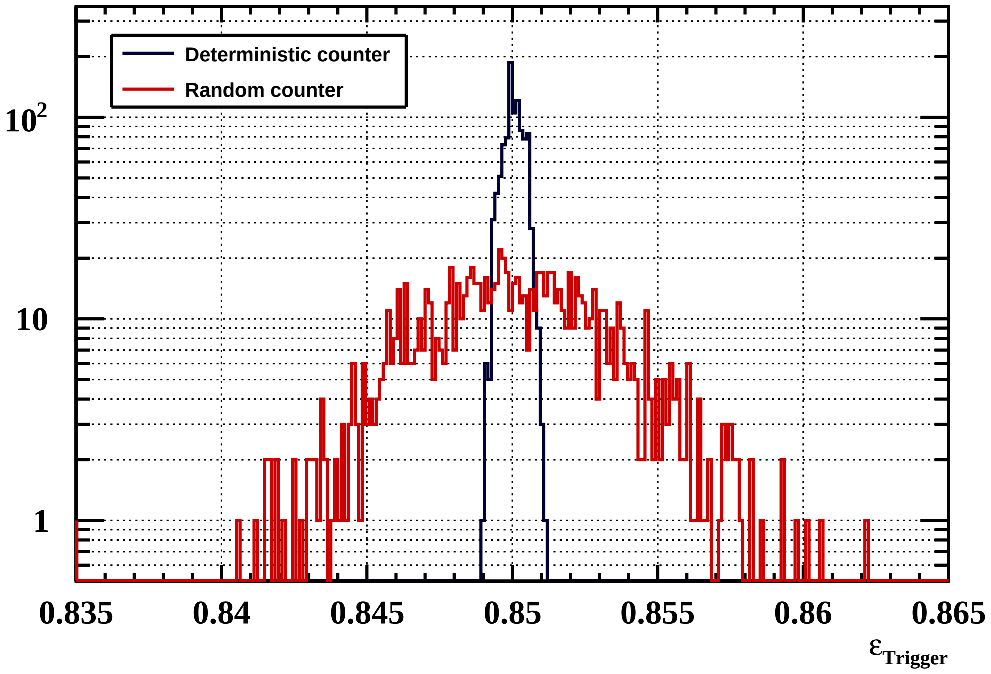

Figure 4.21: Distributions of the estimated trigger efficiencies for the two pre-scaling counters (deterministic and random) for $\varepsilon_{trig} = 0.85$.

In Figure 4.22 we show that this model can accurately describe the fluctuations of the estimation of trigger efficiency for both scenarios and we will adopt the efficiency model for the random pre-scaling counter since this is the most likely real scenario.

Finally, we have all ingredients necessary in order to estimate trigger efficiency (and the

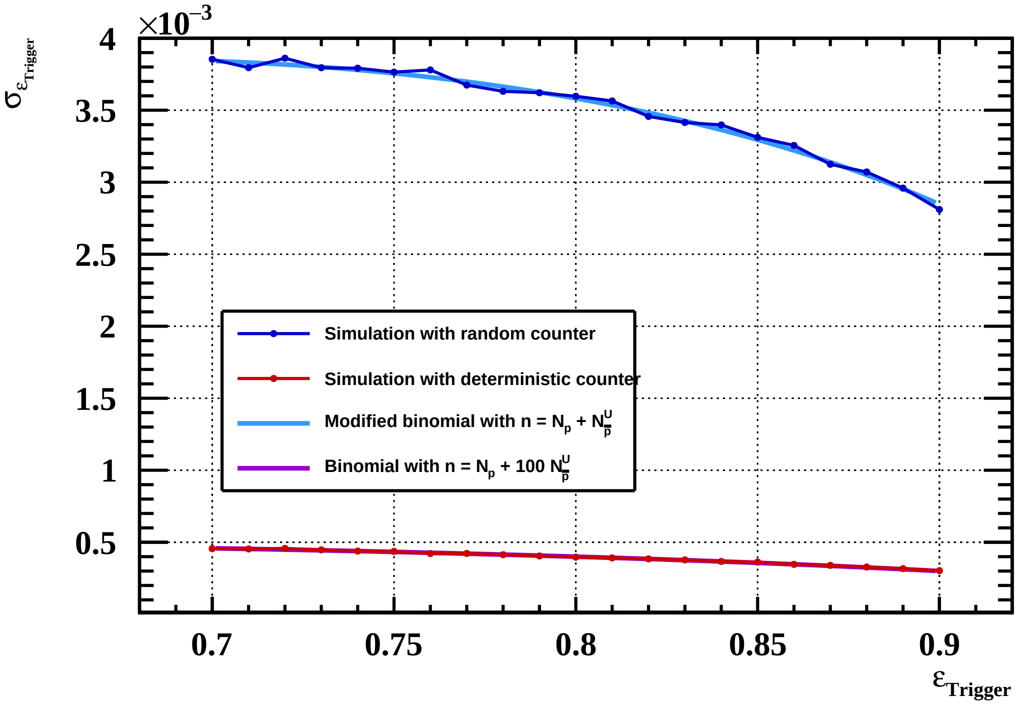

Figure 4.22: Comparison between the two models for trigger efficiency uncertainty and the respective uncertainty models.

respective correction) by applying the following selections:

- **Denominator for unbiased trigger events**
  - Full selection from proton flux selection except for the trigger configuration.
  - Trigger $0x00$ - “Unbiased charged” - 3/4 ToF hits, pre-scaling factor 100
- **Denominator for physical trigger events**
  - Full selection from proton flux selection
- **Numerator**
  - Same as the denominator portion for physical trigger events

The results of this selection can be seen in Figure 4.23.

4.4.7 Total Data-to-Monte-Carlo Corrections

In Figure 4.24 we can see the individual corrections presented for a given time period. Like with the other estimations in this chapter, these will show some variation over time which will be shown later.

These different Data-to-Monte-Carlo corrections can be combined into a single object, allowing us to have a global picture of the total correction applied. The Data-to-Monte-Carlo correction function is defined in Equation 4.16 and it results from the multiplication of these 5 corrections we estimated with the appropriate uncertainty propagation. The total Data-to-Monte-Carlo correction can be found in Figure 4.25.

The biggest contribution to these corrections come from the inner tracker reconstruction efficiency (about 4%) and layer 1 pickup efficiency correction (about 5% at lowest rigidity bins).

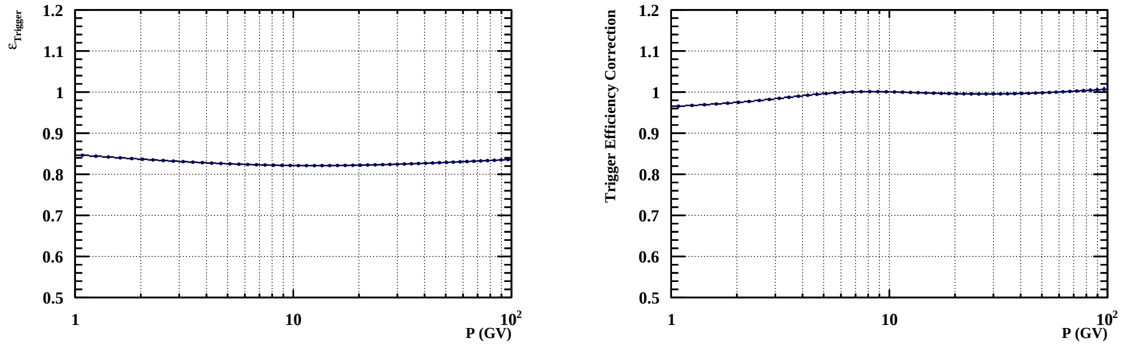

(a) Trigger efficiency for protons.

(b) Data-to-Monte-Carlo correction for trigger efficiency for protons.

Figure 4.23: Trigger efficiency and trigger efficiency correction.

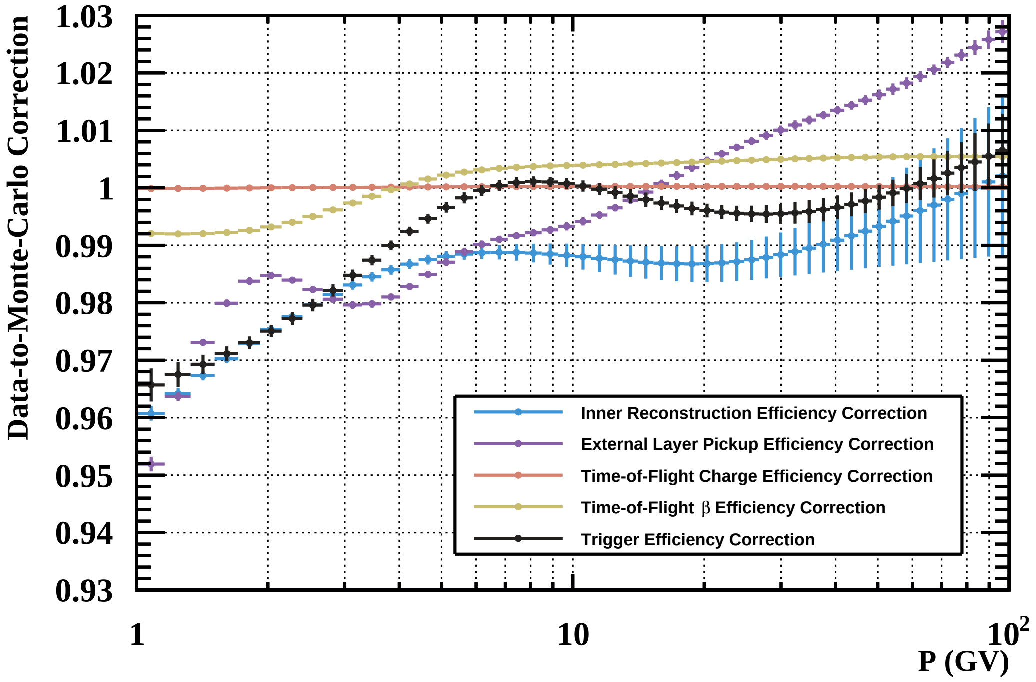

Figure 4.24: Comparison between the different Data-to-Monte-Carlo corrections.

4.4.8 Temporal regularization of Data-to-Monte-Carlo corrections

Aside from major changes in the instrumental setup (such as photomultiplier gain changes or changes in the trigger setup), we expect that the different detector efficiencies, and consequently the Data-to-Monte-Carlo corrections, vary slowly over time and will nor present any major disruptive events. These slow variations can be due to environmental changes such as the rotation of the ISS orbital plane in relation to the Sun, thus changing average detector temperature, or related to the degradation of the performance of some detectors as it ages. Small time-scale variations can be attributed to statistical effects in the determination of efficiencies and should be regularized in order to obtain short-term variations due only to fluctuations in data and thus related to physical processes in the cosmic-ray flux.

Since most of the changes in of the corrections are approximately linear we created a simple

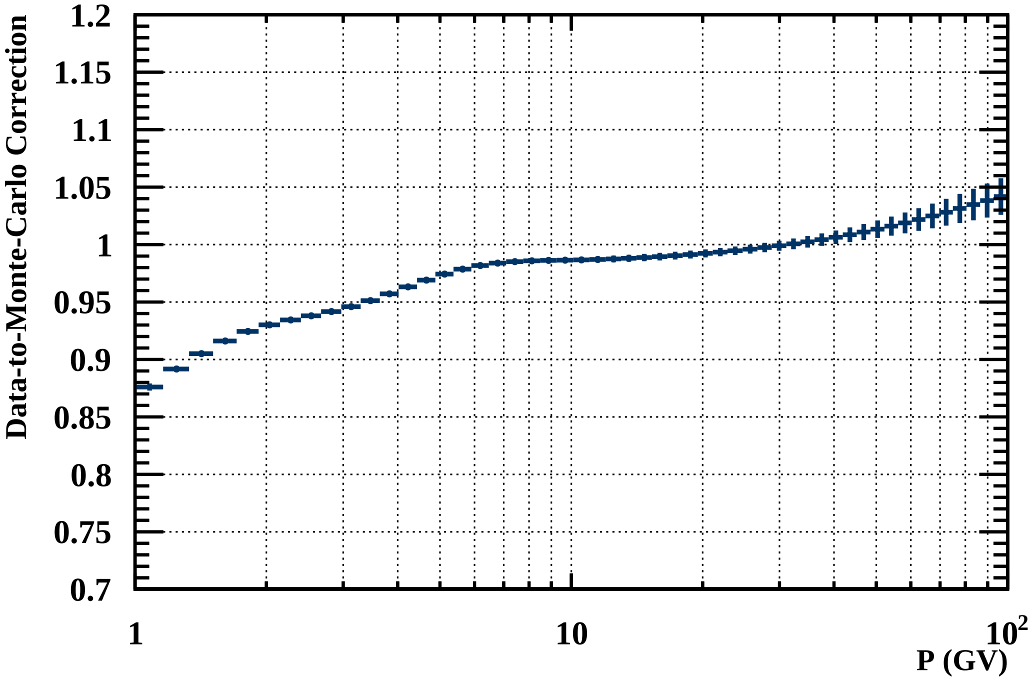

Figure 4.25: Cumulative Data-to-Monte-Carlo corrections.

multilinear model defined by intervals:

$$\tilde{C}(t_i, P_j) = \begin{cases} a_j^0\, t_i + b_j^0 & \text{if } t_i \in [T_0, T_1[\\ a_j^1\, t_i + b_j^1 & \text{if } t_i \in [T_1, T_2[\\ \dots & \\ a_j^n\, t_i + b_j^n & \text{if } t_i \in [T_n, T_{n+1}] \end{cases},$$

where a_j^n and b_j^n is fitted to each time interval we consider to have a linear dependence with time, denoted by the letter n, and for each rigidity bin, denoted by the letter j. T_0 and T_{n+1} coincide with the beginning and end of our time periods in analysis. The different times at which the model changes, denoted by T_n does not depend on rigidity since we are assuming that these large discrete changes of model coincide with a change in the setup of the detector and should be the same for all rigidities of that Data-to-Monte-Carlo correction. The different Data-to-Monte-Carlo corrections present different temporal features.

These time variations of efficiencies and their respective regularizations can be seen in Figure 4.27, 4.28, 4.29, 4.30 and 4.26.

As is shown in Figure 4.26, in 26 November 2013 there was a change of ToF electronics which resulted in an abrupt change in ToF trigger performance, specially at lower rigidities which stabilized thereafter. An explanation for the slow decrease in trigger performance (slow declination of the graph) comes from the natural degradation of the scintillator plastic it uses. As degradation occurred it pulled the signal distribution too close to the threshold (for the initial signal amplification) and so the amount of events that got cut increased drastically as the mean of the signal's distribution approached the threshold edge. A higher signal mean (from the gain increase) provides some headroom for scintillator degradation without impacting performance as much, as can be seen in Figure 4.26 when the inclination suddenly changes.

Later, during 2017 there is another change related to the difference between *pass6* and *pass7* data. This change will be present in most Data-to-Monte-Carlo corrections. There was also some change happening during the TTCS off period in 2013 for some energy bins of some of these corrections, as can be seen in Figure 4.28. Additionally, during the first two periods

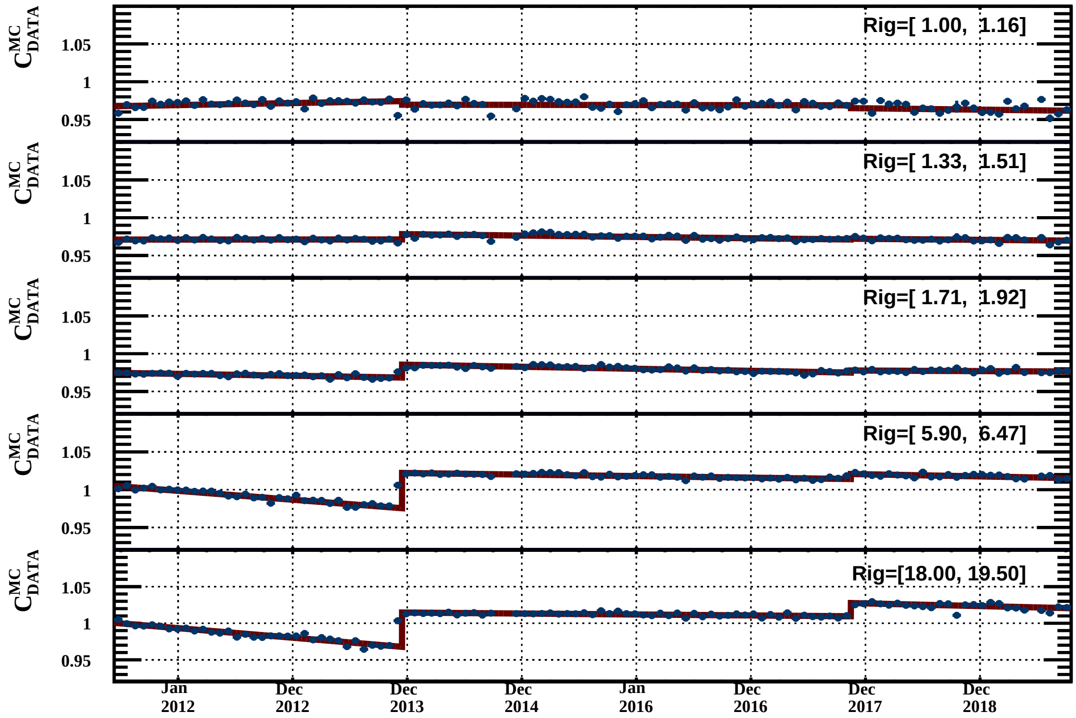

Figure 4.26: Trigger efficiency correction. Regularization in red.

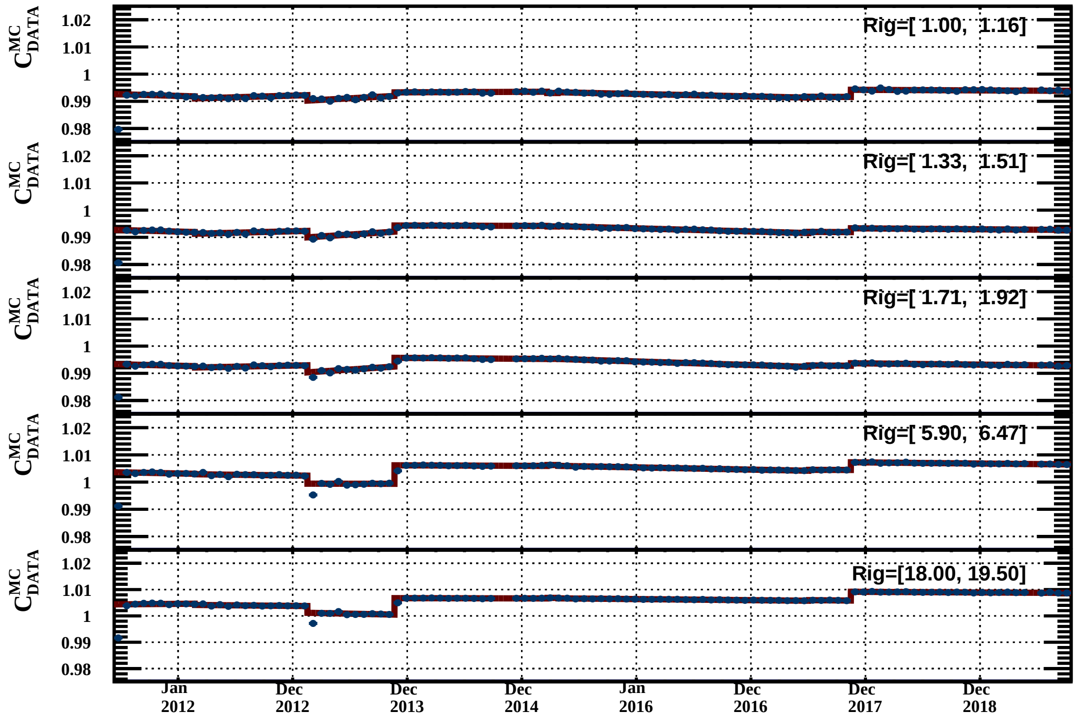

Figure 4.27: Time-of-Flight β efficiency correction. Regularization in red.

of AMS operations there is a drastic change in both the inner tracker reconstruction efficiency and layer 1 pickup efficiency.

The different regularizations were estimated for every rigidity bin, applied in the estimation of the flux replacing the original fluctuating Data-to-Monte-Carlo corrections and systematics were estimated related to this regularization (see subsection 4.5.3).

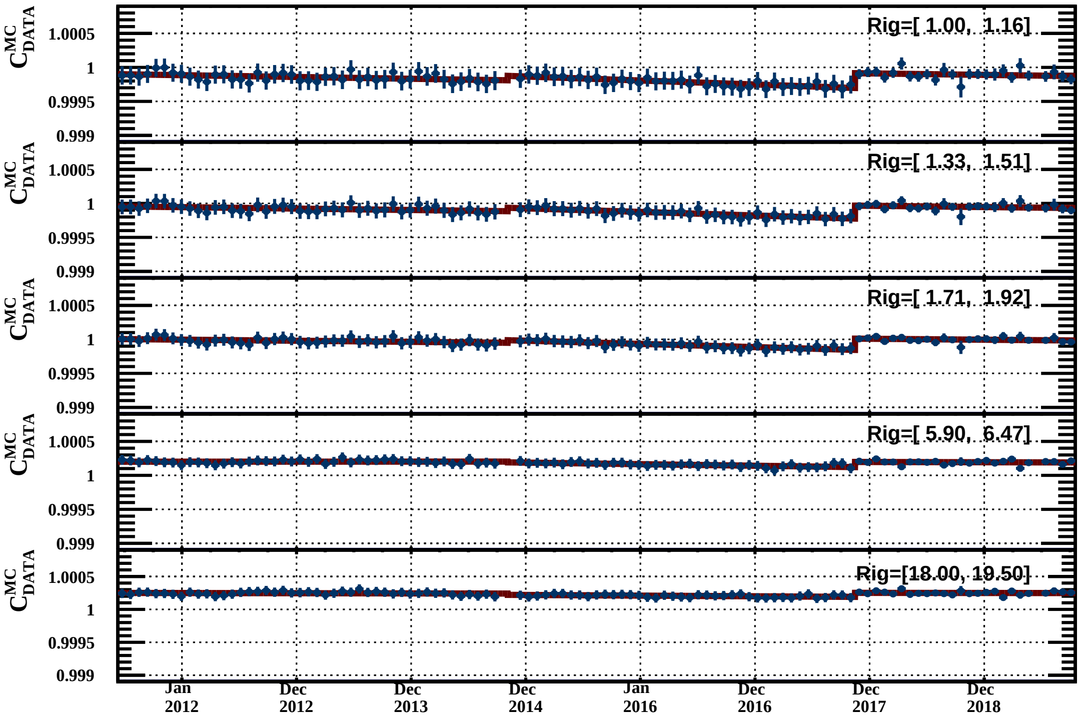

Figure 4.28: Time-of-Flight Charge efficiency correction. Regularization in red.

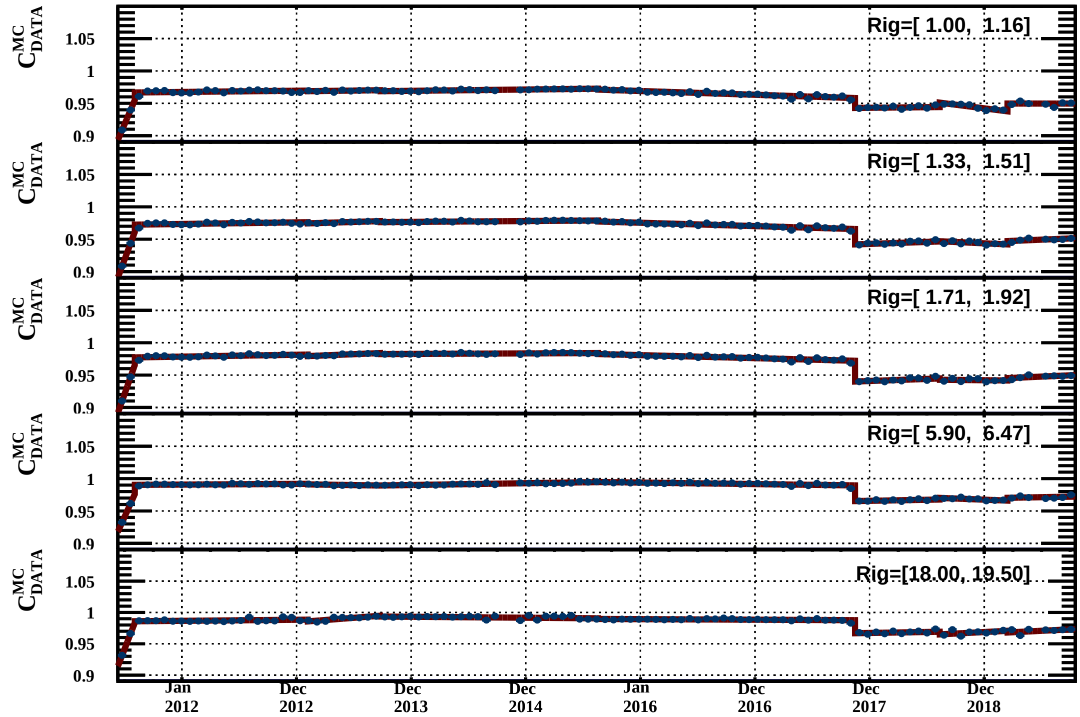

Figure 4.29: Inner tracker reconstruction efficiency correction. Regularization in red.

4.4.9 Unfolding

As previously mentioned in subsubsection 4.4.1.3 we already started the process of correcting for the effects of bin-to-bin migration but we have yet to finalize the process. Different methods can be used in order to correct for these migration effects due to detector uncertainty. A survey of these methods can be found in Cowan, (2002)[112]. Other references of this line of work

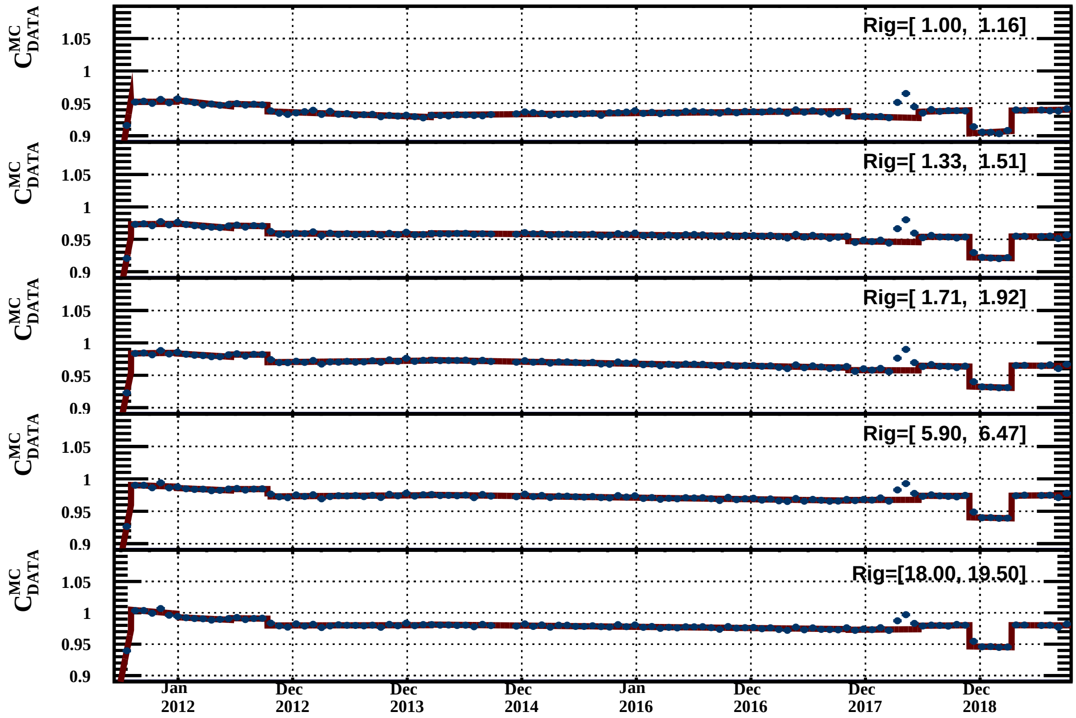

Figure 4.30: External tracker layer pickup efficiency correction. Regularization in red.

include Schmitt, (2012)[113] and the excellent review by Blobel, (2011)[114]. In this work we used an iterative factor correction method.

From our previous calculations and supported by Blobel, (2011)[114], we can see that most of these migration and smearing problems can be expressed as a matrix inversion problem of the form:

$$\begin{aligned}\langle\varphi_{\text{fold}}\rangle(P_i) &= \sum_j \mathcal{P}(P_i \mid P_j)\langle\varphi_{\text{true}}\rangle(P_j)\\ \langle\varphi_{\text{fold}}\rangle_i &= \mathcal{P}_{ij}\langle\varphi_{\text{true}}\rangle_j\\ \langle\varphi_{\text{true}}\rangle_j &= \mathcal{P}_{ij}^{-1}\langle\varphi_{\text{fold}}\rangle_i\,,\end{aligned}$$

where $\mathcal{P}(P_i \mid P_j)$ is our migration probability discretized and built from the migration matrix $M(P_i \mid P_j)$. Our method of solving this problem with correction factors resembles an iterative procedure to solve the matrix equation.

As can be seen in Figure 4.31 the migration matrix for this analysis, built with AMS-02's Monte-Carlo, is mostly diagonal with the majority of its relative migration at lower measured rigidities. Diagonal migration matrices are ideal candidates for factor correction unfolding procedures given the simplicity of the migration.

Interestingly, as we've shown before, our migration matrix is dependent on the generated flux in the Monte-Carlo, creating a recursive problem in which we begin with a tentative flux and use it to extract the different Monte-Carlo quantities required to estimate a flux from our data. After that we need to re-weight Monte-Carlo events in order to simulate a different generation flux. This procedure will then give us a more accurate picture of efficiency and migration and thus generate a more accurate unfolded flux from data. This procedure is depicted in Figure 4.32 and we will show that the algorithm converges very quickly.

This procedure has been used by AMS for a few years [17] and it is based on the principles of *Iterative Bayesian Unfolding*[115]. In contrast, AMS also uses another method which we will not discuss in detailed named *Forward Unfolding* in which a parametric estimation of the

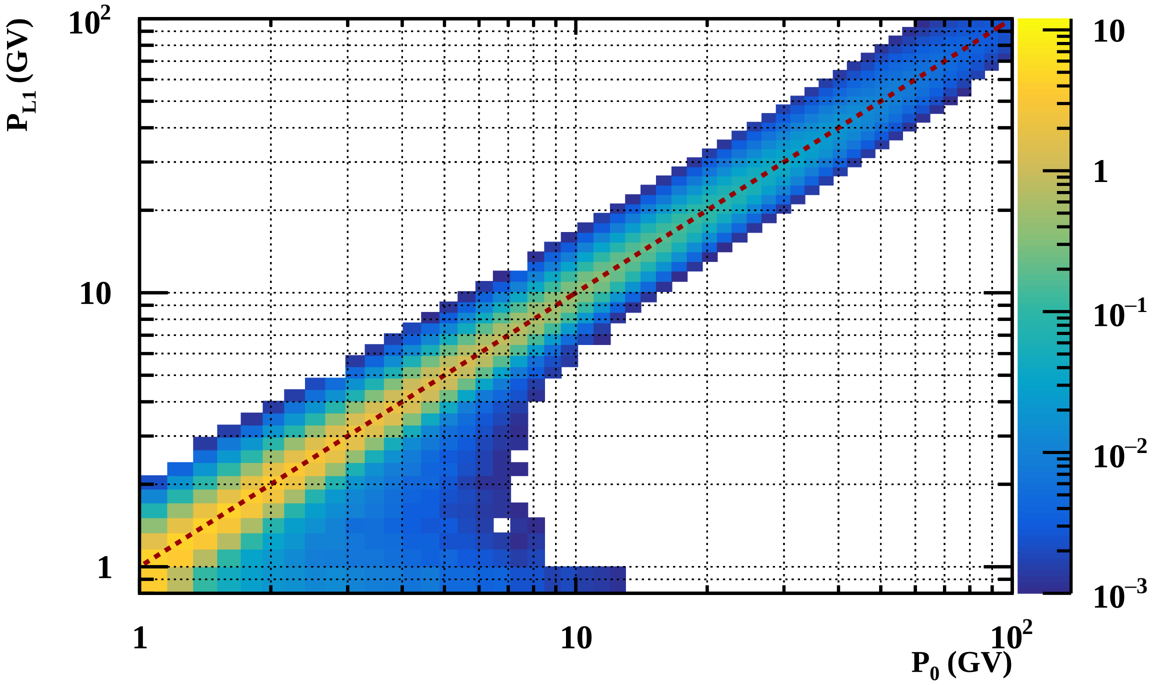

Figure 4.31: Migration matrix for protons on this analysis (*pass6* Monte-Carlo) for a given time period.

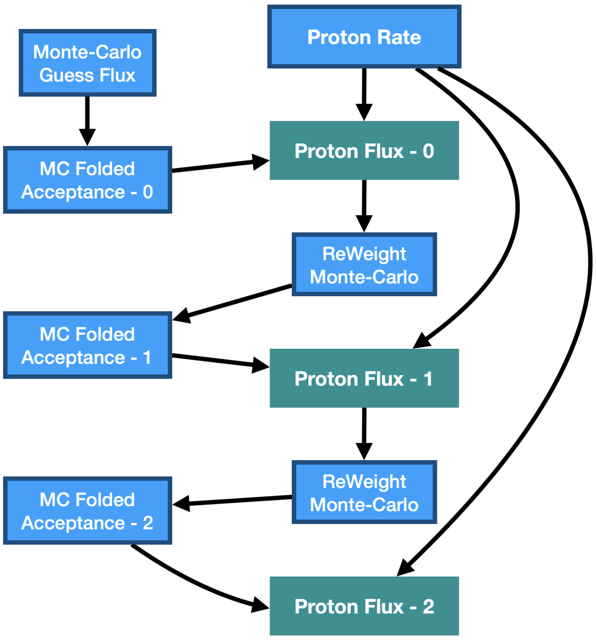

Figure 4.32: Diagram of unfolding procedure up to two iterations.

true flux is made from fitting the folding of this parametrization to observed data [114, 17, 38].

In order to grasp our procedure's convergence a small toy Monte-Carlo was produced and the results can be seen in Figure 4.33. We included a simple relative 20% resolution on measured rigidity, mimicking and exaggerating AMS-02's tracker resolution [38].

As we can see, this procedure converges fairly quickly but a few phenomena can be seen: an increase of uncertainty on the extremes of the result and some oscillations being amplified

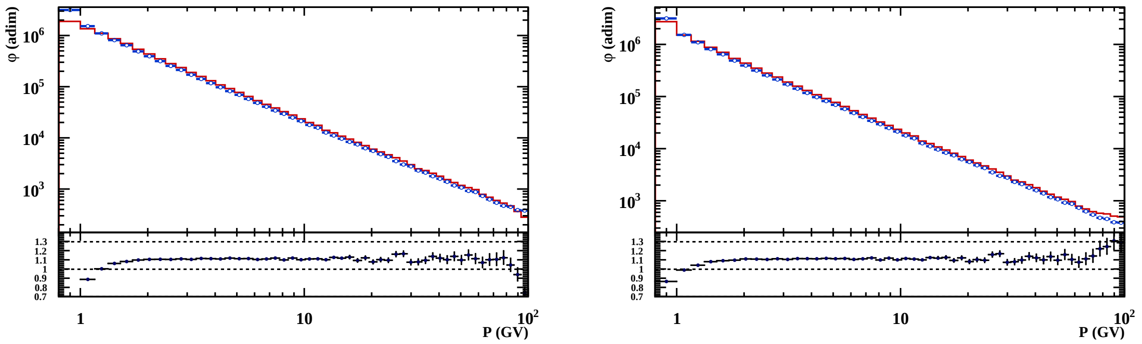

(a) Comparison between iteration 0 of unfolding (red) and the true flux (blue).

(b) Comparison between iteration 1 of unfolding (red) and the true flux (blue).

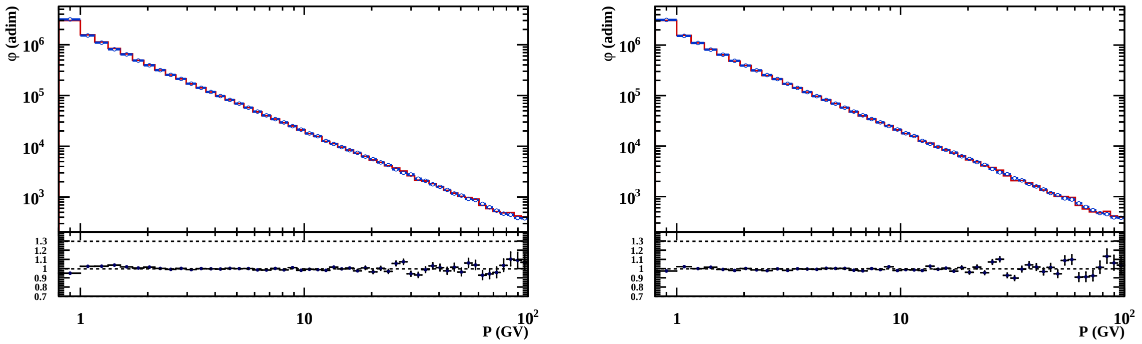

(c) Comparison between iteration 2 of unfolding (red) and the true flux (blue).

(d) Comparison between iteration 3 of unfolding (red) and the true flux (blue).

Figure 4.33: Unfolding tests made from a toy Monte-Carlo.

at the higher end of the flux.

The first issue is due to events migrating outside of our histogram range, thus creating a big dependence on our estimation of the migration (or detector resolution model) at the ends of our result. If our range of generation and measurement is the exact same, on the very ends we will be simulating the amount of events which will migrate outside the histogram bounds, to the underflow, but we will not simulate the ones migrating in. We can be sensitive to this effect but it can usually be corrected by increasing the range of the migration matrix on the generated axis (P_0) since it is produced in Monte-Carlo. In our case, our simulation range is larger than our measurement range. One other step that can be taken is shortening the measurement range if no Monte-Carlo simulation is available that will appropriately simulate the migration to our first and last bins.

The second issue comes from numerical instabilities related to matrix inversion and the fact that at higher rigidities our migration matrix is not as diagonal dominant as at lower energies (our model simple model has a relative resolution which increases with rigidity), generating those wild oscillations which are exacerbated by statistical fluctuations at high energies. We can address this issue by regularizing our flux (as we did before while calculating the efficiencies and their corrections) before reinjecting it into the Monte-Carlo for re-weighting, thus minimizing this effect.

Using the method described we unfolded each our flux for each time period and the result can be seen in Figure 4.34. The results presented in this figure represent the temporal averages and standard deviations of the relative difference between iterations as detailed in the following expressions

$$d_i^{i+1}(P_i, T_j) = \frac{\phi_{i+1}(P_i, T_j) - \phi_i(P_i, T_j)}{\phi_i(P_i, T_j)} \tag{4.22}$$

$$D_i^{i+1}(P_i) = \left\langle d_i^{i+1}(P_i, T_j) \right\rangle_T = \frac{1}{N_T} \sum_{j=1}^{N_T} d_i^{i+1}(P_i, T_j) \tag{4.23}$$

$$\sigma^2_{d_i^{i+1}} = \frac{1}{N_T} \sum_{j=1}^{N_T} \left(d_i^{i+1}(P_i, T_j) - \left\langle d_i^{i+1}(P_i, T_j) \right\rangle_T \right)^2 \tag{4.24}$$

These mean variations and standard deviations are presented in Figure 4.34 as dots (mean) and vertical bars (standard deviation).

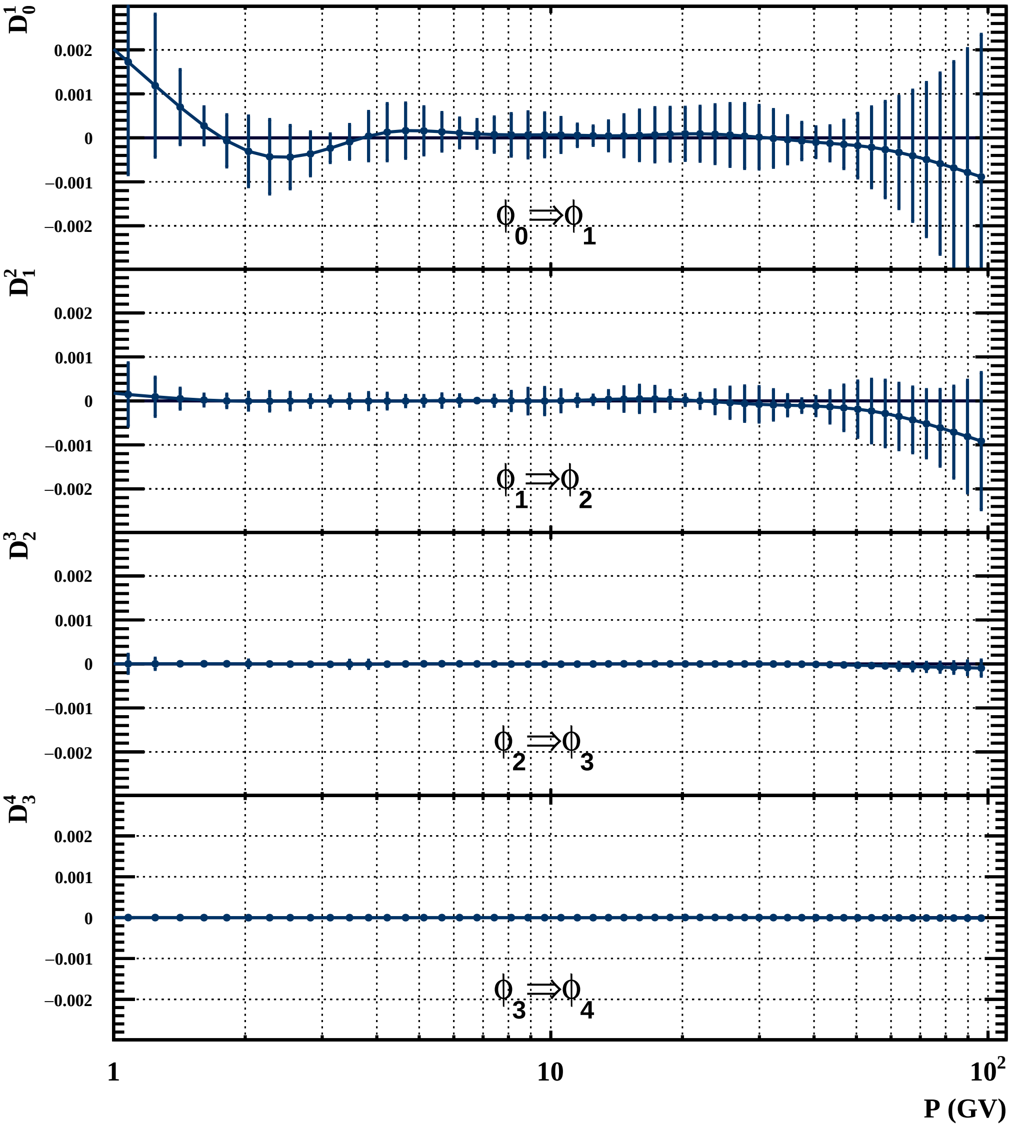

Figure 4.34: Relative difference between iterations of the unfolding process as a function of rigidity. The dots represent the average difference in time ($D_i^{i+1}(P_i)$ from Equation 4.24), for a given rigidity, and the vertical lines represent the standard deviation of the relative differences ($\sigma^2_{d_i^{i+1}}$ from Equation 4.24) for that rigidity.

In Figure 4.34 we can see that the standard deviation between the iterations for the different time bins grows smaller (vertical bars) as the average relative difference (dots) also diminishes. This goes to show that the different time periods unfold at different rates, showing that the convergence rate of unfolding is somewhat dependent on the shape of the cosmic-ray flux, specially at low energies. This process quickly converges after 2 iterations.

The largest differences occur at the extremes of the rigidity range and they are directly correlated with rigidity resolution. As we've seen before (see subsection 3.2.1), tracker resolution can be reasonably well described as Gaussian core on inverse rigidity[116] with non-Gaussian tails. If we plot the migration matrix as a relative difference of inverse measured rigidity to generated rigidity instead of simply choosing measured rigidity we get the result seen in Figure 4.35.

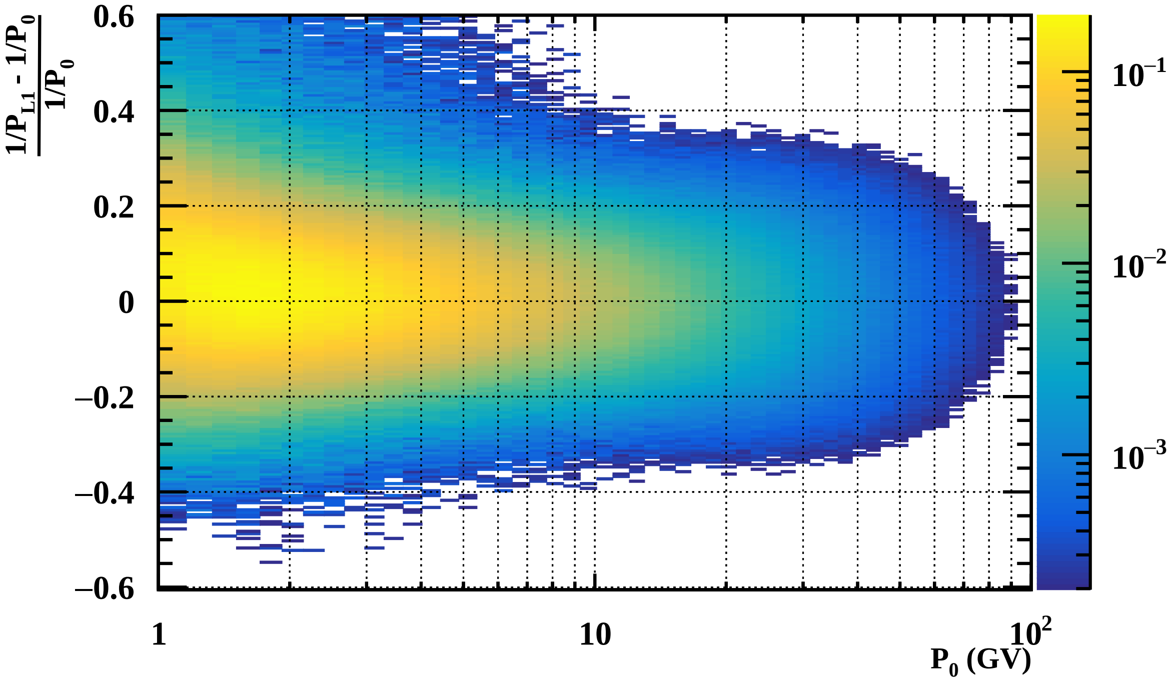

Figure 4.35: Migration matrix for protons on this analysis (*pass6* Monte-Carlo) for a given time period.

This formulation of the migration matrix can be very useful since we can quickly estimate from it a simplistic resolution model which will account for most of our uncertainty. We can slice this migration for fixed rigidities and fit a gaussian model to the peaks in order to make a rough estimate of the tracker resolution for this analysis using the current Monte-Carlo, as can be seen in Figure 4.36.

From distributions modelled in Figure 4.36 we can extract a σ of the main body of the distribution and analyse it. We know from subsection 3.2.1 that a double gaussian or a exponential modified gaussian distribution will accurately describe the tracker uncertainty but we are interested in an overall picture for now. Our estimation of the tracker's resolution can be seen in Figure 4.37.

The graph shows two different behaviours, an initial increase in uncertainty related to energy losses and multiple scattering. For rigidities above 5 GV we see a linear increase in resolution related to the lever effect of the measurement. As rigidity increases, the radius of the particle trajectory inside the magnet also increases, making the sagitta of the trajectory smaller and harder to estimate in this tracker setup, thus increasing uncertainty. This effect is exacerbated by the choice of the fiducial acceptance Layer 1 + Inner of this analysis. The choice of excluding the last tracker layer from the fiducial volume in this analysis greatly increased

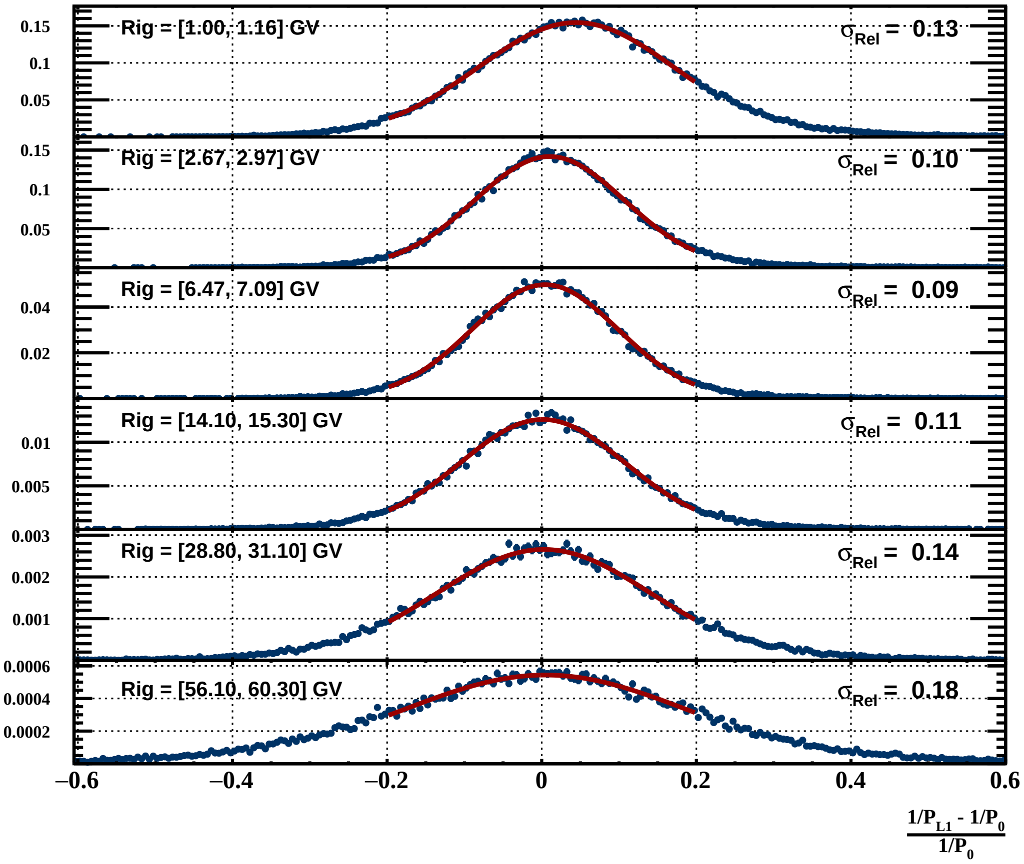

Figure 4.36: Migration matrix for protons on this analysis (*pass6* Monte-Carlo) for a given time period.

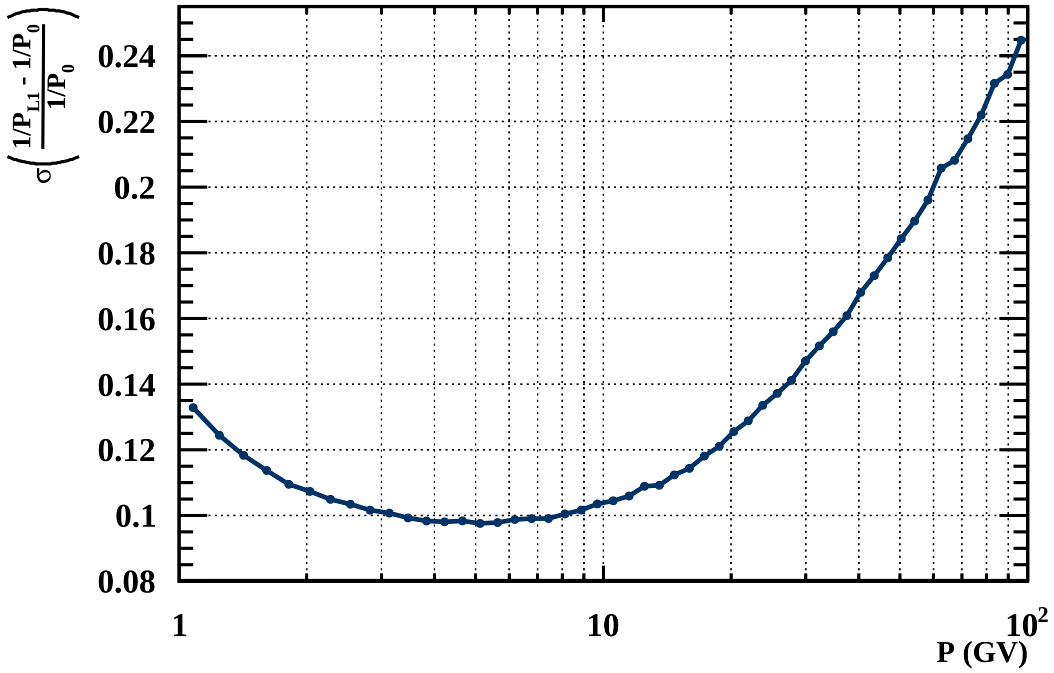

Figure 4.37: Migration matrix for protons on this analysis (*pass6* Monte-Carlo) for a given time period.

the acceptance, specially at lower energies, and increased the overall selection efficiency but it also increases tracker resolution at higher rigidities and thus, the migration effects, as can be seen in Figure 4.36 and Figure 4.34.

At lower energies, our main contribution to migration lies in energy loss. This effect is apparent in both Figure 4.31 and Figure 4.35 in which a tail appears towards lower measured rigidities, for low true rigidities.

In 4.5.5 we will be exploring the results of our unfolding and estimating a global unfolding error for this procedure.

4.5 Statistical and Systematic Uncertainties

Throughout this work a few uncertainties were studied as proposed by Aguilar et al., (2015)[17] and we will be presenting them in this section. Each uncertainty will be related to a bartel rotation. The following uncertainties were considered during this work:

- Statistical uncertainty from number of events
- Acceptance systematic uncertainty from number of Monte-Carlo events
- Systematic uncertainty on Data-to-Monte-Carlo corrections from spline regularization
- Temporal regularization of Data-to-Monte-Carlo corrections
- Rigidity scale systematic
- Geomagnetic cutoff safety factor systematic
- Unfolding systematic

4.5.1 Rate statistical and Monte-Carlo systematic uncertainties

We can begin by presenting both the statistic uncertainty and the acceptance systematic related to the number of events generated for the Monte-Carlo simulation. In the case of the acceptance we considered a Binomial statistic for each bin as previously described. We considered this uncertainty when constructing our smoothing spline and recovered the 68% confidence interval for that fit and used it as the uncertainty of the final smoothed acceptance. In regards to the number of measured events (and the event rate), we considered that it followed a Poisson distribution[109, 99] and thus estimated our statistical uncertainty as being $\sigma_{N_i} = \sqrt(N_i)$ for each bin. These uncertainties can be seen in Figure 4.38.

4.5.2 Data-to-Monte-Carlo correction systematic uncertainties

Every Data-to-Monte-Carlo correction estimated was regularized using a spline fit as we detailed previously. The tool *LxSmoother* and the algorithm employed is detailed in section A.1. Using the fit result, a 68% confidence interval was built and that estimation was used to estimate the systematic uncertainty related to the regularization.

When evaluating the different efficiencies we considered the cut in study as a *last cut*[110, 111] after assuring that it was independent of the rest of the selection, as is common practice. This required that we grouped up the cuts into the different sub-detectors in order to keep the covariances minimal. In this statistical treatment we consider that our efficiency follows a Binomial distribution and the MLE of the probability is simply $p = \varepsilon = N^{sel}/N_0$.

As long as the efficiency is not 1 nor 0, we can treat the uncertainty of this estimation using the variance of the Binomial. There have been several authors [109, 111, 110, 117] that put into question this approach in the edge cases and mostly compare this estimation against

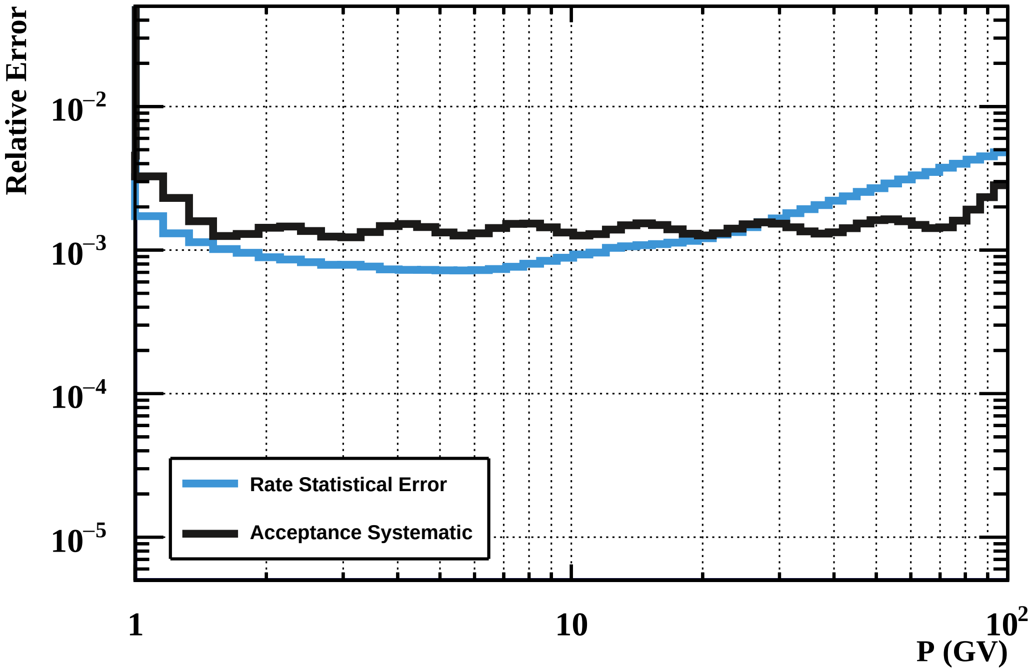

Figure 4.38: Relative statistic uncertainty from number of events and systematic uncertainty related to the number of events generated for the Monte-Carlo simulation.

Bayesian approaches in which the prior probabilities functions fall to zero as the efficiency approaches 0 or 1 since we know that the efficiency needs to be lie somewhere in the interval $]0, 1[$.

Another concern lied in the contribution of the background to the efficiency estimation. In order to guarantee that the effects of the contaminations were minimal (since the signal and background particles can have very different efficiencies to the same cut) some of the charge cuts were tightened during efficiency estimation when the need arose. This was specially important when considering the efficiency of some of the detectors which measured charge and helped select protons.

After estimating the efficiency uncertainty we calculated the corrections by dividing the two efficiencies and propagated the errors according to a standard propagation of independent errors (since one came from data and the other from Monte-Carlo). We then used these errors when estimating our spline regularizations from which we extracted the final total uncertainty for the correction as mentioned before, as can be seen in the next expression:

$$\sigma^{\text{Syst}}_{\text{Corr}} = \sigma^{\text{Syst}}_{\text{InnerRec}} \oplus \sigma^{\text{Syst}}_{\text{L1Pickup}} \oplus \sigma^{\text{Syst}}_{\text{QToF}} \oplus \sigma^{\text{Syst}}_{\beta\text{ToF}} \oplus \sigma^{\text{Syst}}_{\text{Trigger}}$$

Systematic uncertainties were estimated for all the contemplated Data-to-Monte-Carlo corrections: Inner Reconstruction Efficiency, Layer 1 Pickup Efficiency, Time-of-Flight Charge Efficiency, Time-of-Flight β Efficiency and Trigger Efficiency. Results can be found in Figure 4.39.

4.5.3 Temporal regularization systematic uncertainty

The temporal regularization of the aforementioned Data-to-Monte-Carlo corrections will introduce a systematic uncertainty related to the difference between the regularization and the Data-to-Monte-Carlo correction. In order to estimate the uncertainty we simply took the standard deviation of the relative difference between the Data-to-Monte-Carlo correction and the respective temporal regularization as seen in

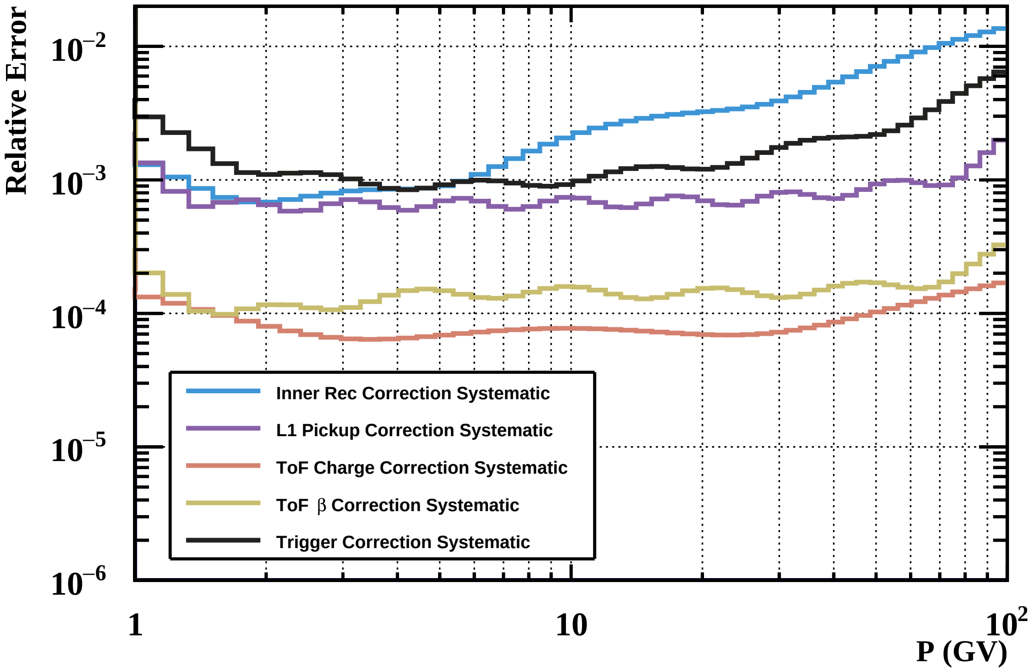

Figure 4.39: Relative systematic uncertainty related to histogram regularization of the Data-to-Monte-Carlo corrections for every correction applied to the result.

$$
\begin{aligned}
d_{ij} &= \frac{C_{MC}^{DATA}(t_j, R_i) - \tilde{C}(t_j, R_i)}{\tilde{C}(t_j, R_i)} \\
\langle d_{ij} \rangle &= \frac{1}{N_{\text{bartel}}} \sum_{j=1}^{N_{\text{bartel}}} \frac{C_{MC}^{DATA}(t_j, R_i) - \tilde{C}(t_j, R_i)}{\tilde{C}(t_j, R_i)} \\
\sigma_{\text{TimeReg}}^{\text{Syst}}(P_i) &= \frac{1}{N_{\text{bartel}}} \sum_{j=1}^{N_{\text{bartel}}} \left(d_{ij} - \langle d_{ij} \rangle\right)^2 ,
\end{aligned}
$$

where $\tilde{C}(t_j, R_i)$ represents our multilinear model as described in subsection 4.4.8. As before, we estimated this relative systematic uncertainty and took it into account in the estimation of the flux. These can be found in Figure 4.40.

4.5.4 Rigidity-Scale systematic uncertainty

Another contribution to uncertainty of our result comes from the binned approximation of the acceptance function. As previously stated, in order to have a measurable result we have binned our events and estimations of all the physical quantities required to both measure the flux and characterize our experiment in terms of its efficiencies. These binned values constitute the average of these functions within teach bin. This effect is highlighted in Figure 4.41.

We need to take into account the systematic uncertainty associated with this average estimation for our acceptance. This systematic is known as *Rigidity Scale Systematic Uncertainty* [17]. The acceptance here considered includes all of the detector effects and efficiencies, varying with rigidity as can be seen in Figure 4.11.

In order to calculate this systematic we will estimate the variation of the acceptance function over the interval assuming that the probability density function of the rigidity is uniform within each bin. This can be seen in Equation 4.25.

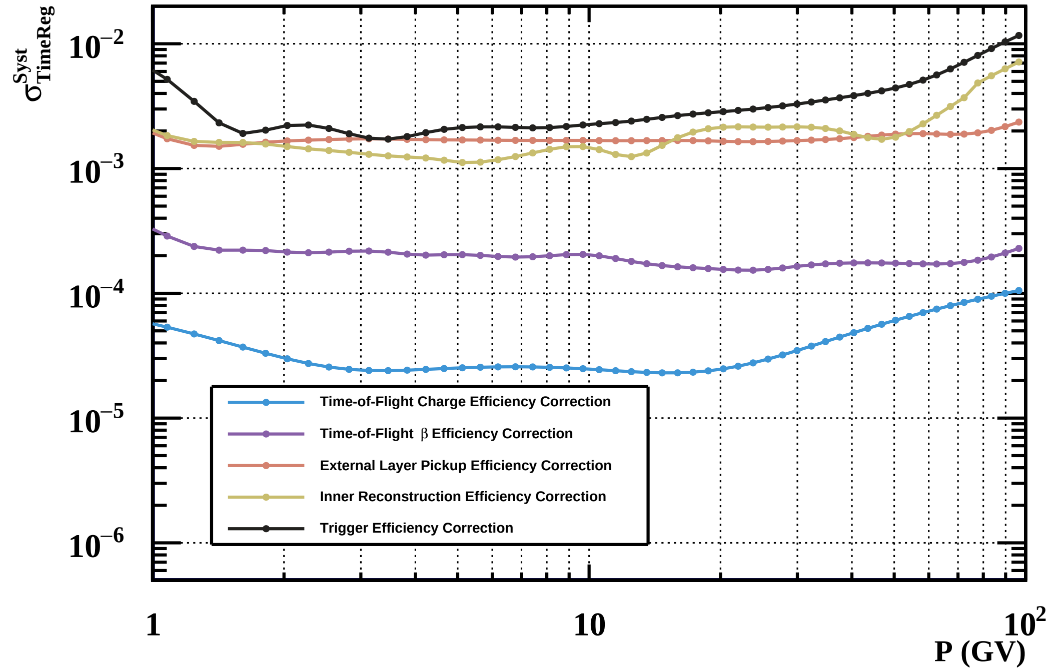

Figure 4.40: Relative systematic uncertainty related to the regularization of the Data-to-Monte-Carlo corrections.

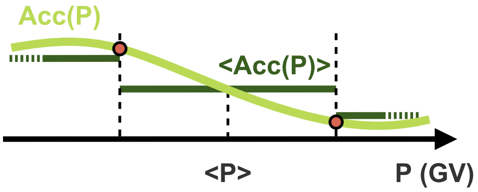

Figure 4.41: Diagram showing the difference between the true acceptance function and the binned value.

$$\sigma^{\mathrm{RigScale}}_{\mathrm{Acc}}(P_i) = \left|\frac{\mathrm{dAcc}}{\mathrm{d}P}(P_i)\right| \sigma_P = \left|\frac{\mathrm{dAcc}}{\mathrm{d}P}(P_i)\right| \frac{\Delta P_i}{\sqrt{12}} \tag{4.25}$$

This result is present in Figure 4.42 and was evaluated for every time period.

4.5.5 Unfolding systematic uncertainty

As previously discussed, the measured flux has to be corrected for migration due to the uncertainty of rigidity measurement. We unfolded the flux using the *Folded Acceptance* method (see subsection 4.4.9) and verified its very fast convergence, in every iteration after the first the flux remained mostly unchanged (0.01% change at low rigidities and 0.1% at high rigidities for the second iteration). This procedure relies mostly on using a *folded acceptance* to estimate the unfolded flux from the measured rate as was detailed in Equation 4.15:

$$\varphi^{\mathrm{Unf}}_{0\to 1}(P_i) = \frac{N(P_i)}{\Delta T(P_i)\, Acc^{Fold}_{0\to 1}(P_i)\, C^{\mathrm{Data}}_{\mathrm{MC}}(P_i)\Delta P_i}\,. \tag{4.26}$$

We want to evaluate the contribution of the unfolding procedure to the overall uncertainty which is deeply tied to the contribution of the acceptance to this uncertainty. Since we've already taken into account the number of Monte-Carlo events used and the rigidity scale

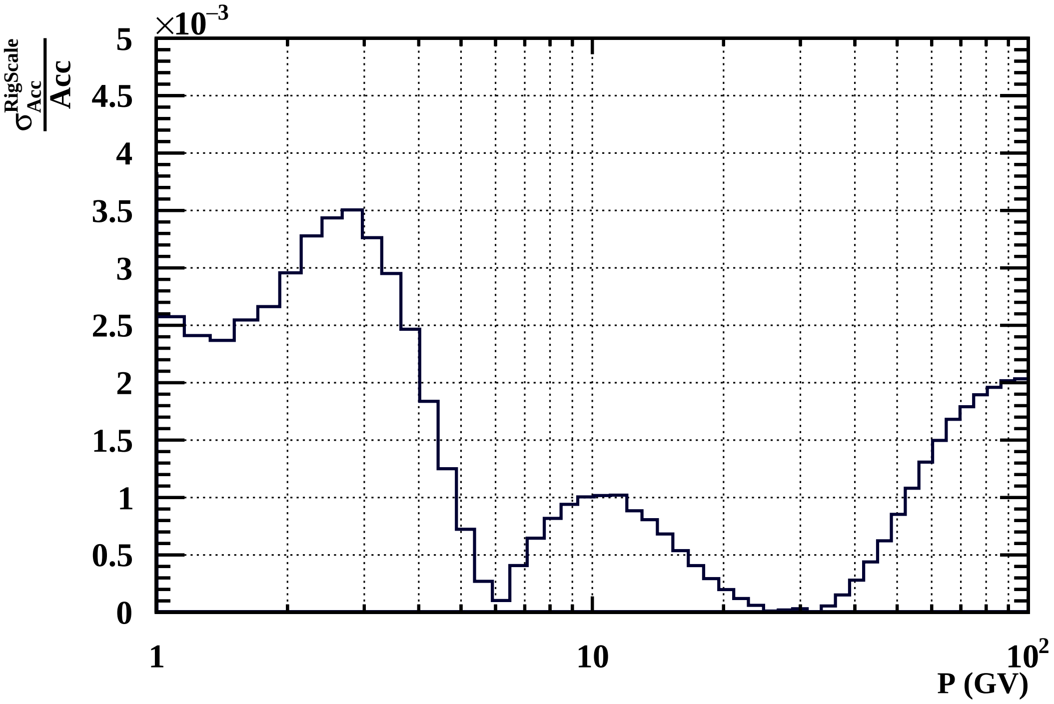

Figure 4.42: Relative systematic uncertainty associated with Rigidity Scale.

effect, we need to consider the impact that the variation of the shape of the acceptance has on the estimated flux. This contribution is tied to how sensitive the spline regularization performed on the acceptance is to statistical variations on the acceptance shape.

The migration matrix remains mostly unchanged through the iterations after the first ($0 \rightarrow 1$), as is evidenced by the very small change in the unfolding iterations after the very first, indicating that the main contribution to the uncertainty in the unfolding procedure comes mainly from the first iteration.

In order to estimate this contribution we ran a toy Monte-Carlo in which we varied the *folded acceptance* according to its own statistical uncertainty (detailed in subsection 4.5.1) by varying each bin according to a Poisson distribution with a standard deviation equal to the bin error. We then smoothed the acceptance histogram using our spline regularization tool, estimated the relative difference between the new unfolded flux and the unfolded flux estimated for the full analysis, for each rigidity bin, and stored this result in a bidimensional histogram. This was then repeated a number of times in order to get the result presented in Figure 4.43.

The standard deviation of the relative difference between the fluxes was then estimated by slicing the above matrix for each rigidity bin as can be seen in figure Figure 4.43.

Using the standard deviations estimated from the rigidity slices presented in Figure 4.43, we were able to estimate the full contribution of the *folded acceptance* to the estimate flux as is presented in Figure 4.45.

This result shows us that we are very sensitive to unfolding at the lowest rigidities but the effect quickly drops below 1% above 3 GV. There is a slight increase at the highest rigidities but still well below 0.3%. The unfolding procedure is responsible for the highest systematic uncertainty contribution to the overall result out of all determined in this section.

4.5.6 Geomagnetic cutoff safety-factor systematic uncertainty

In section 4.3 we discussed the introduction of a safety factor to the geomagnetic cutoff and the removal of orbital seconds from both exposure time and the number of measured events.

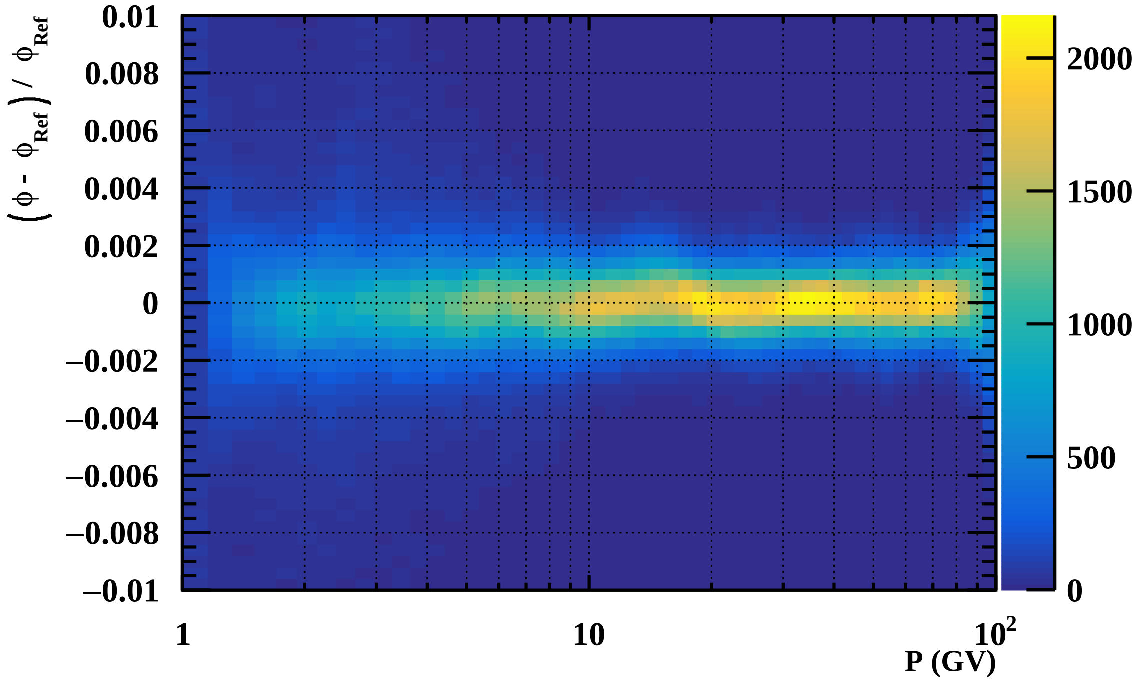

Figure 4.43: Distribution of the relative difference of the flux due to statistical uncertainty of the *folded acceptance*, as a function of rigidity bin.

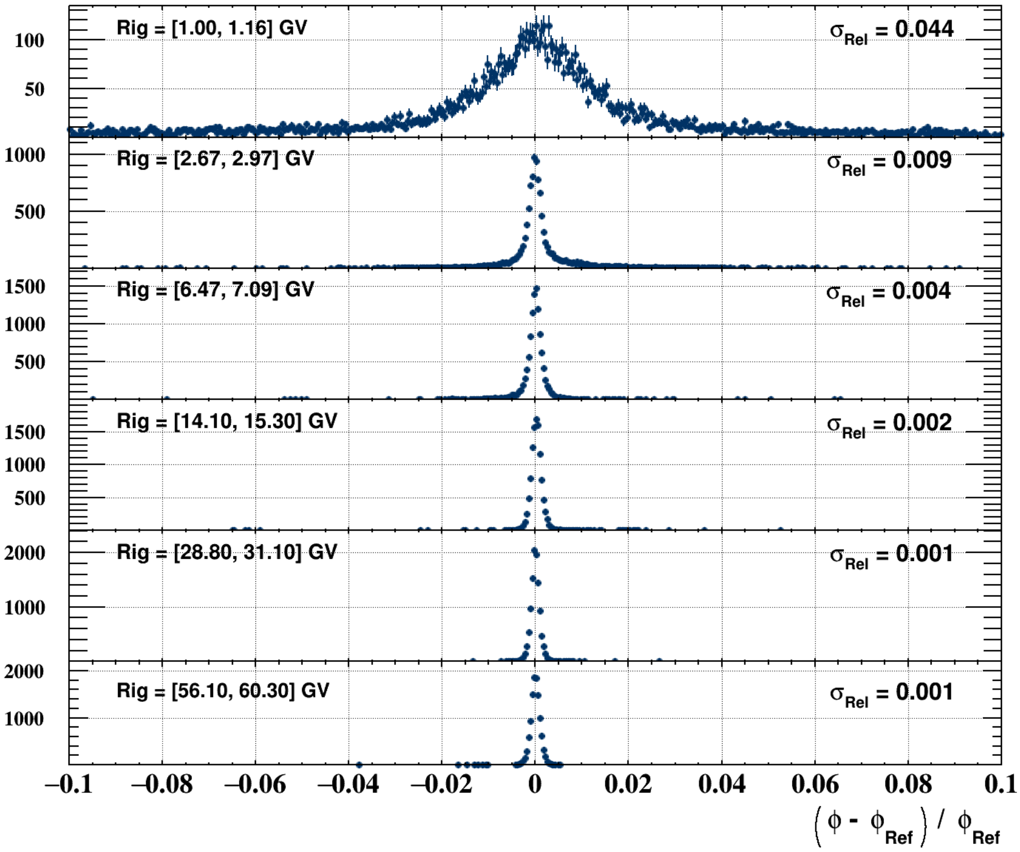

Figure 4.44: Distribution of the relative difference of the flux due to statistical uncertainty of the *folded acceptance*, for a given rigidity bin.

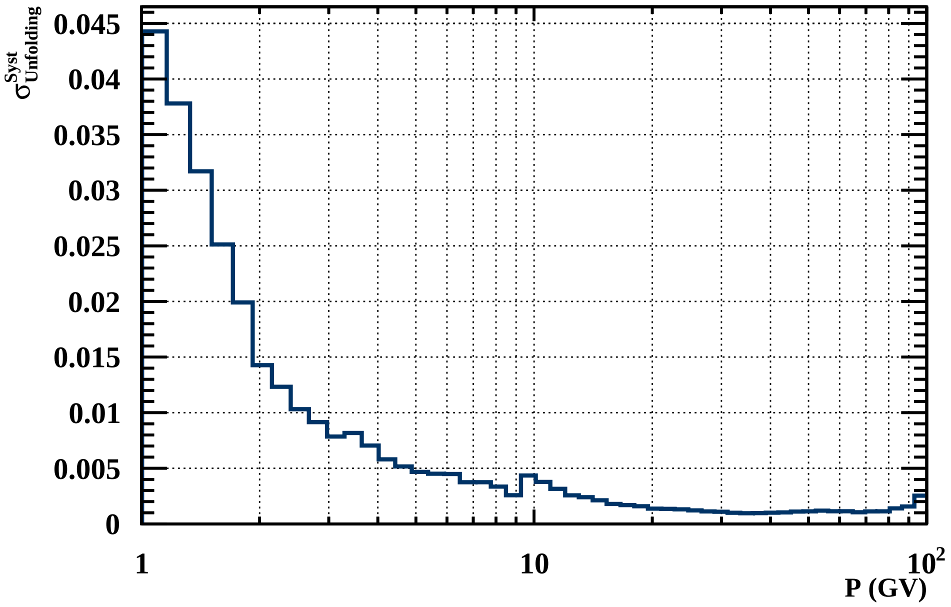

Figure 4.45: Relative systematic uncertainty to the estimated flux due to statistical uncertainty of the *folded acceptance*.

We will now explore in depth the relative importance of the safety factor, show the reasoning behind the choice in safety factor and estimate its contribution to the uncertainty of our result. We will be following some of the results found in Barão et al., (2011)[103] and Barão and Derome, (2011)[107].

The rigidity cutoff due to the geomagnetic field is highly dependent on the orbital position of the ISS and on the direction of the incoming cosmic rays. In order to have a rigidity cutoff that is independent of cosmic-ray direction we choose, for every orbital position, the maximum rigidity cutoff for all available directions (minimum rigidity that a primary particle can have), thus taking a conservative approach. A more parametric approach would be to map the rigidity cutoff for every second, for every direction but that would be rather cumbersome and would make primary-to-secondary separation dependent not only on rigidity measurement resolution but also on the uncertainty of reconstructed direction.

The change in safety factor introduces a change in the angular distribution of cosmic rays. As S increases, the orbits favouring higher particle inclinations (and consequently higher cutoff rigidities) are rejected, thus changing the angular distribution of selected cosmic-rays, as can be seen in Figure 4.46 and Figure 4.47.

Figure 4.47 shows the ratio between a safety factor of 0.5 and 1.5, clearly indicating that the change in safety factor will produce a relative drop of $\sim 4\%$ in number of events at higher inclinations in addition to the expected drop in statistics due to the removal of orbital seconds. We want to understand the impact of this change in angular distribution in the overall result and minimize the loss of statistics by choosing a small safety factor.

Considering that our flux is isotropic, a change in the safety factor represents a removal of orbital seconds (or positions) from our measurement meaning that, at a fixed energy, we are removing the same relative amount from both number of events and time since they are proportional to each other as shown in Equation 4.8, keeping the rate unchanged. The result shown in Figure 4.47 indicates that different angular regions of our acceptance are being sampled when we change S so we need to keep this under consideration when reformulating the rate.

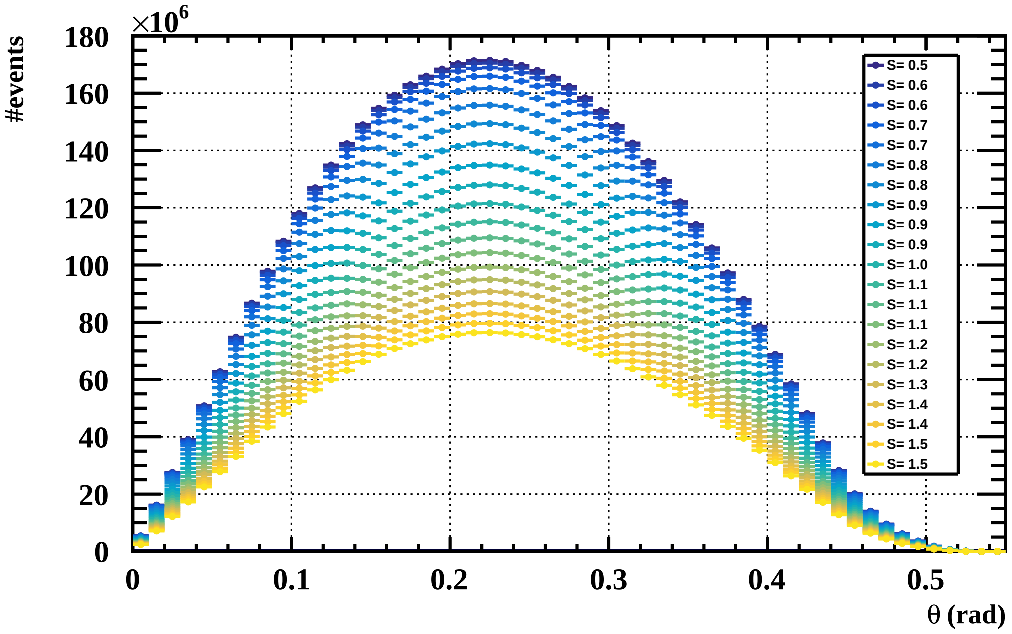

Figure 4.46: Distributions of particle inclination (θ) for the *pass6* period of the data for different safety factors.

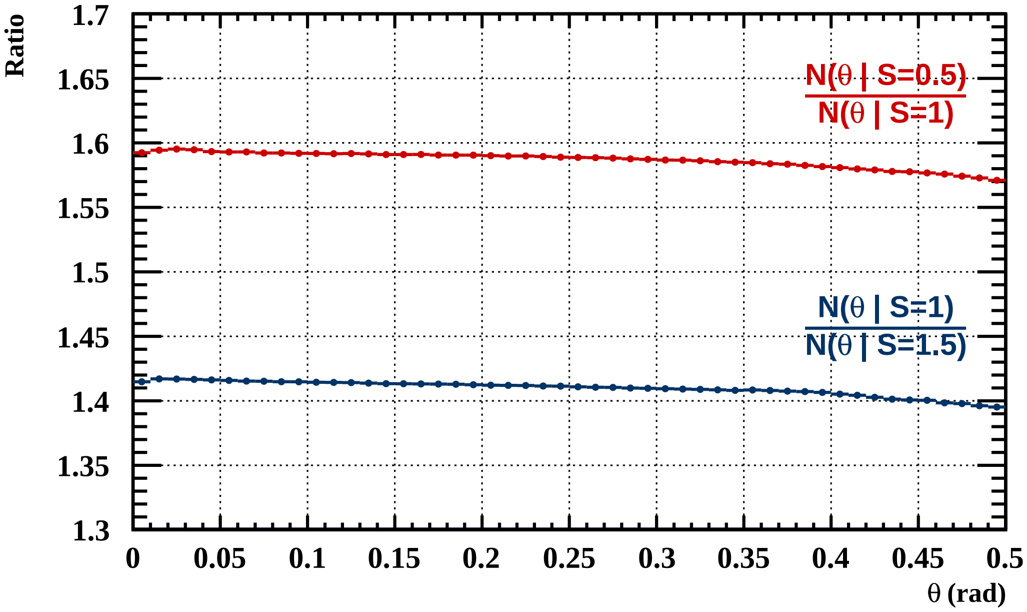

Figure 4.47: Ratio between the distributions of particle inclination (θ) between $S = 0.5$ and $S = 1.5$.

We will begin by writing out the distribution of events as

$$\begin{aligned} \mathrm{d}^5 N(P,\theta) &= \phi_0(P)\,\varepsilon(P,\theta)\,\mathrm{d}A_\perp\,\mathrm{d}P\,\mathrm{d}t\,\mathrm{d}\Omega \\ &= \phi_0(P)\,\varepsilon(P,\theta)\,\underbrace{\cos\theta\,\mathrm{d}A}_{\mathrm{d}A_\perp}\,\mathrm{d}P\,\mathrm{d}t\,\mathrm{d}\phi\,\mathrm{d}\cos\theta \\ &= \phi_0(P)\,\underbrace{\varepsilon(P,\theta)\,\cos\theta\,\mathrm{d}A\,\mathrm{d}\phi\,\mathrm{d}\cos\theta}_{\text{Acceptance}}\,\mathrm{d}P\,\mathrm{d}t\,, \end{aligned}$$

where $\varepsilon(P,\theta)$ represents all of our selection efficiencies related to this analysis and can be estimated with

$$\varepsilon(P,\theta) = \frac{N_{\text{sel}}^{\text{MC}}(P,\theta)}{N_0^{\text{MC}}(P,\theta)}\,.$$

This efficiency function includes all instrumental effects and is independent of the generation flux both in rigidity and θ.

By integrating over the detector area and ϕ, we arrive at the following expression for the differential number of events:

$$\begin{aligned} \mathrm{d}^3N(P,\theta) &= \phi_0(P)\underbrace{\int_0^{2\pi}\int_{A_{\text{det}}} \varepsilon(P,\theta)\,\cos\theta\,\mathrm{d}A\,\mathrm{d}\phi}_{\frac{\mathrm{dAcc}}{\mathrm{d}\cos\theta}}\,\mathrm{d}\cos\theta\,\mathrm{d}t\,\mathrm{d}P \\ &= \phi_0(P)\,\frac{\mathrm{dAcc}}{\mathrm{d}\cos\theta}(P,\theta)\,\mathrm{d}\cos\theta\,\mathrm{d}t\,\mathrm{d}P\,. \end{aligned}$$

This result does not substantially differ from that seen in subsection 4.4.1 except that we have purposely not integrated over θ nor time since we know they are connected through our cutoff effect. Our *differential acceptance*, $\frac{\mathrm{d}Acc}{\mathrm{d}\cos\theta}(P,\theta)$, was built according to Equation 4.27. In Figure 4.48 and we can see this *differential acceptance* as a function of rigidity and θ while in Figure 4.49 θ slices normalized to the last bin on the right.

$$\frac{\mathrm{dAcc}}{\mathrm{d}\cos\theta}(P,\theta) = 2\pi\cos\theta\,S_0\,\frac{N_{\text{sel}}^{\text{MC}}(P,\theta)}{N_0^{\text{MC}}(P,\theta)}\,. \tag{4.27}$$

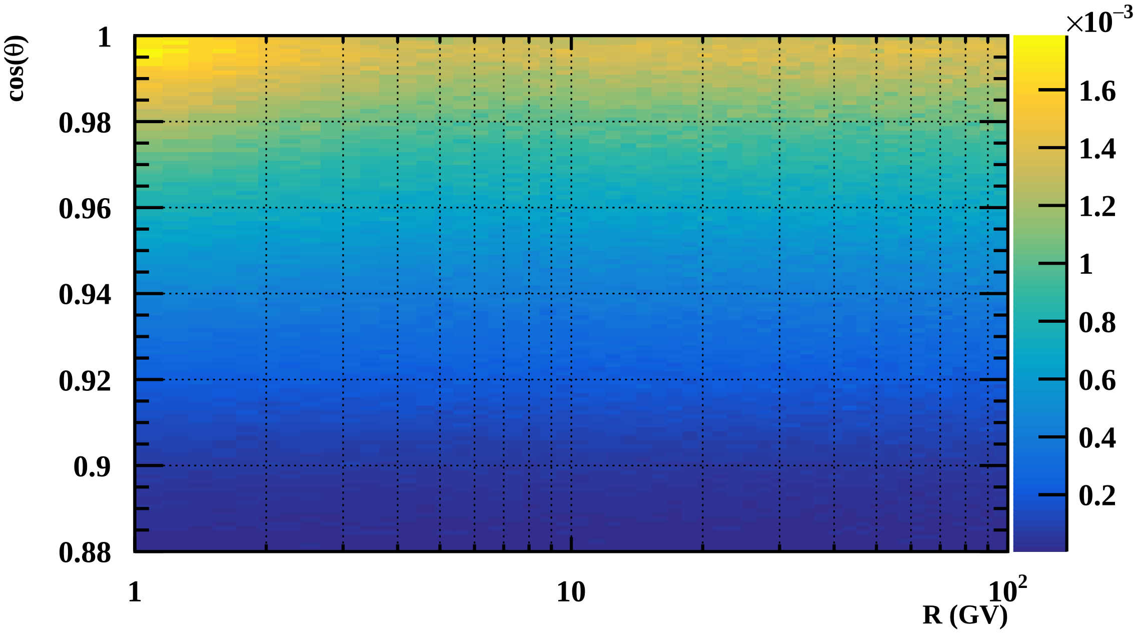

Figure 4.48: Differential acceptance as a function of rigidity and θ.

The integration in time of our number of events is an integration over all the orbital seconds considered in the analysis, which in turn implies a certain angular distribution which is not isotropic even though the cosmic-ray flux is. We will consider this effect as a modulation of the flux in the form of $f(P,\theta|S)$. We expect that this function is normalized such that:

$$\int_\theta f(P,\theta|S)\,\mathrm{d}\cos\theta = 1\,.$$

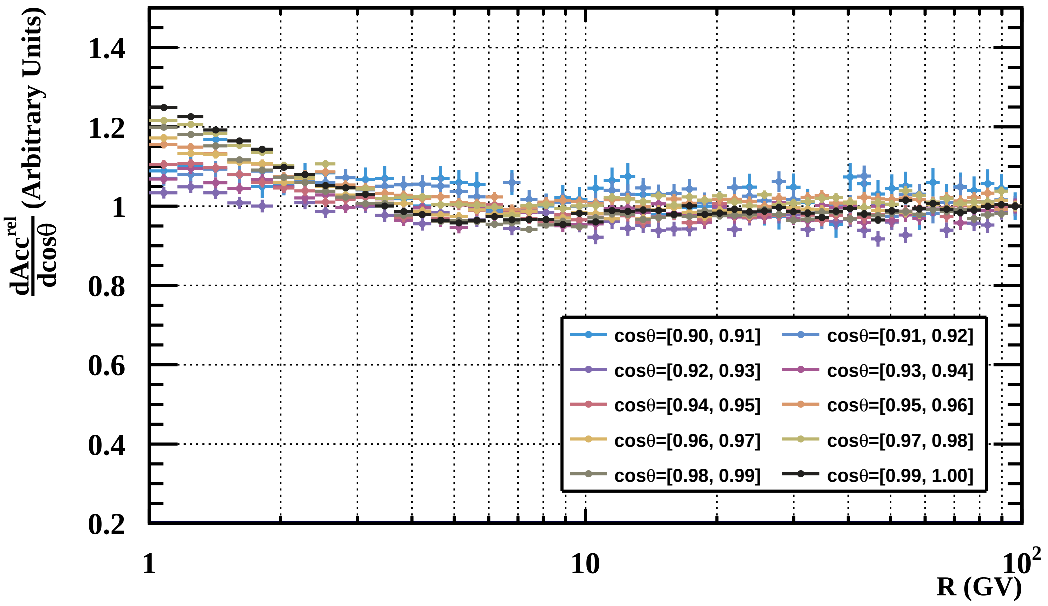

Figure 4.49: Comparison of the differential acceptance for different inclinations normalized to the last bin. Different colours represent the different inclinations.

By rearranging our expression for the number of events and considering the new modulation function we can write out our rate as:

$$\frac{\mathrm{d}^2\mathrm{Rate}(P,\theta|S)}{\mathrm{d}\cos\theta\,\mathrm{d}P} = \phi_0(P)\,f(P,\theta|S)\,\frac{\mathrm{dAcc}}{\mathrm{d}\cos\theta}(P,\theta)\,,$$

which can be rearranged to the form:

$$\frac{1}{\frac{\mathrm{dAcc}}{\mathrm{d}\cos\theta}(P,\theta)}\frac{\mathrm{d}^2\mathrm{Rate}(P,\theta|S)}{\mathrm{d}\cos\theta\,\mathrm{d}P} = \phi_0(P)\,f(P,\theta|S)\,.$$

As we integrate over θ now with the appropriate angular distribution on both sides of the equation and identify our rate within the left-hand side of the expression and noting that the flux does not depend on θ we get the following result,

$$\int\limits_{\theta}\frac{1}{\frac{\mathrm{dAcc}}{\mathrm{d}\cos\theta}(P,\theta)}\frac{\mathrm{d}^2\mathrm{Rate}(P,\theta|S)}{\mathrm{d}\cos\theta\,\mathrm{d}P}\,\mathrm{d}\cos\theta = \phi_0(P)\int\limits_{\theta} f(P,\theta|S)\,\mathrm{d}\cos\theta\,.$$

This results shows that the left-hand term is independent of the angular distribution (and consequently of the safety factor) because the right-hand side is constant in θ. With these results we can construct a *measured flux* from our previous result which is independent of the safety factor, as can be seen in Equation 4.28.

$$\phi(P) = \int\limits_{\theta}\frac{1}{\frac{\mathrm{dAcc}}{\mathrm{d}\cos\theta}(P,\theta)}\frac{\mathrm{dRate}(P,\theta|S)}{\mathrm{d}P\,\mathrm{d}\cos\theta}\mathrm{d}\cos\theta \propto \phi_0(P) \tag{4.28}$$

In Figure 4.50 we show the normalized measured flux in detail for different safety factors for different rigidity bins with a fit overlaid on the plateau. The fit for the plateau was performed for $S \geq 0.9$, varying only slightly in maximum range for the initial rigidity bins. We renormalized the measured flux using this plateau fit in order to see the relative difference of this measured flux as the safety factor varies.

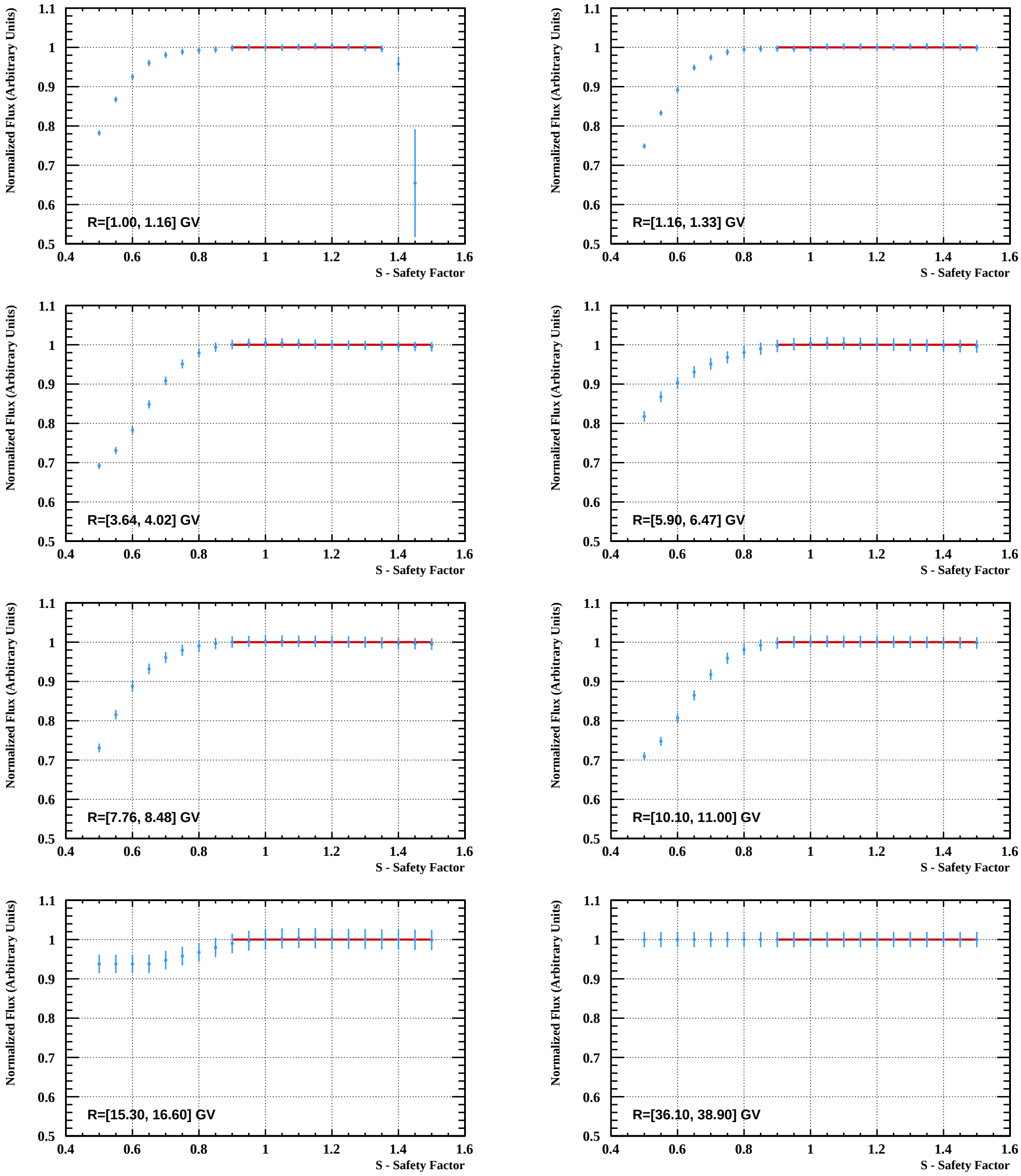

Figure 4.50: Normalized flux as a function of the geomagnetic cutoff rigidity safety factor for different rigidities. The fit result for the plateau is in red.

In Figure 4.50 we can see that we were able to obtain a measured flux that is independent of the safety factor for $S \geq 0.9$ at all rigidities.

At lower safety factors, $S < 0.9$, we see a drop in the flux which is smaller for higher rigidities. As we decrease the safety factor we are increasing our exposure time at a given rigidity because we are considering additional orbits on that rigidity bin. We are somewhat *flattening* our exposure time as a function of rigidity and moving towards the limit of $S = 0$ in which all rigidities are equally accessible at all times so the exposure time loses its dependence on rigidity, becoming flat.

This increase in exposure time is not followed by the number of measured events because we are now artificially considering (in the exposure time) that cosmic rays will not interact with the geomagnetic field (even at the higher magnetic field intensity orbits) when in fact they do. In the orbits in which this increase of the field would result in a change of the flux (direction and intensity) we are considering that it doesn't, creating an attenuation in the number of events that does not reflect on the exposure time. This effect shows the importance of the geomagnetic rigidity cutoff on not only separating primary events from secondary but also in considering the effects of the geomagnetic field in the flux itself.

The fit results for these plateaus, for the different rigidities, presented an extremely strong agreement to data ($\chi^2/Ndf \ll 1$), giving us strong evidence that the weighting of the differential rate (function of P and θ) with the inverse of the differential acceptance corrected for the different angular distributions due to changes in the safety factor was correct. We can use this result to estimate our systematic uncertainty by calculating the standard deviation of the flux calculated for every rigidity considered. The geomagnetic cutoff safety factor systematic uncertainty can be seen in Figure 4.51.

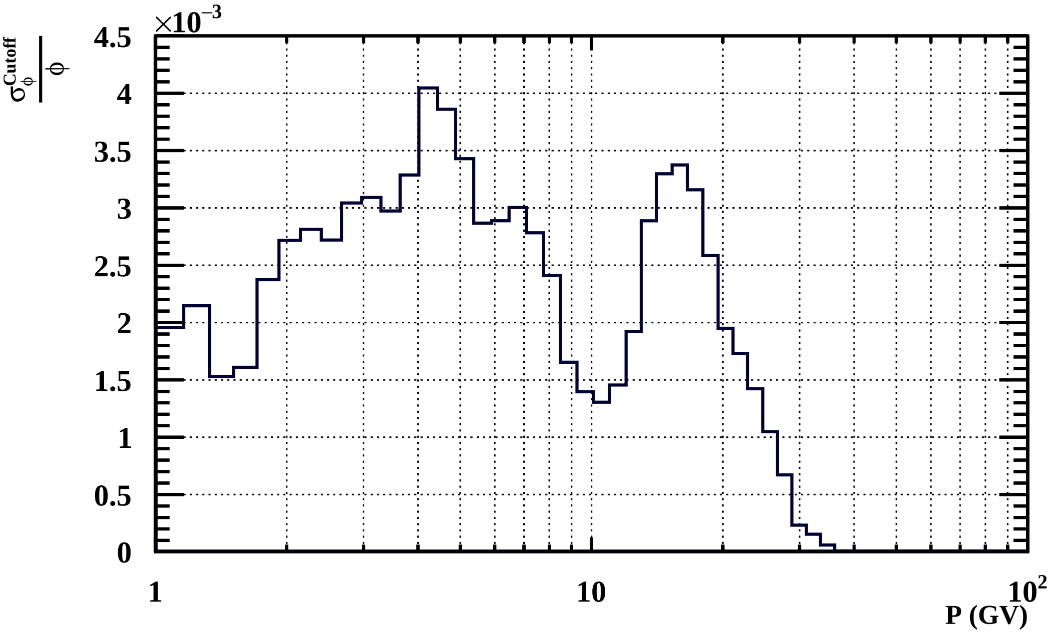

Figure 4.51: Geomagnetic safety factor systematic uncertainty.

4.5.7 Total uncertainty

We then gathered all of the different results from the previous estimations and grouped them into a total systematic uncertainty and total uncertainty as can be seen in Figure 4.52. The total uncertainty is construct according to:

$$\sigma_{\text{Total}} = \sigma^{\text{Stat}} \oplus \sigma_{\text{Acc}}^{\text{Syst}} \oplus \sigma_{\text{Corr}}^{\text{Syst}} \oplus \sigma_{\text{TimeReg}}^{\text{Syst}} \oplus \sigma_{\text{RigScale}}^{\text{Syst}} \oplus \sigma_{\text{Unfold}}^{\text{Syst}} \oplus \sigma_{\text{Geomag}}^{\text{Syst}},$$

where the operation $\oplus$ represents adding the different relative standard deviations in quadrature.

We can see from Figure 4.52 that the uncertainty of the proton flux is about 4.5% at 1 GV but drops bellow 1% from 3 GV up to about 50 GV. Up to 3 GV the error is dominated by the unfolding systematic uncertainty while every other uncertainty is well bellow 0.7%. Throughout the energy range, the rate statistical error is either the smallest or among the smaller contributions to the total error. Above 50 GV the error grows again due in large to contributions from the total Data-to-Monte-Carlo correction systematic and temporal regularization systematic. These uncertainties are compatible with those determined in the AMS published proton Bartel-resolved flux[108].

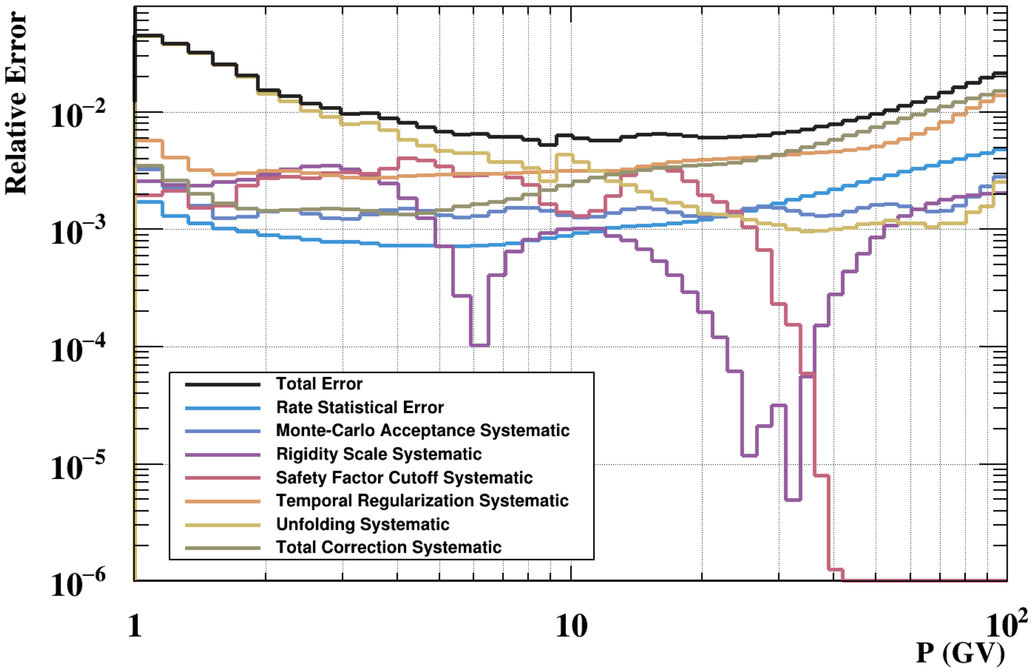

Figure 4.52: Digest of statistical and systematic uncertainties for the Bartel-resolved proton flux for a given Bartel.

4.6 Bartel-Resolved Proton Flux

After presenting the event selection, estimating cut efficiencies, respective Data-to-Monte-Carlo corrections and temporal regularizations, the *folded acceptance* and the different respective uncertainties, the estimated proton cosmic-ray flux is shown in Figure 4.53.

The flux presents a very drastic variation spanning from 1 GV to about 30 GV. These variations are highly correlated with solar activity as we will see in chapter 5. Highlighted in green in Figure 4.53, the minimum flux occurred during the 38th Bartel rotation of this analysis on February 2014, the local maximum for the *pass6* period ocurred at the 82th Bartel rotation on May 2017 and finally, in red, the global maximum occurred for the 113th Bartel rotation on September 2019. Given that the solar activity minimum occurred around December 2019[118] and the solar activity maximum, for cycle 24, occurred around March 2014Sun et al., these results appear to be congruent with reports from solar observations.

As will be further detailed in section 5.5, the drop of the proton in 2017 appears to be very well correlated with a large increase in solar activity starting in April 2017 which lasted until about September 2017. Figure 4.54 shows the impact of these solar events in the flux over several energy bins.

As can be seen in Figure 4.54 the largest flux variation happened between the maximum and minimum previously mentioned with a relative variation of nearly 340% at 1GV.

Figure 4.55 presents an expanded and detailed view of the temporal evolution of the proton flux. The different rigidity bins are detailed below and the temporal periodicity of a full turn is 11 years, the solar activity cycle.

Figure 4.56 details the proton flux in both a bird's eye view and also in temporal slices which showcase both flux variability scale at low energies and consistency at higher energies, indicating the origin of the flux temporal variation as coming from a mainly low-energy process, such as solar modulation. We will show in the next chapters how low-energy variability can be well explained by solar modulation.

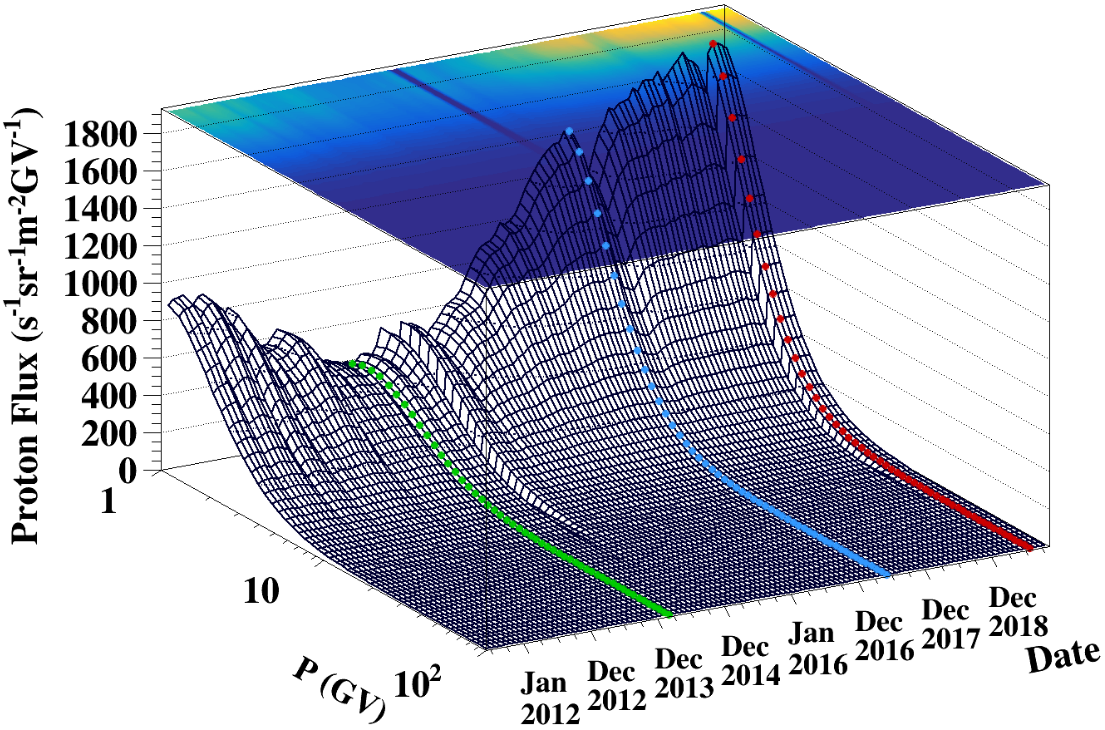

Figure 4.53: Bartel time-resolved proton flux from 11 June 2011 to 14 November 2019. Highlighted are the global minimum of the proton flux (green), the local maximum for the *pass6* time period (light blue) and the global maximum for the full period (red).

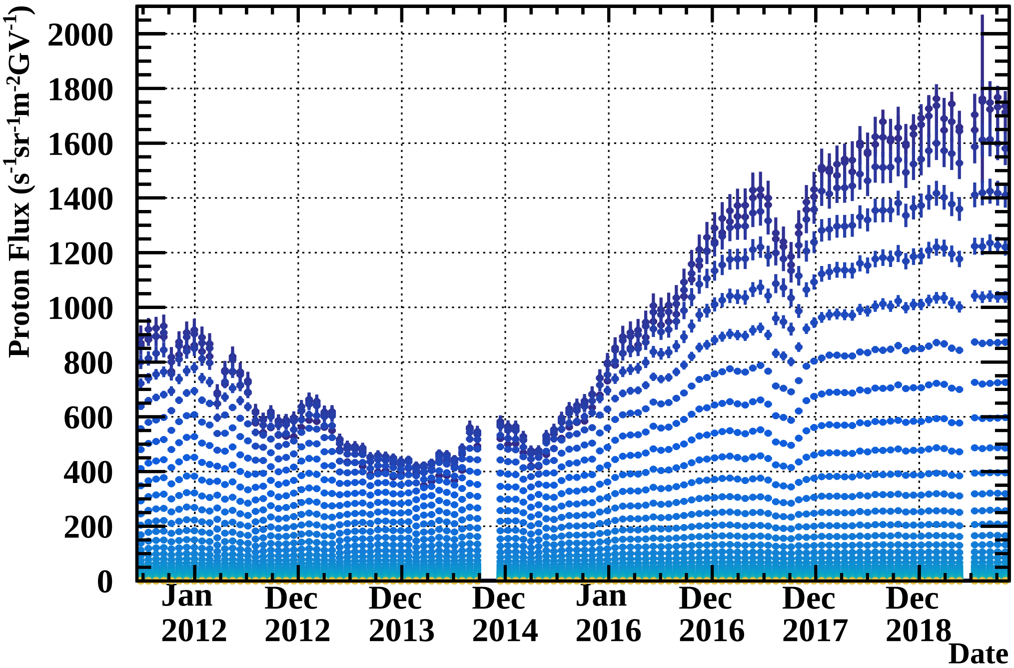

Figure 4.54: Rigidity profiles of the proton flux. Blue tones represent the lowest rigidities and the yellow tones represent the highest.

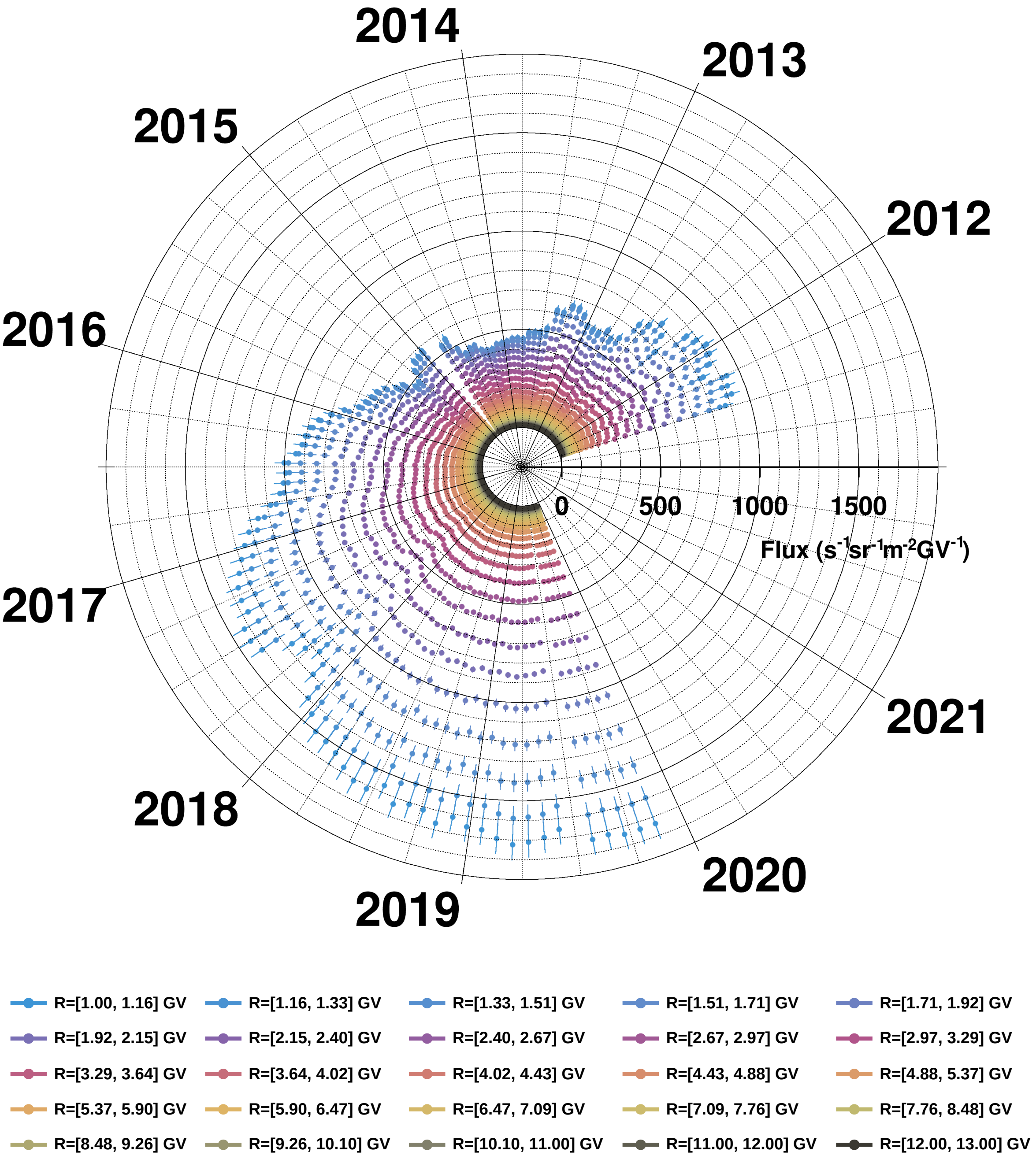

Figure 4.55: Polar plot of flux over time. Different colours represent the proton flux at different rigidities. The time window chosen for a complete turn on the plot was the solar activity cycle periodicity of 11 years.

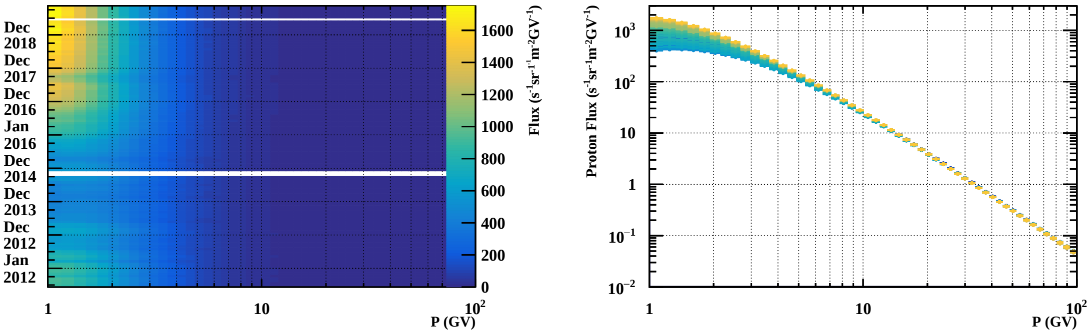

(a) Colormap of the proton flux.

(b) Temporal profiles of the proton flux.

Figure 4.56: Time-resolved flux from this analysis. (right) Time profile colours range from blue to yellow, where blue is the first time bin and yellow is the last time bin.

4.6.1 Bartel-resolved exposure time, Acceptance and efficiencies

In this section we will be showcasing the time-resolved exposure times, Data-to-Monte-Carlo corrections, acceptances and trigger efficiencies.

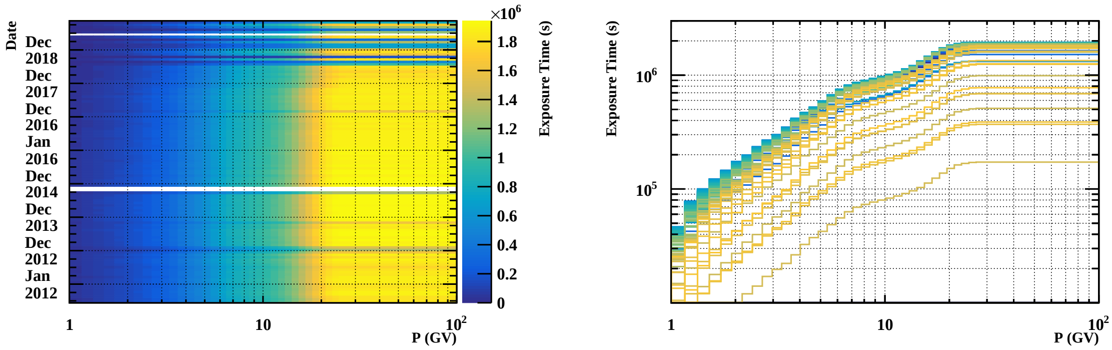

(a) Colormap of exposure time.

(b) Temporal profiles of exposure time.

Figure 4.57: Exposure time for the analysis. Time profile colours range from blue to yellow, where blue is the first time bin and yellow is the last time bin.

Figure 4.57 displays the AMS-02's exposure time for this analysis. It shows the behaviour detailed in section 4.3 and its connection to the geomagnetic cutoff. Most variations in exposure time can be attributed to the slow variation in the ISS's orbit around the Sun and to changes in the detector which would contribute to missing small time periods of exposure.

Notably, fluxes and efficiencies corresponding to the first two time periods will have lower statistics and present higher variances from the rest due to changes in AMS software and hardware configurations during the start of the experiment. The lower exposure time and consequent statistics is apparent in Figure 4.57.

The trigger efficiency reflects the overall performance of the detector at triggering events for the desired particle in study as a function of time and is displayed in Figure 4.58a and Figure 4.58b. As was detailed in subsection 4.4.8, the trigger presents a slight increase at the end of 2013 (see Figure 4.58a) due to changes in the Time-of-Flight detector.

As was detailed in subsection 4.4.9 and subsubsection 4.4.1.3, we see the time-dependence of the *folded acceptance* in Figure 4.58c and Figure 4.58d, as it directly correlates to the proton flux. We can see the total Data-to-Monte-Carlo correction applied to the *folded acceptance* in Figure 4.58e and Figure 4.58f.

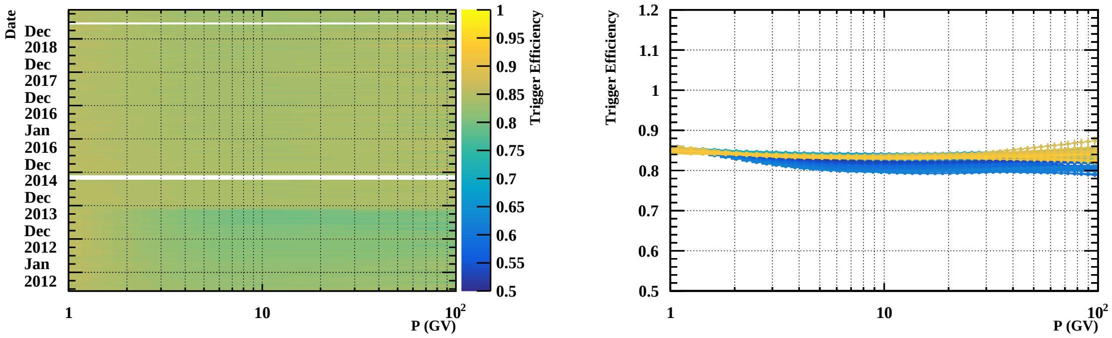

(a) Colormap of trigger efficiency.

(b) Temporal profiles of trigger efficiency.

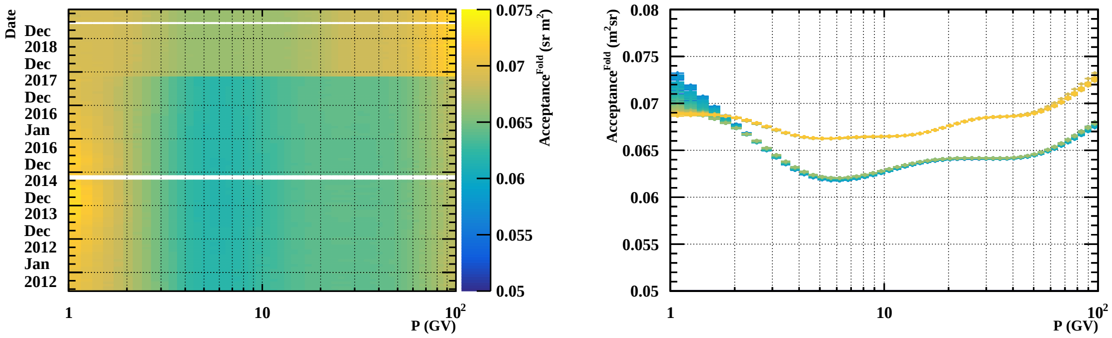

(c) Colomap of *folded acceptance*.

(d) Temporal profiles of *folded acceptance*.

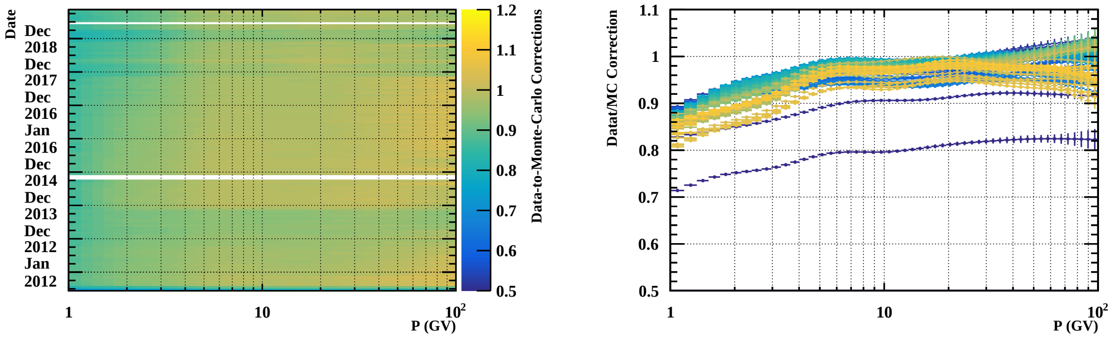

(e) Colomap of Data-to-Monte-Carlo corrections.

(f) Temporal profiles of Data-to-Monte-Carlo corrections.

Figure 4.58: Time-resolved trigger efficiency, *folded acceptance* and total Data-to-Monte-Carlo correction for this analysis. Time profile colours range from blue to yellow, where blue is the first time bin and yellow is the last time bin.

The main time variations of Data-to-Monte-Carlo corrections (see Figure 4.59) are related to changes in trigger efficiency and in the overall tracker performance. TOF appears to be relatively stable for both charge selection and velocity selection.

Inner reconstruction corrections and Layer 1 pickup corrections appear to be the most sensitive corrections to time variations. This could be related to effects not being perfectly reflected on the Monte-Carlo simulation or to changes related to the ISS orbit which changes the detector's temperature due to continued exposure to the Sun. Finally, the biggest differences between *pass6* and *pass7* periods lie in both acceptance and inner reconstruction corrections which shows the very clear difference between the two track reconstruction algorithms.

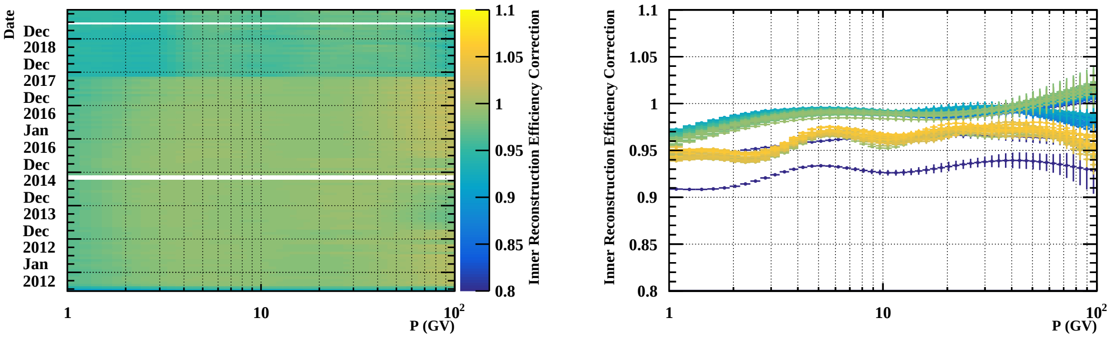

(a) Colomap corrections for inner tracker reconstruction efficiency.

(b) Temporal profiles corrections for inner tracker reconstruction efficiency.

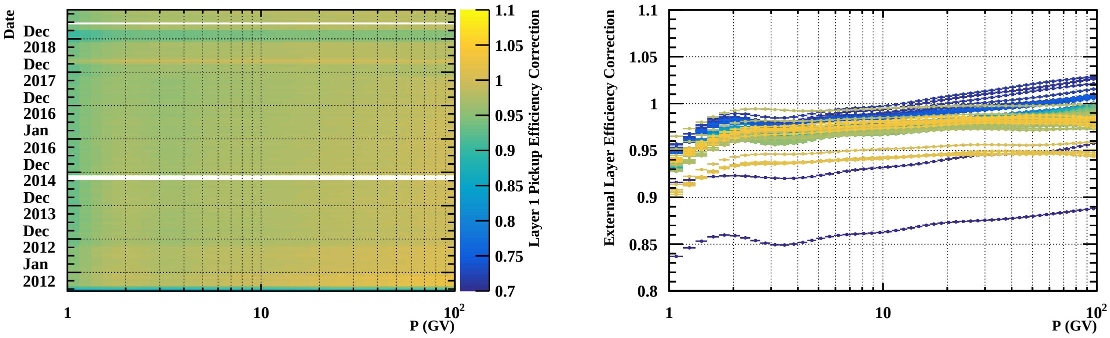

(c) Colomap of the correction for Layer 1 pickup efficiency.

(d) Temporal profiles of the correction for Layer 1 pickup efficiency.

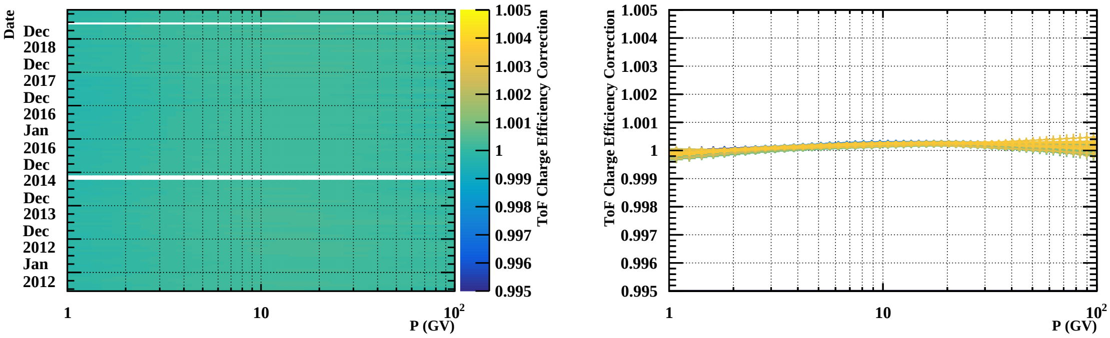

(e) Colomap of the corrections for ToF charge efficiency.

(f) Temporal profiles of the corrections for ToF charge efficiency.

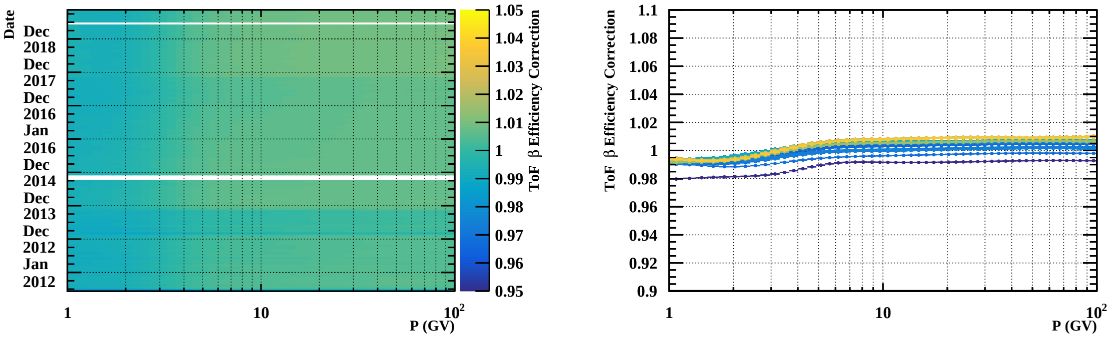

(g) Colomap of the corrections for ToF β efficiency.

(h) Temporal profiles of the corrections for ToF β efficiency.

Figure 4.59: Time-resolved Data-to-Monte-Carlo corrections. Time profile colours range from blue to yellow, where blue is the first time bin and yellow is the last time bin.

On trigger efficiency and tracker efficiencies there is a visible difference between *pass6* data and the *pass7* extension. This is due to changes in the reconstruction algorithm. Additionally, for the inner tracker reconstruction efficiency correction, there are large variations at higher rigidities due to the variability inherent to reconstructing rigidity from ECAL deposited energy, the low statistic associated, compounded with the regularization which will introduce some small variation as well.

4.6.2 Comparison with AMS published flux

As a final step we compared our result to the most recent AMS proton Bartel-resolved flux[108]. Although the two results shares a great deal in terms of selection of the actual events, there are some key differences, mainly in the choice of the geomagnetic safety factor and fiducial volume. The AMS Bartel-resolved published result was done using the full span of the tracker (Layer 1, Inner Tracker and Layer 9). Additionally, for both the AMS Bartel-resolved proton flux[108] and for the Daily-resolved proton flux[116] the acceptance, trigger efficiency and migration effects were evaluated and corrected in a time-dependent manner, the rest of the corrections were performed as being time-independent and all of the associated uncertainties were estimated accordingly.

The analysis here presented estimated all efficiencies, respective Data-to-Monte-Carlo corrections and all uncertainties as being time-dependent except for the geomagnetic safety factor systematic uncertainty and time-regularization systematic uncertainty.

In order to estimate the difference between the two results we sliced the flux in rigidity and estimated the relative difference for each time period for any given rigidity. The method is detailed in Figure 4.60.

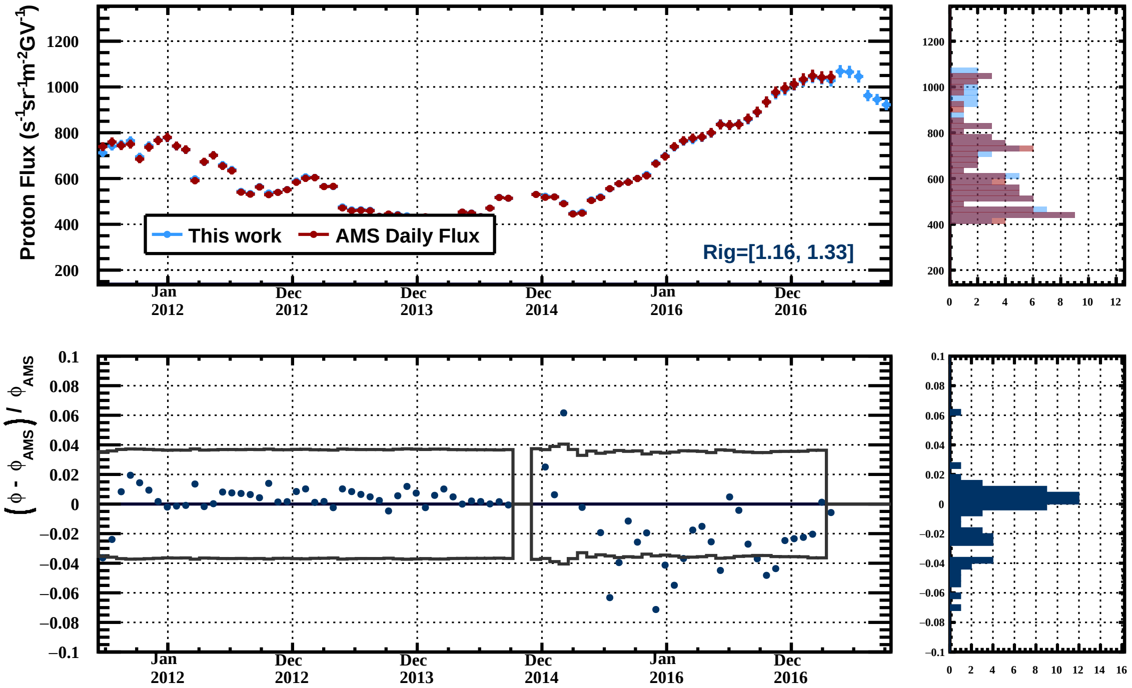

Figure 4.60: Comparison of the bartel-resolved proton flux presented in this work with an internal AMS's bartel-resolved proton flux for the bin [1.16, 1.33]

The mean and standard deviation of the relative difference between the two fluxes was estimated from the individual relative differences for each time in order to produce the result shown in Figure 4.61. The dots represent the mean and the shaded area represents the standard deviation. The bold black lines indicate the estimated error of the relative difference of the two results. This error was calculated using the following expression:

$$\sigma_D = \frac{\phi}{\phi_{\mathrm{AMS}}}\sqrt{\frac{\sigma_\phi^2}{\phi^2} + \frac{\sigma_{\phi_{\mathrm{AMS}}}^2}{\phi_{\mathrm{AMS}}^2}}\,, \quad \text{with} \quad D = \frac{\phi - \phi_{\mathrm{AMS}}}{\phi_{\mathrm{AMS}}}$$

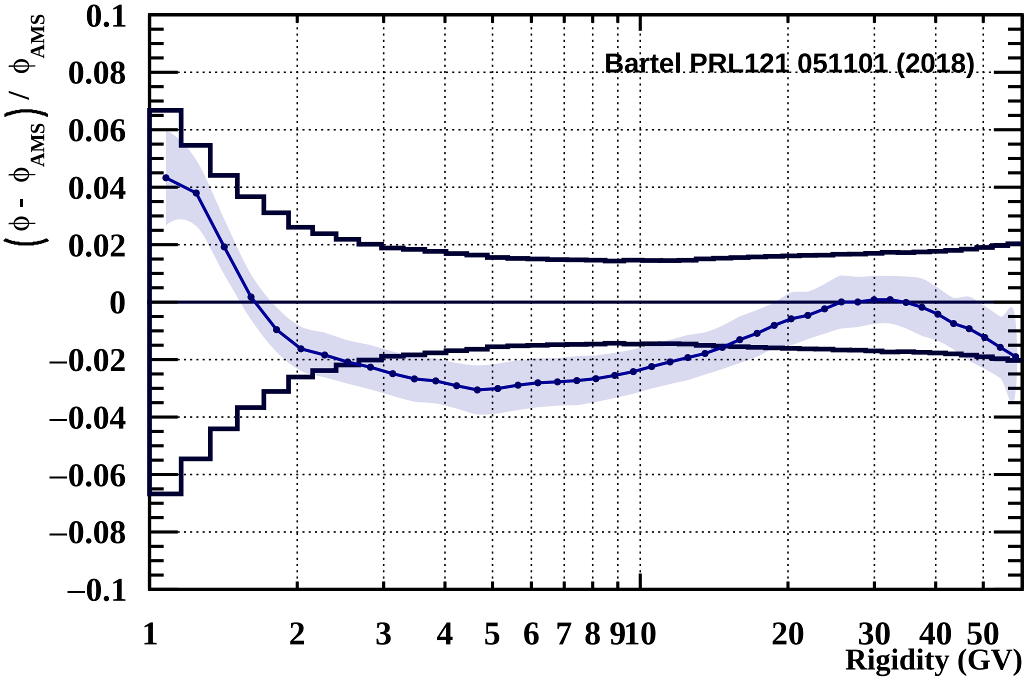

Figure 4.61: Comparison of the bartel-resolved proton flux presented in this work with the bartel-resolved AMS flux published in 2018[108].

4.7 Conclusions and Outlook

The production of the bartel-resolved proton flux was a success. The time-resolved flux was extended from the result in [108] showing a very large variation at lower rigidities while maintaining a flat time profile at higher rigidities, showcasing some of the expectations that these fluctuations can be explained by solar modulation as will be explored in the next chapters. The temporal dependence of the different efficiencies involved was investigated and used in the determination of the proton flux. These were also temporally regularized in order to minimize the effect of unwanted statistical oscillations due to low statistics.

Several studies on the different subdetectors and physical effects were performed and the uncertainties associated with these were estimated. Some of these studies were rather innovative, namely the estimations of the systematic uncertainties for the trigger and the geomagnetic safety-factor cutoff.

Due to time constraints related to the production of the reduced trees for the later portion of the data and to the logistics of securing the space for these trees, this work was not able to fully showcase AMS's full capabilities and high statistics during the *pass7* extension period. This cascaded down to the daily analysis which was intended to use the corrections and Monte-Carlo from the weekly or bartel-resolved flux and combining them with the daily rate for AMS but could not be finished in time for this work. In spite of this the analysis produced a proton flux result compatible with the published AMS result [108] as was shown in Figure 4.61.

These delays affected the development of unfolding tools specific to a time-resolved flux which further complicated the process due to the fact that each of 115 bartel time bins had to be individually unfolded since the Monte-Carlo was re-weighted individually for each of them.

This work also resulted in the development of efficient computational tools for managing and manipulating large quantities of histograms, for handling the proper propagation of systematics and the regularization of data. Following the AMS-LIP's group (led by Fernando Barão) long tradition of maintaining scientific relationships with international partners, all of the code developed during this thesis (including for the next chapters) is widely available in the coding frameworks we maintain and participate in (such as *LxSoft* and *Nuc*).

Finally, a quick mention has to be made on some work which was not used in this particular analysis. During the initial portion of this work, before the migration of the analysis effort into the *Nuc* analysis framework, a parallelization tool for hybrid computer networks was developed to accelerate the processing of data due to the unevenness of the run file sizes. As seen in subsection 3.3.2, depending on the detector's orbital position and on solar conditions, the cosmic-ray event rate can vary greatly and thus generate vastly different file sizes at somewhat arbitrary intervals, resulting in very asymmetric workloads for the analysis programs. Due to this unevenness of the workload, a trivial parallelization will always be inferior to an adaptive workload distribution. To tackle this issue, a *Hybrid Worker Pool Parallelization Scheme* was created. A full report on this tool, with benchmarks and real-world performance is detailed in section A.3. This result is yet to be published.

5

Variability of the AMS-02 Proton Flux

In this chapter we will be analysing the temporal variations of the proton cosmic-ray flux measured by AMS in terms of its periodicities as well as introducing the notion of correlation between the cosmic-ray flux and solar activity.

In order to have a comparable result with other sources, the analysis presented in this chapter and the next will be ran on AMS-02's published time-resolved fluxes for the proton daily[116]flux.

5.1 Time-resolved AMS Proton Flux

AMS-02 has published two time-resolved proton fluxes for both Bartel solar rotation number (about 27 day cycle, commonly described as Bartel rotation or BR) and daily time binning. Both of these are of great interest since they tap into different periodicities although they come at the cost of different uncertainties and data availability. The daily proton flux allows us to do very detailed frequency studies due to its high sampling frequency (1/day) but that comes at the cost of lower statistics, higher systematics and some gaps in data at lower rigidity bins due to the geomagnetic field, as can be seen in Figure 5.1. Given that daily proton flux has a far greater temporal resolution, it will be the flux used in this chapter for analysis for time periodicities as the results for the bartel-resolved flux would produce the same results but with a far lesser frequency resolving power.

The AMS daily proton flux at each rigidity is a time-series with temporal characteristics described in Table 5.1.

First observation:	20th May 2011
Last observation:	29th October 2019
Number of observations (N):	3085
Number of non-null observations:	2824
Time-binning (δt):	1 day
Sampling frequency ($f_s = \frac{1}{\delta t}$):	1 day^{-1}
Minimum measurable period - Nyquist ($\frac{2}{f_s} = 2\delta t$):	2 days
Maximum measurable period ($\frac{N\,\delta t}{2}$):	1542.5 days

Table 5.1: Temporal characteristics of the proton flux time-series.

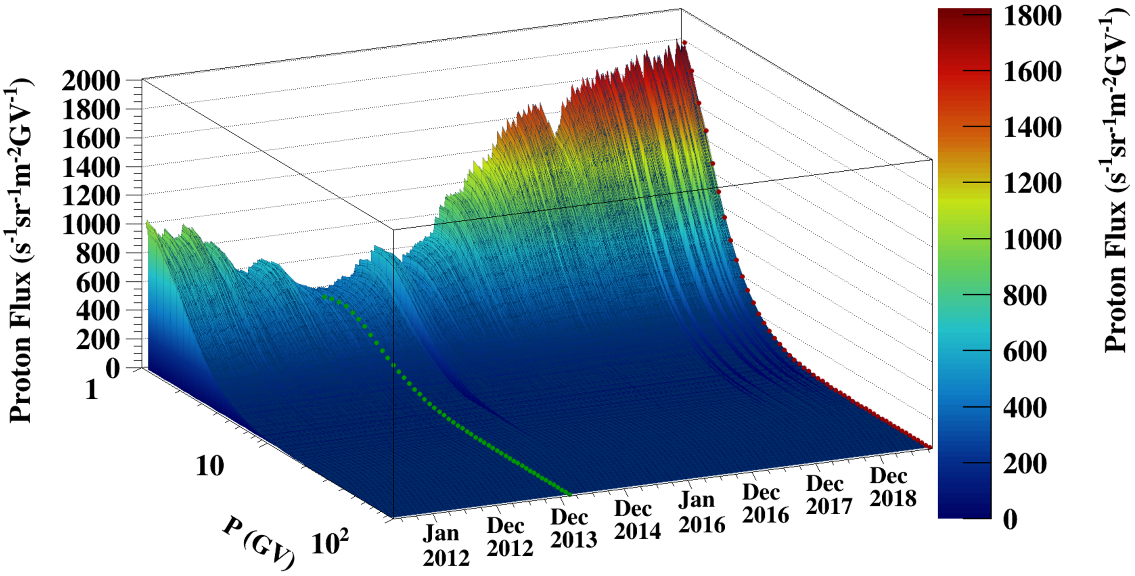

Figure 5.1: AMS daily proton flux as presented in Aguilar et al., (2021)[116]. The green line represents the minimum flux, at 04/03/2014, and the red line represents the maximum, at 24/10/2019.

The Bartel flux provides an integrated measurement over a 27 day period, a solar rotation. This measurement is extremely useful to be compared with computational models since it reduces dimensionality of the problem (it removes the ϕ coordinate). Short time effects such as the crossing of the HCS can be studied using a daily proton flux but not the 27 day flux. We will be referring back to the 27-day flux measurement in the next chapter.

5.2 Fourier Transform

Frequency domain spectral analysis is a very powerful tool to be used in the analysis of time series. It transforms a signal from its time domain to the frequency domain and it can be used to investigate and separate the different components that generate our time-series[119]. One of the most notable tools in this field of study is the Fourier transform which is commonly presented in two forms, as a continuous Fourier transform (for continuous functions with continuous variables) or as a discrete Fourier transform of a discrete time-series (for time-binned data) [120]. The discrete Fourier transform for a real discrete time-series $y(t_n) = y_n$ can be constructed in the following manner[120, 121]:

$$Y(\omega_k) = Y_k = \sum_{n=0}^{N/2} y_n \, e^{-i\omega_k n} = \sum_{n=0}^{N/2} y_n \, e^{-i2\pi \frac{k}{N} n}, \tag{5.1}$$

where N is the number of points in the time-series y_n, n is the index running over the time samples and k is the index running over the frequency sampling.

The Fourier transform constructs a set of complex numbers, each corresponding to the correlation between our time-series and a set of sinusoidal functions each at an angular frequency ω_k. A useful quantity to derive is the squared modulus of this set which defines the Fourier power spectrum of the series[122, 123], following Power$(\omega_k) = |Y_k|^2$. The Fourier power spectrum is often times normalized by the number of points in the series and its variance. All Fourier transform results presented in this work have been calculated using the FFTW3[124] fast Fourier transform package through its integration in the CERN ROOT library.

We can see in Figure 5.2 that our time-series corresponds to a periodic *saw-tooth* signal that is riding a larger-scale signal layered with a noise-like fluctuation.

The power spectrum is displayed in units of variance and can be displayed in terms of frequency (ω_k) or period (T_k). In Figure 5.3 we can see the Fourier transform of the daily proton flux during 2016 for a given set of rigidities, as seen in Figure 5.2.

We can clearly see a continuous background of frequencies with some stand-alone peaks near the indicated red dashed lines. These peak frequencies correspond to relevant *signals / periodicities* in our time-series. Although we are not entirely sensitive to the large-scale signal in the Fourier transform, we can still see the other two components. This larger-scale component comes from the 11 year periodicity related to the Solar Activity Cycle. This phenomenon can be seen in the next chapter in Figure 6.2.

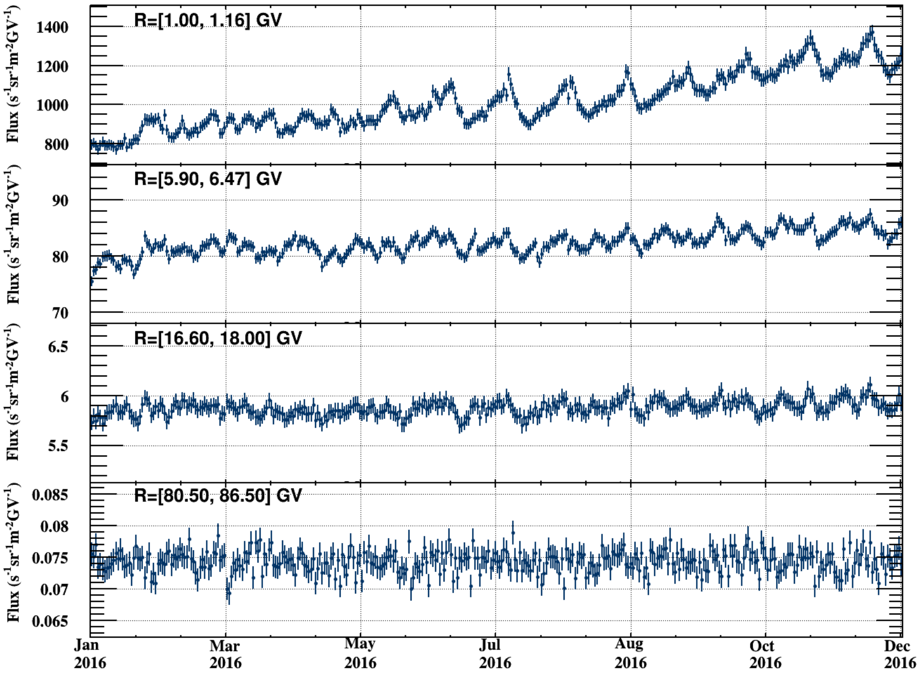

Figure 5.2: Time-series of the AMS daily proton flux[116] for the year of 2016 for the rigidity bins [1.00-1.16], [5.90-6.47], [16.60-18.00] and [80.50-86.50] GV.

.

We chose another two periods to present an apparently *aperiodic* time-series (2012, see Figure 5.6) and a *quasi-periodic* time-series (2015, see Figure 5.4). We will use these 3 time blocks to motivate our choice of a background for these time-series.

An interesting point to note is that the Fourier transform assumes that the frequency of the underlying generating processes will be constant in time, i.e the frequency does not have a time dependence. This is very important since we are interested in studying very complex phenomena which present varying frequency signatures with time, thus showing one of the major limitations of the Fourier transform.

By performing the same analysis on the years of 2012 and 2015, seen in Figure 5.6, Figure 5.7, Figure 5.4 and Figure 5.5, we see that our major periodicities vanished.

The year of 2012 corresponds to very near the maximum of solar activity while 2015 is already mid-cycle and very close to 2016, a year with very pronounced periodicities. We expected 2012 to be relatively aperiodic but the fact that the Fourier transform for the year of 2015 does not show clear peaks indicates the need for an approach with less restrictions than the Fourier transform.

In the next sections we will see that the wavelet transform shows 2015 as a bit *noisy*

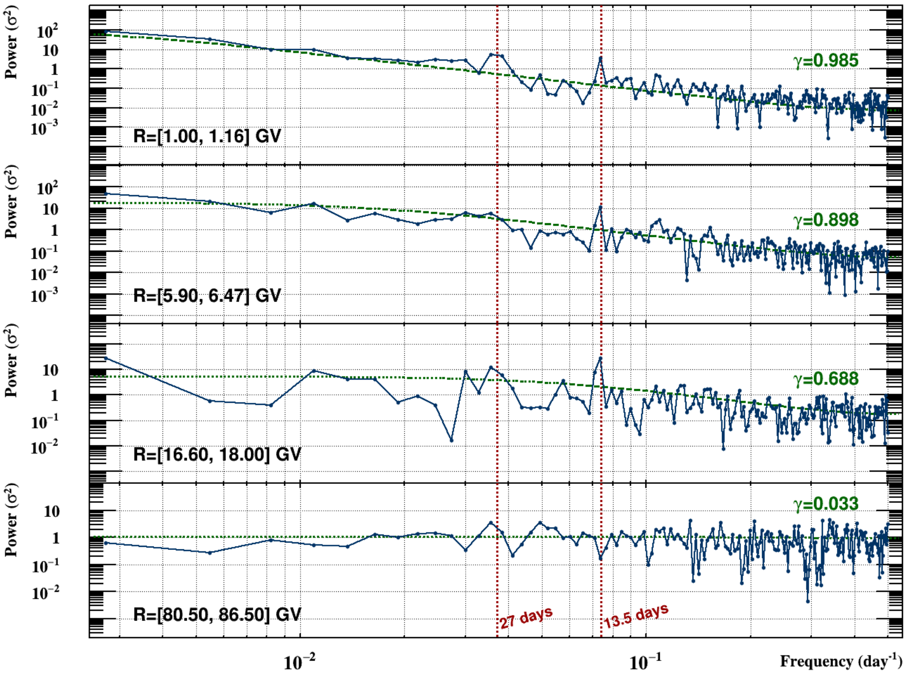

Figure 5.3: Fourier transform of the daily proton flux[116] for the year of 2016 for the rigidity bins [1.00-1.16], [5.90-6.47], [16.60-18.00] and [80.50-86.50] GV. The green dashed line is the red-noise model for this data using the lag-1 correlation indicated on top. The red dashed lines represent the frequencies corresponding to the 27 day periodicity and 13.5 days.

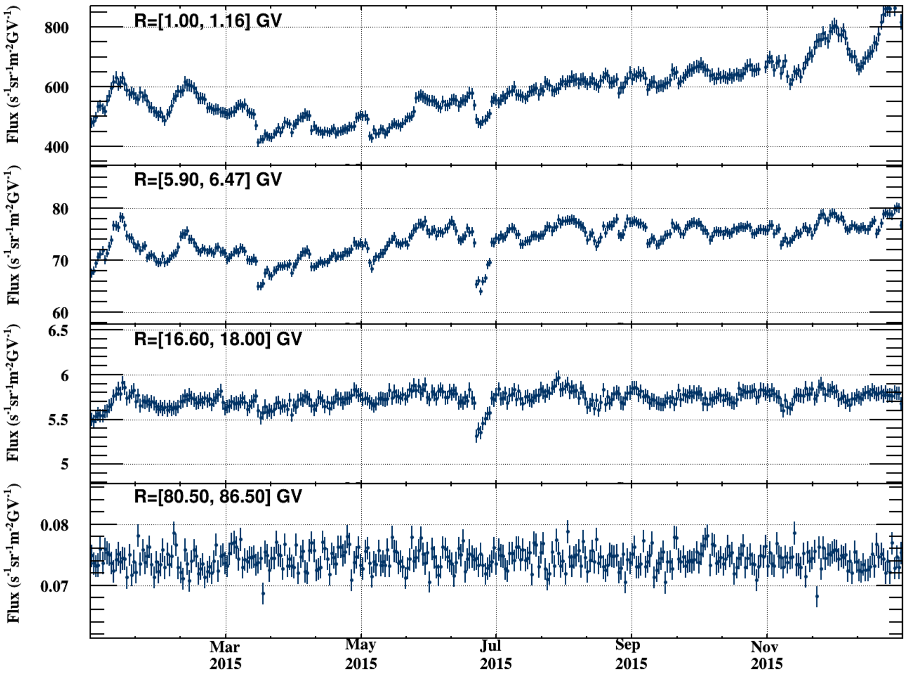

Figure 5.4: Time-series of the AMS daily proton flux[116] for the year of 2015 for the rigidity bins [1.00-1.16], [5.90-6.47], [16.60-18.00] and [80.50-86.50] GV.

towards larger periods (T_k), without the very well defined periodicities seen for 2016 (see section 5.3) but using average wavelet transform (see subsection 5.6.1) we see significant peaks when compared to red-noise background.

In systems including variable frequency components a time-resolved solution is necessary.

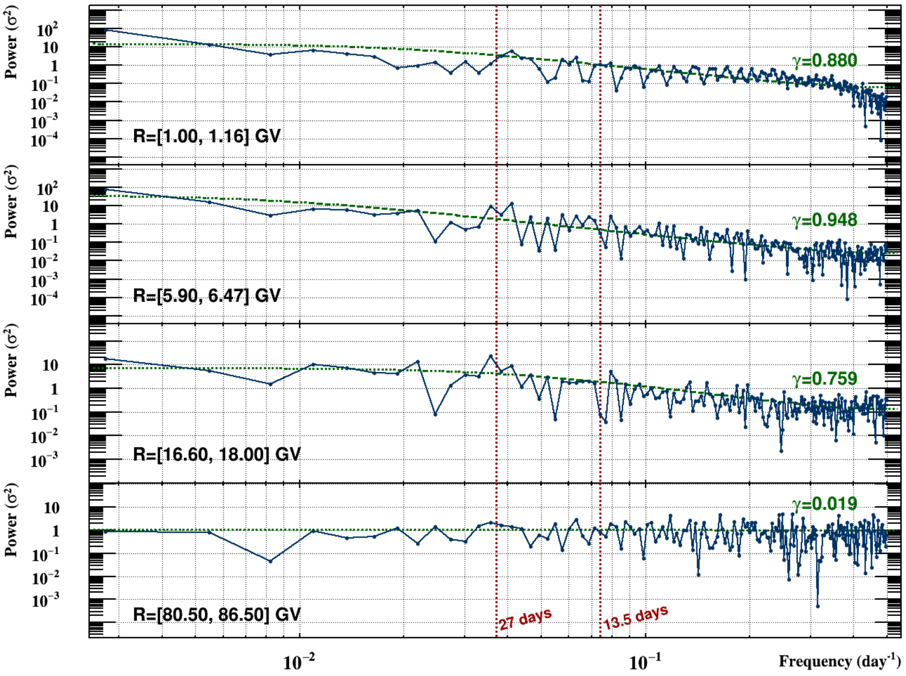

Figure 5.5: Fourier transform of the daily proton flux[116] for the year of 2015 for the rigidity bins [1.00-1.16], [5.90-6.47], [16.60-18.00] and [80.50-86.50] GV. The green dashed line is the red-noise model for this data using the lag-1 correlation indicated on top. The red dashed lines represent the frequencies corresponding to the 27 day periodicity and 13.5 days.

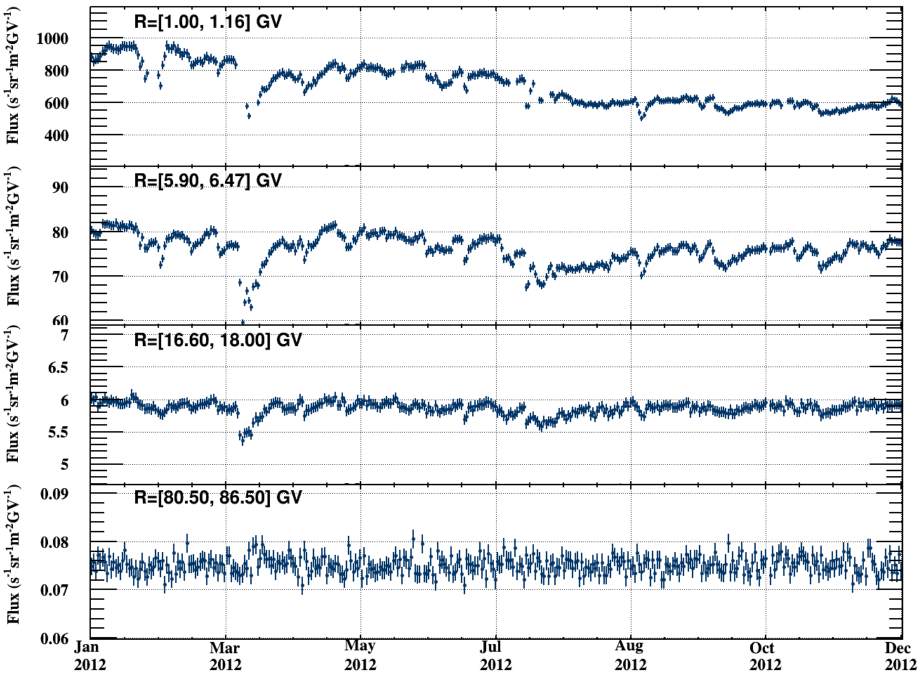

Figure 5.6: Time-series of the AMS daily proton flux[116] for the year of 2012 for the rigidity bins [1.00-1.16], [5.90-6.47], [16.60-18.00] and [80.50-86.50] GV.

One simple approach could be to split the time-series into smaller blocks (like we've done here for yearly time periods) and evaluate the Fourier transform in each of those blocks, generating a somewhat time-resolved frequency spectrum analysis. This comes with the trade-off that the resolving power at lower frequencies (higher periods) will decrease since the total length

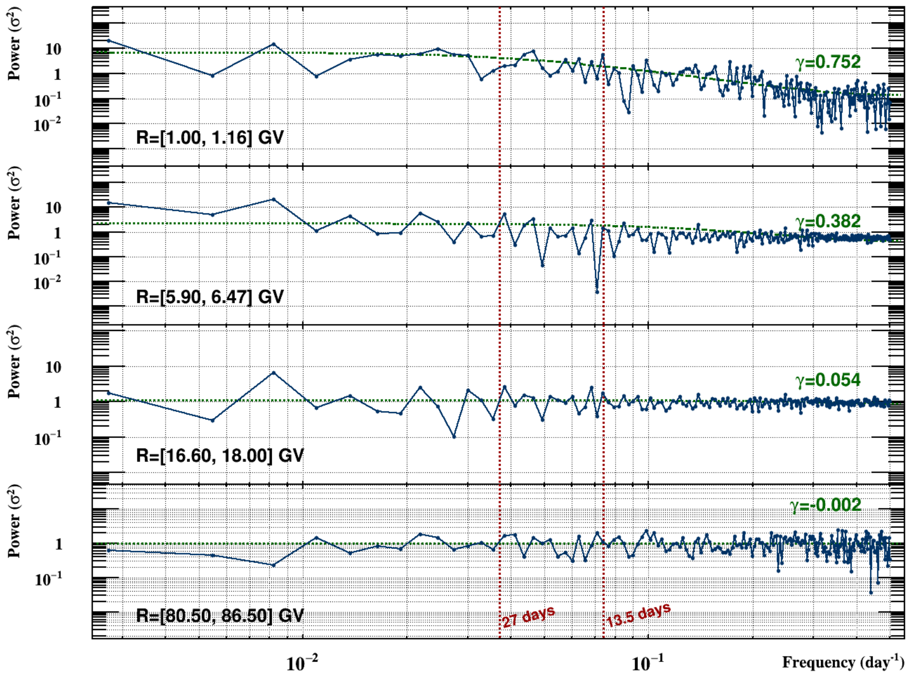

Figure 5.7: Fourier transform of the daily proton flux[116] for the year of 2012 for the rigidity bins [1.00-1.16], [5.90-6.47], [16.60-18.00] and [80.50-86.50] GV. The green dashed line is the red-noise model for this data using the lag-1 correlation indicated on top. The red dashed lines represent the frequencies corresponding to the 27 day periodicity and 13.5 days.

of the sample is now effectively reduced to the size of each block. We are still very dependent on making educated guesses on the *good* sizes of the blocks.

In recent years, a tool has been gaining popularity in the study of these complex time structures, the Wavelet Transform.[125].

5.3 Wavelet Transform

The wavelet transform is very similar in principle to the Fourier transform, it is a transformation of data from the time domain to the frequency domain but using a different basis of functions, the wavelet. The wavelet is characterized by being mostly *contained* in both time and frequency-domain, offering a trade-off in resolution in the frequency-domain while not requiring that the entire series be used for the estimation of the power of the transform at any given frequency. The work in this section will closely follow the methodology presented by Torrence and Compo, (1998)[125], as was also done in Aguilar et al., (2021)[116] in order to uncover the dependence of the principal periodicities in the AMS-02 daily proton flux and their dependence with time and rigidity.

In order to tackle this task two main classes were developed: *LxTimeSeries* and *LxWavelet*. These are described in detail in section A.2.

The wavelet transform of a discrete time-series can be presented in two forms, as a classical estimation of correlation factors between a wavelet ψ and a time-series or as a convolution between the Fourier transform of the wavelet function Ψ and the Fourier transform of the data, which are then inverted back into the time domain. These two formulations can be seen in the following expressions:

$$W_n(s) = \sum_{n'=0}^{N-1} y_{n'}\, \psi^*(u_n(s)), \quad \text{with } u_n(s) = \left(\frac{(n'-n)\,\delta t}{s}\right) \tag{5.2}$$

$$W_n(s) = \sum_{k=1}^{N/2} Y_n\, \Psi^*\left(s\,\omega_k\right)\, e^{i\omega_k n \delta t}\,, \tag{5.3}$$

where Y_n is the Discrete Fourier Transform of our time-series, $\omega_k = 2\pi \frac{k}{N}$, ψ was chosen as the Morlet wavelet (with $\omega_0 = 6$) and s is the scale parameter which directly relates to a period (or frequency) in the Fourier sense by the following relation[125]:

$$\lambda_{\text{Fourier}}(s) = \frac{4\pi\, s}{\omega_0 + \sqrt{2+\omega_0^2}} \approx 1.03\, s \quad (\omega_0 = 6)\ . \tag{5.4}$$

We can interpret this relation as the average frequency / period a wavelet with a given scale parameter s transports (or represents) as it's compared with our data in both time and frequency. It is estimated by calculating the average of the Fourier transform of the Morlet wavelet.

The Morlet wavelet (which can be seen in Figure 5.8) has the following formulation[125]:

$$\psi(\eta) = \pi^{-1/4}\, e^{i\omega_0\eta}\, e^{-\eta^2/2} \tag{5.5}$$

$$\Psi(\omega) = \pi^{-1/4} H(\omega)\, e^{-(\omega-\omega_0)^2/2}\,, \tag{5.6}$$

where $H(\omega)$ is the Heaviside function.

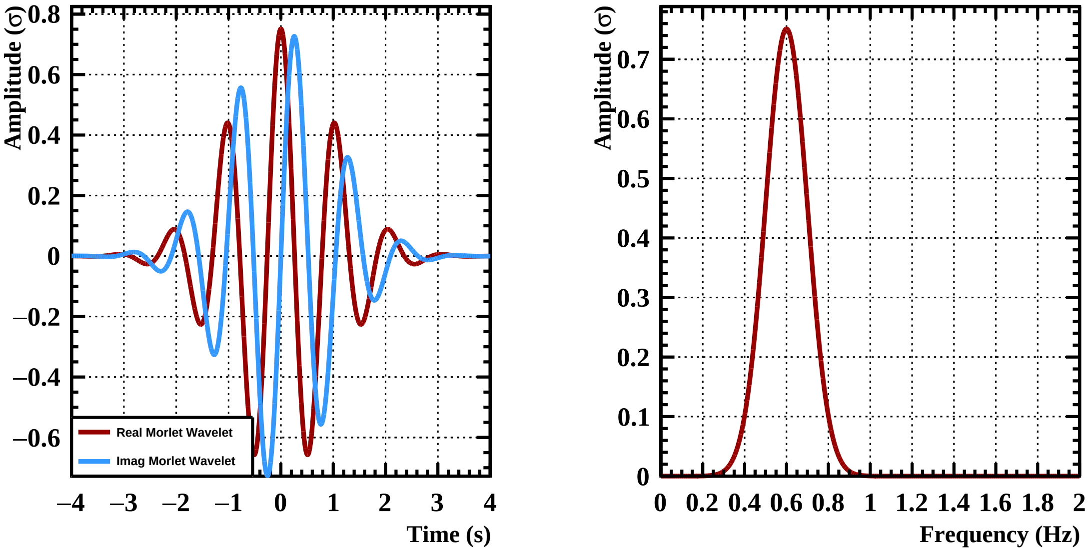

Figure 5.8: (left) Real and imaginary parts of the time-domain Morlet wavelet. (right) Frequency-domain Morlet wavelet. For both wavelets $\omega_0 = 6$ and $s = 10\delta t$.

An interesting property that we will be exploring is that, as can be seen in Figure 5.8, given that the wavelet is somewhat confined in time and frequency, our result is granular and varies with time and frequency. This will lead to the very useful interpretation that at any given time we can extract the relative *importance* (correlation) of the different periodicities present in our signal. We can also follow how a given phenomenon might evolve, at a given frequency, as time goes on.

5.3.1 Cone of Influence

One important feature to consider is the effect of the edges to our result. The process of performing the wavelet transform lies in estimating the compatibility of our time-series with a given wavelet function which carries a specific time-frequency signature (width included). As this comparison is performed for each possible period (width of the wavelet) and for every time, our wavelet is transported through the entire time-series, including the edges. As the wavelet approaches the edges it will no longer have a time-series to compare to, instead it will be compared to the zero-padding done at the edges of our time-series. Due to this we will need to carefully estimate for every period what is effect that the edge will have on our result and the extension of this effect (which is related to the width of the wavelet).

We can define the e-folding time as the time that the power spectrum of a wavelet centred on the edge of our time-series exponentially drops by $1/e$. This time is dependent on the mother wavelet and for the Morlet wavelet it corresponds to $\sqrt{2}s$, where s is the scale factor of our wavelet. This will define a boundary within which our result is considered to be unaffected by the edge effects and is named *Cone of Influence*. This boundary will be estimated and presented for every wavelet done in this work. In order to capitalize on the incredible amount of AMS data available, the wavelet transform was performed in a single temporal batch for each rigidity bin in order to only have to consider two boundaries (May 2011 and late 2019) and to increase the range of periods contemplated by the analysis. Similar to the Fourier transform, the range of periods described is related to the sampling frequency (1/day in this case) and the total time considered.

5.4 Wavelet Transform of the AMS daily proton flux

In order to examine the different rigidity slices of the daily time-series, specially at lower rigidities, minor data regularization had to be done in order for the missing data to not pollute our results too heavily. An absence in data would be reflected in the transform, specially at lower periods, since it represents a very fast decrease in the signal, a very high frequency artificial source in our time-series which, given the nature of the wavelet transform, would propagate upwards in period as it became less important. Nonetheless it would contribute negatively to our result so a choice was made to linearly interpolate the data on these very few missing days in order to bridge these small gaps and minimize the contribution of this abrupt change. This solution is still not perfect since it will still create an absence of the fundamental frequencies of the underlying time-series and the small declination of the line will still have a frequency signature that is artificial.

The wavelet power spectrum of daily proton flux was calculated for the entire time period and is displayed in Figure 5.9 and Figure 5.10.

Wavelet transform results can be difficult interpret when too large of a time interval is displayed. Since the power spectrum comes in units of σ, when the time-series varies in amplitude throughout the whole time interval, so will the σ, making it sometimes difficult to separate the relative importance of the different time periods. In order to tackle this we will split the wavelet power spectrum into yearly blocks in which we only renormalize for the variance of that time period instead of considering the entire time period's variance. In the different transforms shown in Figure 5.9 and Figure 5.10 we can see that the Z-axis range had to be adjusted for visibility while in the results that will follow it will remain relatively constant. This does not raise an issue with the result since we are only interested in relative significance for now. Nevertheless, a lot of information can already be drawn from the current results.

On Figure 5.9a we can see on the top left and top right the edge effects in which the wavelet transform increases greatly outside of the *cone of influence*. We also see a prominent periodicity arise in the 27-day region, marked in a dotted green line, on every rigidity except

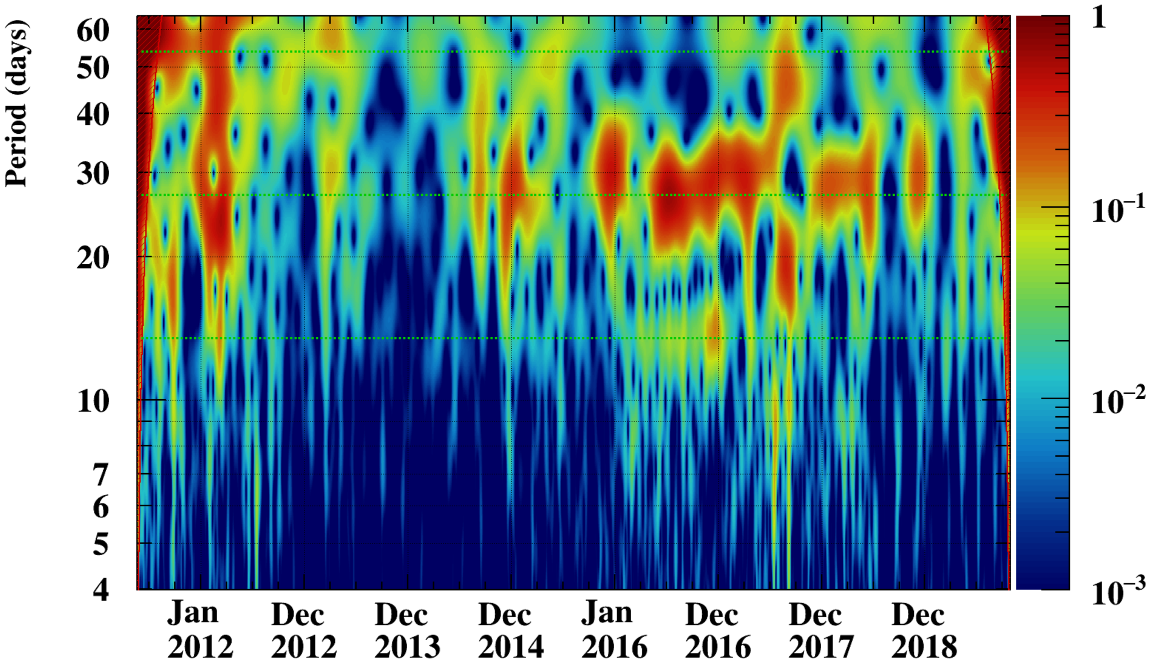

(a) Rigidity: [1.00-1.16] GV

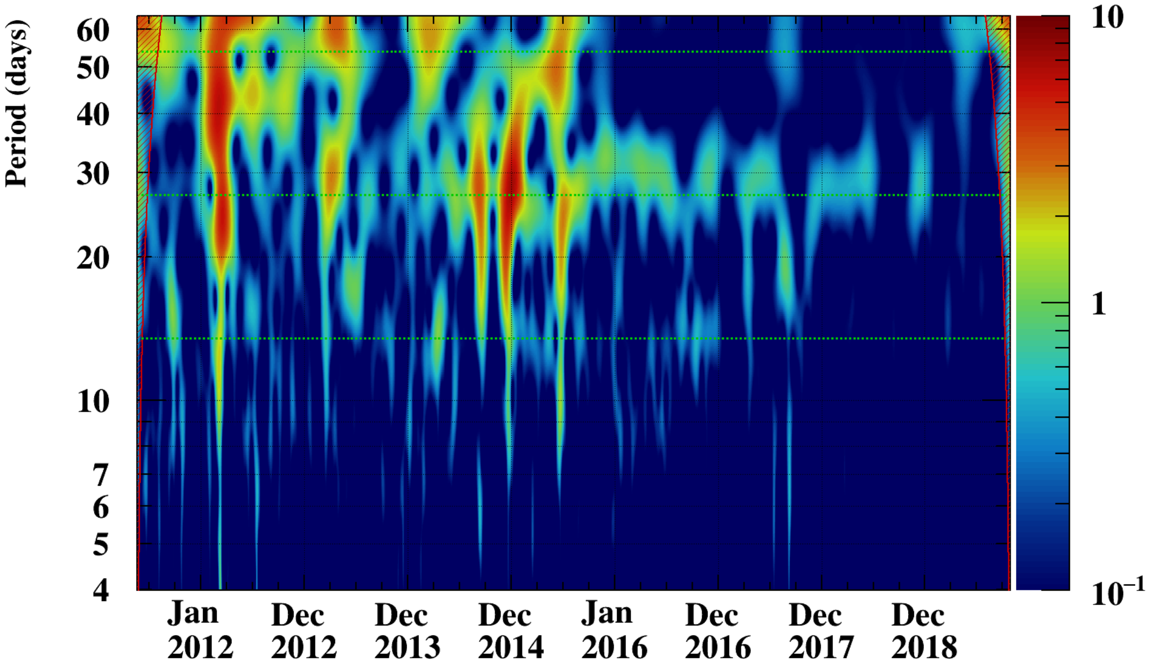

(b) Rigidity: [5.90-6.47] GV

Figure 5.9: Local wavelet power spectrum for AMS-02's daily proton flux[116] for different rigidities, normalized to the flux variance. Vertical axis shows the Fourier period while the horizontal axis shows the date. The red shaded area shows the *cone of influence*. Horizontal green dashed lines represent 13.5, 27 and 54 day periods.

the highest, at which the wavelet transform appears relatively flat aside for a large structure near the end of 2014. This structure is created by the missing data for that time period due to the AMS TTCS being worked on. Although this structure is present at all rigidities, it is

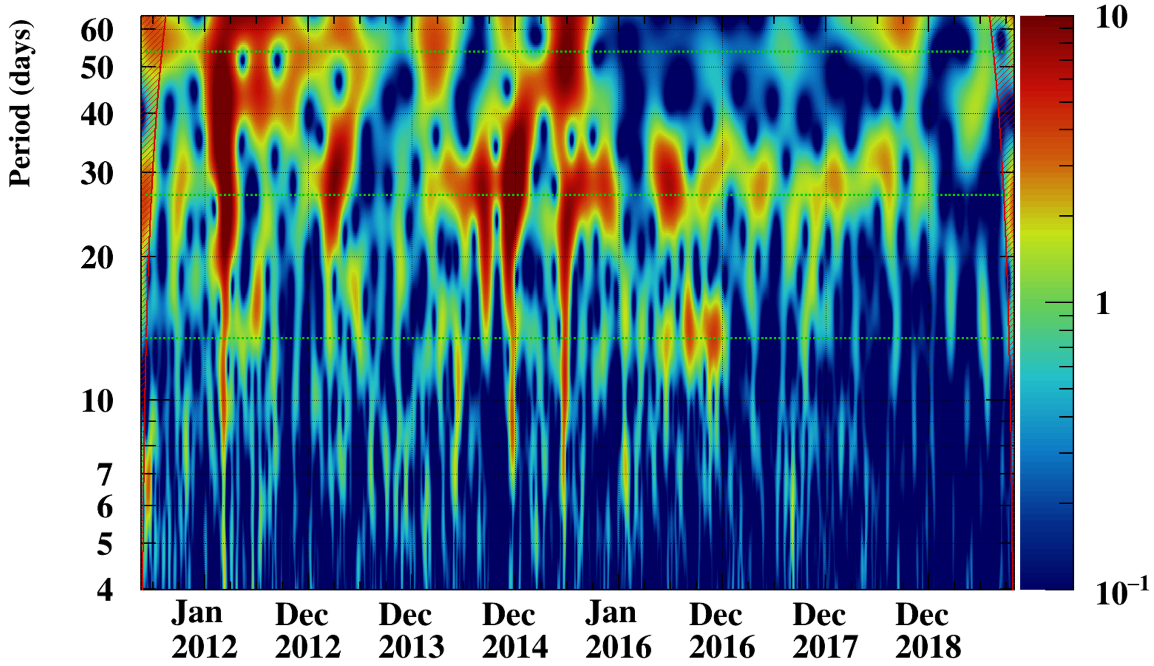

(a) Rigidity: [16.60-18.00] GV

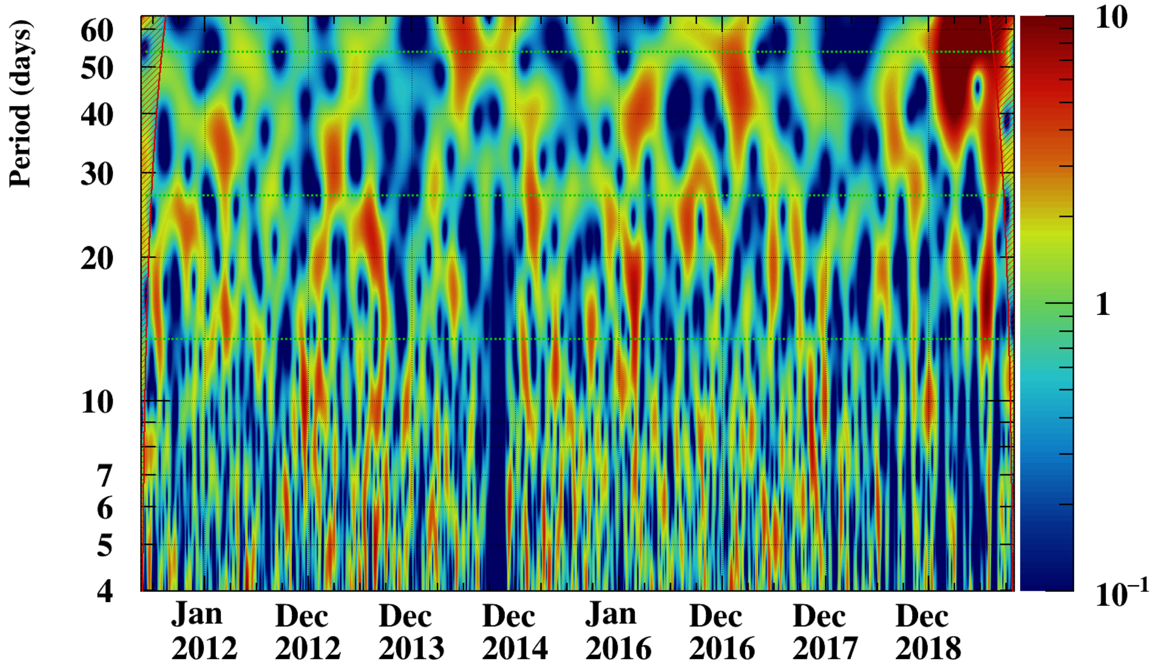

(b) Rigidity: [80.50-86.50] GV

Figure 5.10: Local wavelet power spectrum for AMS-02's daily proton flux[116] for different rigidities, normalized to the flux variance. Vertical axis shows the Fourier period while the horizontal axis shows the date. The red shaded area shows the *cone of influence*. Horizontal green dashed lines represent 13.5, 27 and 54 day periods.

more pronounced at the highest energies due to its relative importance when compared to the relatively flat wavelet transform. As was seen in Figure 5.2 and Figure 5.4, the flux at these energies is relatively flat and dominated by random quasi-white-noise oscillations.

The 13.5-day periodicity is also present but it appears to be more pronounced during 2016 for the [1.00-1.16] GV rigidity bin, from 2012 to the end of 2016 for the [5.90-6.47] GV bin, despite being of very low relative amplitude and seldom showing at the [16.60-18.00] GV aside for the year 2016 again. As results will show later, these periodicities are sometimes merged into the background due to them being of second order importance and due to them mixing in variance with the background of the global wavelet transform.

5.5 Temporal Characterization of the daily proton flux

In order to increase relative power spectrum significance, wavelet transform was applied to the 9 years of data and was cut into the different yearly components, allowing for a snapshot analysis that is binned yearly that still benefits from having one large continuous time-series. In order to have results comparable to each other, each year was normalized by $1/\sigma_\varphi$ according to that year's standard deviation instead of the global standard deviation.

These results are presented in the following subsections which separates the results by rigidity intervals. The power of the local wavelet transform is displayed in Figure 5.11, Figure 5.12, Figure 5.13, Figure 5.14, Figure 5.15, Figure 5.16, Figure 5.17 and Figure 5.18.

5.5.1 Wavelet power spectrum for [1.00-1.16] GV

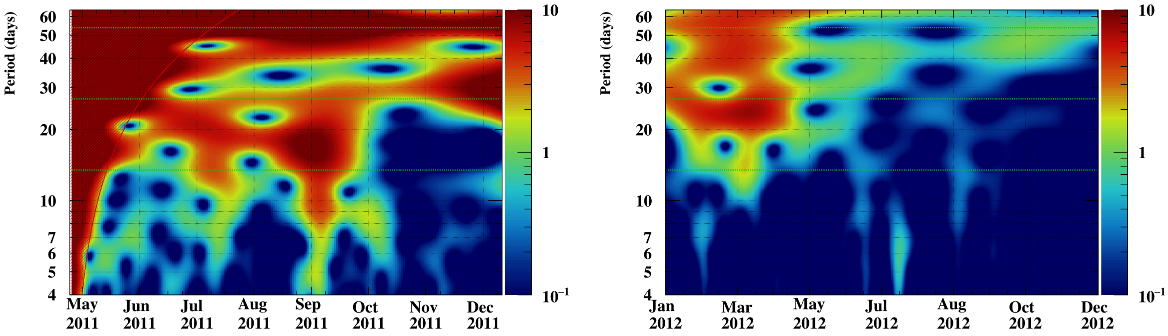

(a) Year: 2011, Rigidity: [1.00-1.16] GV

(b) Year: 2012, Rigidity: [1.00-1.16] GV

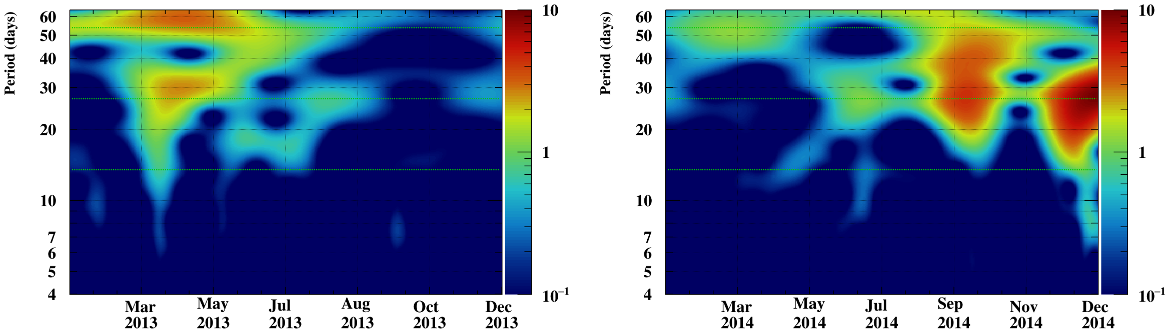

(c) Year: 2013, Rigidity: [1.00-1.16] GV

(d) Year: 2014, Rigidity: [1.00-1.16] GV

Figure 5.11: Local wavelet power spectrum for AMS-02's daily proton flux[116] normalized to the yearly flux variance. Vertical axis shows the Fourier period while the horizontal axis shows the date. The red shaded area shows the *cone of influence*. Horizontal green dashed lines represent 13.5, 27 and 54 day periods.

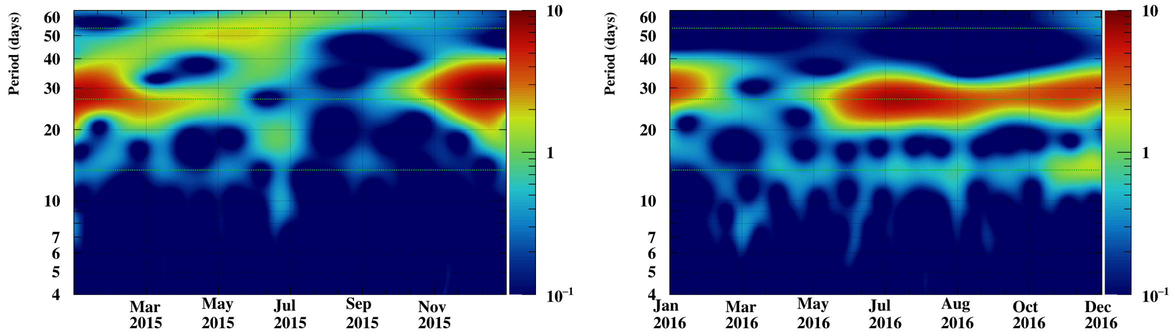

(a) Year: 2015, Rigidity: [1.00-1.16] GV

(b) Year: 2016, Rigidity: [1.00-1.16] GV

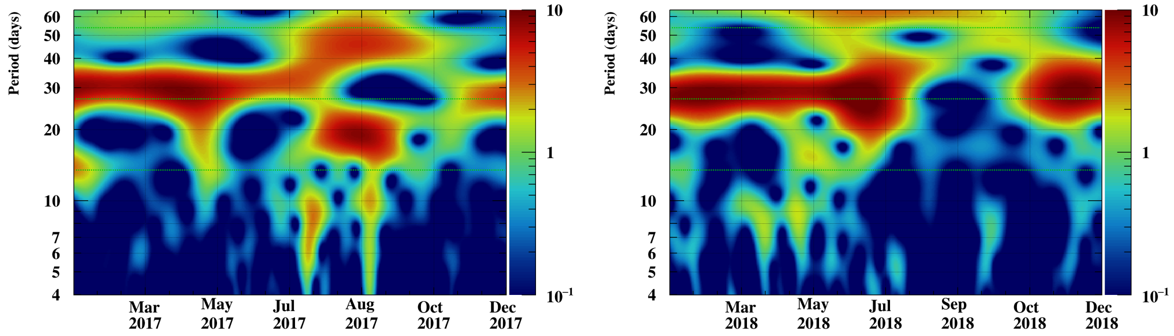

(c) Year: 2017, Rigidity: [1.00-1.16] GV

(d) Year: 2018, Rigidity: [1.00-1.16] GV

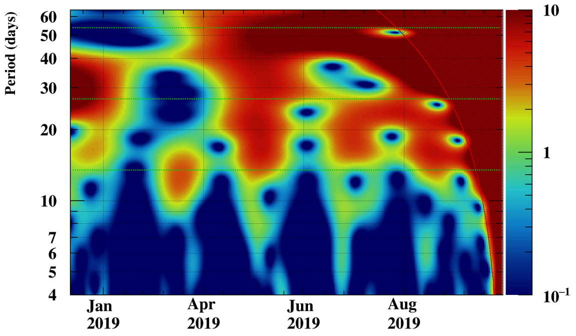

(e) Year: 2019, Rigidity: [1.00-1.16] GV

Figure 5.12: Local wavelet power spectrum for AMS-02's daily proton flux[116] normalized to the yearly flux variance. Vertical axis shows the Fourier period while the horizontal axis shows the date. The red shaded area shows the *cone of influence*. Horizontal green dashed lines represent 13.5, 27 and 54 day periods.

5.5.2 Wavelet power spectrum for [5.90-6.47] GV

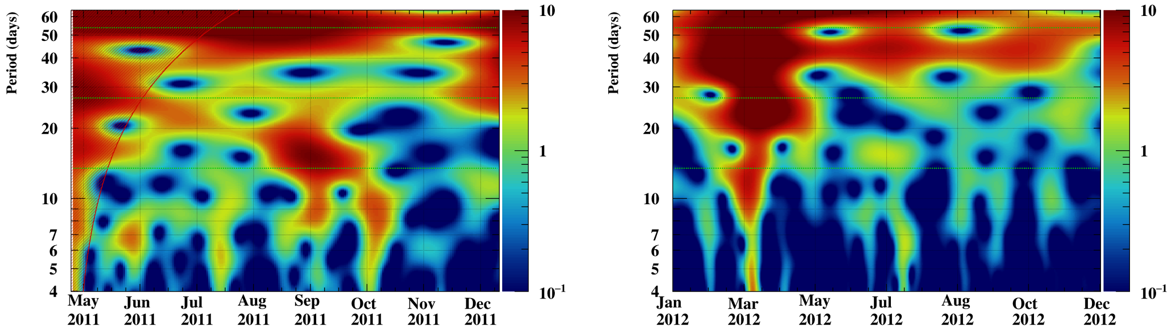

(a) Year: 2011, Rigidity: [5.90-6.47] GV (b) Year: 2012, Rigidity: [5.90-6.47] GV

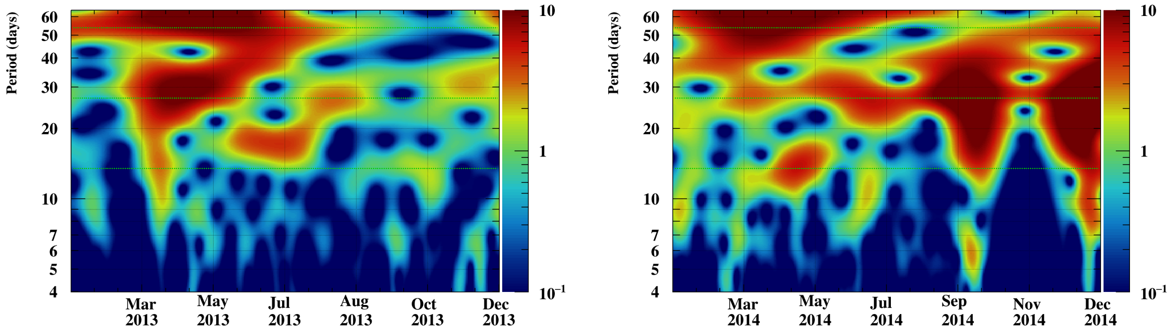

(c) Year: 2013, Rigidity: [5.90-6.47] GV (d) Year: 2014, Rigidity: [5.90-6.47] GV

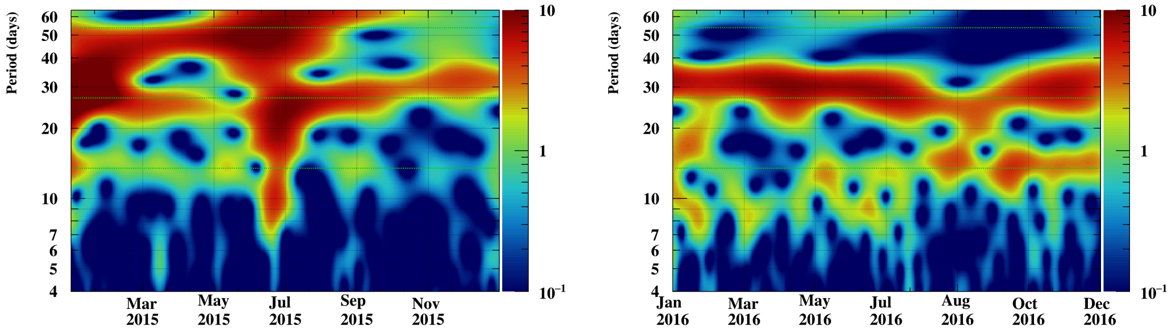

(e) Year: 2015, Rigidity: [5.90-6.47] GV (f) Year: 2016, Rigidity: [5.90-6.47] GV

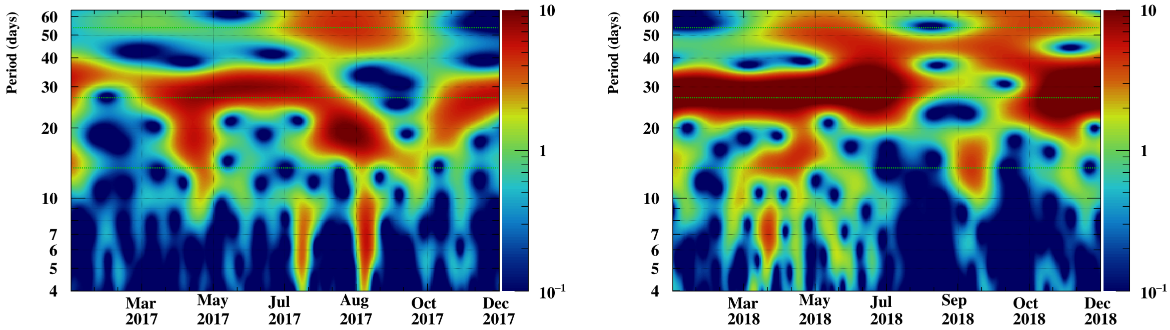

(g) Year: 2017, Rigidity: [5.90-6.47] GV (h) Year: 2018, Rigidity: [5.90-6.47] GV

Figure 5.13: Local wavelet power spectrum for AMS-02's daily proton flux[116] normalized to the yearly flux variance. Vertical axis shows the Fourier period while the horizontal axis shows the date. The red shaded area shows the *cone of influence*. Horizontal green dashed lines represent 13.5, 27 and 54 day periods.

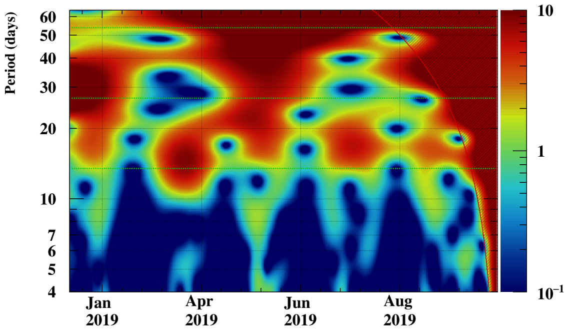

(a) Year: 2019, Rigidity: [5.90-6.47] GV

Figure 5.14: Local wavelet power spectrum for AMS-02's daily proton flux[116] for 2019, normalized to the yearly flux variance. Vertical axis shows the Fourier period while the horizontal axis shows the date. The red shaded area shows the *cone of influence*. Horizontal green dashed lines represent 13.5, 27 and 54 day periods.

5.5.3 Wavelet power spectrum for [16.60-18.00] GV

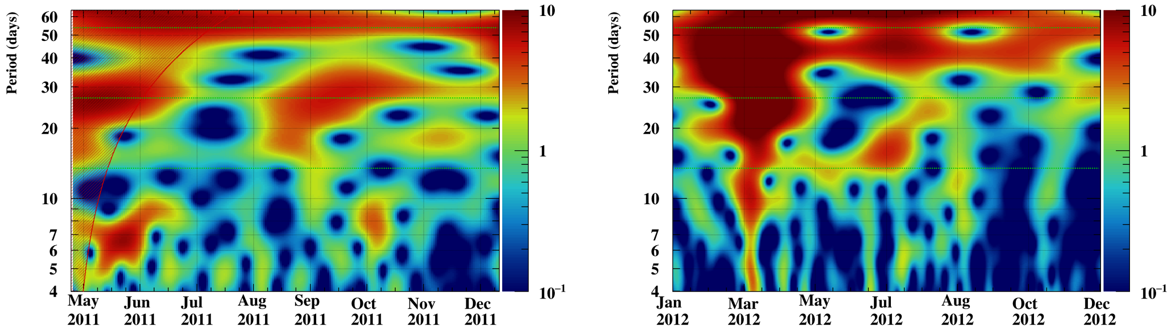

(a) Year: 2011, Rigidity: [16.60-18.00] GV (b) Year: 2012, Rigidity: [16.60-18.00] GV

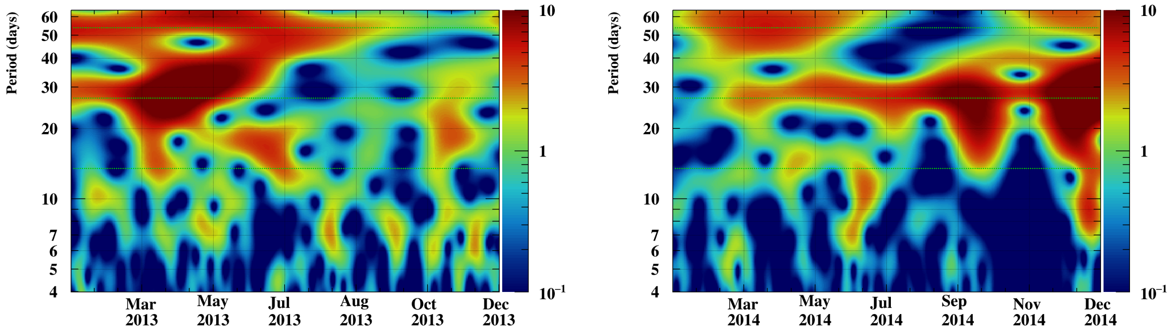

(c) Year: 2013, Rigidity: [16.60-18.00] GV (d) Year: 2014, Rigidity: [16.60-18.00] GV

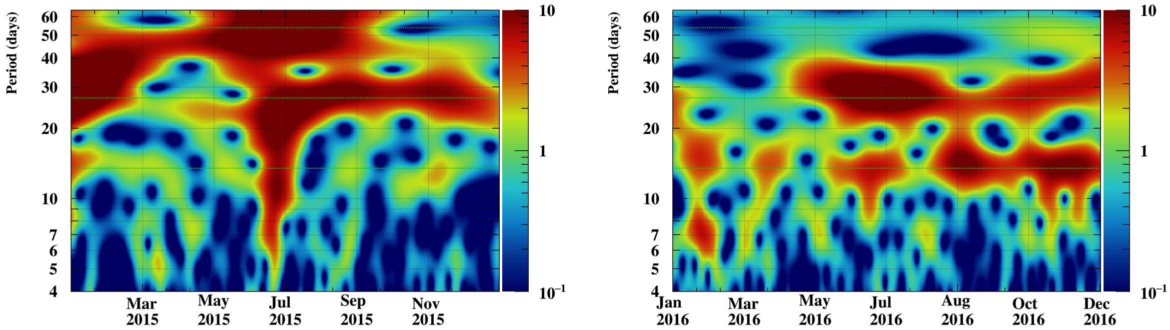

(e) Year: 2015, Rigidity: [16.60-18.00] GV (f) Year: 2016, Rigidity: [16.60-18.00] GV

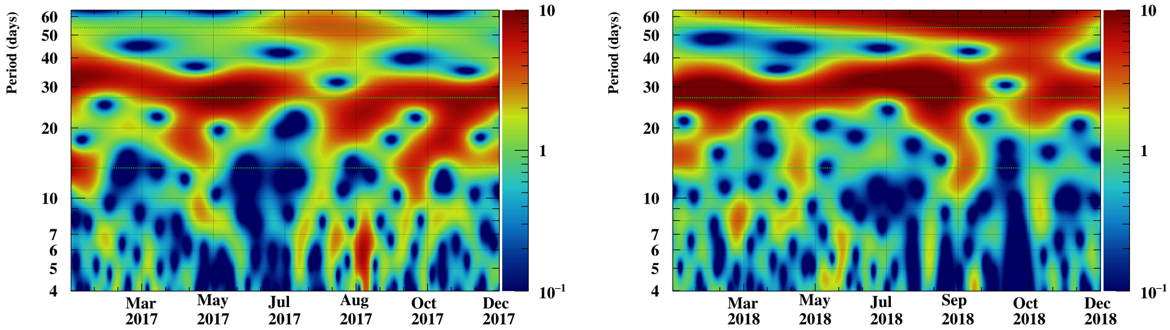

(g) Year: 2017, Rigidity: [16.60-18.00] GV (h) Year: 2018, Rigidity: [16.60-18.00] GV

Figure 5.15: Local wavelet power spectrum for AMS-02's daily proton flux[116] normalized to the yearly flux variance. Vertical axis shows the Fourier period while the horizontal axis shows the date. The red shaded area shows the *cone of influence*. Horizontal green dashed lines represent 13.5, 27 and 54 day periods.

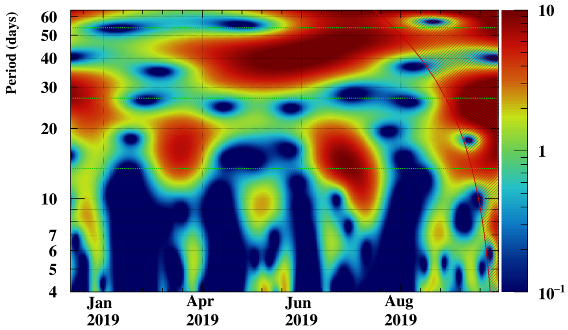

(a) Year: 2019, Rigidity: [16.60-18.00] GV

Figure 5.16: Local wavelet power spectrum for AMS-02's daily proton flux[116] for 2019, normalized to the yearly flux variance. Vertical axis shows the Fourier period while the horizontal axis shows the date. The red shaded area shows the *cone of influence*. Horizontal green dashed lines represent 13.5, 27 and 54 day periods.

5.5.4 Wavelet power spectrum for [80.50-86.50] GV

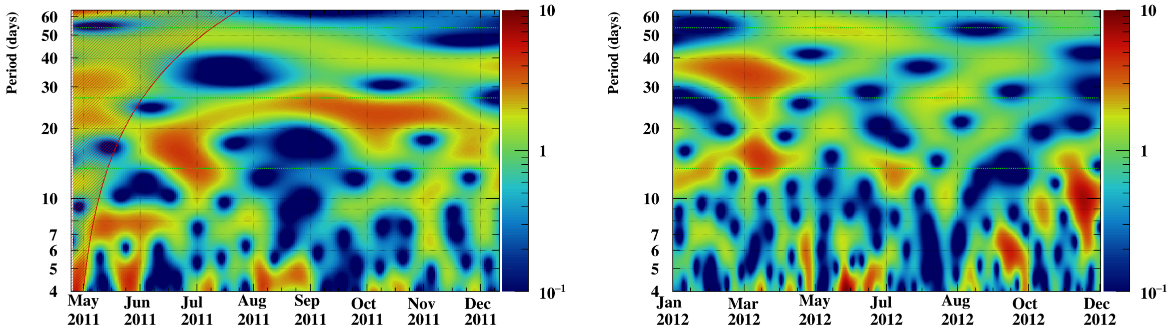

(a) Year: 2011, Rigidity: [80.50-86.50] GV

(b) Year: 2012, Rigidity: [80.50-86.50] GV

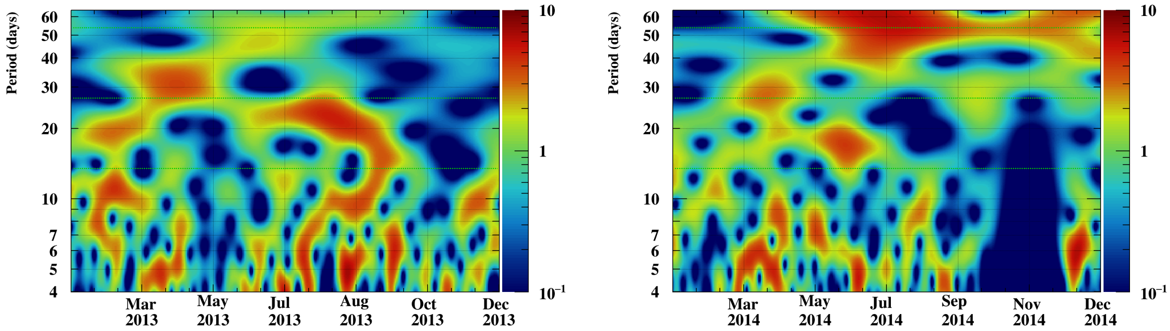

(c) Year: 2013, Rigidity: [80.50-86.50] GV

(d) Year: 2014, Rigidity: [80.50-86.50] GV

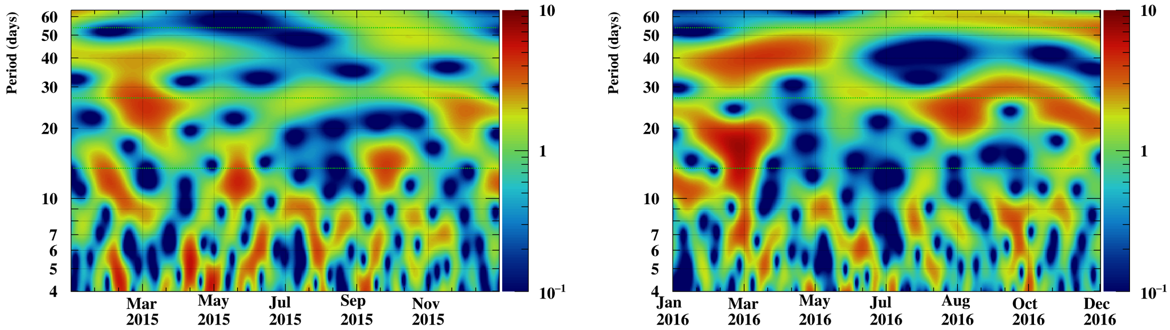

(e) Year: 2015, Rigidity: [80.50-86.50] GV

(f) Year: 2016, Rigidity: [80.50-86.50] GV

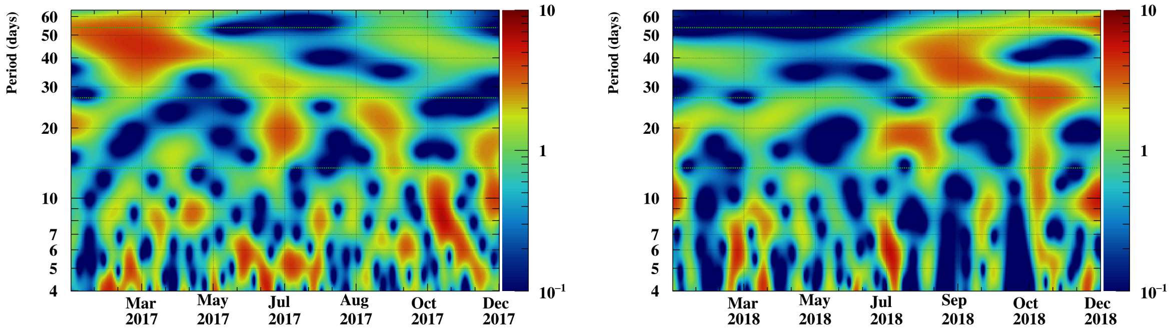

(g) Year: 2017, Rigidity: [80.50-86.50] GV

(h) Year: 2018, Rigidity: [80.50-86.50] GV

Figure 5.17: Local wavelet power spectrum for AMS-02's daily proton flux[116] normalized to the yearly flux variance. Vertical axis shows the Fourier period while the horizontal axis shows the date. The red shaded area shows the *cone of influence*. Horizontal green dashed lines represent 13.5, 27 and 54 day periods.

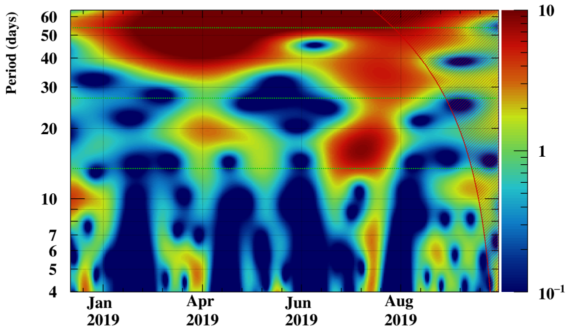

(a) Year: 2019, Rigidity: [80.50-86.50] GV

Figure 5.18: Local wavelet power spectrum for AMS-02's daily proton flux[116] for 2019, normalized to the yearly flux variance. Vertical axis shows the Fourier period while the horizontal axis shows the date. The red shaded area shows the *cone of influence*. Horizontal green dashed lines represent 13.5, 27 and 54 day periods.

5.5.5 Unusual Solar activity of 2017

As was shown in Figure 5.1, there is a dip in the measured flux in 2017. Figure 5.19 shows the flux during 2017 in detail with the major solar flares which occurred during that year. This dip is rather unusual given the fact that solar activity should be diminishing as the flux approaches its maximum. This maximum is correlated with a lower number of solar events, lower dipole tilt angle and a lower number of sunspots overall.

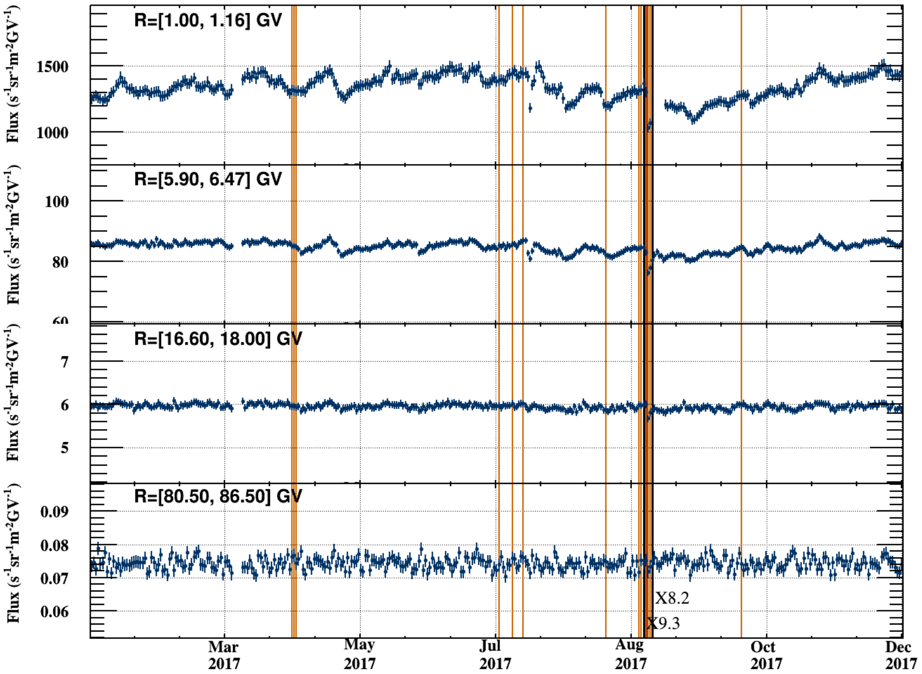

Figure 5.19: Time-series of the AMS daily proton flux[116] for the year of 2017 for the rigidity bins [1.00-1.16], [5.90-6.47], [16.60-18.00] and [80.50-86.50] GV. Orange vertical lines indicate M class solar flares, red lines indicate X class solar flares up to X4 and black lines indicate X class solar flares X5 and above.

The unusual dip can be seen in the wavelet power spectra as a change in the periodicity pattern (see Figure 5.20) of rigidity intervals [1.00-1.16] GV and [5.90-6.47] GV but it is notably absent in [16.60-18.00] GV and [80.50-86.50] GV. It presents itself as somewhat of a shift to higher and lower periodicities, while showing a clear void in the 27-day range for the time period after the biggest flares specifically. This is most likely due to the increase in solar activity during the late stages of Solar Cycle 24[126].

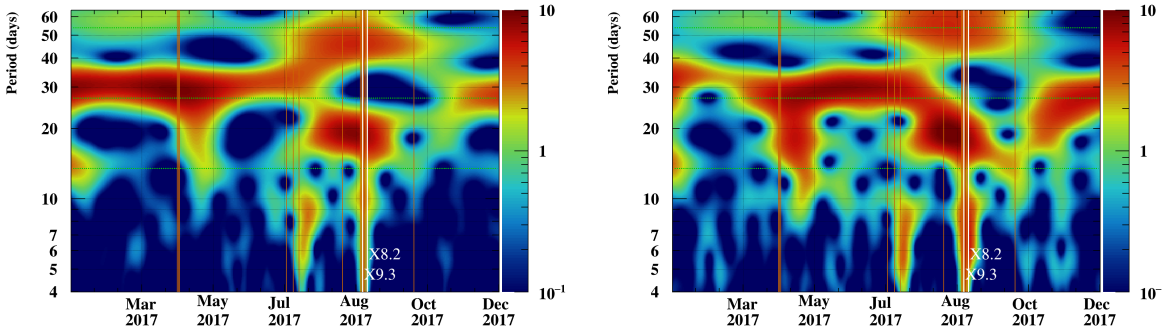

(a) Year: 2017, Rigidity: [1.00-1.16] GV

(b) Year: 2017, Rigidity: [5.90-6.47] GV

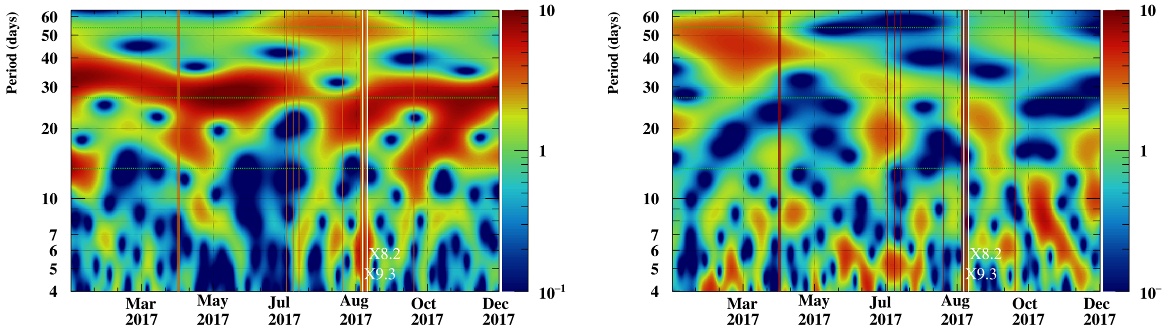

(c) Year: 2017, Rigidity: [16.60-18.00] GV

(d) Year: 2017, Rigidity: [80.50-86.50] GV

Figure 5.20: Local wavelet power spectrum for AMS-02's daily proton flux[116] from 1 January 2017 to 31 December 2017, normalized to the yearly flux variance. Vertical axis shows the Fourier period while the horizontal axis shows the date. Horizontal green dashed lines represent 13.5, 27 and 54 day periods. Orange vertical lines indicate M class solar flares, red lines indicate X class solar flares up to X4 and white lines indicate X class solar flares X5 and above.

Solar flares can be divided into classes, B, C, M and X which grow in powers of 10 in relation to each other and are classified in terms of peak flux (W/m^2) of X-rays from 0.1 to 0.8 nm wavelengths. These are currently being monitored by the GOES spacecraft[127]. A listing of the number of solar flares measured by GOES[126] during the analysis period can be seen in Table 5.2.

Starting around April 2017, there was a spike in solar activity starting with 7 M-Class solar flares in April, 3 M-class flares in July and finally, in September, the Sun saw its peak activity for 2017 with 22 M-Class solar flares and 4 X-class solar flares, X2.2 in 06/09/2017, X9.3 in 06/09/2017, X1.3 in 07/09/2017 and finally X8.2 in 10/09/2017. These concentrated high-intensity solar flares appear to be concentrated near the void present in the wavelet power spectrum. Large solar flares are usually correlated with other solar events such as coronal mass ejections - CME. CME's are known to have an effect on the cosmic-ray flux, decreasing it substantially in a physical process known as *Forbush Decrease*[68]. This decrease can be clearly seen in Figure 5.19.

This result is specially interesting because we can inspect a degree of energy dependence these solar events introduce in the flux since we were much less sensitive to this dip at the rigidity bin [16.60-18.00] GV and higher.

Year	X5+-class	X-class	M-class
2011	1	7	42
2012	1	6	43
2013	0	12	38
2014	0	16	34
2015	0	2	48
2016	0	0	16
2017	2	2	39
2018	0	0	0
2019	0	0	0

Table 5.2: Number of solar flares per year. Solar flare data taken from *Space Weather Prediction Center (SWPC), National Oceanic and Atmospheric Administration (NOAA)*[126].

5.5.6 Daily Proton Flux for 2016

The results for 2016 (from 1 January 2016 to 31 December 2016) are presented in Figure 5.21 for the following rigidity slices: [1.00-1.16] GV, [5.90-6.47] GV, [16.80-18.00] GV and [80.50-86.50] GV.

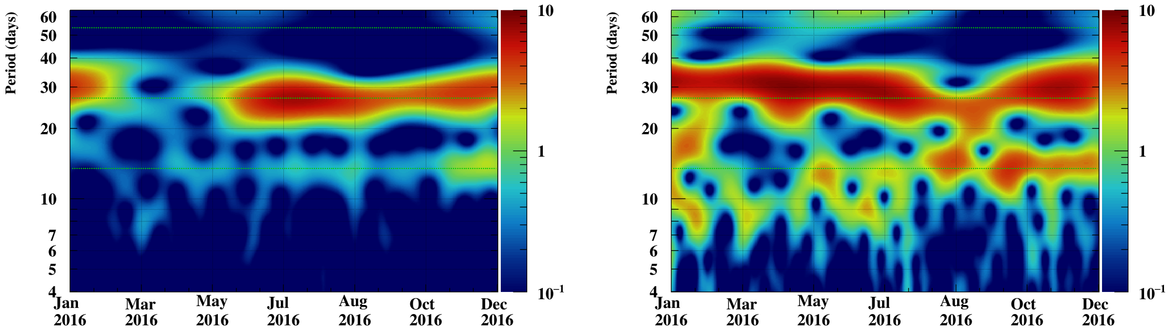

(a) Year: 2016, Rigidity: [1.00-1.16] GV (b) Year: 2016, Rigidity: [5.90-6.47] GV

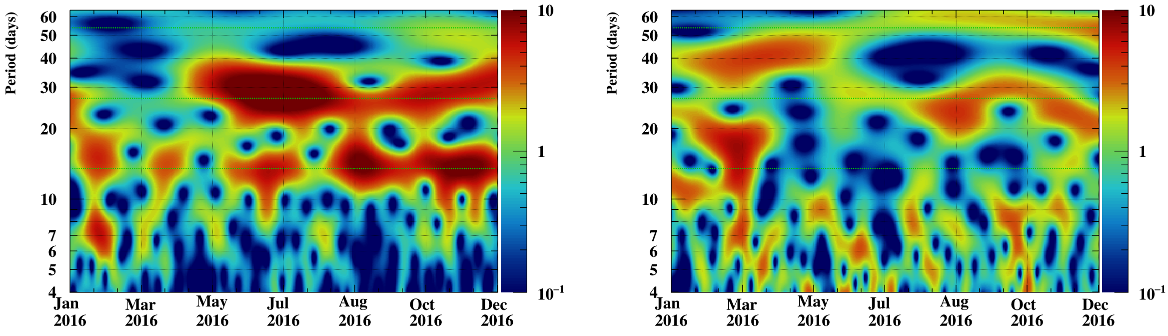

(c) Year: 2016, Rigidity: [16.60-18.00] GV (d) Year: 2016, Rigidity: [80.50-86.50] GV

Figure 5.21: Local wavelet power spectrum for AMS-02's daily proton flux[116] from 1 January 2016 to 31 December 2016, normalized to the yearly flux variance. Vertical axis shows the Fourier period while the horizontal axis shows the date. The red shaded area shows the *cone of influence*. Horizontal green dashed lines represent 13.5, 27 and 54 day periods.

Examining the local power spectrum for AMS-02's daily proton flux for 2016, seen in Figure 5.21, we can see a clear continuous frequency signal, specially on Figure 5.21a and Figure 5.21b where the 27 day signal is very apparent and clearly the one carrying the highest power, specially on Figure 5.21a at [1.00-1.16] GV rigidity. As we increase in rigidity the 13.5

day periodicity increases.

5.6 Wavelet Significance and Red-Noise

When trying parametrize the random oscillations shown in Figure 5.6, Figure 5.4 and Figure 5.2 we found that the continuous background power spectrum was well described by a red-noise process.

Our significance will then be derived from the relative difference between our power spectra and that of a red-noise process with parameters derived from the noise levels of our time-series.

A red-noise process corresponds to an auto-regressive series which describes a random process which contains memory[128]. In our case the process is autocorrelated with a time-lag of 1. This process relates a given observation to the previous in the following manner:

$$u_t - \bar{u} = \gamma\,(u_{t-1} - \bar{u}) + \alpha\, z_t \quad \text{with} \quad z_t \sim \mathcal{N}(0,1)\,, \tag{5.7}$$

where u_t is our time-series, $\bar{u}$ is the process mean, γ is the correlation between consecutive observations, α is the variance of our underlying random process and z_t is the underlying Gaussian (white-noise) process with null mean and unitary variance. For simplicity we will subtract the mean from our time-series in order to simplify some of the later calculations:

$$y_t = \gamma\, y_{t-1} + \alpha\, z_t \quad \text{with} \quad z_t \sim \mathcal{N}(0,1)\,. \tag{5.8}$$

This white-noise process is a series of uncorrelated observations each following a Gaussian (with the same variance) and its Fourier power spectrum is flat, showing that this process uniformly represents all frequencies (as seen in Figure 5.23).

Red-noise presents a spectrum[129] that favours lower frequencies and will show a theoretical continuous power spectrum of the form:

$$\mathrm{P}_{\mathrm{red-noise}}(\omega) = \frac{2\,\tau}{1+\omega^2\,\tau^2}\,, \quad \text{with} \quad \tau = \frac{-1}{\ln\gamma}\,, \tag{5.9}$$

where τ is known as e-folding time and represents the time required for the auto-correlation function to decay $1/e$. This expression represents the theoretical power spectrum of the continuous red-noise process.

The discrete Fourier power spectrum the red-noise process is described by the following expression[130]:

$$\mathrm{P}_{\mathrm{red-noise}}(\omega_k) = \frac{1-\gamma^2}{1+\gamma^2 - 2\gamma\cos(\omega_k\,\delta t)}\,, \tag{5.10}$$

where γ is the same correlation coefficient described above, δt is the sampling time of our time-series and ω_k is the usual angular frequency defined before.

In figure Figure 5.22 we present examples of time-series generated by a white-noise process with $\sigma_{y_t} = 1$ and a red noise process with $\gamma = 0.65$ and $\alpha = \sqrt{1-\gamma^2}$ to guarantee that $\sigma_{y_t} = 1$, and in Figure 5.23 we present their respective Fourier power spectra. The mean discrete Fourier power spectrum for both white and red-noise (as described by Equation 5.10) is also presented on Figure 5.23.

Additionally, in Figure 5.24 we present the average of 100 Fourier power spectra of time-series generated according to the white and red noise processes described. This results reinforces the notion that the Fourier power spectrum at a given frequency is itself a random variable and, as such, is also subject to random fluctuations.

We empirically showed in previous figures (such as Figure 5.7) that the AMS daily proton power spectrum loosely follows a red-noise power spectrum but only through sampling different time-series of the same process, in the same conditions, could we increase our degree of certainty.

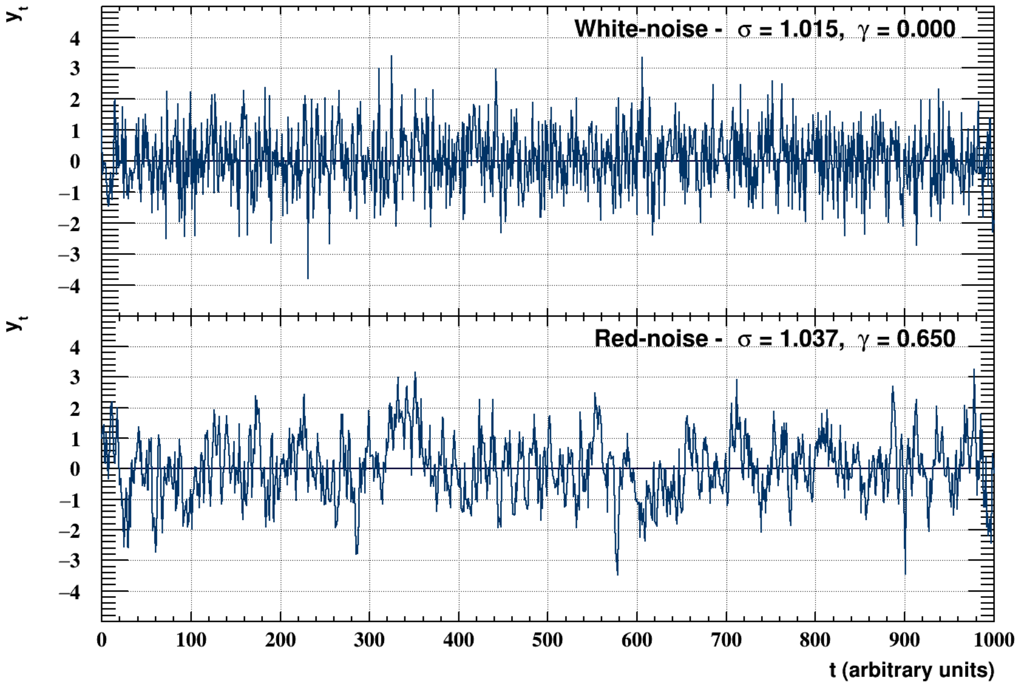

Figure 5.22: Randomly generated time-series according to a white-noise process (top) with $\sigma_y = 1$ and red-noise process (bottom) with $\gamma = 0.65$ and $\alpha = \sqrt{1-\gamma^2}$ to guarantee that $\sigma_y = 1$.

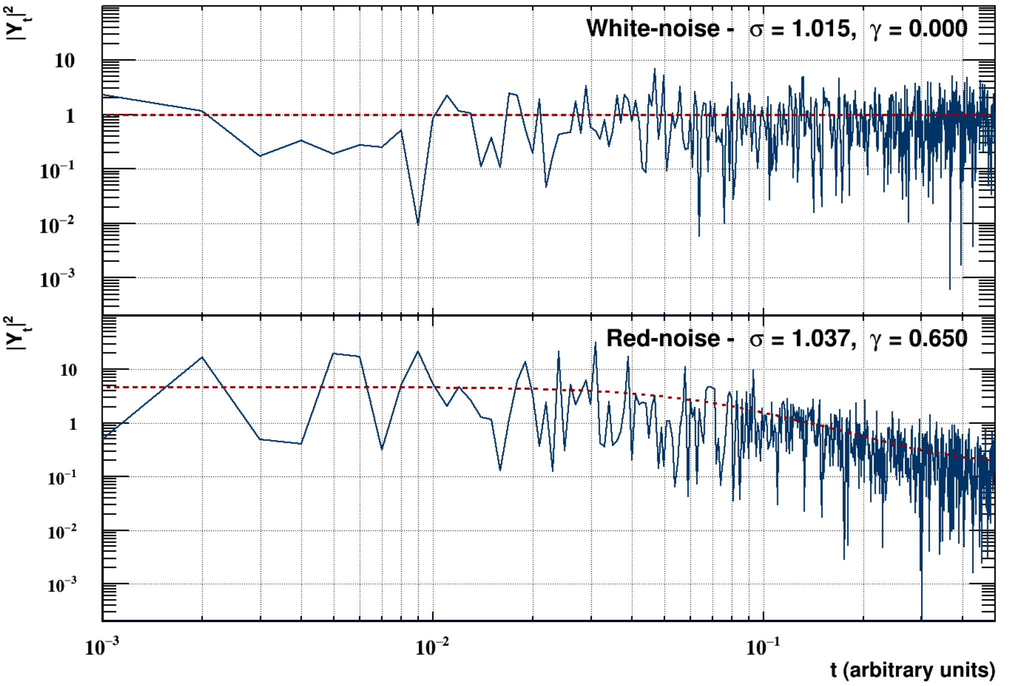

Figure 5.23: Fourier transform power spectrum of randomly generated time-series according to a white-noise process (top) with $\sigma_{y_t} = 1$ and red-noise process (bottom) with $\gamma = 0.65$ and $\alpha = \sqrt{1-\gamma^2}$ to guarantee that $\sigma_{y_t} = 1$. The respective mean white and red noise power spectra are displayed as red dashed curves.

In order to infer the most likely parameters for the background spectra Vaughan, S., (2005)[122] proposed least-squares fitting of the power spectra when studying power-law noise spectra ($P(\omega_k) \propto \omega_k^{\alpha}$) or red-noise spectra when they are nearly power-law noise. Due to the agreement we've seen in daily AMS data between the spectra and a red-noise power spectrum, at different time intervals and at different energies, we will be assuming a red-noise process generating the background signal of our time-series moving forward.

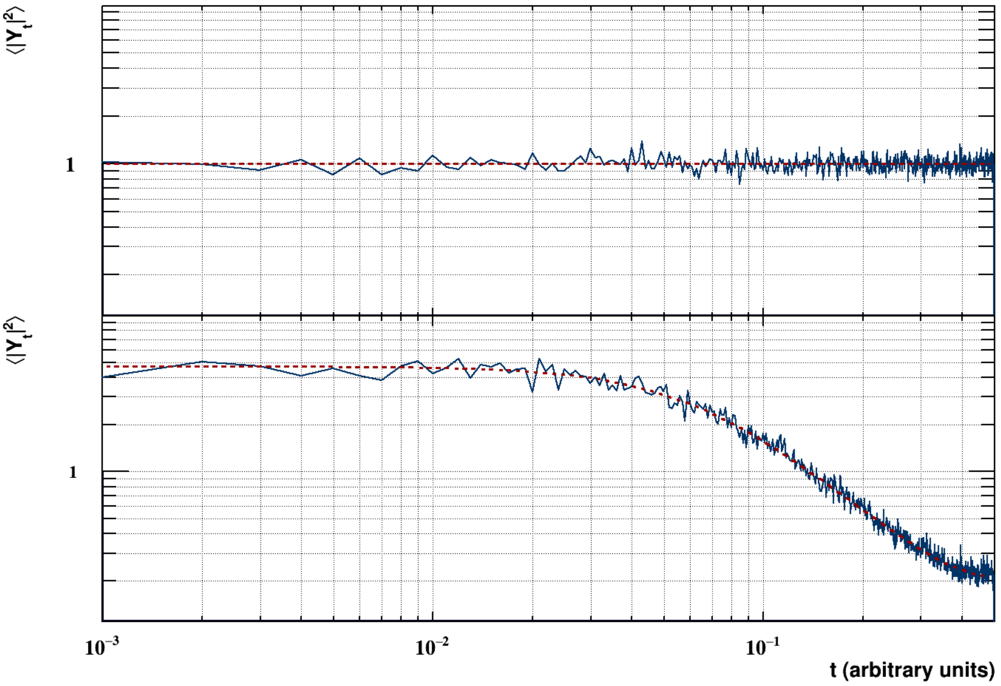

Figure 5.24: Average Fourier transform power spectrum of 100 randomly generated time-series according to a white-noise process (top) with $\sigma_{y_t} = 1$ and red-noise process (bottom) with $\gamma = 0.65$ and $\alpha = \sqrt{1-\gamma^2}$ to guarantee that $\sigma_{y_t} = 1$. The respective mean white and red noise power spectra are displayed as red dashed curves.

Since we are looking to produce a red-noise that would be mostly to reproduce our data we need to extract the two parameters (γ and α) from our data. If we assume that our data would be a red-noise according to Equation 5.8 we can look at what estimators we could use to estimate γ and α.

The mean of our signal offers very little information since we can easily see that it follows a null expected value. Variance of our time-series can be seen to be

$$\begin{aligned}\mathrm{Var}(y_t) &= \gamma^2\,\mathrm{Var}(y_{t-1}) + \alpha^2\,\mathrm{Var}(z_t)\\ \mathrm{Var}(y_t) &= \gamma^2\,\mathrm{Var}(y_{t-1}) + \alpha^2\,,\end{aligned}$$

where if we assume stationarity[128] (i.e. the variance of our time-series does not change with time - $\mathrm{Var}(y_t) = \mathrm{Var}(y_{t-1})$), follows that

$$\begin{aligned}\mathrm{Var}(y_t) &= \gamma^2\,\mathrm{Var}(y_t) + \alpha^2\\ \mathrm{Var}(y_t) &= \frac{\alpha^2}{1-\gamma^2}\,.\end{aligned}$$

This result shows that our time-series will have an increased variance due to the correlation between observations, hinting that the two will be coupled somehow on other observables.

As we can see in Equation 5.9 and Equation 5.10, the power spectrum of the red-noise is a function of only the γ factor. By using the covariance between the time-series and the time-series with a lag-1 (this is known as auto-covariance of lag-1) we can gain some further insight on the relations between red-noise parameters and the time-series

$$\begin{aligned}
\mathrm{Cov}(y_t, y_{t-1}) &= \mathrm{E}\left[(y_t - \mathrm{E}[y_t])(y_{t-1} - \mathrm{E}[y_{t-1}])\right] \\
&= \mathrm{E}[y_t\, y_{t-1}] \\
&= \mathrm{E}[(\gamma\, y_{t-1} + \alpha\, z_{t-1})\, y_{t-1}] \\
&= \gamma\, \mathrm{E}\left[y_{t-1}^2\right] + \alpha\, \mathrm{E}[z_{t-1} y_{t-1}] \\
&= \gamma\, \mathrm{Var}(y_{t-1}) + \alpha\, \mathrm{Cov}(z_{t-1} y_{t-1}) \\
&= \gamma\, \mathrm{Var}(y_t) + \alpha\, \mathrm{Cov}(z_t y_t) \quad \text{where by definition} \quad \mathrm{Cov}(z_t y_t) = 0 \\
&= \gamma\, \mathrm{Var}(y_t) = \gamma\, \frac{\alpha^2}{1-\gamma^2}\,.
\end{aligned}$$

The result $\mathrm{Cov}(z_t y_t) = 0$ comes from the fact that the white-noise process is, by definition, uncorrelated to the rest of the series. To note that variance is simply the auto-covariance of lag-0. For convenience we can then define $c_l = \mathrm{Cov}(y_t, y_{t-l})$.

We can now use these results to derive that our parameter γ can be written as

$$\gamma = \frac{\mathrm{Cov}(y_t, y_{t-1})}{\mathrm{Var}(y_t)} = \frac{c_1}{c_0} = \gamma\, \frac{\alpha^2}{1-\gamma^2}\, \frac{1-\gamma^2}{\alpha^2} = \gamma\,.$$

We can then estimate our auto-covariance lag-1 and our variance of the series by using the following expressions:

$$\widehat{c_0} = \frac{1}{N-1} \sum_{i=1}^{N-1} \left(y_t - \mathrm{E}[y_t]\right)^2 \tag{5.11}$$

$$\widehat{c_1} = \frac{1}{N-1} \sum_{i=1}^{N-1} \left(y_t - \mathrm{E}[y_t]\right)\left(y_{t-1} - \mathrm{E}[y_{t-1}]\right) \tag{5.12}$$

Allen, (1992)[131] has shown that these estimators c_l all share a bias that makes them smaller than the parameters of the time-series and that the correction for this bias leads to the system:

$$\begin{aligned}
\frac{\widehat{c_1}}{\widehat{c_0}} = \frac{\tilde{\gamma} - \mu^2(\tilde{\gamma})}{1 - \mu^2(\tilde{\gamma})} \quad \text{with} \quad \mu^2(\gamma) &= \frac{1}{N} + \frac{1}{N^2} \sum_{k=1}^{N-1} 2\,(N-k)\gamma^k \\
&= -\frac{1}{N} + \frac{2}{N^2}\left[\frac{N - \gamma^N}{1-\gamma} - \frac{\gamma\left(1-\gamma^{N-1}\right)}{(1-\gamma)^2}\right].
\end{aligned}$$

This expression can be solved by fixed-point method in order to find the unbiased parameter $\tilde{\gamma}$. This technique is described in Allen and Smith, (1996)[128] and was used in the estimation of every red-noise power spectrum in this work.

In order to estimate the order of magnitude of the correction on the determination of the γ factor we created a small toy Monte-Carlo in which we generated time-series with varying γ factors, ranging from 0.15 to 0.95, and estimated both the lag-1 auto-correlation factor and $\tilde{\gamma}$. This process was repeated 10^6 times for each γ factor and the results are presented in 5.25.

Some of these are presented in Figure 5.3 and Figure 5.5 where we see the clear dependence of the correlation parameter with rigidity. As rigidity increases the correlation parameter decreases and the process becomes essentially white-noise, centred on the average daily flux.

Now that we are able to accurately estimate the parameters of the red-noise present in our time-series, we can estimate the distribution of the red-noise power spectrum in order to

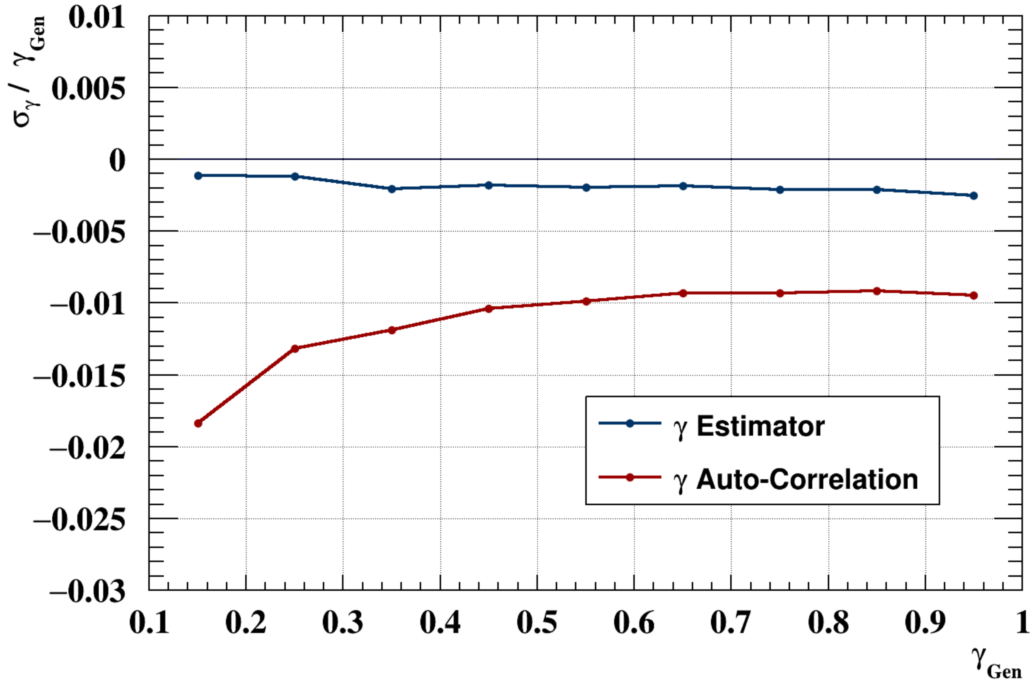

Figure 5.25: Relative difference between estimated γ factor and generated γ_{Gen}. The comparison is drawn between the lag-1 auto-correlation in red and $\tilde{\gamma}$ in blue.

construct confidence intervals which we can use to determine relative significance of our signals in relation to this confidence interval.

It can be shown[125] that the local wavelet power spectrum follows the mean Fourier spectrum and as such we only need to analyse the red-noise Fourier power spectrum to compare it to our wavelet results. The power spectrum of red-noise is distributed, at each frequency, following a χ^2 distribution with two degrees of freedom[123, 125, 122]:

$$\frac{2\,|Y_k|^2}{N\,\sigma^2\,\mathrm{P}_{\mathrm{red-noise}}(\omega_k)} \sim \chi_2^2\,. \tag{5.13}$$

This result provides us with the distribution of our noise in terms of the power spectrum for any given frequency.

The factor of 2 and the degrees of freedom in the χ^2 distribution are related to the Fourier transform of a Gaussian process, such as white-noise, having both real and imaginary parts also distributed by normal distributions[125, 121]. When we compute the square of the modulus of the Fourier transform we are constructing a variable that is the sum of two normally distributed variables squared and thus, a χ^2 distributed variable with two degrees of freedom. To note that at the null frequency (also known as the DC component of a signal) the imaginary part of the Fourier transform is zero meaning that the power of the null frequency is distributed by a χ^2 distribution with only one degree of freedom and without the factor of 2 present, as can be seen in Figure 5.26.

The result in Figure 5.26 was constructed by recreating the series from Figure 5.22 10000 times and sampling the power at fixed frequencies following Equation 5.13.

With the knowledge of the pdf of our background process we can now construct a 95% confidence interval by estimating the power at which the cumulative distribution function (cdf) is valued 0.95. This limit gives us a 95% probability that any peak below it can be explained by the background. Any peak above this threshold cannot be reasonably explained by our red-noise process, making it a significant signal we must explain by some other process. In our case we are aiming at identifying and understanding any periodicity related to solar modulation.

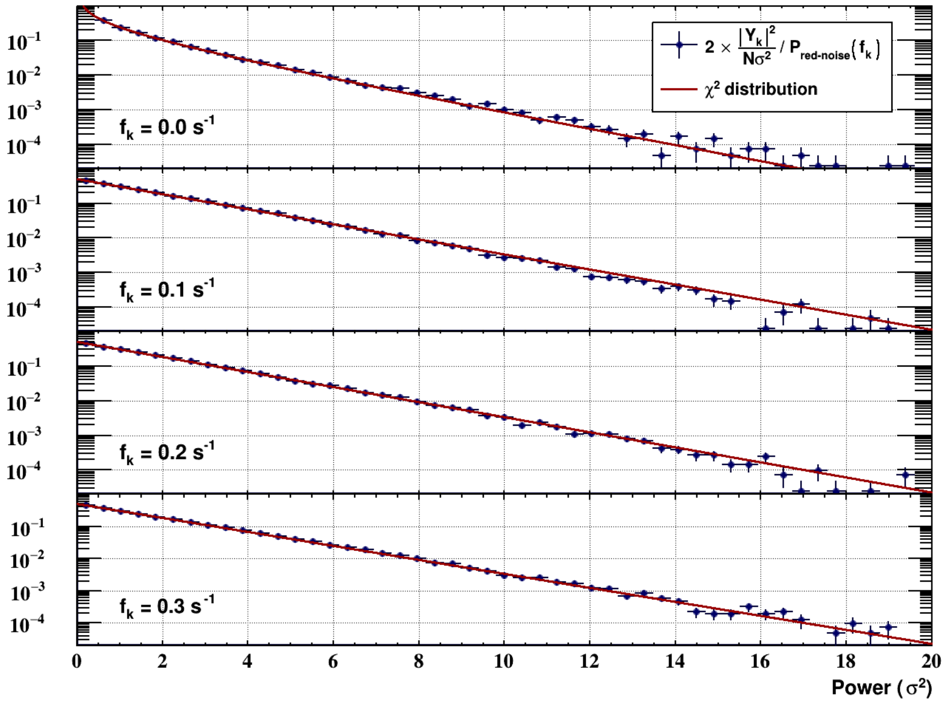

Figure 5.26: Distribution of the Fourier power spectrum of a red-noise series with $\gamma = 0.65$ and $\alpha = 1$, for frequencies $f_k = 0$, $f_k = 0.1$, $f_k = 0.2$ and $f_k = 0.3$.

In Figure 5.27 we can see how these confidence levels are determined and how they depend on the number of degrees of freedom of the χ^2 distribution. This will be important later when we estimate the average wavelet transform.

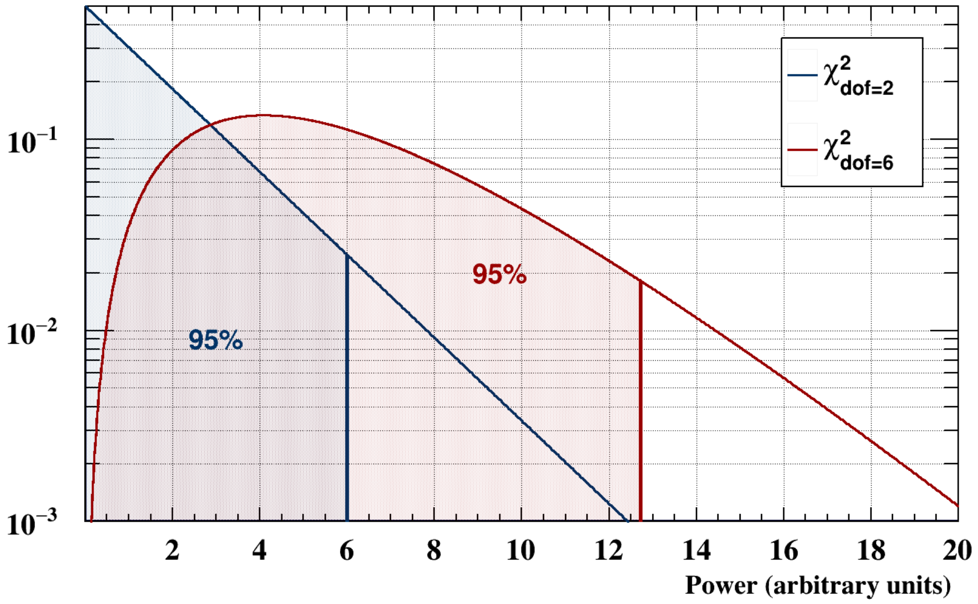

Figure 5.27: χ^2 distributions for number of degrees of freedom of 2 and 6.

The red-noise process is commonly present in several fields such as astrophysics[122] or climate sciences[128] and is compatible with the power spectrum of our time-series, as can be seen in Figure 5.5 and Figure 5.3.

We've already shown that in a time-series as long as ours, the wavelet power spectrum varies considerably due to changes in the variance of our data. Now that we established and parametrized our expected background we would like to know the significance of our peaks in relation to this background. Doing so for every time bin would be a cumbersome task and would offer little information beyond the inspection of the wavelet itself. One tool at our disposal is the average wavelet transform which would let us compare the significance for different periods of time.

5.6.1 Average Wavelet Transform

An average of the wavelet transform[125] was also computed for each semester of each year at the aforementioned rigidity bins according to:

$$\langle W\rangle^2(s) = \frac{1}{n_a}\sum_{n=0}^{n_a-1} |W_n(s)|^2 \ , \tag{5.14}$$

where $\langle W\rangle^2(s)$ is the average wavelet transform estimated for the duration of the fraction of the time-series being considered denoted by the number of temporal slices n_a.

The power spectrum of the average wavelet transform of a red-noise time-series presents a similar distribution as the simple wavelet transform seen in Equation 5.13 but with the subtlety of having to estimate the number of degrees of freedom associated with the average. Torrence and Compo showed an empiric relation between the number of temporal slices of the wavelet transform being averaged over with the number of degrees of freedom of the corresponding χ^2 distribution, as given by:

$$\nu = 2\sqrt{1+\left(\frac{n_a\,\delta t}{\tau_d\, s}\right)^2} \ ,$$

where n_a is the number of temporal slices being averaged over, δt is the time difference between two points of the time-series, τ_d is a decorrelation factor estimated by Monte-Carlo by Torrence and Compo, (1998)[125] which is 2.32 for the Morlet wavelet and s is the scale being considered. The wavelet transform $W_n(s)$, centred around t_n, will be less affected by observations in the time-series the further away they are from t_n. This decorrelation factor not only measures the degree of temporal influence of the wavelet over a time range but also the amount of new information gained by a wavelet centred around a point neighbouring t_n when calculating the average wavelet transform. The effective number of degrees of freedom then becomes a function of the *width* of the wavelet (which is related to the scale) and the length of the time period being averaged over which is $\frac{n_a\,\delta t}{\tau_d}$.

$$\frac{\nu\,\langle W\rangle^2(s)}{N\,\sigma^2\,\mathrm{P}_{\mathrm{red-noise}}(\omega_k)} \sim \chi^2_\nu \,. \tag{5.15}$$

These results are presented in Figure 5.28, Figure 5.29, Figure 5.30, Figure 5.31 and Figure 5.32a, compared to the red-noise power spectrum at a 68% and 95% confidence level[125, 132, 129, 122, 128].

Interestingly we can note that the 27 day periodicity varies with time and presents a slightly higher period of about 30 days instead of the expected $\sim$ 27 days which is close to the the Carrington synodic rotation (27.2753 days). This shift in period can be clearly seen in Figure 5.30b and Figure 5.30b. In it we can clearly see that at all 3 rigidities our 13.5 day signal is significantly above the confidence level and mostly centred around 13.5. Interestingly, near the 27 day periodicity we can see that the lower energy rigidity is quite significant and is mostly comprised of of a regular 27 day period signal while the higher rigidity signals are quite shifted from the 27 days, specially the [5.90-6.47] GV spectrum which is significantly

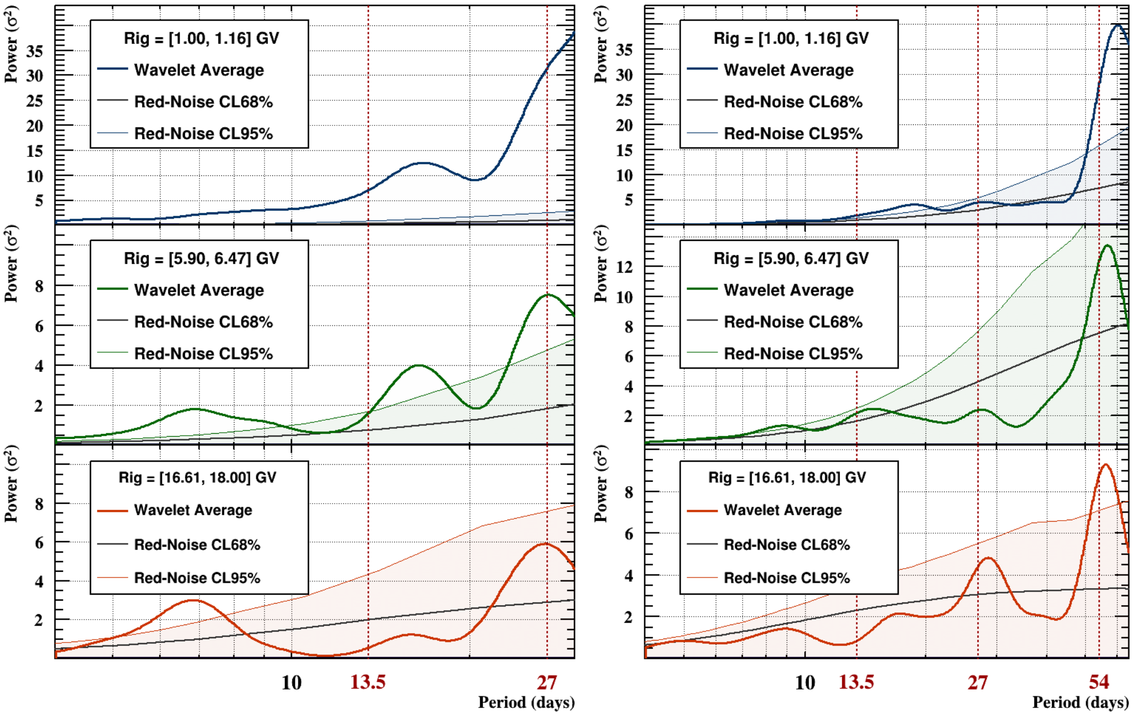

(a) Year: 2011 (left from 01/01 to 31/06, right from 01/07 to 31/12)

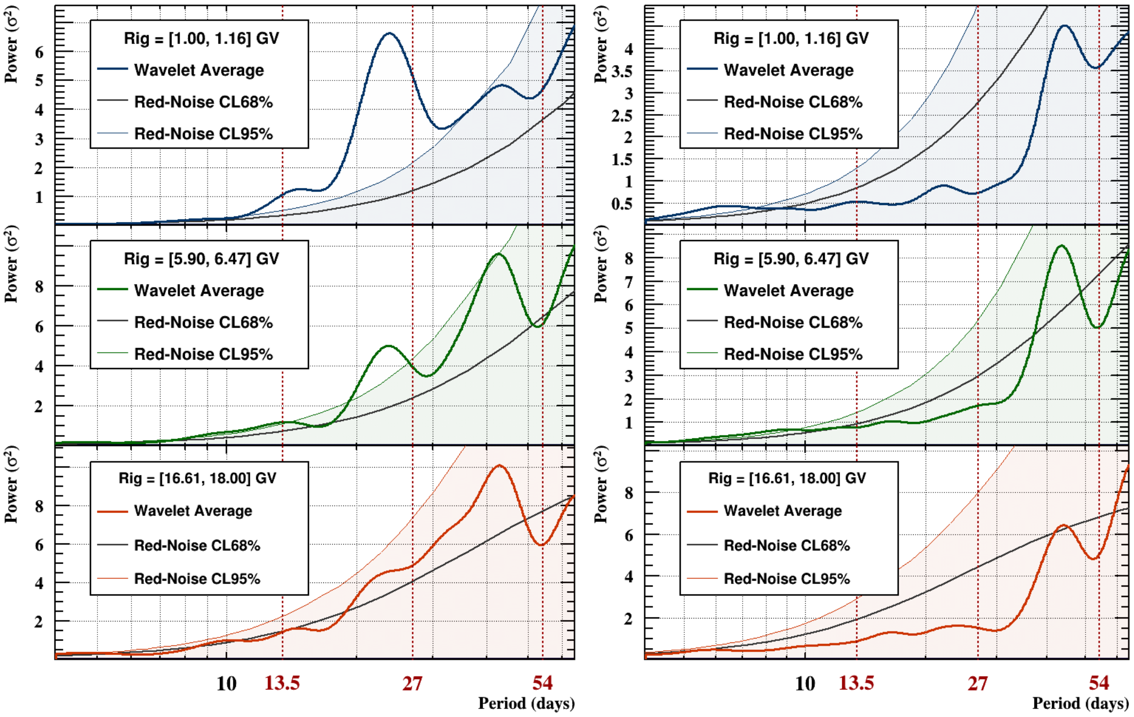

(b) Year: 2012 (left from 01/01 to 31/06, right from 01/07 to 31/12)

Figure 5.28: 6-month average of local wavelet power spectrum for AMS-02's daily proton flux [116], normalized to the 6-month flux variance. Red-noise power spectrum on a 95% confidence level[125, 132, 129, 122, 128]. Vertical red dashed lines represent the periodicities of 13.5, 27 and 54 days.

shifted towards the 30 day period. Although not significant enough, the higher energy result shifts back towards the 27 days.

The 27-day periodicity is related to the magnetic polarity of the solar wind being reversed

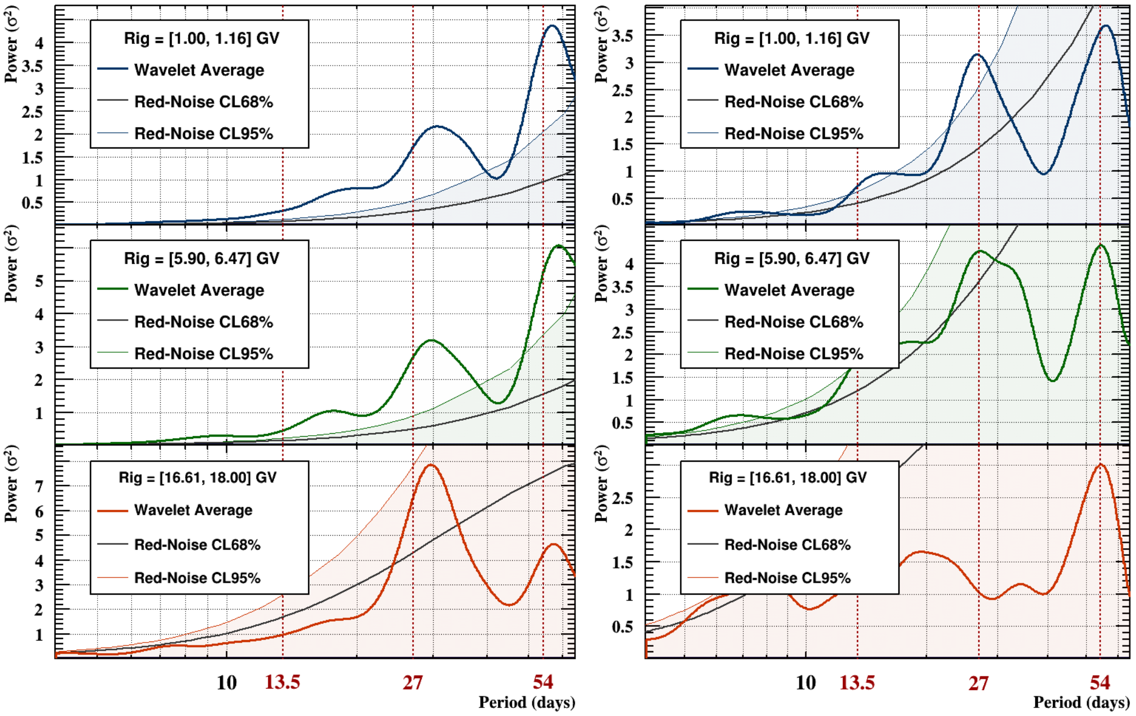

(a) Year: 2013 (left from 01/01 to 31/06, right from 01/07 to 31/12)

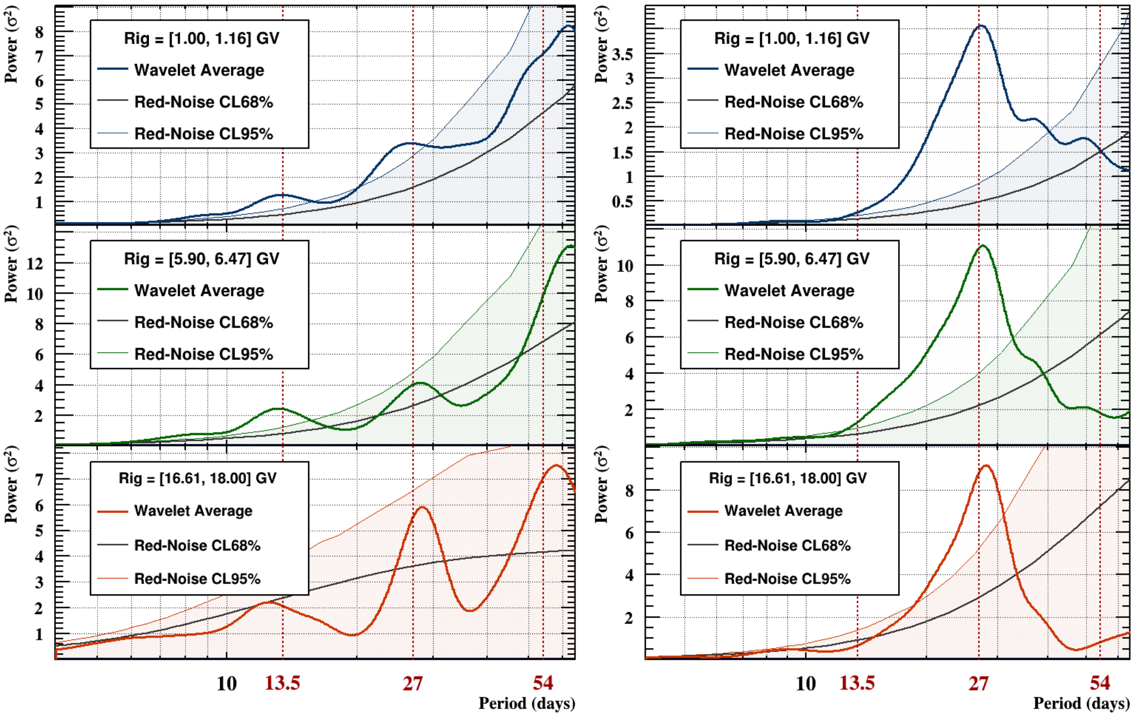

(b) Year: 2014 (left from 01/01 to 31/06, right from 01/07 to 31/12)

Figure 5.29: 6-month average of local wavelet power spectrum for AMS-02's daily proton flux [116], normalized to the 6-month flux variance. Red-noise power spectrum on a 95% confidence level[125, 132, 129, 122, 128]. Vertical red dashed lines represent the periodicities of 13.5, 27 and 54 days.

at the HCS. As the Earth crosses this surface the environment around it changes and so do the fluxes it is exposed to. As we saw on chapter 2, the existence of the two polarities separated by this surface will give rise to a periodicity of 27 days which relates to the magnetic field

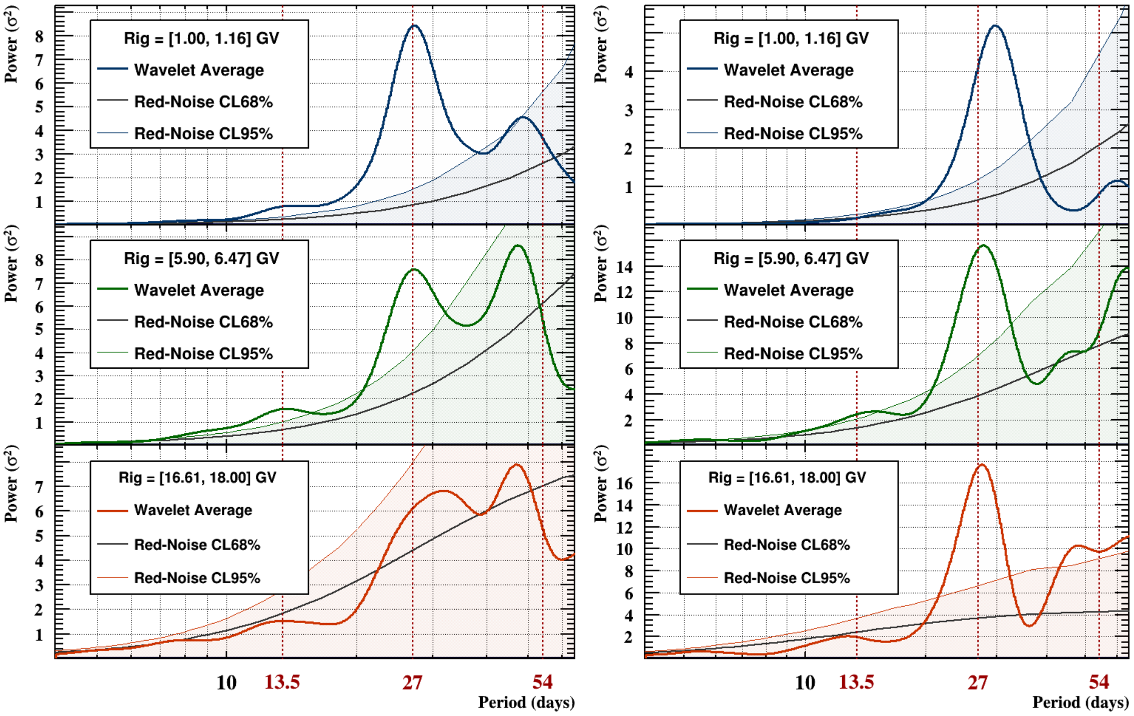

(a) Year: 2015 (left from 01/01 to 31/06, right from 01/07 to 31/12)

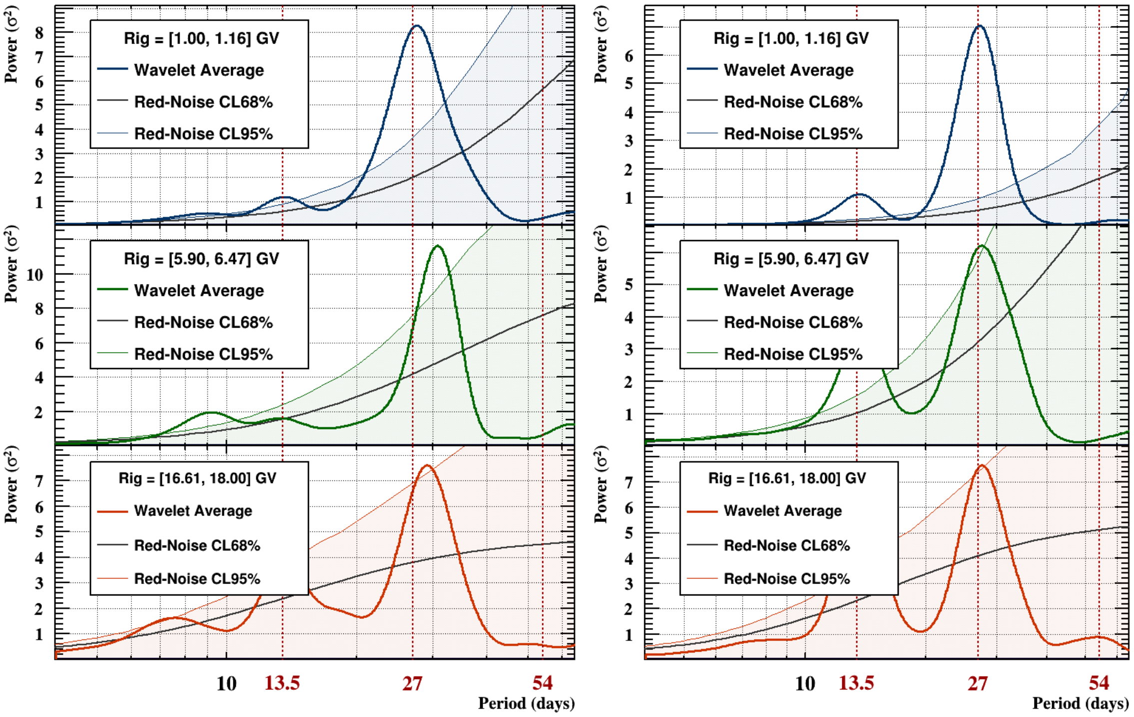

(b) Year: 2016 (left from 01/01 to 31/06, right from 01/07 to 31/12)

Figure 5.30: 6-month average of local wavelet power spectrum for AMS-02's daily proton flux [116], normalized to the 6-month flux variance. Red-noise power spectrum on a 95% confidence level[125, 132, 129, 122, 128]. Vertical red dashed lines represent the periodicities of 13.5, 27 and 54 days.

changing from positive to negative and back to positive again. This change however does not explain the 13.5 day periodicity.

The 13.5 day periodicity is related to the crossing of the HCS itself, which happens 2

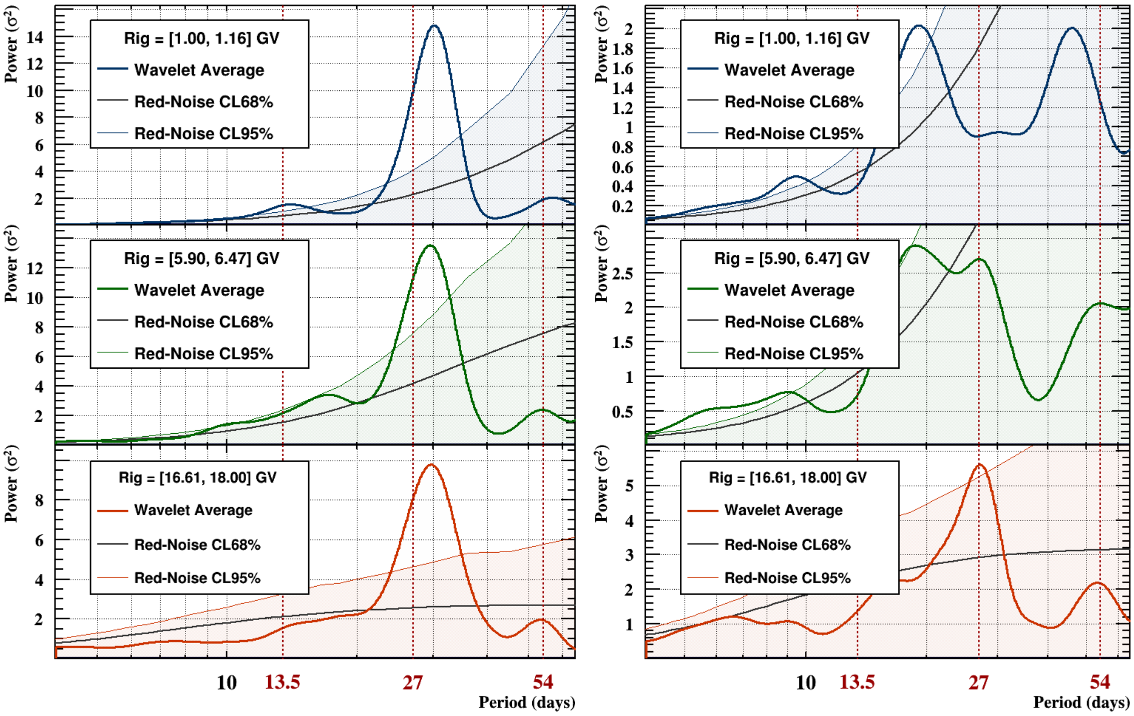

(a) Year: 2017 (left from 01/01 to 31/06, right from 01/07 to 31/12)

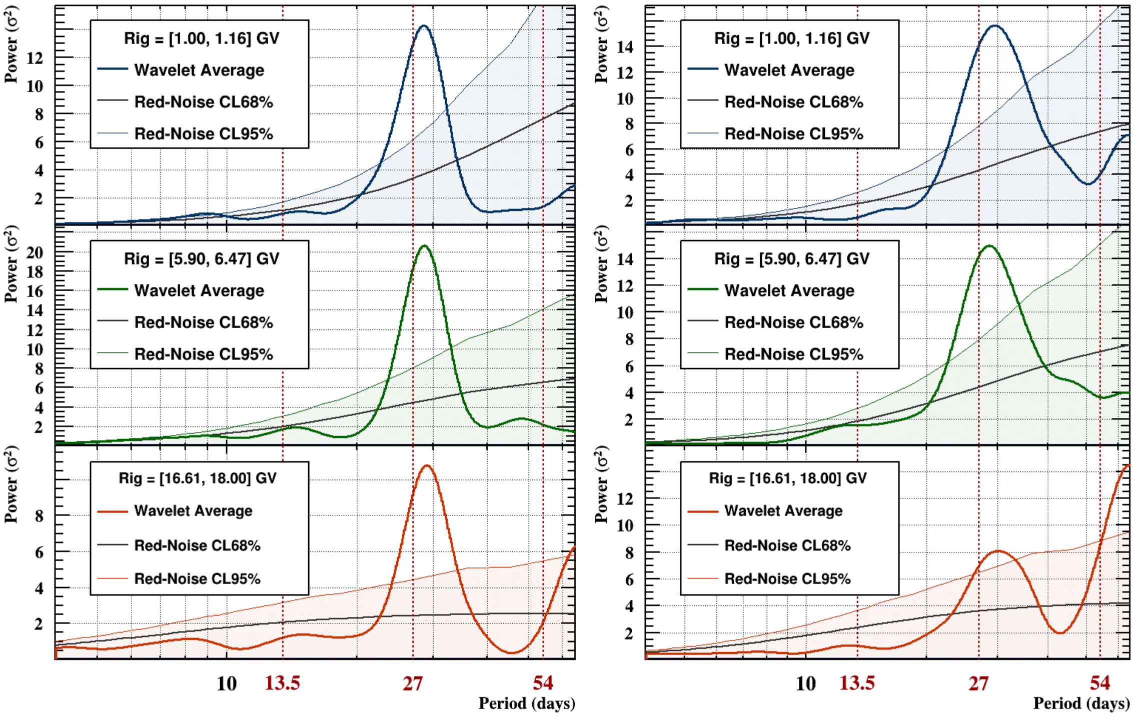

(b) Year: 2018 (left from 01/01 to 31/06, right from 01/07 to 31/12)

Figure 5.31: 6-month average of local wavelet power spectrum for AMS-02's daily proton flux [116], normalized to the 6-month flux variance. Red-noise power spectrum on a 95% confidence level[125, 132, 129, 122, 128]. Vertical red dashed lines represent the periodicities of 13.5, 27 and 54 days.

times per solar rotation. The presence of the 13.5-day periodicity can be evidence of the drifts associated with the HCS itself as cosmic-rays close enough to this structure will follow this sheet due to the sudden change in magnetic polarity. This mechanism was described by

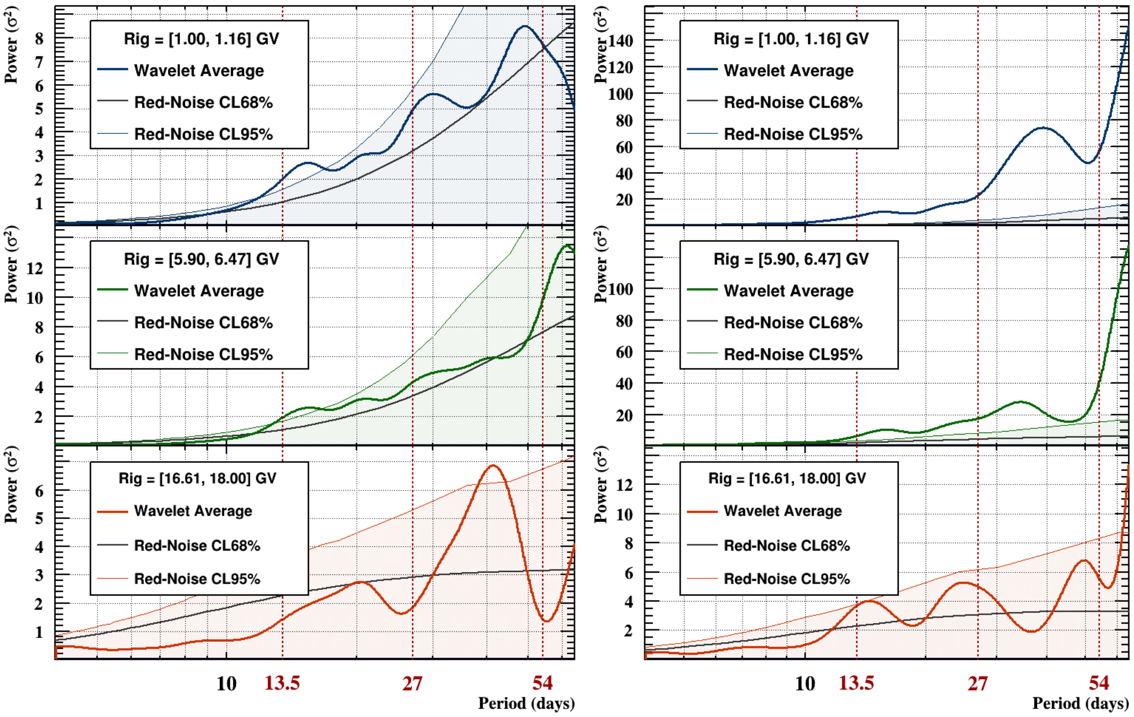

(a) Year: 2019 (left from 01/01 to 31/06, right from 01/07 to 31/12)

Figure 5.32: 6-month average of local wavelet power spectrum for AMS-02's daily proton flux [116], normalized to the 6-month flux variance. Red-noise power spectrum on a 95% confidence level[125, 132, 129, 122, 128]. Vertical red dashed lines represent the periodicities of 13.5, 27 and 54 days.

Burger, Moraal and Webb, (1985)[80] and will follow the direction of the global magnetic drifts but it is only present when the Earth is close to the HCS, thus presenting a periodicity which is half of the periodicity associated with the Sun's rotation.

Every yearly result presented in Figure 5.28, Figure 5.29, Figure 5.30, Figure 5.31 and Figure 5.32a has their different rigidity slices quite aligned aside from some notable minor shifts but a common trend in all of them is the increase in significance as time progresses towards 2019. The year of 2016 presents the most significant peaks on the 13.5 periodicity at every rigidity. The previous year, 2015, and the next year, 2017, show a slight bump near the same region but, in 2017 this periodicity shifted upwards quite heavily and mixed with the main 27 day frequency.

At the very highest rigidities our clear periodicities dissipate, creating a flatter and less significant power spectrum as can be seen in the different average wavelet results.

We summarize the results of the average wavelet transform in Figure 5.33 which displays the location of the peaks closest to the 27 day periodicity as a function of time. This graph shows a rising trend in which the peak periodicity near the Sun's rotational period increases and reaches a maximum of about 30 days. Notably, the peaks do not appear to be a function of rigidity.

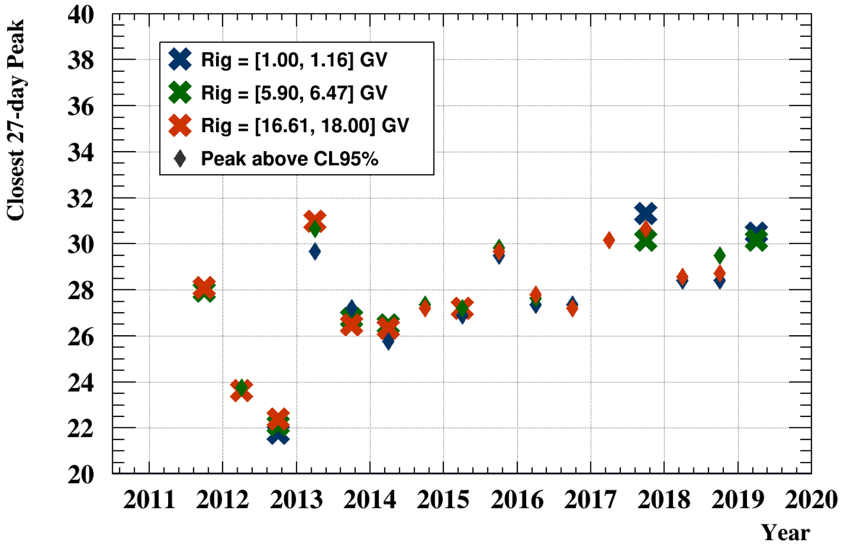

Figure 5.33: Peak period of the yearly average of local wavelet power spectrum for AMS-02's daily proton flux [116], normalized to the yearly flux variance. Significance above red-noise power spectrum on a 95% confidence level is marked with triangles while circles mark a badly defined peak.

5.7 Wavelet transform of Interplanetary Magnetic Field

Since we will mostly be investigating the 27-day modulation of cosmic-rays in the next chapter, we will now explore the daily variations of the flux by comparing it with a direct measurement of the IMF, coming from the Sun. To do so we resort to the measurements made by the ACE[133] satellite. We will use the measurement of IMF on Earth-Sun direction, taken from *NASA OMNIWeb Plus*[1].

Since ACE is in the L_1 Lagrange point of the Sun-Earth system and this measurement of IMF is aligned in the Earth-Sun axis of the Geocentric Solar Ecliptic (GSE) coordinate system, it provides a detailed picture of the local variations near the equatorial region of the heliosphere, where Earth is located. Notably we can use it to inspect Earth's crossing of the HCS and observe a possible fluctuation in the flux that derives from the change in the local magnetic orientation and change in drift particle motion around the Earth.

The results of the wavelet transform of the IMF measurement can be found in Figure 5.34. The local wavelet power spectrum for ACE IMF measurement in the Earth-Sun axis shows a very distinct periodicity in the 27-day period. It also shows some periodicities in the 13.5 and 9 day periods but, most notably, it shows a periodicity near the 365 day period which might correlate to the yearly variations of the distance of the ACE satellite to the Sun as it orbits in the L_1 Lagrange point in an elliptic manner.

As was done before, the wavelet transform was split into yearly blocks in order to improve visual clarity and periodicity contrast. These can be seen in Figure 5.35.

5.7.1 Cross-Wavelet Transform - Daily Flux and Interplanetary Magnetic Field

We have used the wavelet transform for qualitative inspection of these data-series and investigated the significance of the different periodicities found in the data by constructing wavelet time-averages and comparing them to a 95% confidence level constructed from a red-noise

---

[1] `https://omniweb.gsfc.nasa.gov/`

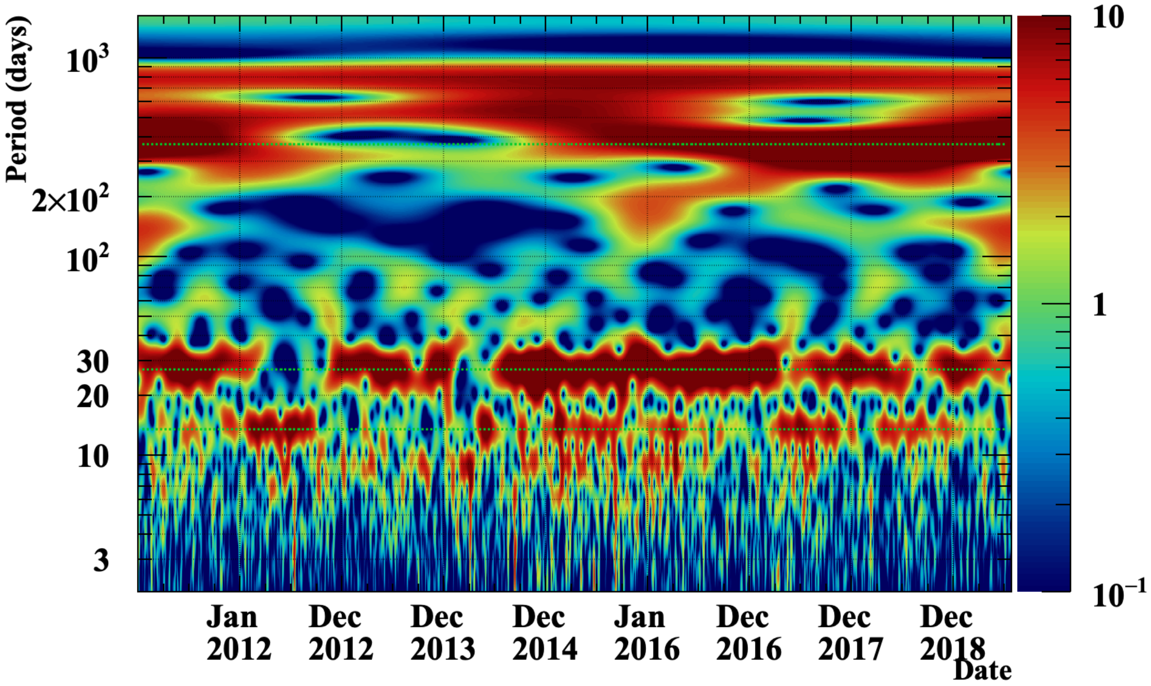

(a) 2011 to 2020

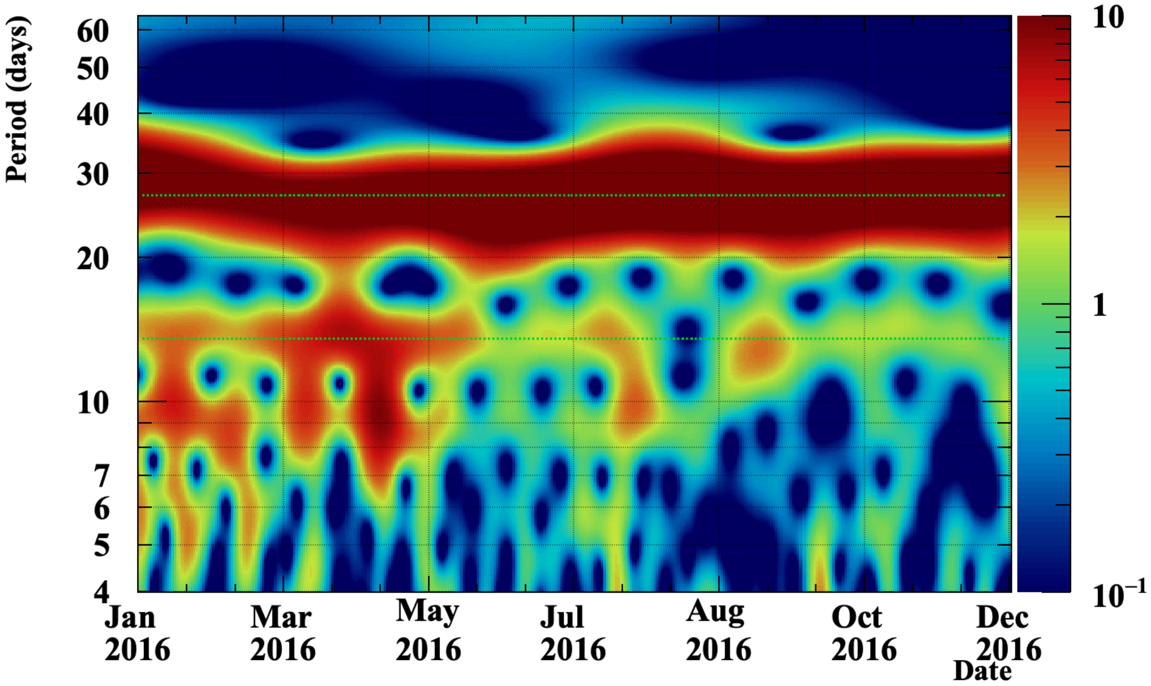

(b) 1 Jan 2016 to 31 December 2016

Figure 5.34: Local wavelet power spectrum for ACE IMF measurement in the Earth-Sun axis for different time periods. This data was taken from *NASA OMNIWeb Plus*1. In 5.34a the green dashed lines show the 13.5, 27 and 365 day periods while in 5.34b the green dashed lines show the 13.5 and 27 day periods.

background assumption. Another very useful feature of this tool lies in the direct comparison between two wavelet transforms by *correlation* which in turn also compares the two time-series for the periodicities in common. This is done by estimating the cross-wavelet spectrum of two

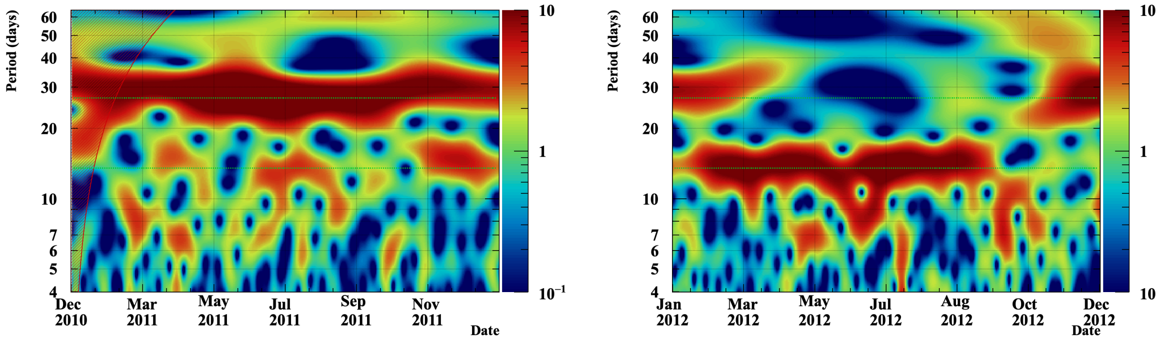

(a) Year: 2011 (b) Year: 2012

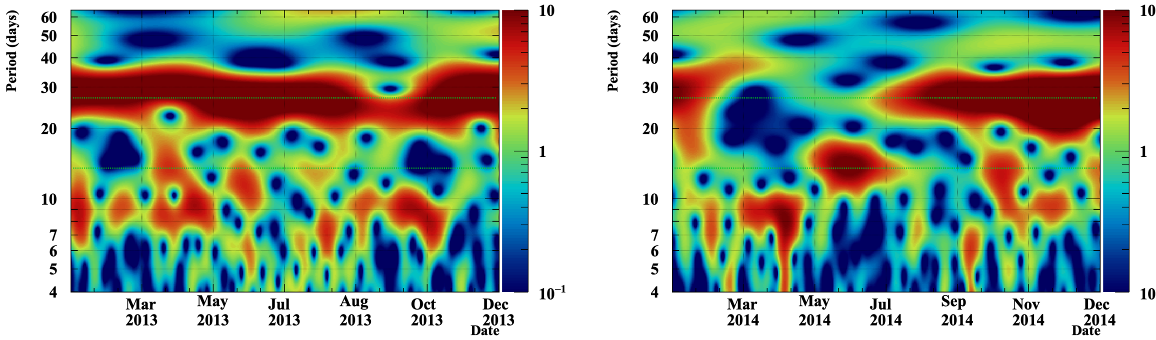

(c) Year: 2013 (d) Year: 2014

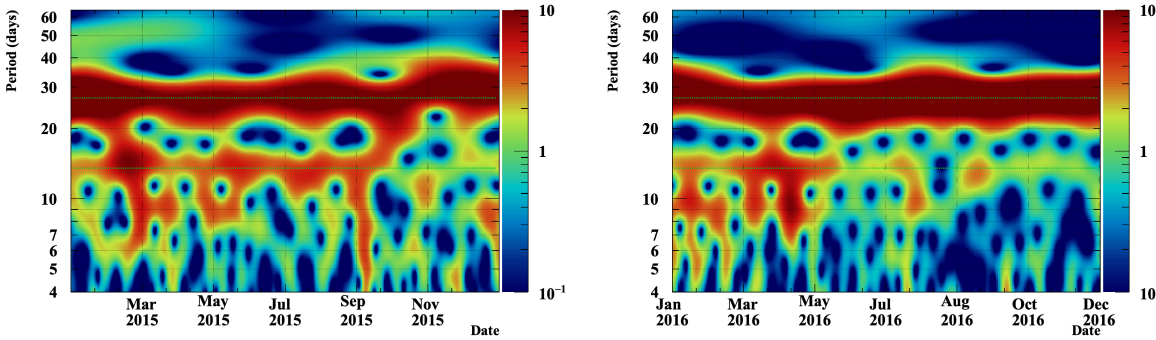

(e) Year: 2015 (f) Year: 2016

Figure 5.35: Local wavelet power spectrum for ACE IMF measurement in the Earth-Sun axis for different time periods. This data was taken from *NASA OMNIWeb Plus*1. In 5.34a the green dashed lines show the 13.5, 27 and 365 day periods while in 5.34b the green dashed lines show the 13.5 and 27 day periods.

time series which is defined[125] as

$$W_n^{XY}(s) = \frac{\left|W_n^X(s)\, W_n^{Y*}(s)\right|}{\sigma_X\, \sigma_Y}\,, \tag{5.16}$$

where $W_n^X(s)$ is the wavelet transform of the series X, $W_n^{Y*}(s)$ is the complex conjugate of the wavelet transform of series Y and σ_X and σ_Y represent the standard deviations of the series X and Y, respectively.

The cross-wavelet spectrum can be seen in its entirety in Figure 5.37 and, for the rigidity interval [5.90-6.47] GV, in Figure 5.38. It shows evidence of a strong correlation between the two series on the 27 day period which evolves with time.

During 2012 the periodicity vanishes and reappears sporadically until the end of 2014 in which it becomes rather constant until the end of the time period, aside from some intervals.

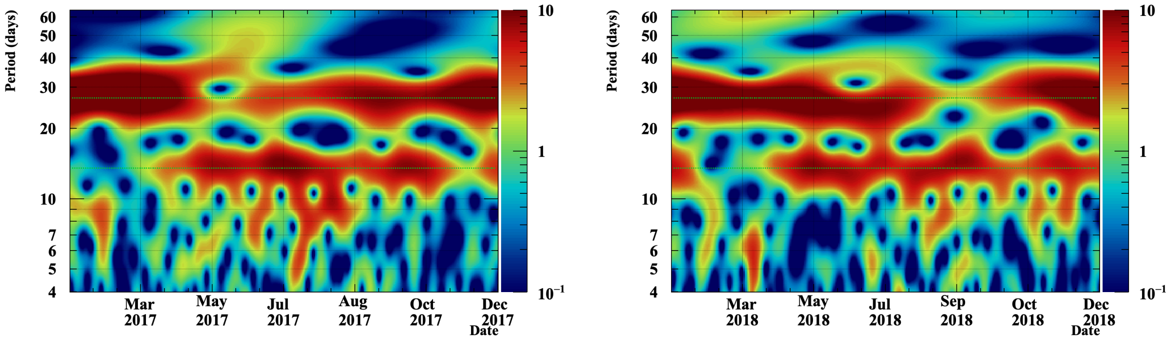

(a) Year: 2017

(b) Year: 2018

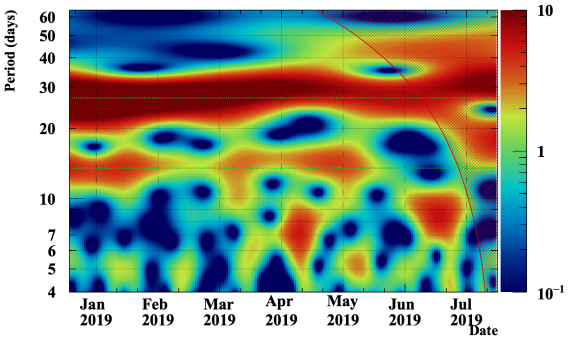

(c) Year: 2019

Figure 5.36: Local wavelet power spectrum for ACE IMF measurement in the Earth-Sun axis for different time periods. This data was taken from *NASA OMNIWeb Plus*1. In 5.34a the green dashed lines show the 13.5, 27 and 365 day periods while in 5.34b the green dashed lines show the 13.5 and 27 day periods.

This result gives evidence that the crossing of the HCS structure is correlated with fluctuations in the daily proton flux except near the maximum of the solar activity cycle. This is a very interesting result because it might inform on the relative impact of the crossing of the HCS in relation to diffusion in the context of propagation of cosmic-rays through the heliosphere. Further investigation would be required specially using other variables such as the other directions of the magnetic field from ACE, solar wind direction and speed, among other solar observables.

One other possible cause for the periodicity would be the interaction with the fast solar wind emanating from the polar regions of the sun [60]. This wind is limited to the higher polar regions of the Sun so it flows closer to Earth's equatorial position when the tilt angle is high. This limits the effect it will have on cosmic-ray propagation near Earth during the quieter periods of the solar activity cycle while the tilt angle is small. The fast solar wind still plays a role in general propagation[60] but we expect that its effects will be relatively limited when compared to the direct measurements made by ACE which will also include the effect of fast solar wind during the higher activity periods and, during those periods, we've found a lower correlation with solar rotation (see Figure 5.38).

The cross-wavelet spectrum for these two time-series also presents a dependence with the chosen rigidity interval. At the lowest rigidity interval [1.00-1.16] GV, there seems to only be one periodicity present, a near 30-day periodicity. Interestingly, it is non-existent for the very beginning of the series and it only gains significance from the middle of 2014 to the end of 2018. This result is very interesting because it shows a clear time and rigidity dependence between the correlation of the proton and the IMF near Earth. One explanation could come from the energy dependence of drift velocities for different solar magnetic field polarities, as

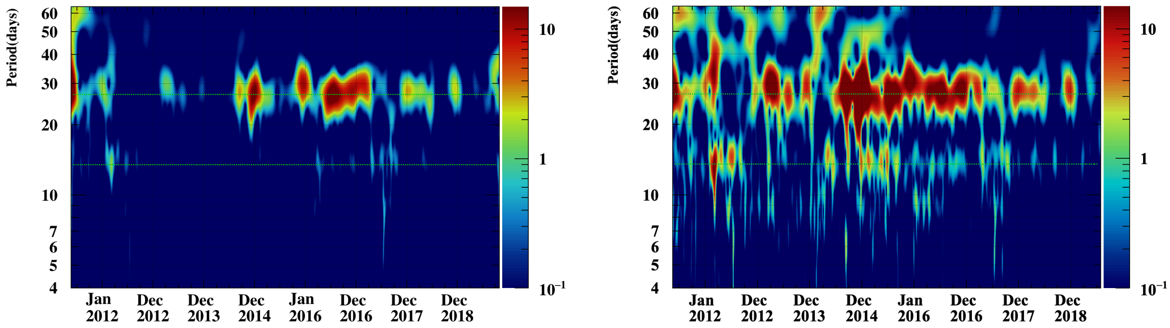

(a) Rigidity [1.00-1.16] GV

(b) Rigidity [5.90-6.47] GV

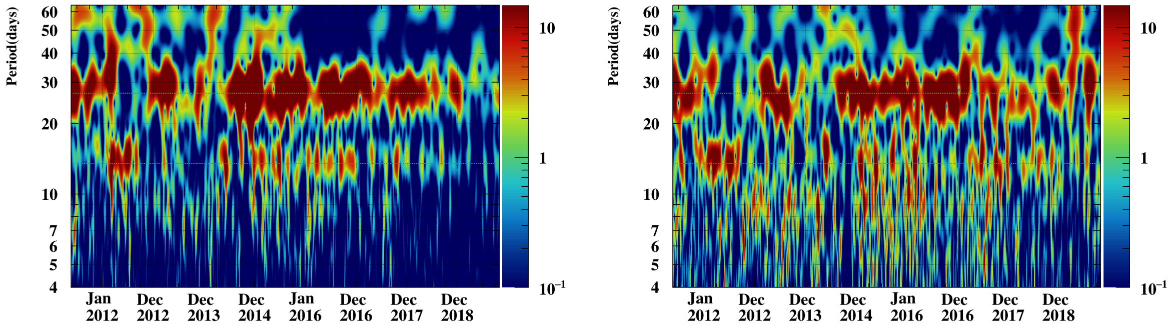

(c) Rigidity [16.60-18.00] GV

(d) Rigidity [80.50-86.50] GV

Figure 5.37: Local cross-wavelet power spectrum between for AMS-02's daily proton flux [116] and ACE IMF on Earth-Sun direction, for the entire AMS flux period, normalized to the product of the yearly variance of both series ($\sigma_\varphi \, \sigma_{IMF}$). The vertical axis shows the Fourier period (in days) while the horizontal axis shows the date. The red shaded area shows the *cone of influence*, region in which edge effects are relevant. Horizontal green dashed lines represent 13.5 and 27 day periods.

we've explored in subsection 2.4.5. Lower energy particles will be relatively more impacted by drift organized motion, specially by the HCS drift velocity which is highly dependent on the particle's Larmor radius. The lower the rigidity, the smaller the gyroradius which means that the particle is more likely to be *dragged* along the HCS structure. Notably, during Solar Cycle 24, the polarity was negative, meaning that protons near the equatorial plane will suffer drift motions outwards from the equatorial plane (where Earth and AMS is located) while protons at the equatorial plane will *dragged* towards the Sun. This can cause a drop in the measurement of protons at lower energies relative to after the magnetic reversal as ocurred (after 2014) and, additionally, move the average trajectory of the the proton cosmic-ray away from the equatorial plane where the HCS would be most relevant and thus, losing the 27-day periodicity caused by the interaction with the HCS.

The modelling of propagation parameters from observation of flux variations is a path that has proven fruitful in the past as can be seen in Tomassetti et al., (2018)[134] and Tomassetti et al., (2019)[135], among others works in the field.

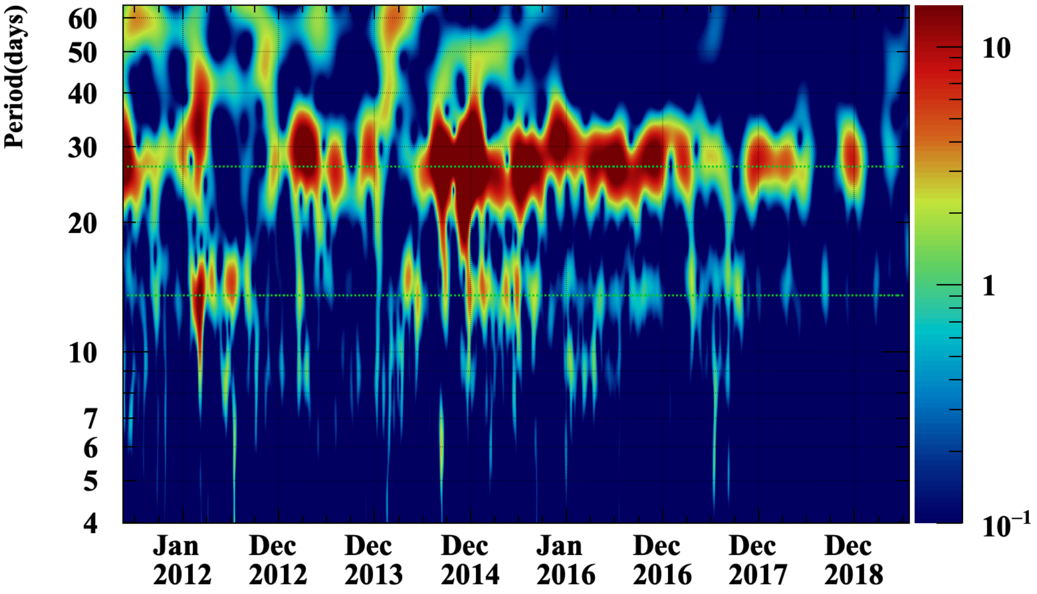

Figure 5.38: Local cross-wavelet power spectrum between for AMS-02's daily proton flux [116] and ACE IMF on Earth-Sun direction, for the entire AMS flux period, normalized to the product of the yearly variance of both series ($\sigma_\varphi \sigma_{IMF}$), for the rigidity bin [5.90-6.47] GV. The vertical axis shows the Fourier period (in days) while the horizontal axis shows the date. The red shaded area shows the *cone of influence*, region in which edge effects are relevant. Horizontal green dashed lines represent 13.5 and 27 day periods.

5.8 Conclusions and Outlook

We introduced a time and frequency domain tool called Wavelet Transform which we used to investigate the periodicities in AMS-02's daily proton flux.

We showcased the presence of 13.5 and 27 day periodicities and their relative significance as a function of time and rigidity.

We modelled our noise floor as red-noise and estimated its Fourier power spectrum for each of our time-series, using it to determine significance levels of the signals observed in the average wavelet transform.

We examined the changes in periodicity that occurred during 2017 and found correlations of the general flux dip with a spike in solar activity.

Additionally we examined the time and energy dependence of the wavelet transform of the Interplanetary Magnetic Field measured by the ACE instrument. We estimated the cross-wavelet power spectrum between the IMF and the daily proton flux, correlating some of the structures found in the plot as being caused by magnetic drift motion protons endure as they traverse the solar system.

6

Interpretation of results under Solar Modulation

As we've shown in previous chapters, the cosmic-ray flux presents very distinct time signatures which appear to be related to solar activity. In this chapter we will interpret these variations under solar modulation models by exploring data from different cosmic-ray experiments [136, 137, 138, 139, 108], from solar observatories and solar data analysis centres, namely *Royal Observatory of Belgium*[1], *Wilcox Solar Observatory*[2] and *Sodankyla Geophysical Observatory*[3]

We will show the correlation between the different solar observables and the cosmic-ray flux and introduce the concept of a time-lag between these variables. We will also show published results on this topic and will report on it in detail.

Given the availability of 27-day binned solar data and given the models we will use to explain the cosmic-ray flux, we will be focusing mainly on this periodicity and not on the daily variations of these variables as we did on the previous chapter.

6.1 Solar Observables

As we've seen on chapter 2, the solar activity cycle is a very complex phenomenon in which the Sun alters itself and the heliosphere drastically, presenting a set of heavily correlated variables which we can use to tap into some of the parameters of cosmic-rays propagation in the heliosphere and study it in a time-dependent manner. Some of these variables can be seen in Figure 6.1.

Using long-term observations of some of these variables and some of the tools we've developed, we can clearly see that their variation is deeply connected to the solar activity cycleFigure 6.2, making our main goal not only to find the correlation between these variables and the flux but also which ones are most correlated with it and if we can find significantly explicative relationships between these variables and specific parameters of Parker's transport equation in order to on simulate and predict the cosmic-ray flux.

While Figure 6.2b shows a clear peak near the 11 year period, Figure 6.3 shows the absence of a 27 day period. As expected, sunspot numbers are heavily modulated by the solar activity cycle but no meaningful Bartel rotation periodicity was found.

---

[1] `http://www.sidc.be`

[2] `http://wso.stanford.edu`

[3] `https://cosmicrays.oulu.fi/`

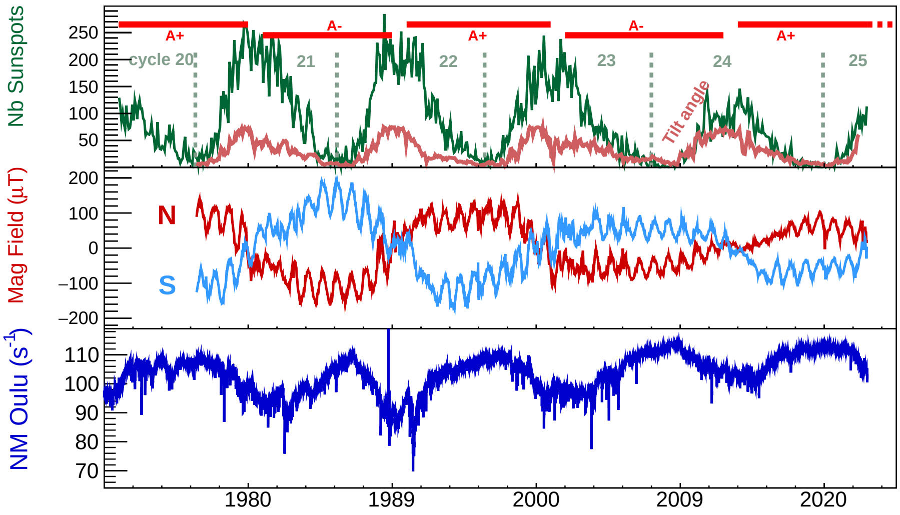

Figure 6.1: Comparison between sunspot number, tilt angle, Sun's polar field strength and Oulu neutron monitor rate[140, 141].

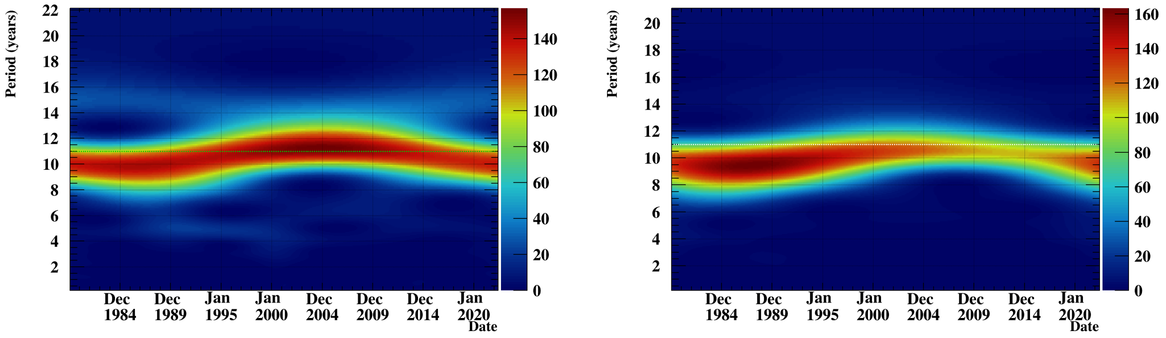

(a) Solar magnetic dipole tilt angle.

(b) Sunspot number.

Figure 6.2: Local wavelet power spectrum of 27-day resolved solar variables from 1980 to 2022. Tilt angle taken from *Wilcox Solar Observatory*2 and sunspot number taken from *Royal Observatory of Belgium*1.

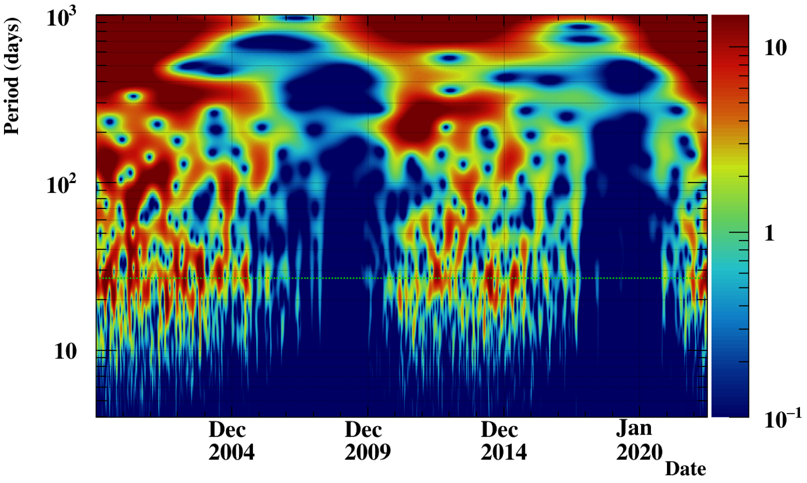

Figure 6.3: Local wavelet power spectrum of daily sunspot number from *Royal Observatory of Belgium*1 from 2000 to 2022.

6.2 The Force-Field Approximation

In 1968, Gleeson and Axford proposed a solution to the cosmic ray transport equation, the **Force-Field** solution. Due to its simplicity, this is the most used approximation to describe the Solar modulation phenomenon and comes in the shape of a transformation over the Local Interstellar Spectrum (LIS). It takes the final form of

$$\frac{J(r,E)}{E^2-E_0^2}=\frac{J_{\mathrm{LIS}}(E+\Phi)}{(E+\Phi)^2-E_0^2}, \tag{6.1}$$

where J is the observed intensity, E is the total energy and Φ is the so-called Force-Field energy loss that particles suffer as they propagate inwards into the heliosphere.

In the literature, the most commonly used modulation parameter is not Φ but ϕ which comes from $\phi = \Phi/(Ze)$. Since Φ represents an energy lost, the ϕ represents a modulation potential. In this view, Gleeson and Urch, in 1973, re-derived the Force-Field solution in a more transparent way, which will be presented here.

6.2.1 The Local Interstellar Flux

The Solar modulation of Galactic cosmic-rays is an initial-value problem, one must somehow know what the Galactic cosmic ray spectrum is before we can estimate how the Solar magnetic field affects it. The initial spectra used in the solutions to follow were those introduced by Webber and Higbie. They were created using a Monte-Carlo Diffusion model and a Leaky Box Model for the propagation in the Galaxy and based on data provided from the Voyager 1 experiment (as can be seen in Figure 6.4). Their forms are given by

$$\begin{aligned} J_{\mathrm{LIS}}^{\mathrm{Proton}}(T)&=\frac{dN}{dT}=\frac{18.9\left(\frac{T}{1\,\mathrm{GeV}}\right)^{-2.79}}{1+6.75\left(\frac{T}{1\,\mathrm{GeV}}\right)^{-1.22}+1.30\left(\frac{T}{1\,\mathrm{GeV}}\right)^{-2.80}+0.0087\left(\frac{T}{1\,\mathrm{GeV}}\right)^{-4.32}},\\ J_{\mathrm{LIS}}^{\mathrm{Helium}}(T)&=\frac{dN}{dT}=\frac{0.99\left(\frac{T}{1\,\mathrm{GeV}}\right)^{-2.77}}{1+4.14\left(\frac{T}{1\,\mathrm{GeV}}\right)^{-1.09}+0.65\left(\frac{T}{1\,\mathrm{GeV}}\right)^{-2.79}+0.0094\left(\frac{T}{1\,\mathrm{GeV}}\right)^{-4.20}}. \end{aligned} \tag{6.2}$$

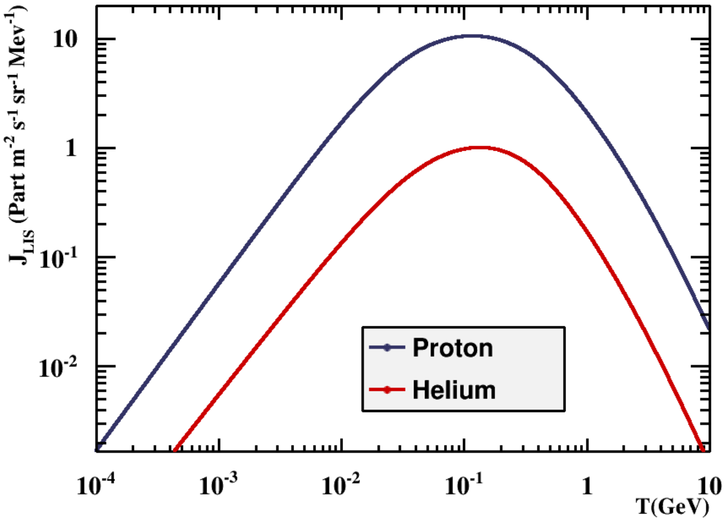

Figure 6.4: Local Interstellar primary cosmic ray flux for protons and helium nuclei [144].

6.2.2 Force-Field Solution

Starting from Parker's transport equations

$$\frac{\partial f}{\partial t} + \nabla \cdot (\vec{V} f - \mathbf{k} \cdot \nabla f) - \frac{1}{3}(\nabla \cdot \vec{V}) \frac{\partial f}{\partial \ln p} = q \,, \tag{6.3}$$

this solution comes from assuming that the Solar wind is constant, the diffusion coefficient is isotropic, the solution is spherically symmetric, that there is no drift and, in addition, that the solution is stationary ($\frac{\mathrm{d}f}{\mathrm{d}r} = 0$) and steady-state, which leads to

$$\frac{VP}{3} \frac{\partial f}{\partial P} - k \frac{\partial f}{\partial r} = 0. \tag{6.4}$$

The solutions of 6.4 are characteristic curves where f is constant in the (r, P) plane since

$$\frac{\mathrm{d}f}{\mathrm{d}r} = \frac{\partial f}{\partial r} + \frac{\partial P}{\partial r} \frac{\partial f}{\partial P} = 0, \tag{6.5}$$

which in turn implies,

$$\frac{\partial P}{\partial r} = \frac{VP}{3k}. \tag{6.6}$$

If $k = k_0 \beta P$, which is one result of QLT, we get

$$\frac{\partial P}{\partial r} = \frac{VP}{3k_0 \beta P}, \tag{6.7}$$

or

$$\beta \frac{\partial P}{\partial r} = \frac{V}{3k_0}, \tag{6.8}$$

which amounts to

$$\frac{\partial E}{\partial r} = \frac{V}{3k_0}, \tag{6.9}$$

since $\frac{\mathrm{d}E}{\mathrm{d}P} = \beta$. Integrating both side in dr from some distance r up to the heliosphere (r_H), we get

$$E(r = r_H) - E(r) = \Phi_{SM} \frac{r_H - r}{r_H - 1(AU)}, \; \Phi_{SM} = \int_{1\,AU}^{r_H} \frac{V}{3k_0} \,\mathrm{d}r = V \frac{r_H - 1}{3k_0}. \tag{6.10}$$

Finally, since f is constant along the characteristic curve

$$f(1AU, E(r_H) - \Phi_{SM}) = f(r_H, E(r_H)) \implies \frac{J_T(1AU, E(r_H) - \Phi_{SM})}{(E(r_H) - \Phi_{SM})^2 - m^2)} = \frac{J_T(r_H, E(r_H))}{E^2(r_H) - m^2}, \tag{6.11}$$

or, rearranging the terms and making them clearer, so that the flux becomes a function of energy measured in Earth instead of original energy,

$$J_T(1\,AU, E) = J_{\mathrm{LIS}}(E + \Phi_{SM}) \frac{E^2 - m^2}{((E + \Phi_{SM})^2 - m^2)}. \tag{6.12}$$

Typical values range from 0.2 GeV to 1.3 GeV [145]. It is important to emphasize that this is only valid in the case where $k \propto P$.

This analytical solution is a good way to parametrize the problem in broad terms as it describes the entire Solar modulation phenomenon as a simple mean energy loss suffered by Galactic cosmic rays as they traverse the heliosphere. This simple solution does not take into account the particular shape of the magnetic field and assumes a diffusion coefficient proportional to $k \propto P$. In some of our recent work [134, 135], using observations cosmic-ray flux observations published by AMS[108], we have shown that in fact this is a very good approximation to the diffusion coefficient model.

Since Parker's transport equation does not have an analytical solution in its most complex form (taking into account complex drifts, diffusion coefficients and the general shape of the magnetic field), the only way to properly include all effects is to solve it numerically or stochastically, which will be explored in the sections to come.

6.2.2.1 Comparison with Sunspot number

Despite the simplicity of this approach to solving Parker's transport equation, we can extract some information from it. From Equation 6.10 we see a clear relation between the modulation potential and the inverse of the diffusion coefficient. Given that the modulation potential can be estimated from ground-based neutron monitor measurements[145, 146, 147], we can explore the different solar variables and inspect their correlation to the modulation potential and, indirectly, to the diffusion coefficient.

We found such a relationship between the logarithm of the sunspot number and the inverse of the solar modulation potential ϕ_M (as can be seen in Figure 6.5) and, more interestingly, we found evidence of a time delay between the two time series of about 8 months. The delay was found by scanning the delay between the two time-series until the correlation was at an absolute maximum.

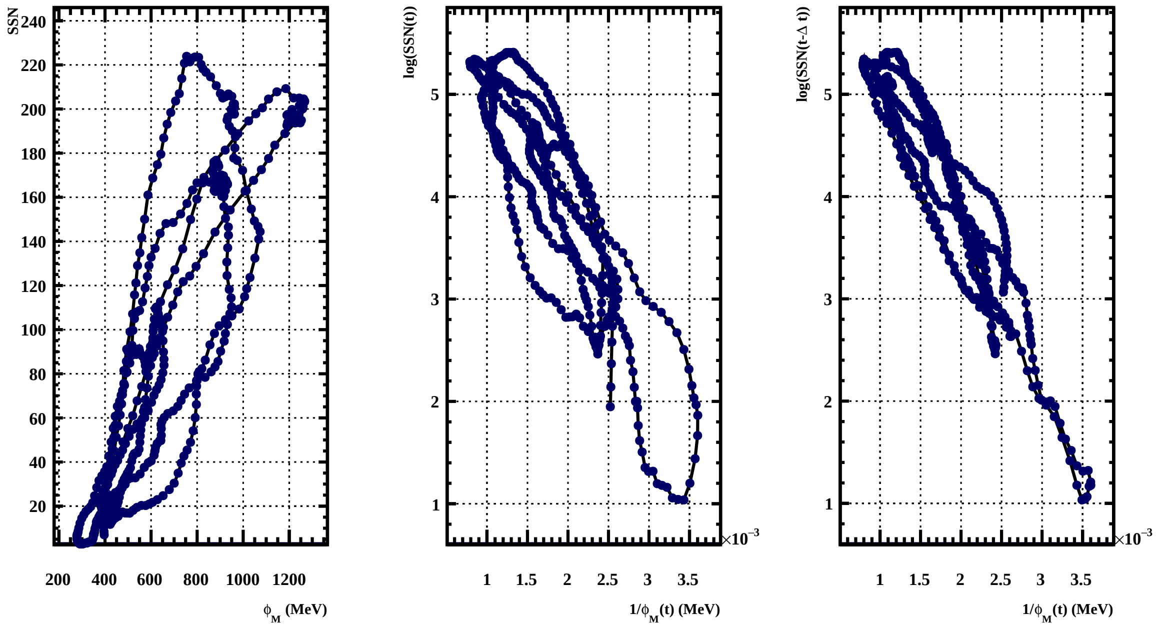

Figure 6.5: Correlations between modulation potential ϕ_M and the number of sunspots. (left) Scatter plot of the sunspot number and modulation potential ϕ_M. (center) Scatter plot of the logarithm of the sunspot number and the inverse of ϕ_M. (right) Scatter plot of the logarithm of the sunspot number time-series, delayed by 8 months, and the inverse of ϕ_M. Solar modulation potential ϕ_M was taken from *Sodankyla Geophysical Observatory*3 and sunspot number was taken from *Royal Observatory of Belgium*1.

6.3 Stochastic Differential Equations

Given the clear indications of the relationship between solar observables and transport parameters, we sought to link cosmic-ray propagation parameters inside the heliosphere through solving Parker's equation in a time-dependent fashion.

Once more, we will start from the source-less Parker's transport equation,

$$\frac{\partial f}{\partial t} + \nabla \cdot (\vec{V} f - \mathbf{k} \cdot \nabla f) - \frac{1}{3}(\nabla \cdot \vec{V}) \frac{\partial f}{\partial \ln p} = 0 \,. \tag{6.13}$$

Parker's transport equation is a Fokker-Plank equation which can be rewritten as a set of Stochastic Differential Equations (SDE)[148, 149]. One of the great appeals of SDE lies in the ease of plugging in propagation parameter models, their numerical stability and their scalability since they are trivially parallelizable.

Generally, SDE are defined[150] as any equation that can be cast into the general form

$$\frac{dx(t)}{dt} = a(x,t) + b(x,t)\,\zeta(t)\,, \tag{6.14}$$

where $a(x,t)$ and $b(x,t)$ are continuous functions which encode part of the underlying physical processes and $\zeta(t)$ represents a rapidly varying stochastic function[150]. The elements on the right-hand side of this formulation are usually referred to as *drift* or deterministic term for the first term and *diffusive* term for the second. A very good review of SDE can be found in Strauss and Effenberger, (2017)[150] and a good review on the underlying stochastic processes can be found in Lemons, (2002)[151].

Due to the nature of our problem, we will be considering SDE of the form

$$dx = a(x,t)\,dt + b(x,t)\,dW(t)\,, \tag{6.15}$$

where $W(t)$ is the Wiener process which can be integrated[150] and solved iteratively by assuming the form

$$x(t+\Delta t) = x(t) + a(x,t)\,\Delta t + b(x,t)\,\Delta W(\Delta t) = x(t) + a(x,t)\,\Delta t + b(x,t)\,\sqrt{\Delta t}\,\Lambda(t)\,, \tag{6.16}$$

where $\Lambda(t)$ is a Gaussian distributed random number with mean zero and standard deviation of one[92, 150]. This will form the basis of what we will call the trajectory of the *pseudo-particle*, which actually represents the temporal evolution of an ensemble of real-particles, i.e. a density element in phase-space.

This can be generalized for the n-dimensional problem which assumes the following formulation

$$dx_i = a_i(x_i,s)\,ds + \sum_{j=1}^{n} b_{ij}(xi,s)\,dW_i(s)\,, \tag{6.17}$$

, where a_i is an n-dimensional vector, b_{ij} is a $n \times n$ matrix and s is the *time-marching* coordinate which we changed from t to indicate that it can be either advancing (forward) in time our reversing (backwards). The need to define this s time-marching coordinate because we will be interested in solving the backwards in time the SDE for Parker's transport equations.

The set of SDE to solve the 1-dimensional forward-in-time Parker equation can be written[152, 92] as

$$\begin{aligned} \Delta r &= \left(-V + \frac{2\,k_{rr}}{r}\right)\Delta t + \sqrt{2\,k_{rr}\,\Delta t}\,d\omega_r\,, \\ \Delta T &= \frac{2\,V}{3\,r}\,\frac{T^2 + 2\,T\,m}{T+m}\Delta t\,, \end{aligned} \tag{6.18}$$

where r is the radial coordinate, m is the particle mass, T is the kinetic energy and V is the constant radial solar wind speed. Time coordinate t will be incremented by Δt at each iteration. In order to solve this system we begin with a distribution of cosmic-rays (which is one of our boundary conditions) and we propagate a number (N) of pseudo-particles according to that distribution for sufficiently large time and we measure the amount of pseudo-particles that are near Earth. This results in a 2-dimensional distribution in both r and T coordinates. Usually we bin our result after a long enough time in order to group data and select the location we will use to represent our solution which is, in this case for Earth $r = 1$AU.

6.3.1 Solving Parker's Equation with SDEs

When using SOLARPROP we will be solving the 2-dimensional backwards-in-time SDE for Parker's transport equation, including drifts and the HCS structure we discussed in chapter 2. SOLARPROP incorporates several models and we will be using a modified one.

The set of equations we solved, as proposed by Kappl, (2016)[92] are the following:

$$\begin{aligned}
\Delta r &= \left(-V - V_{D,r} - V_{HCS,r} + \frac{1}{r^2}\frac{\partial r^2 k_{rr}}{\partial r}\right)\Delta t + \sqrt{2\, k_{rr}\, \Delta t}\, d\omega_r \,, \\
\Delta\theta &= \left(-\frac{V_{D,\theta}}{r} + \frac{1}{r^2 \sin\theta}\frac{\partial \sin\theta k_{\theta\theta}}{\partial\theta}\right)\Delta t + \frac{\sqrt{2\, k_{\theta\theta}\, \Delta t}}{r}\, d\omega_\theta \,, \\
\Delta T &= \frac{2\, V}{3\, r}\,\frac{T^2 + 2\, T\, m}{T + m}\Delta t \,,
\end{aligned} \tag{6.19}$$

where, as we've seen before in section 2.4, the diffusion tensor has to be rewritten in the appropriate coordinate system

$$\begin{aligned}
k_{rr} &= k_{\parallel}\, \cos^2\psi + k_{\perp}\, \sin^2\psi = \frac{1}{1+\Gamma^2}\left(k_{\parallel} + k_{\perp}\Gamma^2\right) \\
k_{\theta\theta} &= k_{\perp}
\end{aligned} \tag{6.20}$$

where ψ is defined as the usual spiral angle (see Equation 2.26) related to the Parker spiral magnetic field,

$$\tan\psi = \Gamma = \frac{\Omega\, r \sin\theta}{V} \,.$$

All we need now is to define the models we will be using for diffusion and drift:

$$\begin{aligned}
k_{\parallel} &= \begin{cases} k_0 \frac{|A|}{3\,B}\beta \cdot 0.1 = k_0 \beta \frac{1}{30}\frac{r^2}{\sqrt{1+\Gamma^2}} & P < 0.1\text{GV} \\ k_0 \frac{|A|}{3\,B}\beta P = k_0 \beta \frac{\sqrt{T^2+2Tm}}{3\,|Z|}\frac{r^2}{\sqrt{1+\Gamma^2}} & P \geq 0.1\text{GV} \end{cases} \,, \\
k_{\perp} &= 0.02\, k_{\parallel} \,,
\end{aligned} \tag{6.21}$$

which modifies our SDE derivates in the following manner:

$$\begin{aligned}
\frac{1}{r^2}\frac{\partial r^2 k_{rr}}{\partial r} &= \frac{2}{r}\left(k_{rr} + \left(k_{\perp} - k_{\parallel}\right)\frac{\Gamma^2}{\left(1+\Gamma^2\right)^2} + k_{rr}\frac{2+\Gamma^2}{2\,\left(1+\Gamma^2\right)}\right) \,, \\
\frac{1}{r^2 \sin\theta}\frac{\partial \sin\theta k_{\theta\theta}}{\partial\theta} &= \frac{1}{1+\Gamma^2}\frac{k_{\perp}}{r^2}\cot\theta \,.
\end{aligned}$$

All that is left is the need to define the drifts. Once more we will follow Kappl, (2016)[92] and present the drifts as follows:

$$\begin{aligned}
V_{D,r} &= q\frac{2\beta r}{3A}\sqrt{T^2 + 2Tm}\, \cot\theta\, \frac{\Gamma}{\left(1+\Gamma^2\right)^2}\, f(r,\theta,\alpha_{HCS}) \,, \\
V_{D,\theta} &= q\frac{2\beta r}{3A}\sqrt{T^2 + 2Tm}\, \frac{\Gamma\left(2+\Gamma^2\right)}{\left(1+\Gamma^2\right)^2}\, f(r,\theta,\alpha_{HCS}) \,, \\
V_{HCS,r} &= q\frac{\beta r}{3A}\sqrt{T^2 + 2Tm}\, \frac{\Gamma}{1+\Gamma^2}\, f'(r,\theta,\alpha_{HCS}) \,,
\end{aligned} \tag{6.22}$$

where, for computational reasons, the wavy HCS can be modelled as a smooth functions f and its derivative f', as proposed by Potgieter and Moraal, (1985)[82]:

$$f = \frac{1}{\alpha_{HCS}}\arctan\left(\left(1 - \frac{2\theta}{\pi}\right)\tan\alpha_{HCS}\right) \,, \tag{6.23}$$

$$f' = -\frac{2}{\pi\alpha_{HCS}}\frac{\tan\alpha_{HCS}}{1 + \left(1 - \frac{2\theta}{\pi}\right)^2 \tan^2\alpha_{HCS}} \,, \tag{6.24}$$

$$\alpha_{HCS} = \arccos\left(\frac{\pi}{2\theta_{1/2}} - 1\right) \,, \tag{6.25}$$

$$\theta_{1/2} = \frac{\pi}{2} - \frac{1}{2}\sin\left(\alpha + \frac{2R_L}{r}\right) = \frac{\pi}{2} - \frac{1}{2}\sin\left(\alpha + \frac{\sqrt{T^2+2Tm}}{|Z|}\frac{2r}{|A|\sqrt{1+\Gamma^2}}\right) \,. \tag{6.26}$$

From this set of equations and models, we can delineate the fundamental solar model parameters for our simulation: the scaling factor of the diffusion tensor k_0 from Equation 6.21 and the tilt angle from Equation 6.26. As we saw in subsubsection 6.2.2.1 we will be introducing a parametrization of the diffusion coefficient but we can use the observed tilt angle since it plugs in directly into the system. Investigations on the nature of the diffusion coefficient are still ongoing [88, 134, 75, 77, 76] but, as we will be reporting on the next6.4 section, these two variables, sunspot number and tilt angle, were enough to build a time-dependent simulation of the cosmic-ray flux and to estimate a delay between it and these solar observables.

6.4 Observation of a Time-Lag

As we've shown throughout this work, the effect of solar modulation on Galactic cosmic rays is a time-dependent phenomenon that is caused by the transport of these particles through the magnetized plasma of the heliosphere.

In this section we will present the work done on Tomassetti et al., (2017)[153] which presents new calculations of CR fluxes near-Earth that account for the dynamics of CR modulation in the expanding heliosphere and expand on the understanding of the correlation between solar parameters and the CR fluxes. Using a large collection of modulated and interstellar CR data collected in space, we have constructed a predictive and measurement-validated model of solar modulation which depends only on direct solar activity observables: the sunspot number (SSN) and the tilt angle of the heliospheric current sheet (HCS). We will also present the extension of this work as was detailed in Orcinha et al., (2019)[154].

Using a data-driven model of cosmic-ray transport in the heliosphere, in combination with a large collection of data, we showed evidence for a eight-month time lag between observations of solar activity and measurements of cosmic-ray fluxes in space. As we will discuss, this result enables us to forecast the cosmic ray flux at Earth well in advance by monitoring solar activity. We also compare our predictions with some multi-channel measurements of cosmic rays operated by the AMS experiment in space.

6.4.1 Physical context

New-generation experiments of cosmic ray (CR) detection have reached an unmatched level of precision that is bringing transformative advances in astroparticle physics [49, 41]. Along with calculations of CR propagation in the galaxy, the interpretation of the data requires detailed modelling of the so-called *solar modulation effect*. Solar modulation is experienced by all CR particles that enter the heliosphere to reach our detectors near Earth. Inside the heliosphere, CRs travel through a turbulent magnetized plasma, the solar wind, which significantly reshapes their energy spectra. This effect is known to change with time, in connection with the quasi-periodical 11-year evolution of the solar activity, and to provoke different effects on CR particles and antiparticles [155].

Observationally, an inverse relationship between solar activity (often monitored by the number of solar sunspots) and the intensity of CRs at Earth is known for a long time. The effect of solar modulation in the low-energy CR spectra ($E \lesssim$ GeV) is measured by several experiments [156, 157]. Solar modulation is caused by a combination of basic particle transport processes such as diffusion, convection, adiabatic cooling, or drift motion, yet the underlying physical mechanisms and their associated parameters remain under active investigation.

Solar modulation models are dependent on two crucial factors:

(i) precise knowledge of the interstellar spectra (LIS) of CRs outside the heliosphere;

(ii) availability of time-series of CR data on different species.

Recent accomplishments from strategic space missions have enabled us to make significant progress in this field. The entrance of Voyager-1 in the interstellar space provided us with the very first LIS data on CR protons and electrons [158, 159]. Long-duration space experiments PAMELA (on orbit since 2006) and AMS (since 2011) have been releasing a continuous stream of monthly-resolved data on CR particles and antiparticles [160, 161, 108, 47].

These measurements add to a large wealth of low-energy CR data collected in the last decades by space missions CRIS/ACE [133] IMP-7/8 [162], *Ulysses* [163], and more recently EPHIN/SOHO [139], as well as from ground data provided continuously by the neutron monitor (NM) worldwide network [140, 141].

6.4.2 Methodology

The transport of CRs in heliosphere is described by the Parker equation for the omni-directional phase space density $\psi(t,p,\boldsymbol{r})$ expressed as function of time t, momentum p, and position $\boldsymbol{r}$ [74]:

$$\frac{\partial\psi}{\partial t} = -(\boldsymbol{V}+\boldsymbol{v_d})\cdot\nabla\psi + \nabla\cdot(\boldsymbol{K}\cdot\nabla\psi) + \frac{1}{3}(\nabla\cdot\boldsymbol{V})\frac{\partial\psi}{\partial\ln p} \tag{6.27}$$

The various terms represent convection with a solar wind of speed $|\boldsymbol{V}| \cong 400\,\mathrm{km/s}$, drift motion with average speed $\boldsymbol{v_d}$, spatial diffusion with tensor $\boldsymbol{K}$, and adiabatic momentum losses.

We simulated this physical process in a minimal 2D description using $\boldsymbol{r} = (r,\theta)$, radius and heliolatitude [164]. In terms of diffusion coefficient, the parallel component was defined as

$$K_{\parallel} = \kappa^0 \frac{10^{22}\beta p/\mathrm{GeV}}{3B/B_0}\,, \tag{6.28}$$

in units of cm^2/s, where we have factorized an adimensional scaling factor, κ^0, of the order of unity. The perpendicular component is $K_{\perp} \cong 0.02\,K_{\parallel}$ [165].

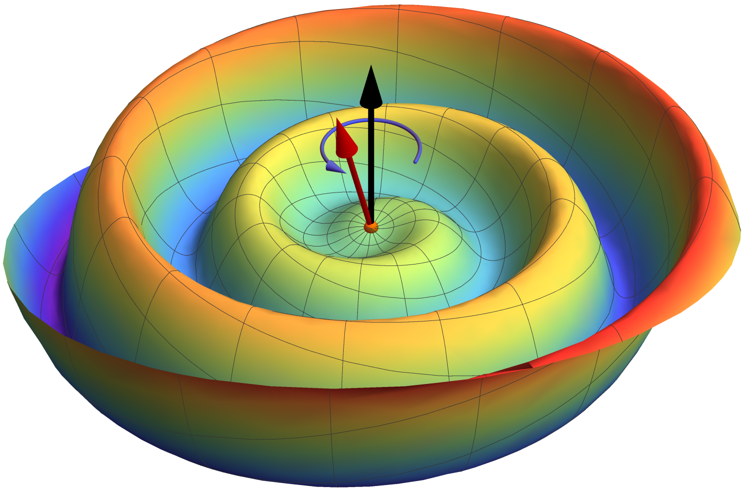

Figure 6.6: Graphical representation of the heliospheric current sheet in a Parker solar wind model. The black arrow represents the axis of rotation and the red one the magnetic dipole direction. Tilt angle is then defined as the angle between these two vectors.

The regular solar magnetic field (HMF) is modelled using the usual Parker structure,

$$B = \frac{B_0 A}{r^2}\sqrt{1+\Gamma} \tag{6.29}$$

$$\Gamma = (\Omega r/V)\sin\theta\,, \tag{6.30}$$

where $\Omega = 2.866 \cdot 10^{-6}\,\mathrm{rad\,s^{-1}}$ is the angular rotation of the Sun, $B_0 \cong 3.4\,\mathrm{nT\,AU^2}$ is the field intensity at $r_0 = 1\,\mathrm{AU}$, and $A = \pm 1$ represents the magnetic polarity cycle of the Sun. The polarity is positive (negative) when the HMF points outward (inward) in the north hemisphere.

In this model we account for gradient and curvature drift effects. In particular, drift is important across the wavy layer of the HCS, *i.e.* the surface where magnetic polarity changes from north to south, the angular extension (and waviness) of which is described by the tilt angle α (see Figure 6.6). The drift velocity components v_r and v_θ are both proportional to $qA\frac{2\beta r p}{3B_0}$, so that the sign of $\boldsymbol{v_d}$ depends on the product qA [155].

With this setting, we compute the CR propagation from the termination shock (TS) to Earth's orbit using the stochastic differential equation approach of [92]. This method consists of a backwards-in-time propagation of a large number of pseudo-particles from Earth to the boundaries [166, 167, 168]. For a given particle type, steady-state solutions of Equation 6.27 ($\partial\psi/\partial t = 0$) are then obtained by sampling. In our model we disregard re-acceleration effects occurring at the TS or modulation in the heliosheath [169, 170].

The LIS fluxes J^{IS} were calculated using an improved model of CR acceleration and propagation [51, 171, 172], being well constrained by Voyager-1 and AMS data [159, 17]. Positron LIS relies on secondary production calculations so it has larger uncertainties [172].

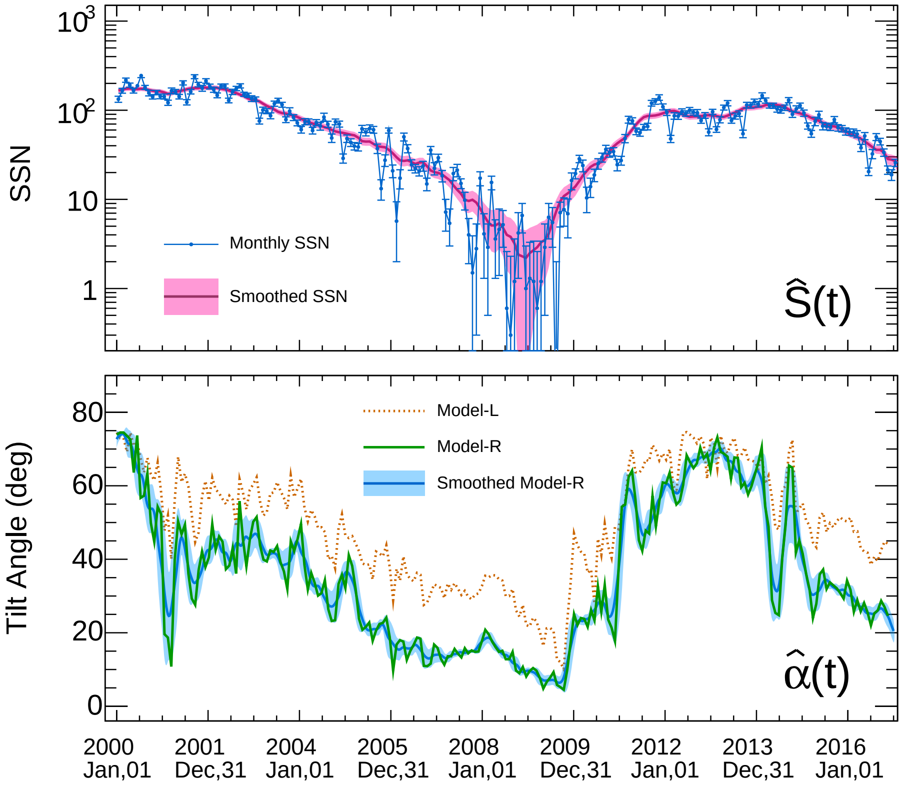

Figure 6.7: Reconstruction of the sunspot number ($\hat{S}(t)$) and tilt-angle of the heliospheric current sheet ($\hat{\alpha}(t)$) as function of time. Figure taken from [153].

The role of positive and negative particles interchanges with polarity as can be seen in Figure 6.11. This phenomenon is due to sign-dependence of the the drift motion of particles. Depending on solar polarity CR particles and antiparticles sample different parts of the heliosphere. Along with qA, the interplay of the various physics processes depends on the levels of HCS waviness (see Figure 6.6) and HMF irregularities, that are here parametrized by α and κ^0. Tilt-angle measurements $\hat{\alpha}$ are provided on 10-day basis from the *Wilcox Solar Observatory*2 using two reconstruction procedures: the "classic" model-L, and the improved model-R

(both shown in Figure 6.7). The latter was used for this work [69, 173]. A basic diagnostic for the HCS turbulence level is the manifestation of solar sunspots [174], so that SSNs and κ^0 are related each other [175, 164]. We used the the monthly-series of SSNs provided by the *Royal Observatory of Belgium*1. Both α and SSN were smoothly interpolated in order to create the functions $\hat{\alpha}$ and $\hat{S}$ For diffusion we adopted a simple two-coefficient relation $\kappa^0 \equiv a + b\log\left(\hat{S}\right)$.

The temporal behaviour of these quantities, shown in Figure 6.7 from 2000 to 2017, is at the basis of the time-dependent nature of solar modulation. In practice, the problem is modelled under a *quasi-steady* fashion, *i.e.*, by providing a time-series of steady-state solutions corresponding to a time-series of input parameters. Due to the nature of the phenomenon, a finite amount of time is needed, in fact, for the properties observed in the solar corona to be transported in the outer heliosphere by the plasma. This motivated us to introduce a parameter ΔT in our calculation, describing a time-lag between the solar activity indices of Figure 6.7 and the medium properties of the modulation region, *i.e.*, the spatial region effectively sampled by CRs. Evidence for a lag of $\sim$6-12 months have been previously reported in NM-based studies [176, 177, 178, 179, 180, 181].

Our model is then specified by three free parameters only, a, b, and ΔT, that we constrain using a large amount of data. We use monthly-resolved proton data from the PAMELA experiment [160] collected between July 2006 and January 2010, and data from the EPHIN/SOHO space detector [139], yearly-resolved between 2000 and 2016. We also include data from the BESS Polar-I (Polar-II) mission from 13 to 21 December 2004 (from 23 December 2007 to 16 January 2008) [137, 138]. These measurements are given in terms of time-series of energy spectra $\hat{J}_{j,k} = \hat{J}(t_j, E_k)$, where each spectrum is a *snapshot* of the CR flux near-Earth at epoch t_j. Calculations $J(t_j, E_k)$ are performed using retarded functions of the physics inputs

$$\begin{aligned} \alpha_j &= \hat{\alpha}(t_j - \Delta T) \\ \kappa^0_j &= a + b\log\left(\hat{S}(t_j - \Delta T)\right) . \end{aligned}$$

We then build a global χ^2-estimator:

$$\chi^2(a, b, \Delta T) = \sum_{j,\,k} \left[\frac{J(t_j, E_k; a, b, \Delta T) - \hat{J}_{j,k}}{\sigma_{j,k}} \right]^2 . \tag{6.31}$$

The quantity $\sigma_{j,k}$ includes experimental errors in the data and model uncertainties due to finite statistics of the pseudo-particles simulation. The following sources of systematic uncertainties are also accounted: (i) uncertainties in the LIS, from the constraints provided by Voyager-1 and AMS data; (ii) uncertainties on $\hat{\alpha}(t)$, from the discrepancy between L and R models and from the smoothing procedure; (iii) uncertainties on $\hat{S}(t)$ from the smoothed SSN variance, see Figure 6.7. The free parameters are estimated by means of standard minimization techniques.

6.4.3 Results

The global fit has been performed to 3993 proton data points collected between 2000 and 2012 (in $A < 0$ conditions) at kinetic energy between 0.08 and 50 GeV. The best-fit parameters are $\hat{a}$ =3.88 ± 0.87, $\hat{b}$ =-1.30 ± 0.29, and $\widehat{\Delta T}$=8.1 ± 0.9 months, giving χ^2/df = 2651/3990. The fit was repeated after fixing $\Delta T \equiv 0$, *i.e.*, under a more conventional "unretarded" scenario. returning $\hat{a}$ =3.36 ± 0.76, $\hat{b}$ =-1.08 ± 0.24, and χ^2/df =4979/3991. Results are shown in Figure 6.10, illustrating the time and energy dependence of calculations in comparison with the data. The fits give satisfactory results at all energies and epochs. From Figure 6.10, it can be seen that the model reproduces very well the time evolution of the proton flux, at $E = 1.5$ GeV and after the 2013 polarity reversal, the proton flux is predicted to increase with time.

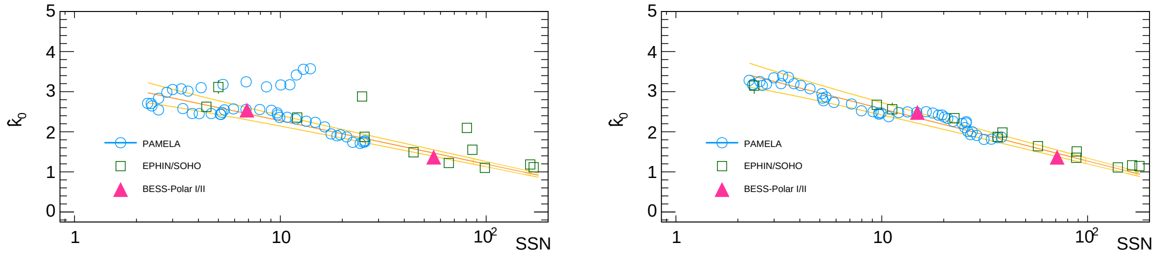

(a) Without a temporal delay.

(b) With a temporal delay.

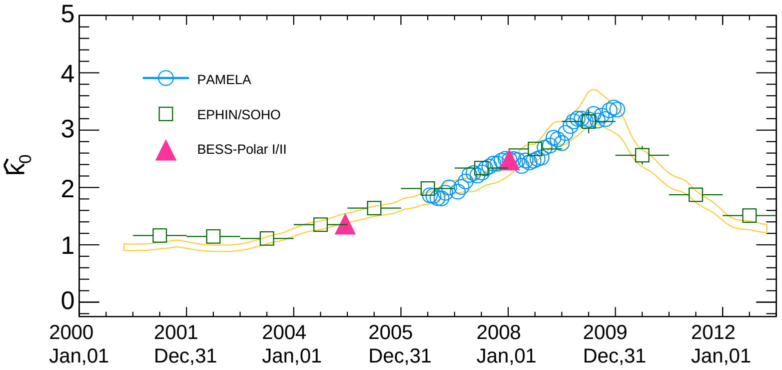

(c) Global fit with temporal delay.

Figure 6.8: Comparison between the fitted global model diffusion scale parameter $\hat{\kappa}^0$ (in orange) against the individually fitted diffusion parameters for the different time measurements of the flux without (top left) and with (top right) a temporal delay, as a function of the number of sunspots. (bottom) Fitted diffusion scale parameter $\hat{\kappa}^0$ for the global model as a function of time (in orange) against the individually fitted diffusion parameters for the different time measurements of the flux with a temporal delay, as a function of time.

It is also clear from the figure that the retarded scenario (with $\Delta T \equiv 8.1$ months, thick red line) allows for a much better description of the time evolution of the proton flux. Additionally, for comparison, recent AMS and PAMELA data were overlaid as well even though they are not used for the fit. The prediction shows great agreement with this recent data but some fine tuning is required. Due to the change of particle drift motion during and after a magnetic reversal, we expect that a new ΔT has to be determined for each epoch.

Additionally, we have also performed a time-series of fits to single energy spectra $\hat{J}_j$ by directly using the diffusion scaling as free parameter. This provided time-series of 62 $\hat{\kappa}^0_j$-values corresponding to various epochs t_j, which were done after fixing $\Delta T \equiv \widehat{\Delta T} = 8.1$ months. Inspecting the relation between $\hat{\kappa}^0_j$ and the "delayed" SSN revealed a correlation coefficient of $\rho_{\Delta T} = -0.89$ against the $\rho_0 = -0.66$ for the scenario of $\Delta T = 0$. Figures for both $\Delta T = 8.1$ months and $\Delta T = 0$ scenarios can be found in Figure 6.8.

In Figure 6.8 we can clearly see the effects of the inclusion of a time-lag on the parametrization of the diffusion coefficient by the sunspot number. We had already seen a similar result in Figure 6.5 but, in this case, the result is compared against a full description of the cosmic-ray proton flux over several years and through a great range of energy.

In Figure 6.9 we can see the global fit of the model when compared to the data. As expected, we are most sensitive to the time delay for the first rigidity bins since it is the region which presents the most prominent temporal variations due to solar modulation. Thanks to the clear temporal signature of the flux maximum which presents a long steady increase followed by a faster decrease, we were able to capture the time-delay effectively through the global fit. This temporal signature also changes with rigidity, further increasing the sensitivity to the exact value of the time-delay.

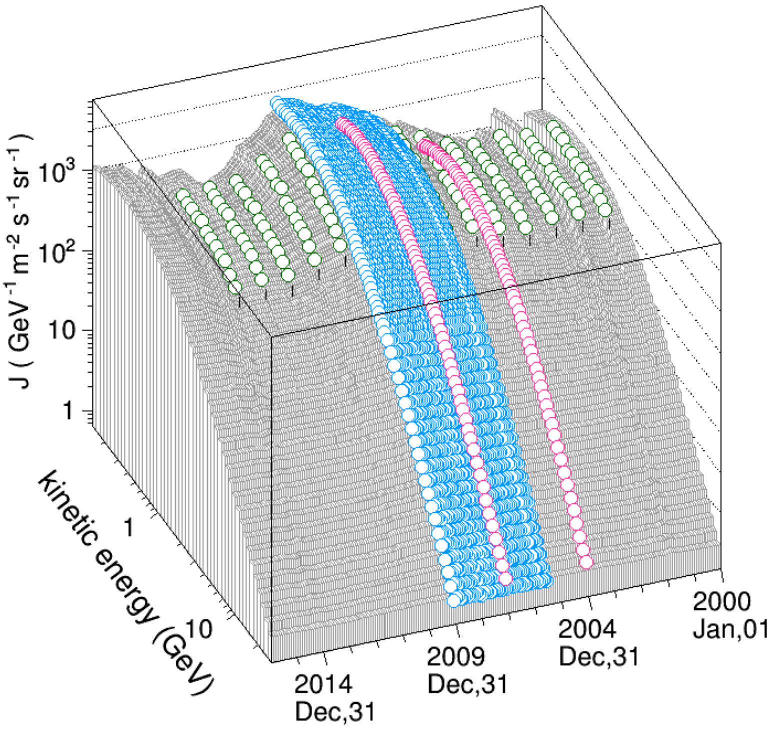

Figure 6.9: Proton flux calculations as a function of kinetic energy and time in comparison with the data from PAMELA[160], EPHIN/SOHO[139], and BESS[137, 138]. The global best-fitted model, including a time-delay, is represented by the histogram in grey.

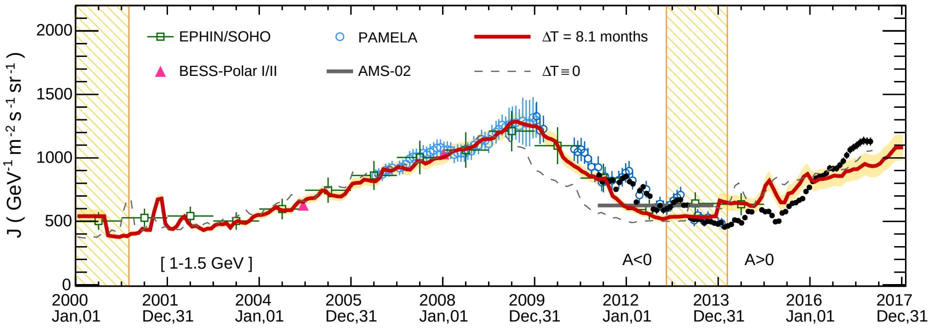

Figure 6.10: Time profile of the proton flux at $E = [1 - 1.5]$ GeV. Best-fit calculations are shown as thick solid line, along with the uncertainty band, in comparison with the data [160, 139, 137, 138, 17, 108, 136]. The most recent AMS data[108] is shown in black and PAMELA data[136] in dark blue. The shaded bars indicate the magnetic reversals of the Sun's polarity [70]. Figure taken from [153].

These findings explain why other authors, when proposing simple relations between κ^0 and SSN, had to adopt different coefficients for descending and ascending phases [164, 175]. Remarkably, this problem is naturally resolved in our model: once the time-lag is properly accounted, the κ^0-SSN relations can be described by a unique function.

Finally, our model was used to predict the time evolution of antimatter-to-matter ratios such as the e^+/e^-. Our calculations are shown in Figure 6.11 for ΔT=8.1 months. The calculations were also done for ΔT=0 but were not shown in this figure. Measurements of the relative variation of the ratios are shown as reported by AMS [47] and PAMELA [161].

For the e^+/e^- ratio, we note that calculations within $\Delta T = 8.1$ month are favoured, although the data does not permit a resolute discrimination. Across the magnetic reversal, shown in the figure as shaded bars, a remarkable increase of the e^+/e^- ratio is predicted. It should be noted, however, that the dynamics of the transition could not be modelled during reversal, because the HMF polarity is not well defined. Nonetheless, a rise in the e^+/e^- ratio profile has been detected in both AMS [47] and PAMELA data [161], and this rise is found to occur a few months after completion of the Sun's polarity reversal.

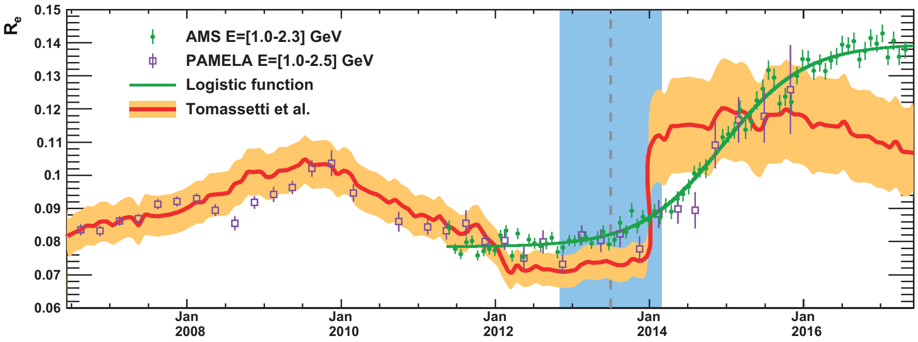

Figure 6.11: Time profile of the ratios R_e e^+/e^- at $E = 1 - 2.3\,\mathrm{GeV}$ for AMS data[47] and at $E = 1 - 2.5\,\mathrm{GeV}$ for PAMELA data. Model predictions and their corresponding uncertainties, are shown in comparisons with the data [161, 182]. The shaded bars indicate the magnetic reversals of the Sun's polarity [70]. Figure taken from the supplementary material of [47].

Using new high-statistics measurements of CRs in space determined the evolution of CR fluxes near Earth with unmatched time resolution. This data allowed us to perform detailed studies of the solar modulation effect and its dynamical connection with the evolving solar activity. In this work, we have reported new calculations of CR modulation based on a simple but physically consistent numerical model that accounts for particle diffusion, drift, convection and adiabatic cooling. We have adopted a simple formulation where the time-dependent physics inputs of the model consist only in SSN and HCS tilt angle. We have shown that this model reproduces well the time evolution of the Galactic proton spectra measured by AMS, PAMELA, EPHIN/SOHO, and BESS experiments. Our model is highly predictive once the correspondence between modulation parameters and solar activity indices is established. Our study revealed an interesting aspect of the dynamics of CR modulation in the expanding wind, that is, the presence of time-lag ΔT between solar data and the condition of the heliosphere.

Using a large ensemble of CR proton data we found $\Delta T = 8.1 \pm 0.9$ month, which is in agreement with basic expectations and with recent NM based analysis [183, 180, 181]. An interesting consequence of this result is that the galactic CR flux at Earth can be predicted, at any epoch t, using solar activity indices observed at the time $t - \Delta T$. This result is of great interest for real-time space weather forecast, which is an important concern for human space-flight.

In our results, the parameter ΔT has been determined using CR protons during negative polarity. This parameter has to be viewed as an effective quantity representing the average of several CR trajectories in the heliosphere during $A < 0$ conditions (see Figure 6.12).

Further elaborations may include the use of NM data, for larger observation periods, or the accounting for a latitudinal dependence in the wind profile or in the diffusion coefficient. Since CR particles and antiparticles sample different regions of the heliosphere, we expect slightly different time-lags, $\Delta T_\pm$ depending on the sign of qA (and in particular, $\Delta T_- \lesssim \Delta T_+$). With the precision of the existing data, we were unable to test this hypothesis. A detailed re-analysis of our model, in this direction, will be possible after the release of monthly-resolved data from AMS on CR particle and antiparticle fluxes.

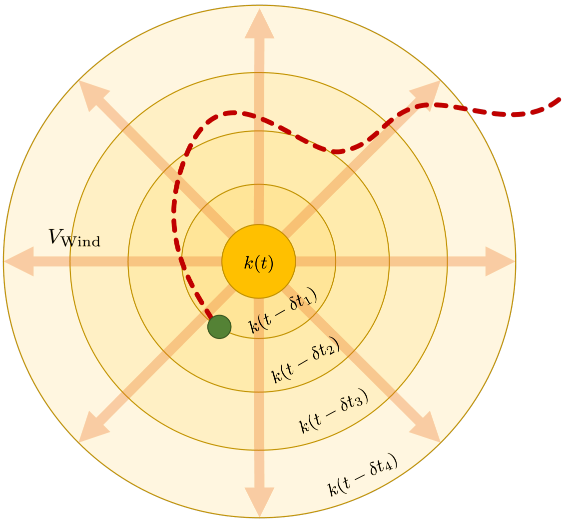

Figure 6.12: Diagram of the gradual transport of solar parameters through the solar wind as it expands radially towards the edge of the heliosphere. The red dashed line depicts a cosmic-ray particle traversing the solar system and being subjected to a plasta with properties correlated to delayed solar parameters.

6.5 Conclusions and Outlook

We examined some of the different solar observables available and used them to correlate the solar activity cycle with the long-term variations of the cosmic-ray flux measured by different experiments. We explored different techniques to simulate the cosmic-ray flux using parametrizations that are dependent on solar parameters in order to construct a time-dependent simulation of the cosmic-ray flux which we can compare to experimental results from space-based experiments. We developed a highly predictive model after building a correspondence between modulation parameters and solar observables. We observed a time delay ΔT between cosmic-ray flux variations and solar observables and estimated it with a great degree of precision and agreement with data. In our results, we determined a parameter $\Delta T = 8.1\,\text{months}$ using CR protons during negative polarity. This parameter has to be viewed as an effective quantity representing the average of several CR trajectories in the heliosphere during $A < 0$ conditions. Even though we showed a degree of predictability using other cosmic-ray particles, in order to produce a result with the same level of agreement, different parametrizations had to be explored.

7

Conclusions and Prospects

In this work we have presented a brief introduction to cosmic rays and their history. We briefly discussed the AMS-02 detector and the different sub-detectors that compose it, emphasizing the physical quantity they observe and their measurement principle. We discussed the space environment in which AMS is inserted and the effect that has on the cosmic rays observed by AMS.

In chapter 2 we briefly explained the history of the field of Solar Modulation, beginning with the initial formulations of Parker's transport equation and then we explored it thoroughly in order to provide a theoretical motivation for the phenomenological studies performed in the rest of the work. We also briefly touched on the solar activity cycle and what is observed in the different solar variables and physical channels available.

In chapter 4 we estimated the Bartel rotation (27-day) time-resolved cosmic-ray flux from 11 June 2011 to 14 November 2019, corresponding to the Bartel number 2427 up to 2541, producing a total of 115 time bins, with the exclusion of Bartel rotations 2472 and 2473. We worked through the process of estimating the proton cosmic-ray flux in the context of the instrument used, AMS. We referred back to the different processes and detectors involved and corrected for their effects on our estimative of the proton cosmic-ray flux. These were studied for every Bartel rotation in order to take into account their temporal variations and to accurately correct the flux for the respective temporal effects it was subjected to.

In chapter 5 we sought to explore the different periodicities present in the daily and Bartel rotation time-resolved proton flux as measured by AMS. We related these temporal variations with particle rigidity and compared them with the ACE measurement of the IMF near Earth and present the cross-wavelet spectrum between this two series. The local wavelet power spectrum was shown for every year of the flux, for 4 selected rigidity intervals. The periodicities of 2017 were analysed in relation to exceptional solar activity present during that year. The effects related to a shift in periodicity and an energy dependence was observed.

In chapter 6 we examined some of the different solar observables available and used them to correlate the solar activity cycle with the long-term variations of the cosmic-ray flux measured by different experiments. We explored different techniques to simulate the cosmic-ray flux using parametrizations that are dependent on solar parameters in order to construct a time-dependent simulation of the cosmic-ray flux which we can compare to experimental results from space-based experiments. Our model is highly predictive once the correspondence between modulation parameters and solar activity indices is established. We observed a time delay ΔT between cosmic-ray flux variations and solar observables and estimated it with a great degree of precision and agreement with data. In our results, we determined a parameter ΔT using CR protons during negative polarity. This parameter has to be viewed as an effective quantity representing the average of several CR trajectories in the heliosphere during $A < 0$ conditions. Even though we showed a degree of predictability using other cosmic-ray particles, in order to produce a result with the same level of agreement, different parametrizations had to be explored.

Finally, in Appendix A we have highlighted some of the computational tools developed during the course of this work. An effort was made to develop performant code that would solve the problem and, at the same time, be made usable by others in the scientific community through documentation and standardization of inputs and functionalities. During the analysis, the usage of free open-source scientific libraries was a constant and, keeping up with the AMS-LIP group's long history of international scientific collaboration, all of this code has been made readily available to other collaborators with the group and is intended to be maintained and improved as the group grows and delves deeper into this field of study. Usually, a lot of this computational work is invisible so an effort was made to reference most of the code used and developed during the course of this work and credit the authors of such codes that made this work possible through being made available for others to use, just as the code in this thesis will be as well.

A

Algorithms and Code

In this chapter we will detail the different algorithms and analysis frameworks developed during the course of this work. The algorithms implemented will be explained and respective codes will be overviewed, showcasing the technical challenges faced by the topics explored in this thesis while maintaining a high standard of computing performance and code scalability. Most of these libraries utilize ROOT[184] as a wrapper for statistical objects and drawing functionality as well as some core functionalities such as access to MINUIT[185] and random number generation.

A.1 LxSmoother - Spline Regularization of Histograms

The *LxSmoother* is spline-based regularization tool for histograms. It is the second iteration of the efforts made during this work to develop a smoothing tool. The first tool (*LxAdaptiveSplineFit*) was based on recursively testing every possible combination of bins as nodes to perform the spline which will represent the histogram. The new class is a complete overhaul on this concept. The nodes for the spline are fitted to the data.

The field of data smoothing through parametric or non-parametric estimation is rather rich and several approaches can be taken to tackle this issue[186, 187, 188]. For this work the main constraints were reliability of the result, speed of the estimation (it is used several hundreds of times per analysis due to the amount of temporal bins), resistance of result to statistical oscillations, capability of producing splines with logarithmic spacing and a robust estimation of uncertainty introduced to the smoothed result. One of the dependences of this class is the ROOT library but this was done for convenience since it is one of the main scientific libraries used in this field of work. It can be easily adapted to any array of points regardless of ordering and errors. For mathematical flexibility B-splines[189] are usually used in these spline regularization methods but we opted for using the spline-3 convention[190]. Some of the key problems in these analyses lie in the choice of number of nodes, optimal initial position of nodes in order to include the most information and the least noise according to some ad-hoc principle such as a penalization which is used in penalized b-spline fitting [191].

Our spline selection criteria is the BIC. Criteria such as Akaike Information Criteria (AIC) or BIC have been commonly used[192, 188, 193] to select between different models. This is a great improvement upon simply comparing χ^2/Ndf between the different node configurations since, for a large enough number of nodes, the best fit would be that in which the spline simply crosses all the data points or matches all of the data's fluctuations and our smoothing objective would have failed. A diagram of *LxSmoother*'s algorithm can be seen in Figure A.1.

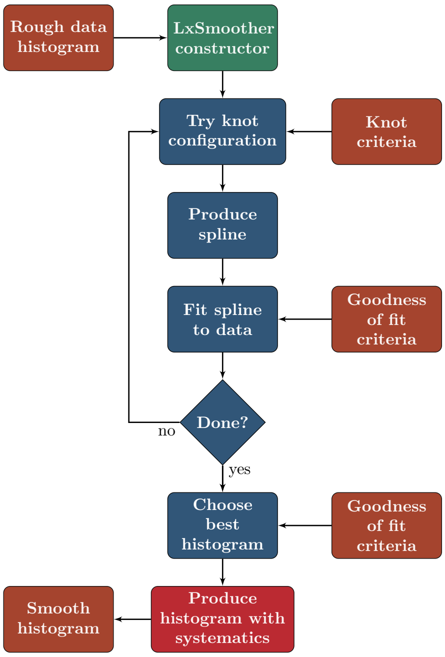

Figure A.1: Diagram of LxSmoother algorithm.

The class contains several node spacing strategies and will test every number of nodes possible in that strategy up to a reasonably high number (while penalizing this increase). Currently there are 3 node spacing strategies available: uniform, Chebyshev node spacing[194] and uniform spacing with a percentage of nodes on points weighted by the first and second derivative of the smoothed histogram. An example of these node spacings can be found in Figure A.2.

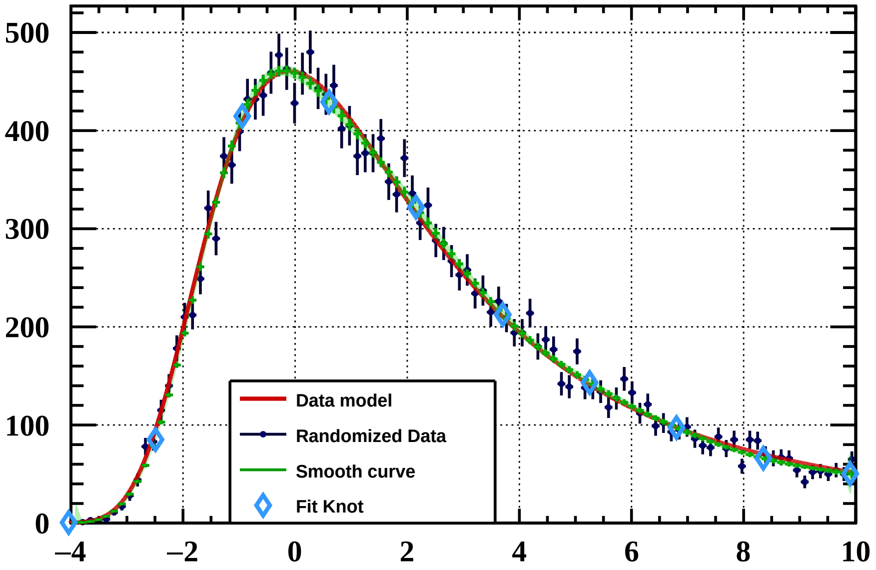

(a) Uniform node spacing.

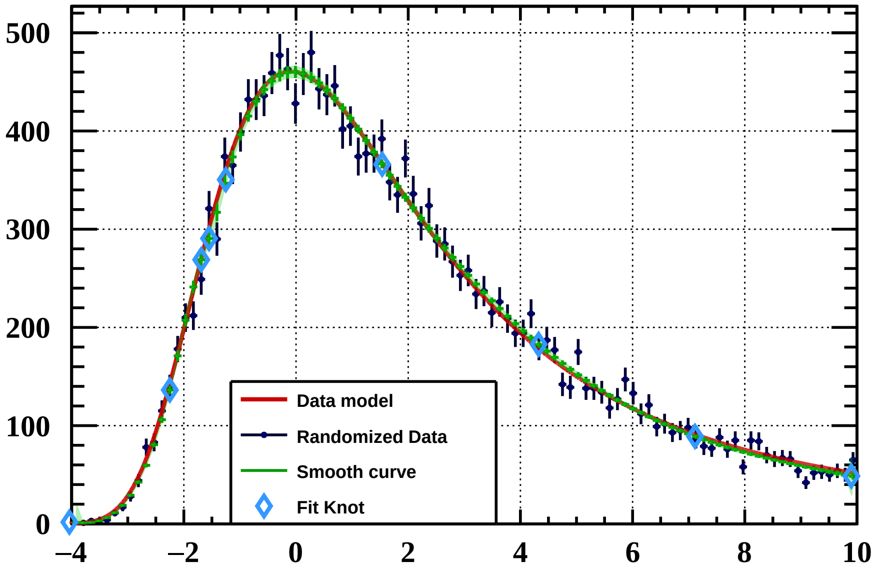

(b) Derivative Weight node spacing.

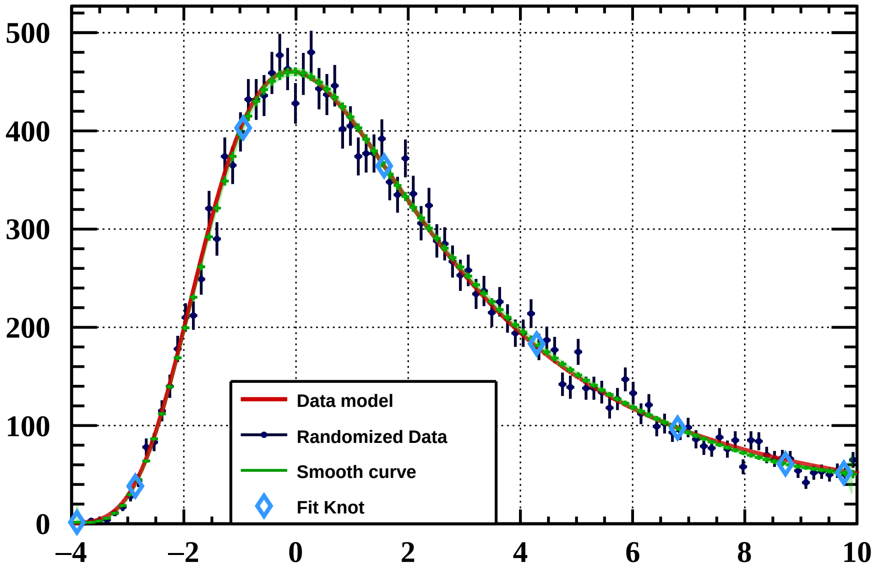

(c) Chebyshev node spacing.

Figure A.2: Comparison between the different node strategies in LxSmoother. Data was generated randomly according to a Landau curve.

The usage of the BIC criteria allows us to achieve convergence using a small number of nodes without overfitting. These results can be seen in Table A.1 and, for every node distribution, we have achieved a very satisfactory result ($\chi^2 \sim 1$) for a very reduced number of knots using the BIC criteria instead of χ^2.

Additionally, the class contains a very important feature for cosmic-flux estimation which is the capability of spacing the nodes in these strategies in logarithmic scale and being able to extrapolate the splines in every strategy. The logarithmic spacing is important due to instabilities which arise in spline-3 due to non-linear spacing between nodes.

Number	Uniform		Derivative		Chebyshev	
of Nodes	χ^2/Ndf	BIC/Ndf	χ^2/Ndf	BIC/Ndf	χ^2/Ndf	BIC/Ndf
3	54.2297	54.3736	51.6531	51.7971	48.705	48.8489
4	44.5383	44.7322	45.8213	46.0152	18.3329	18.5268
5	39.0623	39.3073	3.11025	3.3552	22.0995	22.3444
6	22.738	23.0351	1.35195	1.64905	14.7503	15.0474
7	9.92896	10.2794	1.20295	1.55335	3.68589	4.03628
8	3.7456	4.15045	1.11354	1.51839	0.915711	**1.32056**
9	1.4772	1.93772	0.992374	**1.45289**	1.23771	1.69822
10	1.00703	**1.52447**	0.957013	1.47445	1.13779	1.65522
11	0.970567	1.54621	0.964991	1.54064	0.920267	1.49591
12	0.942798	1.57799	0.947578	1.58277	0.918526	1.55372
13	0.93613	1.63226	0.945777	1.64191	0.869189	1.56532
14	0.940826	1.69932	0.956746	1.71524	0.866437	1.62494
15	0.872489	1.69484	0.95483	1.77718	0.89643	1.71878
16	0.87555	1.76329	0.953592	1.84134	0.861438	1.74918
17	0.868141	1.82287	0.941116	1.89585	0.869	1.82373
18	0.861866	1.88524	0.913443	1.93681	0.887219	1.91059
19	0.866227	1.95996	0.95221	2.04594	0.864224	1.95795
20	0.871468	2.03733	0.968332	2.1342	0.894543	2.06041
21	0.873499	2.11335	0.979935	2.21979	0.858118	2.09797
22	**0.85731**	2.17307	0.900307	2.21607	0.879838	2.1956
23	0.860493	2.25416	0.873514	2.26718	0.855196	2.24887
24	0.884451	2.35811	0.885161	2.35882	**0.85486**	2.32851
25	0.875316	2.43112	0.83666	2.39246	0.871783	2.42758
26	0.869093	2.50929	**0.823287**	2.46349	0.876808	2.51701
27	0.900057	2.627	0.827272	2.55421	0.875795	2.60273
28	0.893693	2.70982	0.885223	2.70135	0.891091	2.70721
29	0.892944	2.8008	0.890985	2.79884	0.894774	2.80263
30	0.898936	2.90118	0.866063	2.86831	0.891528	2.89378

Table A.1: χ^2 and BIC for the fits presented in Figure A.2. The numbers highlighted in green correspond to the minima for the BIC criterium and the red correspond to the χ^2 minimum, for each node distribution.

A.1.1 LxSmoother Header

The header for the class can be seen in Listing A.1.

Listing A.1: Minimalistic header for the LxSmoother class.

```
enum HintOption {
  Uniform,
  Chebyshev,
  Derivative
};

enum MinimizerOption {
  Chi2,
  BIC
};

class LxSmoother {
 public:
```

```
LxSmoother();
~LxSmoother();

/**
  GetSmoothHist
  @param histo histogram to smooth
  @param nodes number of nodes to use
  @param x_fit_min start of the smoothing
  @param x_fit_max end of the smoothing
  @param Nbins_refit if the smoothed histogram should have a new number of bins
  @param Xbins_refit new bins for the smoothed histogram
  @return smoothed histogram
 */

TH1D* GetSmoothHist(TH1D* histo, int nodes = 10, double x_fit_min = -1, double
    x_fit_max = -1, int Nbins_refit = -1, double* Xbins_refit = nullptr);

/**
  GetSmoothHist
  @param histo histogram to smooth
  @param nodes number of nodes to use
  @param x_fit_min start of the smoothing
  @param x_fit_max end of the smoothing
  @param Nbins_refit if the smoothed histogram should have a new number of bins
  @param Xbins_refit new bins for the smoothed histogram
  @return smoothed histogram
 */

TH1D* ScanSmoothHist(TH1D* fhisto_data, double x_fit_min = -1, double x_fit_max = -1,
     int Nbins_refit = -1, double* Xbins_refit = nullptr);

// get fit results
double GetChi2();
double GetNdf();
double GetChi2Norm();

TH1D* GetChi2Distribuition();
TH1D* GetChi2NormDistribuition();
TH1D* GetSystematicEnvelopeHistogram();
TH1D* GetSystematics();

// get the knots
std::vector<std::pair<double,double>> GetFitKnots();
std::vector<double> GetFitXKnots();

// get the function
TF1* GetF();
TF1* GetF_ToZero();
void SetExtrapolationMode(std::string opt = "linear") // flat, linear or exponential

void SetAddDataError(bool val = true) {isAddDataError = val;}
void SetHintOption(HintOption opt) {hintoption = opt;}
void SetLogx(bool val = true) {isLogX = val;}
void SetLogy(bool val = true) {isLogY = val;}
void SetFix_X(bool val = true) {fix_x_nodes = val;}
void SetPadding(double val) {padding = val;}
double GetPadding();
void SetSplineBoundaryBegin(double val){spline_val_beg = val;}
```

```
  void SetSplineBoundaryEnd(double val){spline_val_end = val;}
  void SetSplineBoundaryOption(string s){spline_opt = s;}

  void Draw();

  static void SetDefaultHintOption(HintOption opt);
  static void SetDefaultMinimizerOption(MinimizerOption opt);
};
```

A.2 LxTimeSeries & LxWavelet

Increased interest from the scientific community in data science, several extremely powerful libraries have come out for the *Python* programming language, notably *Numpy*[195], *SciPy*[196] and *Pandas*[197, 198]. These libraries define a set of objects and operations optimized for handling very large amounts of data with efficiency and ease. Due to the amount of data being handled during the course of this work, inspired in some of the objects and operations present in *DataSeries* in *Pandas*, we developed the class *LxTimeSeries* with the sole purpose of handling time-series in an efficient and practical manner. This is a common theme of many tools developed in this chapter. The header for the class *LxTimeSeries* can be found in Listing A.2.

LxTimeSeries was developed to tackle the issue of working with these volumes of data and handling the complex operations required to standardize the data (i.e. removing mean, smoothing, handling NaN values, interpolate missing data, resample data, selecting subsets of data, parallelized mass operations, etc.) or analyse it through statistical estimators (i.e. mean, standard deviation, autocorrelation, correlation, etc.).

After developing a tool to handle the data we built the class that we would use to analyse these time-series for periodicities. We developed a class for calculating the wavelet transform of a time-series in a parallelized fashion using *std::threads* based ont he algorithm presented by Torrence and Compo, (1998)[125]. The class also calculates red-noise confidence levels and is capable of calculating the cross-wavelet transform between two time-series. In order to test *LxWavelet* class implementation the results from Torrence and Compo, (1998)[125] were reproduced in an independent manner using the same data with great success. These can be seen in Figure A.3.

The header for the class *LxWavelet* can be found in Listing A.3.

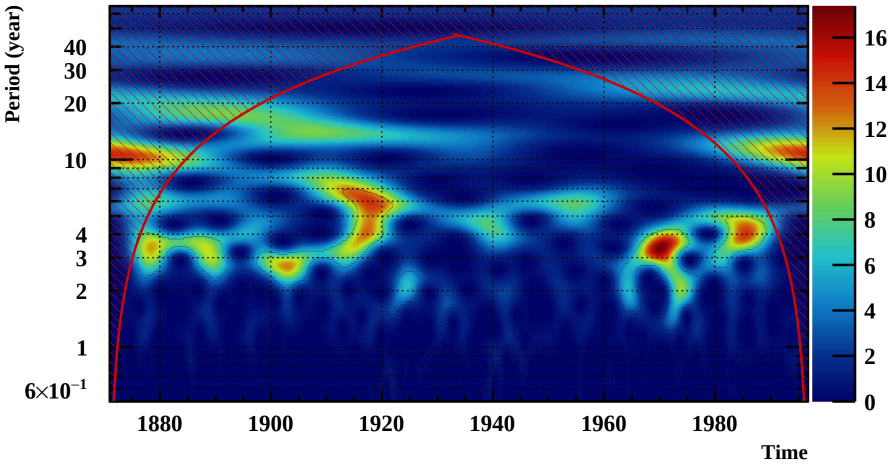

Figure A.3: Local wavelet power spectrum of the Niño3 SST using the Morlet wavelet, normalized by $1/\sigma^2$ ($\sigma^2 = 0.54°$ C). The thin black contour encloses the regions of greater than 95% confidence for a red-noise process with a lag-1 coefficient of 0.716531. Red cross-hatched regions indicate the "cone of influence", where edge effects become important.

A.2.1 LxTimeSeries Header

Listing A.2: Minimalistic header for the LxTimeSeries class.

```
enum resample_operations {op_sum, op_mean};
```

```
class LxTimeSeries {
 public:
  // constructors
  LxTimeSeries();
  LxTimeSeries(std::vector<double>, std::vector<double>);
  LxTimeSeries(int N, double* futimes, double* fseries);
  LxTimeSeries(const LxTimeSeries&);
  LxTimeSeries(LxTimeSeries&&);
  LxTimeSeries(TGraph*);
  LxTimeSeries(TH1D* histo);

  ~LxTimeSeries();

  // data accessors
  LxTimeSeries& operator=(const LxTimeSeries&);
  double& operator[](int);
  double operator[](int) const;
  unsigned int Size() const;
  TGraph* GetGraph() const;
  TF1* GetSpline() const;
  void Print() const;

  // generic accessors
  const std::vector<double>& Series() const;
  const std::vector<double>& Time() const;
  double TimeInterval() const;
  void Append(double time, double point);
  void Remove(int i);

  // manipulation methods
  void Resize(int n);
  LxTimeSeries Shift(int i) const;
  LxTimeSeries FillNa() const; // this method interpolates the series onto itself to
      remove nan values
  LxTimeSeries Interpolate(double T0, double dT, int N) const; // using TSpline3 object
  LxTimeSeries Interpolate(const std::vector<double> &futime) const; // using TSpline3
      object
  LxTimeSeries LinearInterpolate(double T0, double dT, int N) const; // using TGraph
      object
  LxTimeSeries LinearInterpolate(const std::vector<double> &futime) const; // using
      TGraph object
  LxTimeSeries MovingAverage(int window) const; // Centred
  LxTimeSeries MovingAverageBackward(int window) const; // Backward
  LxTimeSeries MovingAverageForward(int window) const; // Forward
  LxTimeSeries GaussianFilter(int window) const;
  LxTimeSeries Resample(int window, std::string operation="mean") const;
  LxTimeSeries Apply(std::function<void(double&)> func) const;

  LxTimeSeries operator+(double x);
  LxTimeSeries operator-(double x);
  LxTimeSeries operator*(double x);
  LxTimeSeries operator/(double x);

  // statistical operators
  double Mean() const;
  double StandardDeviation() const;
  double Min() const;
  double Max() const;
```

```
  double CorrelationPearson(const LxTimeSeries&, double dT_tolerance=1.E-8) const;
  double CorrelationSpearman(const LxTimeSeries&, double dT_tolerance=1.E-8) const;
  double CorrelationPearsonSpline(const LxTimeSeries&, double dT, double delay=0) const
      ;
  double CorrelationPearsonMeanEnvelope(const LxTimeSeries&, double dT, double delay=0)
       const;

  TGraph* PearsonDelayAnalysis(const LxTimeSeries& fseries, double
      interpolation_resolution, double delay_min, double delay_max, double delay_step,
      double scale=1., std::string method="spline");

  double AutoCorrelation(int shift) const;
  TGraph* GetFFT(double time_scale_factor = 1.) const;
  double** FFT(double time_scale_factor = 1.) const;

  // cohesiveness
  bool Test();

  // envelope functions
  TF1* GetMaximaEnvelope() const;
  TF1* GetMinimaEnvelope() const;
  TF1* GetEnvelopeMean() const;

  // auxiliar functions
  double GetRedNoiseParam();
};
```

A.2.2 LxWavelet Header

Listing A.3: Minimalistic header for the LxWavelet class.

```
class LxWavelet {
 public:
  LxWavelet(const LxTimeSeries&, double time_scale_factor=1.);

  std::vector<TH2D*> GetDWT(double delta_j=0.005);

  TGraph* GetConeOfInfluence();

  std::vector<TH2D*> GetCrossWaveletTransform(LxWavelet& other, double delta_j=0.005);

  LxTimeSeries GetSeries();

  TGraph* GetRedNoisePowerSpectrum(double alfa, double percentile, int ndf=2);
  TGraph* GetRedNoisePowerSpectrumAveraged(double alfa, double percentile, int npoints)
      ;

  TGraph* GetConfidenceContours(TH2D* hdwt, double alfa=-1000, double percentile=0.95,
      int ndf=2);

  std::vector<std::vector<std::complex<double>>> DWT();
  std::vector<double> ConeOfInfluence();

  std::vector<std::pair<double,double>> RedNoisePowerSpectrum(double alfa, double
      percentile=0.95, int ndf=2);

  (...)
```

```
};
```

A.3 Hybrid Worker Pool Parallelization Scheme

This section contains an internal report on a *Hybrid Worker Pool Parallelization Scheme* developed during the course of this work. At the beginning of this work we started developing AMS reduced data trees so the necessity arose to develop a parallelization platform that was flexible enough to accommodate a hybrid network of computers while being performant.

This framework was developed using C++ and the *OpenMPI*[199] implementation of the Message Passing Interface (MPI) specification. The AMS data processing itself was done using AMS software chain and data management was done using *LxSoft* libraries.

A.3.1 Motivation

AMS is a cosmic ray detector installed on the International Space Station (ISS) since 19 May 2011. It aims to study the existence of antimatter and dark matter. AMS makes use of a set of sub-detectors that make complementary measurements in order to be able to identify the type of particle incident on it and to accurately study the cosmic ray fluxes arriving on Earth from the galaxy. Since its launch into space, AMS has collected more than 90 billion events.

In order to make use of the gigantic data stream that AMS produces, optimising the event selection process becomes critical to be able to produce timely physics results and take advantage of the experiment's long time exposure and measurement accuracy.

A.3.2 Event Selection

A.3.2.1 The LxSoft platform

The Portuguese AMS group developed an analysis platform called LxSoft written mostly in C++. This is the base of the whole class structure that is used by the Portuguese group in their analysis. It contains elements for local and remote data access and management (ROOT, AMS, EOS, Castor, ...), data selection, event reconstruction in AMS, statistical analysis, manipulation of histograms and other data structures, simulation of physical phenomena and numerical problem solving.

The LXSoft platform relies heavily on the ROOT scientific library developed at CERN.

Throughout this project some of these classes have been used.

A.3.2.2 LxAMSdataManager and LxAMSdata

Listing and managing ROOT files is done by the *LxAMSdataManager* class. Using a factory *design pattern* and according to what the user requires, *LxAMSdataManager* produces a class that inherits from *LxAMSdata* and contains all the information necessary to access the AMS data (access preambles from the XRootD platform, local access, Castor or EOS access, Kerberos authentication).

After the databases have been queried and the data files listed, they are aggregated into a class that inherits from *LxAMSdata* and manages individual file access. It contains all the methods required to access the individual files.

Listing A.4: Example of remote access to data using EOS

```
LxAMSdataManager::SetStorageAccess("EOS");
LxAMSdata* data = LxAMSdataManager::AcessDataList("Data", "ISS.B950/pass6");
```

Listing A.5: Example of local access to AMS data

```
LxAMSdata* pData = new LxAMSlip("local", "./DATA/");
```

A.3.3 Data organization at AMS

AMS events, once transferred from ISS, are processed and stored in *AMSevent* classes. These events are then stored in *AMSchain* classes that inherit and make use of the *TTree* class and *TChain* (*TTree*'s management class) belonging to ROOT.

As the ISS orbits around the earth with a period of approximately 90 minutes, it passes twice through the equator, the period of lowest frequency of events (due to the earth's magnetic field), where the calibration of the different sub-detectors is done. From the equator to the pole, a 22-minute Run is made in which the events are acquired uninterruptedly. This process is repeated between the pole and the equator, thus generating 4 Runs per orbit.

A.3.3.1 LxAMSana

After the organization comes the query of the *AMSevent* events that store all the information regarding the particle that triggered the AMS detection.

To facilitate the analysis of the events, a *LxAMSana* class was designed from which the user must inherit (as was done in the LxDSTprotonflux class) and which facilitates the query of the events and storage of the results.

A.3.3.2 LxDSTprotonflux

This class is the class responsible for selecting the events, producing the histograms with the results and storing them in ROOT files. The *LxDSTprotonflux* class inherits from the *LxAMSana* class and receives the files (local or remote access) from the *LxAMSdataManager* class.

Listing A.6: Usage example for the LxDSTprotonflux class

```
LxDSTprotonflux user;
string NTupleName(Form("./OUT/%d_%d.root",Tmin,rank));
for (....) {
  ...
  string s(filename);
  user.AddFile(s.c_str());
}
user.CreateUserTree("proton_data", NTupleName);
user.UserBook();
user.LoopOnEvents(100000);
user.CloseUserTree("proton_data");
```

Internally this class has a selection that is run over all events and, for each selected event, fills the appropriate histograms with the variables of interest.

A.3.4 Design and constraints

Events in AMS are uncorrelated with each other and can be analysed individually. Discretization and parallelization can be done at the event level. With 500000-800000 events per Run, parallelizing at the event level requires intense management between processes to guarantee that there is no repetition of events. In this scenario, the distribution of events across the different selection processes needs to be managed.

This fragmentation of the problem raises questions regarding the determination of the exposure time.

A fundamental quantity to flow estimation is the exposure time of the detector. In the AMS organisation, the evaluation of the detector dead time is done when reprocessing the data and is separated into 1-second intervals. For each second, what fraction of the time the detector is operational is evaluated.

In the single event parallelization scheme, it becomes complex to manage the events in order to include (or exclude) them in the second under analysis in order to preserve temporal ordering. The simplest way would be to do a double pass in which events are selected and then the exposure time is evaluated, having a strong impact on the parallelization and reducing its efficiency (double disk/network access and loading of the event into memory). A duplication of the contribution of the serial part of the code arises.

The natural granularity of parallelization would then become the second. In this scenario the seconds are distributed among the processes and the workload would be essentially equal per process (assuming a constant selection time per event, something that does not happen).

In both of the above cases, you always need a global event manager that coordinates the processes *Worker* in live time or a long process prior to the analysis that divides the times sisterly among the processes before the selection is made. Currently, this is how the analysis is typically done, N Runs are distributed per worker and it is expected that on average the Runs are equal and the work is well distributed. It is then verified that at the end of the analysis, there are always some processes that are left behind and that slow down the process of merging the resulting histograms. Parallelisation management in this case is usually done at the executable level using a grid system (Sun Grid or LSF).

Finally, the last hypothesis is to parallelize at the Run level. This guarantees that a file is only accessed by one *Worker* at a time and thus data integrity is guaranteed. The workload then becomes unequal for the different *Worker* processes since the files are not equal. This scenario then requires a system that in real time manages the workload of the *Worker*'s and distributes work when they finish.

Given the organisation of the data into 22 minute Runs, this will be the granularity adopted by this work for parallelisation purposes.

The different parallelisation schemes can be seen in the figure A.4. In this it is possible to see the difference in the times that arises from a blind distribution of work by *Workers*.

A.3.5 Algorithm's organization

The code is divided into three algorithms: the *DataManager*, the *WorkerPool* and the *Workers*. A description of these algorithms will then be given.

A.3.5.1 Worker

Of the three major functions, the *Worker* is among the simplest and most linear. As you can see in Figure A.5, the *Worker* simply waits for work, parses the events and saves them to a ROOT file, updates its state in the *WorkerPool* and returns to the inert state of waiting for instructions.

This is the simplest and most versatile to work with, it is a wrapper for the analysis you want to do.

The code contains space for file staging routines, network authentication or even an event-by-event (or event-time based) analysis to be as versatile as possible.

A.3.5.2 DataManager

Second in order of complexity comes the DataManager. This is the central function that does the initial reading of files and manages them. It communicates with both the *WorkerPool* and the *Worker*'s allocated to it. The flowchart of this function can be found in the figure A.6a.

This function is also responsible for triggering the termination of the code when there are no more files to analyze.

Additionally, one of the parameters accessible to this function is the number of files that is allocated to the *Worker* provided by the *WorkerPool*. This allows assigning asymmetric

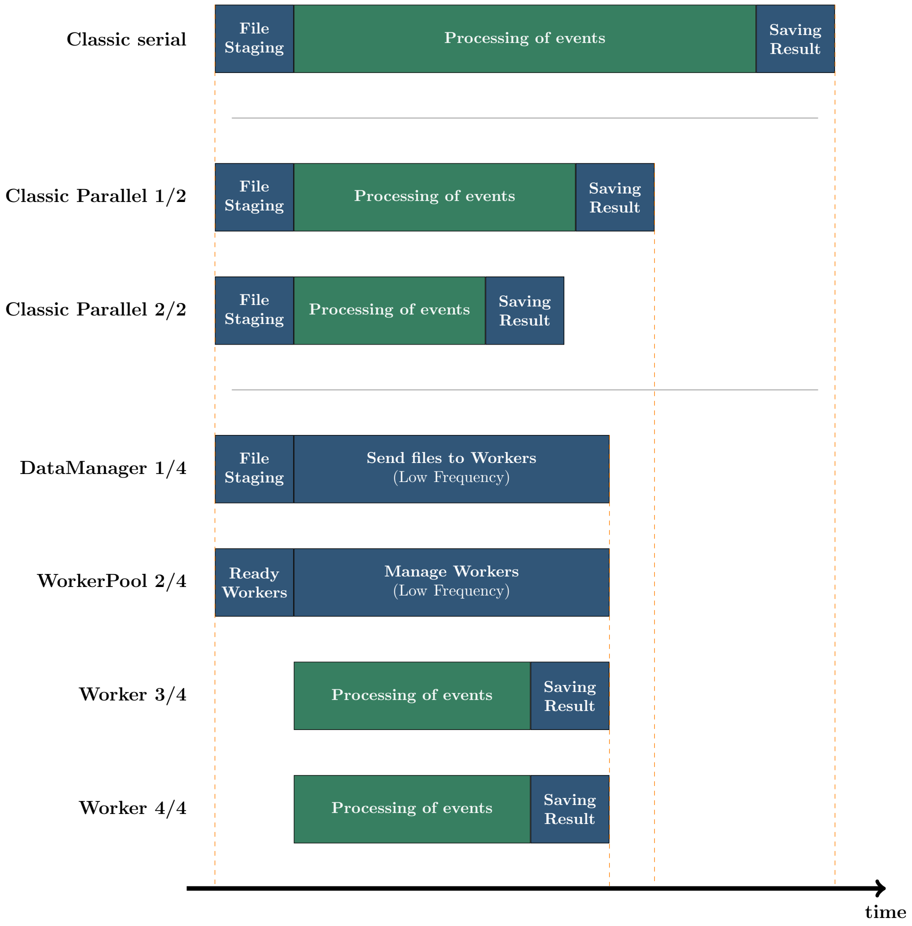

Figure A.4: Temporal occupancy of the algorithm in different scenarios. The fraction of non-parallelizable workload is represented in blue and the the parallelizable fraction is represented in green.

work based on file size, number of events per Run or even a priority list based on process rank (which can be associated with CPU speed, for example).

A.3.5.3 WorkerPool

Finally comes the manager of the *Worker*'s, the *WorkerPool*. This role is responsible for managing each of the *Worker*'s, giving them work as soon as they are freed from their previous task, also dialoguing with the *DataManager* to ensure the correct transfer of information, and at the end, after the *DataManager* has given the signal, closing them down in a controlled manner.

As can be seen in the figure A.6b, this function manages the *Worker*'s between two queues, the "busy" and the "idle". Using an asynchronous request scheme and status management, the *WorkerPool* waits for the completion of these requests as a signal that the *Worker* has successfully completed its work and can now have more work assigned to it.

The choice of this (apparently) symmetric work distribution scheme (the number of Runs assigned to each *Worker* is a constant) but with a control system based on FIFO (First in First out), always guarantees that any asymmetry that the system may have is compensated, since processes do not wait for the others to wait to present a result (commonly used in numerical schemes where work is sibling distributed). This scenario can be seen in the figure A.7.

Imagining a solution of a differential equation, the space is divided into equal fractions

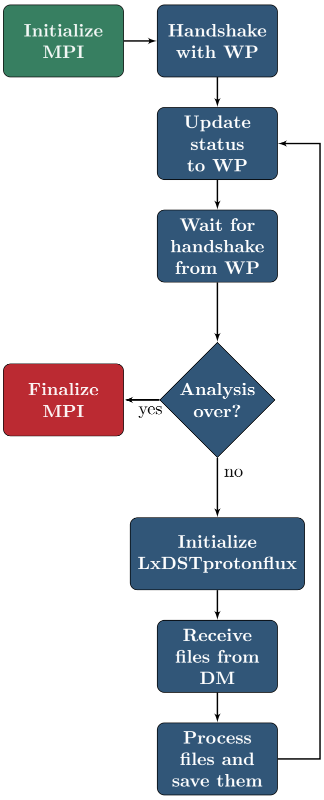

Figure A.5: Worker diagram where **W** stands for worker, **WP** stands for WorkerPool and **DM** stands for DataManager.

and distributed equally between the processes, at the end being merged the different partial results. In a mixed network of different processors, this blind scheme would result in a very high dead time. With few adaptations, this scheme can be used in these numerical systems. Between iterations the speed (or occupancy rate) of each processor can be evaluated and the work can then be distributed based on that.

This choice is ideal for this case given the disparity in size between different AMS files (from 5Gb to 10Gb per Run).

A final advantage of this process management system arises when the computing system is hybrid and different machines of different performance levels are used at the same time. The management processes (*DataManager* and *WorkerPool*) can be allocated to slower machines and the *Worker*'s to faster machines, optimising the occupation of the processors.

Finally, for system stability reasons, whenever possible, communications were designed to take the form of handshakes (send 1 → 2, answer 2 → 1, answer 1 → 2) with controlled outputs. The dependence on a stable connection to CERN and the EOS system requires some safeguards to be ensured so that in the event of data corruption or loss of Internet connection, it is not necessary to redo the whole analysis.

A.3.6 Performance

At three separate times, performance tests were performed on the code, based on runtime.

The results are presented with the number of processes starting at 3 since the program under study requires at least 3 processes to run (*Worker*, *WorkerPool* and *DataManager*). The relative time gain (also known as *speedup*) $G(N)$[200] is calculated using the following

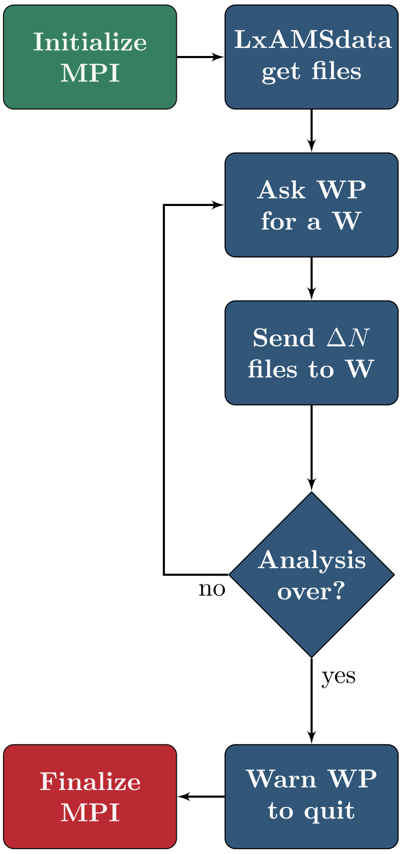

(a) DataManager diagram where **W** stands for worker, **WP** stands for WorkerPool and **DM** stands for DataManager.

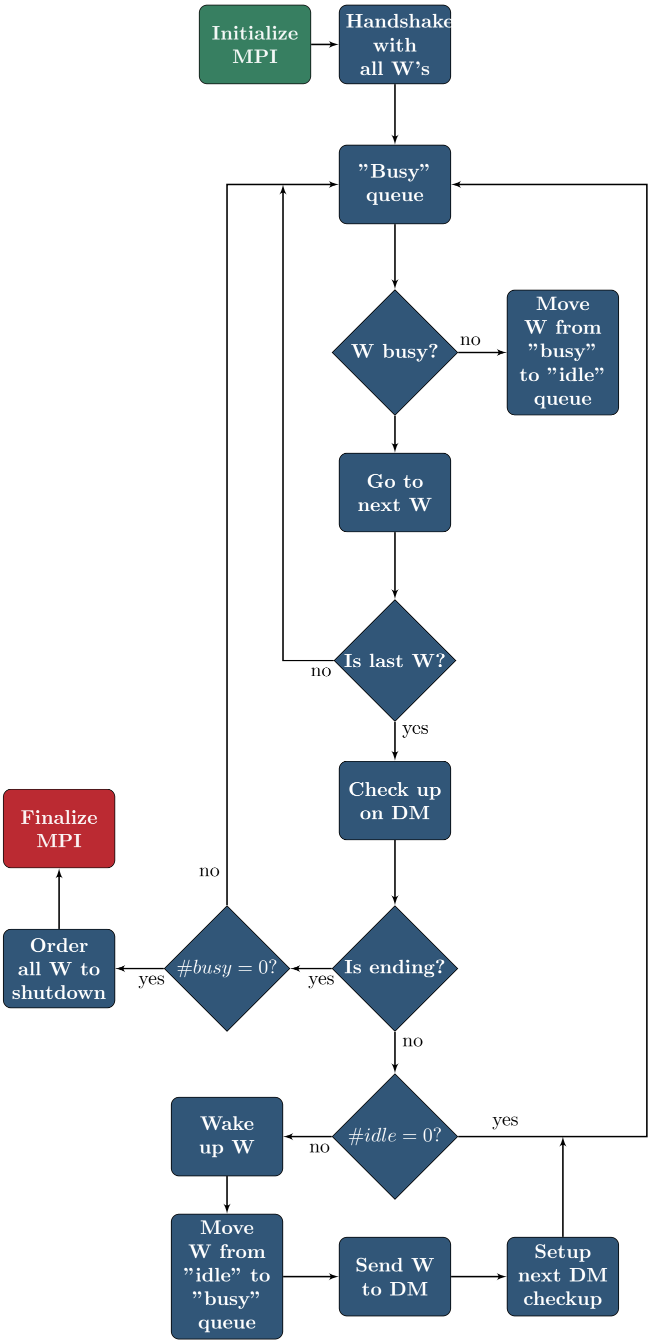

(b) WorkerPool diagram where **W** stands for worker, **WP** stands for WorkerPool and **DM** stands for DataManager.

expression:

$$G(N) = \frac{T(3)}{T(N)}$$

where $T(N)$ is the execution time in seconds for a number N of processes.

The gain represents how much faster the code gets when parallelised, and is a representation of the increased time efficiency of the code due to the reduction in time spent on the parallelisable fraction of the code [200].

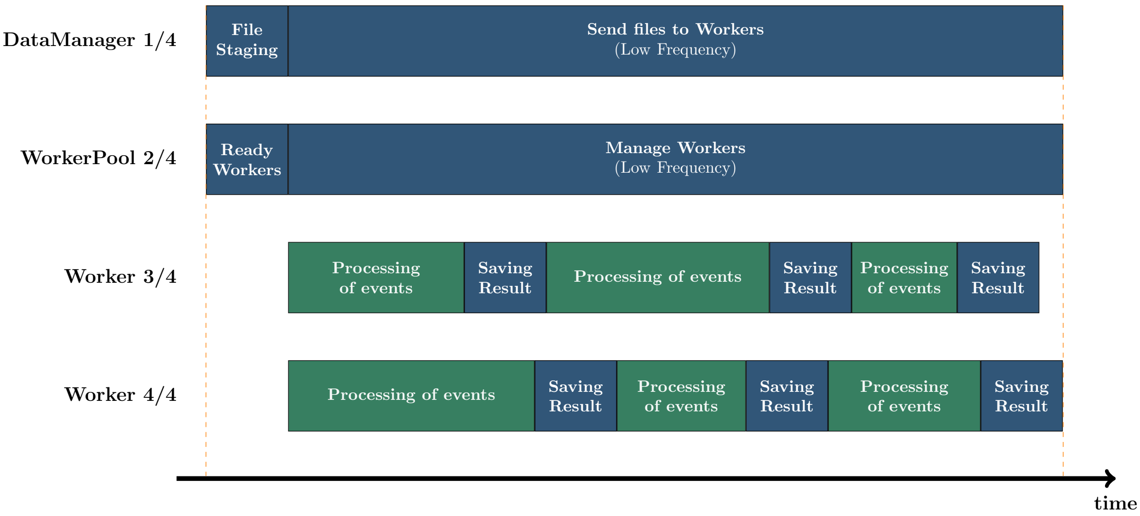

Figure A.7: Temporal occupancy of the algorithm in the FIFO scenario. The fraction of non-parallelizable workload is represented in blue and the the parallelizable fraction is represented in green.

A.3.6.1 Intel i7

On an Intel i7 4770HQ 2.20 GHz processor with 4 colours on a personal computer. In this case, all events from each file were processed and 1 file out of 14 was assigned to each *Worker* at a time. Results are shown in Figure A.8.

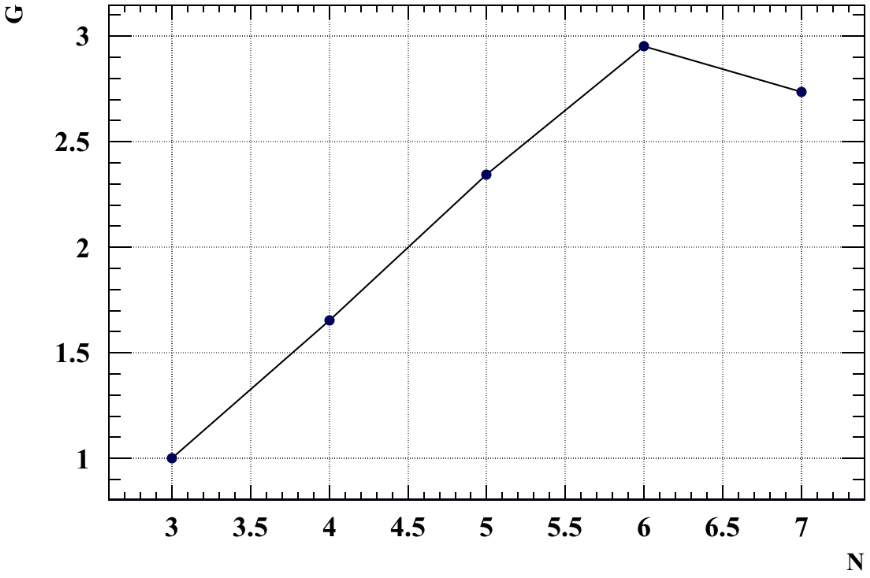

Figure A.8: Temporal gain of the algorithm for the i7 processor.

By inspection of Figure A.8 it is possible to observe a linear improvement until saturation is reached.

This behaviour indicates a good application of parallelisation, there is a reduction in the time spent on the part of the code that is parallelisable and this gain outweighs the serialised [201] part. This system is represented in the figure A.4.

The linear effect of parallelism disappears when the number of processes is increased to more than 6 (4 *Worker*'s). Given that the processor in this case has only 4 colours, it is possible to observe that the internal hyperthreading management (which doubles the performance in the best case scenario), done by the processor, continues to have gains up to 6 processes. From this value on the occupancy rate of each of the colours is increased and the addition of one more process generates such a dead time between processor clocks that a reduction in efficiency is seen (which is reflected in the gain) and an increase in the total execution time.

This very low impact that management processes have on total execution time shows that a comparison can be made with the classic case of parallelism (done only at the file level).

It is important to note that for this processor, the data was on an SSD disk connected by a USB 3 connection.

A.3.6.2 Intel Xeon

In a new platform, performance tests were performed again for the same code. It consists of a farm of 3 Intel Xeon L5420 2.50 GHz processors with 8 colours each. In this scenario, all the events present in a total of 49 Runs (files) were processed. These 49 files occupy 265Gb and are equivalent to approximately 19 days of data which, at the time of writing, is a small fraction of the AMS data that has been in acquisition for over 2000 days.

The storage capacity of this system allowed the use of more files and, using a process management system (SUN Grid), it was possible to do the temporal analysis efficiently (the slowest process takes more than 3 hours to run).

A.3.6.3 Results

The code to be analysed on this platform was run for different numbers of processes and the results are shown in figure A.9.

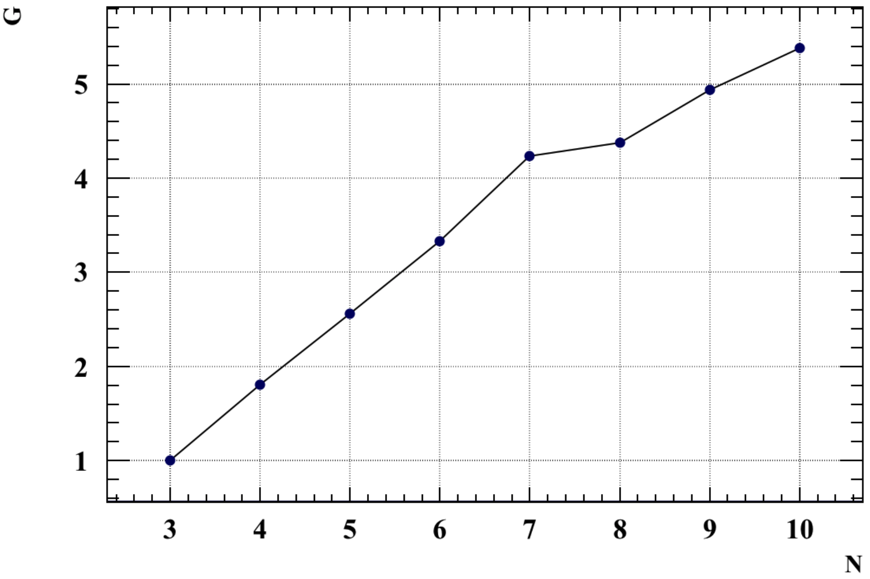

Figure A.9: Temporal gain of the algorithm for the Xeon processor.

In the A.9 figure a linear improvement of the gain is observed, similar to the previous case.

A.3.6.4 Benchmarking

To have a term of comparison, a test was made to measure the time taken by the algorithm when run serially under all the files and, then, the execution time was measured in the case of classic parallelization of this code, that is, the code was run under subsets of files and the time taken was measured until all the files had been analysed. These subsets were constructed by doing the integer division of the total number of files ($49 = 25 + 24 = 17 + 16 + 16 = \dots$) by alphabetical order of the files. The timing test was done in the case of the Xeon processor to ensure that there is a large enough variety of files to reduce sensitivity to the error associated with the integer division of the total number of files.

Table A.2: Benchmarking results. ΔT represents the temporal difference between the longest and shortest process.

Processes	1	2	3	4	5	6
T (s)	11430	7005	4901	4428	2804	2483
		4601	3255	3274	2660	2211
			2786	2627	1771	1625
				2433	1762	1481
					1468	1406
						1255
$T_{\max}$ (s)	11430	7005	4901	4428	2804	2483
ΔT	0	2404	2115	1995	1336	1228
$\varepsilon = 1 - \frac{\Delta T}{T_{\max}}$	1	0.657	0.5568	0.550	0.524	0.505

The maximum times recorded during these tests are shown in figure A.10. The comparison is made between the parallelized code and the maximum execution time of the subprocesses in the classical case given that, from the point of view of Physics analysis, one cannot start analysing the histograms until all the events are selected.

By inspection of the A.2 table it can be seen that there is inherent inefficiency in processing files of different sizes. This effect increases with the number of processes since the processing time of an additional file represents a higher inefficiency in relation to the total execution time of the analysis.

This is precisely the effect that we intend to overcome with the algorithm proposed in this paper.

Additionally, one must take into account that the serial component of the code is not, by definition, reduced by parallelization, implying that with larger numbers of processes, the total execution time tends towards the serial component of the code.

By inspection of the figure A.10 it can be seen that for all the numbers of processes analysed, the execution time of the algorithm under analysis is always lower than the classical case. This effect can be attributed to the loss of some serial time that is controlled by the 2 management processes and that have very low impact on the CPU and to the increased processor occupancy efficiency that these processes implement.

The comparison of the relative gain of the two parallelization methods can be seen in figure A.11.

In this one can see that the algorithm proposed in the article still has a higher gain than the classical method. The only moment in which the classical method becomes superior to the algorithm under study comes from a lowering of gain of the algorithm under study whose causes will be studied next. Even with this difference in gain, it should be noted that the execution time of the classical method is still superior to the algorithm proposed in this paper.

In the figure A.12 the change in slope can be seen. This lowering of efficiency may be related to disk access time. The data was on mechanical disks and querying different physical zones of the same disk could result in a *bottleneck* effect, reducing the efficiency of the algorithm. This effect would be visible both when reading the files and writing the results.

Other causes may be related to problems in the MPI library itself and in the local installation done, or to the latency associated with communication between the different processors (from 8, the machine either changes processor or over allocates the processor on which it is

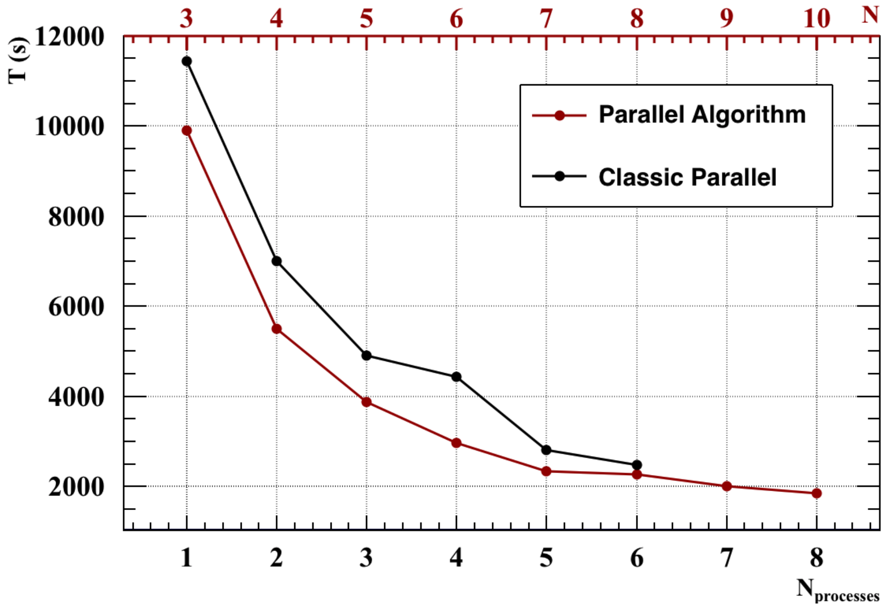

Figure A.10: Execution time for the classic parallelization scheme in comparison with the algorithm being reported on. The red axis represent the number of processes used in the algorithm.

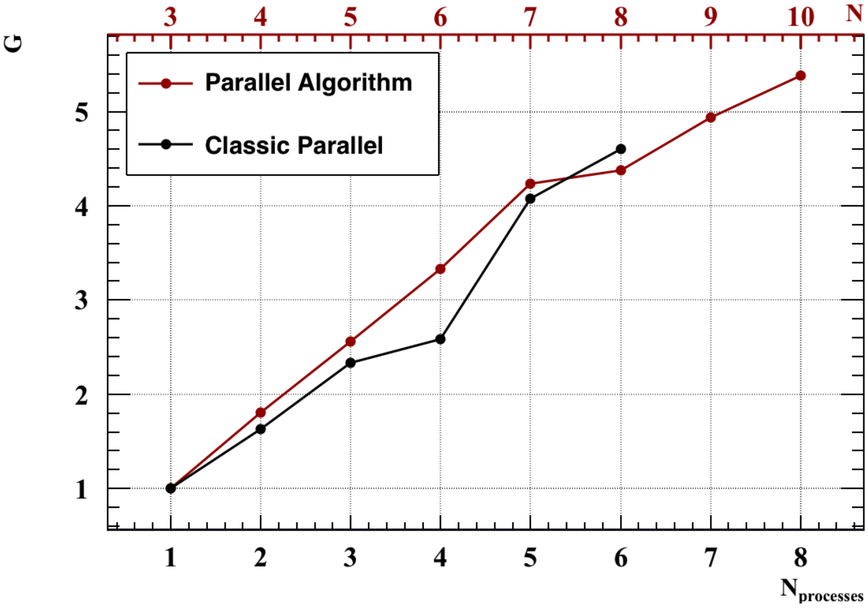

Figure A.11: Gain comparison between the algorithm being reported on and classic parallelization scheme.

executing the other processes). The selection processes were designed to be independent of each other (reducing communication latency) and the management processes have a very low data flow for the same reason.

A.3.7 Platform comparison

After the tests on both platforms have been made, an increase in the performance of the algorithm compared to the classical method has been verified, and it has been seen that the management processes induce a positive effect and a negligible CPU occupation, it is necessary

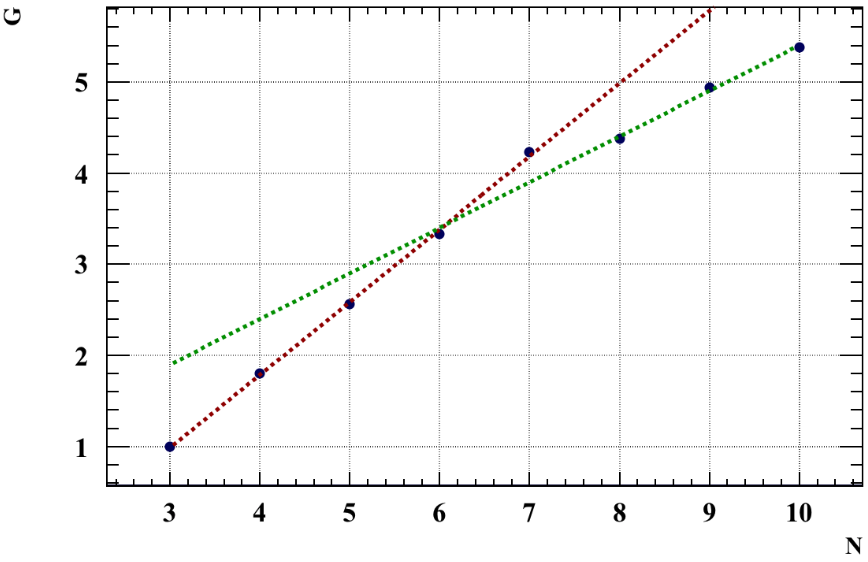

Figure A.12: Temporal gain of the algorithm for the Xeon processor with trend lines for the first 5 points and for the last 3.

to compare the algorithm on the two platforms to look for hardware-related differences. The results are shown in figure A.13.

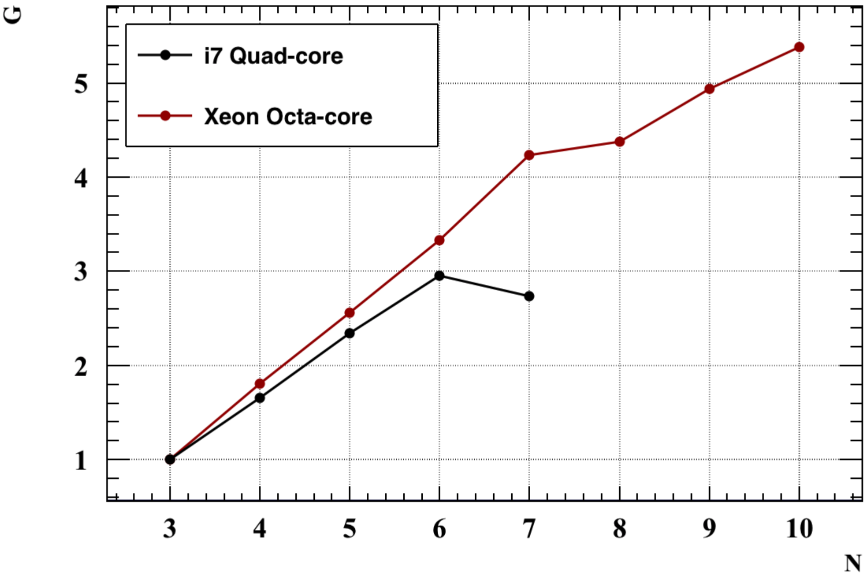

Figure A.13: Results comparison.

By inspection of the figure A.13 it can be seen that the platforms show similar results although the slight difference between slopes indicates that there is a slight difference in the performance of the algorithm with the platform. It is difficult to assess exactly where the Xeon architecture is optimised for this application but its use seems to be comparable to the use of the i7 architecture that has a more commercial focus. Cost per performance has a non-negligible weight in the real world.

Possible causes for this difference in declivity may lie in the non-exclusivity of the i7 processor (which was found in a personal computer). The processes running on the Xeon platform were on a little used farm that contained a process manager.

The over occupation of the processor with the management processes does not seem to be the cause of the slope since if they were, there would be a drop in gain for 5 and 6 processes in the Intel i7 case (in total, 4 *Worker*'s + 2 managers). This did not occur.

For the Xeon platform some instability of the gain is noticeable (for values higher than 7 processes) and this may be due to the disk access time. As said before, all the 250 Gb of files used in this analysis were in a set of mechanical disks. If several files are on the same disk, physical access to the data can result in a strong decrease in access time, especially if several requests are made at the same time by distinct processes for very different areas on the disk.

A.3.8 Conclusions and Prospects

In this work the OpenMPI library was used to parallelize a selection of events in the framework of AMS.

The different possible parallelization scenarios are evaluated and a heterogeneous model with FIFO (first in first out) is chosen to manage the occupation of the different selection processes.

The concept of efficiency improvement was proved showing the linear decrease of execution time with the level of code parallelization. This performance analysis was done for three different scenarios and distinct behaviours were seen in which some causes for the performance degradation for larger numbers of processes were pointed out.

Regarding the efficiency of the scheme, the use of 2 low-frequency processes (only management), which can be seen as an addition of a serial fraction in a code that is intended to be parallelized, does not have a significant negative impact on the processor occupation but has a positive impact on the management that allows the files and the analysis processes to be done.

This parallelisation scheme is currently being tested for use in the analysis of the temporal variations of proton fluxes in AMS. It is intended to transform this system into a wrapper class from which it inherits and which parallelizes the algorithm in question.

It is also intended to extend this algorithm to hybrid computer networks in which the lower performance tasks (*DataManager* and *WorkerPool*) are given to weaker processors due to their lower demand.

As a last criticism, it should be pointed out that in another topology, the use of two managers could be merged into one since the tasks of worker management and file distribution are two inherently linked processes.

Bibliography

[1] R. L. Workman et al. 'Review of Particle Physics'. In: *PTEP* 2022 (2022), p. 083C01. DOI: `10.1093/ptep/ptac097`.

[2] Theodor Wulf. 'Observations on the radiation of high penetration power on the Eiffel tower'. In: *Physikalische Zeitschrschift* 11 (1910), p. 811.

[3] Albert Gockel. 'Observations on the radiation of high penetration power on the Eiffel tower'. In: *Physikalische Zeitschrschift* 12 (1911), p. 595.

[4] 'Nobel Prize for Physics: Prof. Victor F. Hess'. In: *Nature* 138.3499 (Nov. 1936), pp. 873–873. ISSN: 1476-4687. DOI: `10.1038/138873b0`. URL: `https://doi.org/10.1038/138873b0`.

[5] Victor Francis Hess. 'On the observation of the penetrating radiation in seven free balloon campaigns'. In: *Physikalische Zeitschrschift* 13 (1912), p. 1084.

[6] W. Kolhörster. 'Messungen der durchdringenden Strahlungen bis in Höhen von 9300 m.' In: *Verhandlungen der Deutschen Physikalischen Gesellschaft* 16 (1914), pp. 719–721.

[7] R. A. Millikan and G. H. Cameron. 'The Origin of the Cosmic Rays'. In: *Phys. Rev.* 32 (4 Oct. 1928), pp. 533–557. DOI: `10.1103/PhysRev.32.533`. URL: `https://link.aps.org/doi/10.1103/PhysRev.32.533`.

[8] Jacob Clay. 'Penetrating radiation'. In: *Proceedings of the Royal Academy of Amsterdam* 30 (1927), pp. 1115–1127.

[9] Bruno Rossi. 'On the Magnetic Deflection of Cosmic Rays'. In: *Physical Review* 36 (1930), p. 606.

[10] Thomas H. Johnson. 'The Azimuthal Asymmetry of the Cosmic Radiation'. In: *Physical Review* 43 (1933), pp. 834–835.

[11] Luis Alvarez and Arthur Holly Compton. 'A Positively Charged Component of Cosmic Rays'. In: *Physical Review* 43 (1933), pp. 835–836.

[12] Bruno Rossi. 'Directional Measurement on the Cosmic Rays Near the Geomagnetic Equator'. In: *Physical Review* 45 (1934), pp. 212–214.

[13] Homi Bhabha and Walter Heitler. 'The Passage of Fast Electrons and the Theory of Cosmic Showers'. In: *Proceedings of the Royal Society of London* 159 (1937), pp. 432–458.

[14] Alessandro De Angelis. 'Spontaneous ionization to subatomic physics: Victor Hess to Peter Higgs'. In: *Nuclear Physics B - Proceedings Supplements* 243-244 (2013). Proceedings of the IV International Conference on Particle and Fundamental Physics in Space, pp. 3–11. ISSN: 0920-5632. DOI: `https://doi.org/10.1016/j.nuclphysbps.2013.09.008`. URL: `https://www.sciencedirect.com/science/article/pii/S092056321300532X`.

[15] Enrico Fermi. 'On the Origin of the Cosmic Radiation'. In: *American Physical Society* 75.8 (1949), pp. 1169–1174.

[16] Elena Amato. ‘The origin of galactic cosmic rays’. In: *International Journal of Modern Physics D* 23.7 (1430013 2014). DOI: `10.1142/S0218271814300134`.

[17] M. Aguilar et al. ‘Precision Measurement of the Proton Flux in Primary Cosmic Rays from Rigidity 1 GV to 1.8 TV with the Alpha Magnetic Spectrometer on the International Space Station’. In: *Phys. Rev. Lett.* 114 (17 Apr. 2015), p. 171103. DOI: `10.1103/PhysRevLett.114.171103`. URL: `https://link.aps.org/doi/10.1103/PhysRevLett.114.171103`.

[18] M. Aguilar et al. ‘Precision Measurement of the Helium Flux in Primary Cosmic Rays of Rigidities 1.9 GV to 3 TV with the Alpha Magnetic Spectrometer on the International Space Station’. In: *Phys. Rev. Lett.* 115 (21 Nov. 2015), p. 211101. DOI: `10.1103/PhysRevLett.115.211101`. URL: `https://link.aps.org/doi/10.1103/PhysRevLett.115.211101`.

[19] M. Aguilar et al. ‘Properties of Neon, Magnesium, and Silicon Primary Cosmic Rays Results from the Alpha Magnetic Spectrometer’. In: *Phys. Rev. Lett.* 124 (21 May 2020), p. 211102. DOI: `10.1103/PhysRevLett.124.211102`. URL: `https://link.aps.org/doi/10.1103/PhysRevLett.124.211102`.

[20] M. Aguilar et al. ‘Properties of Iron Primary Cosmic Rays: Results from the Alpha Magnetic Spectrometer’. In: *Phys. Rev. Lett.* 126 (4 Jan. 2021), p. 041104. DOI: `10.1103/PhysRevLett.126.041104`. URL: `https://link.aps.org/doi/10.1103/PhysRevLett.126.041104`.

[21] A. D. Panov et al. ‘Elemental Energy Spectra of Cosmic Rays from the Data of the ATIC-2 Experiment’. In: *Bull. Russian Acad. of Science: Physics* 71.4 (2007).

[22] K. Abe et al. ‘MEASUREMENTS OF COSMIC-RAY PROTON AND HELIUM SPECTRA FROM THE BESS-POLAR LONG-DURATION BALLOON FLIGHTS OVER ANTARCTICA’. In: *The Astrophysical Journal* 822 (2016). ISSN: 65. DOI: `10.3847/0004-637X/822/2/65`.

[23] H. S. Ahn et al. ‘Energy spectra of cosmic-ray nuclei at high energies’. In: *Astrophys. J.* 707 (2009).

[24] Dietrich Mueller et al. ‘Energy Spectra and Composition of Primary Cosmic Rays’. In: *The Astrophysical Journal* 374 (June 1991), p. 356. DOI: `10.1086/170125`.

[25] H. S. Ahn et al. ‘Charge composition and energy spectra of cosmic-ray nuclei for elements from Be to NI - Results from HEAO-3-C2’. In: *Astron. & Astrophys.* 233.1 (1990).

[26] F. Aharonian et al. ‘First ground-based measurement of atmospheric Cherenkov light from cosmic rays’. In: *Phys. Rev. D* 75 (4 Feb. 2007), p. 042004. DOI: `10.1103/PhysRevD.75.042004`. URL: `https://link.aps.org/doi/10.1103/PhysRevD.75.042004`.

[27] K. Asakimori et al. ‘Cosmic-Ray Proton and Helium Spectra: Results from the JACEE Experiment’. In: *The Astrophysical Journal* 502.1 (July 1998), pp. 278–283. DOI: `10.1086/305882`.

[28] O. Adriani et al. ‘PAMELA Measurements of Cosmic-Ray Proton and Helium Spectra’. In: *Science* 332.6025 (2011), pp. 69–72. DOI: `10.1126/science.1199172`. eprint: `https://www.science.org/doi/pdf/10.1126/science.1199172`. URL: `https://www.science.org/doi/abs/10.1126/science.1199172`.

[29] V. A. Derbina et al. ‘Cosmic-Ray Spectra and Composition in the Energy Range of 101000 TeV per Particle Obtained by the RUNJOB Experiment’. In: *Ap. J.* 628 (2005).

[30] M. Ave et al. ‘Composition of Primary Cosmic-Ray Nuclei at High Energies’. In: *The Astrophysical Journal* 678.1 (2008), pp. 262–273.

[31] A. Archer et al. 'Measurement of the iron spectrum in cosmic rays by VERITAS'. In: *Phys. Rev. D* 98 (2 July 2018), p. 022009. DOI: `10.1103/PhysRevD.98.022009`. URL: `https://link.aps.org/doi/10.1103/PhysRevD.98.022009`.

[32] M. Aguilar et al. 'Observation of the Identical Rigidity Dependence of He, C, and O Cosmic Rays at High Rigidities by the Alpha Magnetic Spectrometer on the International Space Station'. In: *Phys. Rev. Lett.* 119 (25 Dec. 2017), p. 251101. DOI: `10.1103/PhysRevLett.119.251101`. URL: `https://link.aps.org/doi/10.1103/PhysRevLett.119.251101`.

[33] K. A. Lave et al. 'GALACTIC COSMIC-RAY ENERGY SPECTRA AND COMPOSITION DURING THE 2009–2010 SOLAR MINIMUM PERIOD'. In: *The Astrophysical Journal* 770.2 (2013). DOI: `10.1088/0004-637X/770/2/117`.

[34] G.A. de Nolfo et al. 'Observations of the Li, Be, and B isotopes and constraints on cosmic-ray propagation'. In: *Advances in Space Research* 38.7 (2006). Galactic and Extragalactic Astrophysics, pp. 1558–1564. ISSN: 0273-1177. DOI: `https://doi.org/10.1016/j.asr.2006.09.008`. URL: `https://www.sciencedirect.com/science/article/pii/S0273117706004947`.

[35] R. P. Murphy et al. 'GALACTIC COSMIC RAY ORIGINS AND OB ASSOCIATIONS: EVIDENCE FROM SuperTIGER OBSERVATIONS OF ELEMENTS 26Fe THROUGH 40Zr'. In: *The Astrophysical Journal* 831.2 (2016). DOI: `10.3847/0004-637X/831/2/148`.

[36] B. F. Rauch et al. 'COSMIC RAY ORIGIN IN OB ASSOCIATIONS AND PREFERENTIAL ACCELERATION OF REFRACTORY ELEMENTS: EVIDENCE FROM ABUNDANCES OF ELEMENTS 26Fe THROUGH 34Se'. In: *The Astrophysical Journal* 697.2 (2009). DOI: `10.1088/0004-637X/697/2/2083`.

[37] K. Lodders, H. Palme and H.-P. Gail. *4.4 Abundances of the elements in the Solar System: Datasheet from Landolt-Börnstein - Group VI Astronomy and Astrophysics · Volume 4B: "Solar System" in SpringerMaterials (https://doi.org/10.1007/978-3-540-88055-4_34)*. Ed. by J.E. Trümper. accessed 2023-02-08. Springer-Verlag Berlin Heidelberg. DOI: `10.1007/978-3-540-88055-4_34`. URL: `https://materials.springer.com/lb/docs/sm_lbs_978-3-540-88055-4_34`.

[38] M. Aguilar et al. 'The Alpha Magnetic Spectrometer (AMS) on the international space station: Part II - Results from the first seven years'. In: *Physics Reports* 894 (2021). The Alpha Magnetic Spectrometer (AMS) on the International Space Station: Part II - Results from the First Seven Years, pp. 1–116. ISSN: 0370-1573. DOI: `https://doi.org/10.1016/j.physrep.2020.09.003`. URL: `https://www.sciencedirect.com/science/article/pii/S0370157320303434`.

[39] M. Ackermann et al. 'Detection of the Characteristic Pion-Decay Signature in Supernova Remnants'. In: *Science* 339.6121 (2013), pp. 807–811.

[40] Pasquale Blasi. 'The origin of galactic cosmic rays'. In: *The Astronomy and Astrophysics Review* 21.1 (Nov. 2013), p. 70. ISSN: 1432-0754. DOI: `10.1007/s00159-013-0070-7`. URL: `https://doi.org/10.1007/s00159-013-0070-7`.

[41] Isabelle A. Grenier, John H. Black and Andrew W. Strong. 'The Nine Lives of Cosmic Rays in Galaxies'. In: *Annual Review of Astronomy and Astrophysics* 53.1 (2015), pp. 199–246. DOI: `10.1146/annurev-astro-082214-122457`. eprint: `https://doi.org/10.1146/annurev-astro-082214-122457`. URL: `https://doi.org/10.1146/annurev-astro-082214-122457`.

[42] Andrew W. Strong, Igor V. Moskalenko and Vladimir S. Ptuskin. 'Cosmic-Ray Propagation and Interactions in the Galaxy'. In: *Annual Review of Nuclear and Particle Science* 57.1 (2007), pp. 285–327. DOI: `10.1146/annurev.nucl.57.090506.123011`. URL: `https://doi.org/10.1146/annurev.nucl.57.090506.123011`.

[43] Ilya Usoskin. 'Heliospheric Physics and Cosmic Rays'. Lecture Notes from Heliospheric Physics and Cosmic Rays course at University of Oulu. 2003.

[44] R. A. Mewaldt, A. C. Cummings and E. C. Stone. 'Anomalous cosmic rays: Interstellar interlopers in the heliosphere and magnetosphere'. In: *Eos, Transactions American Geophysical Union* 75.16 (1994), pp. 185–193. DOI: `https://doi.org/10.1029/94EO00864`. eprint: `https://agupubs.onlinelibrary.wiley.com/doi/pdf/10.1029/94EO00864`. URL: `https://agupubs.onlinelibrary.wiley.com/doi/abs/10.1029/94EO00864`.

[45] M. Aguilar et al. 'Observation of New Properties of Secondary Cosmic Rays Lithium, Beryllium, and Boron by the Alpha Magnetic Spectrometer on the International Space Station'. In: *Phys. Rev. Lett.* 120 (2 Jan. 2018), p. 021101. DOI: `10.1103/PhysRevLett.120.021101`. URL: `https://link.aps.org/doi/10.1103/PhysRevLett.120.021101`.

[46] L. Accardo et al. 'High Statistics Measurement of the Positron Fraction in Primary Cosmic Rays of 0.5–500 GeV with the Alpha Magnetic Spectrometer on the International Space Station'. In: *Phys. Rev. Lett.* 113 (12 Sept. 2014), p. 121101. DOI: `10.1103/PhysRevLett.113.121101`. URL: `https://link.aps.org/doi/10.1103/PhysRevLett.113.121101`.

[47] M. Aguilar et al. 'Observation of Complex Time Structures in the Cosmic-Ray Electron and Positron Fluxes with the Alpha Magnetic Spectrometer on the International Space Station'. In: *Phys. Rev. Lett.* 121 (5 July 2018), p. 051102. DOI: `10.1103/PhysRevLett.121.051102`. URL: `https://link.aps.org/doi/10.1103/PhysRevLett.121.051102`.

[48] M. Aguilar et al. 'Antiproton Flux, Antiproton-to-Proton Flux Ratio, and Properties of Elementary Particle Fluxes in Primary Cosmic Rays Measured with the Alpha Magnetic Spectrometer on the International Space Station'. In: *Phys. Rev. Lett.* 117 (9 Aug. 2016), p. 091103. DOI: `10.1103/PhysRevLett.117.091103`. URL: `https://link.aps.org/doi/10.1103/PhysRevLett.117.091103`.

[49] Elena Amato and Pasquale Blasi. 'Cosmic ray transport in the Galaxy: A review'. In: *Advances in Space Research* 62.10 (2018). Origins of Cosmic Rays, pp. 2731–2749. ISSN: 0273-1177. DOI: `https://doi.org/10.1016/j.asr.2017.04.019`. URL: `http://www.sciencedirect.com/science/article/pii/s0273117717302995`.

[50] M. Aguilar et al. 'Properties of Cosmic Helium Isotopes Measured by the Alpha Magnetic Spectrometer'. In: *Phys. Rev. Lett.* 123 (18 Nov. 2019), p. 181102. DOI: `10.1103/PhysRevLett.123.181102`. URL: `https://link.aps.org/doi/10.1103/PhysRevLett.123.181102`.

[51] Nicola Tomassetti and Fiorenza Donato. 'THE CONNECTION BETWEEN THE POSITRON FRACTION ANOMALY AND THE SPECTRAL FEATURES IN GALACTIC COSMIC-RAY HADRONS'. In: *The Astrophysical Journal* 803.2 (Apr. 2015), p. L15. ISSN: 2041-8213. DOI: `10.1088/2041-8205/803/2/l15`. URL: `http://dx.doi.org/10.1088/2041-8205/803/2/L15`.

[52] Yoann Génolini et al. 'Current status and desired precision of the isotopic production cross sections relevant to astrophysics of cosmic rays: Li, Be, B, C, and N'. In: *Phys. Rev. C* 98 (3 Sept. 2018), p. 034611. DOI: `10.1103/PhysRevC.98.034611`. URL: `https://link.aps.org/doi/10.1103/PhysRevC.98.034611`.

[53] G. Jóhannesson et al. 'BAYESIAN ANALYSIS OF COSMIC RAY PROPAGATION: EVIDENCE AGAINST HOMOGENEOUS DIFFUSION'. In: *The Astrophysical Journal* 824.1 (2016). DOI: `10.3847/0004-637X/824/1/16`.

[54] H. Moraal. 'Cosmic-Ray Modulation Equations'. In: *Space Science Reviews* 176.1–4 (2011), pp. 299–319.

[55] Ludwig Biermann and Arnulf Schlüter. 'Cosmic Radiation and Cosmic Magnetic Fields. II. Origin of Cosmic Magnetic Fields'. In: *Physical Review* 82.6 (1951), pp. 863–868.

[56] Ludwig Biermann, B. Brosowski and H. U. Schmidt. 'The interaction of the solar wind with a comet'. In: *Solar Physics* 1.2 (1967), pp. 254–284.

[57] P. Jenniskens NASA Ames Research Center/K. Jobse. *This is an artist's concept of a comet dust trail and dust tail. The trail can only be seen in the light of radiated heat. The dust trail is made of particles that are the size of sand grains and pebbles. They are large enough that they are not affected much by the Sun's light and solar wind. The dust tail, on the other hand, is made of grains the size of cigarette-smoke particles. These grains are blown out of the dust coma near the comet nucleus by the Sun's light.* (Visited on 13/02/2019).

[58] E. N. Parker. 'Dynamics of the Interplanetary Gas and Magnetic Fields'. In: *The Astrophysical Journal* 128 (1958), pp. 664–676.

[59] H. C. Spruit. 'Essential Magnetohydrodynamics for Astrophysics'. In: *arXiv:1301.5572 [astro-ph.IM]* (2017). URL: `https://arxiv.org/pdf/1301.5572.pdf`.

[60] Mathew J. Owens and Robert J. Forsyth. 'The Heliospheric Magnetic Field'. In: *Living Reviews in Solar Physics* 10.1 (Nov. 2013), p. 5. ISSN: 1614-4961. DOI: `10.12942/lrsp-2013-5`. URL: `https://doi.org/10.12942/lrsp-2013-5`.

[61] Norman F. Ness, Clell S. Scearce and Joseph B. Seek. 'Initial Results of the Imp 1 Magnetic Field Experiment'. In: *American Geophysical Research* 69.17 (1964), pp. 3531–3569.

[62] E. N. Parker. 'A history of early work on the heliospheric magnetic field'. In: *Journal of Geophysical Research* 106.A8 (2001), pp. 15797–15801.

[63] E. N. Parker. 'The Stellar-Wind Regions.' In: *Astrophysical Journal* 134 (July 1961), p. 20. DOI: `10.1086/147124`.

[64] D. J. McComas et al. 'The Heliosphere's Interstellar Interaction: No Bow Shock'. In: *Science* 336 (2012), pp. 1291–1293.

[65] K. Dialynas et al. 'The bubble-like shape of the heliosphere observed by Voyager and Cassini'. In: *Nature Astronomy* 1.5 (Apr. 2017), p. 0115. ISSN: 2397-3366. DOI: `10.1038/s41550-017-0115`. URL: `http://dx.doi.org/10.1038/s41550-017-0115`.

[66] Margaret G. Kivelson and Christopher T. Russel. *Introduction to Space Physics*. Cambridge University Press, 1995.

[67] NASA/SDO. *An M-class solar flare erupts from the right side of the sun in this image from shortly before midnight EST on Jan. 12, 2015. The image blends two wavelengths of light – 171 and 304 angstroms – as captured by NASA's Solar Dynamics Observatory.* 2014. URL: `https://www.nasa.gov/content/goddard/nasa-releases-images-of-1st-notable-solar-flare-of-2015` (visited on 13/04/2022).

[68] S. E. Forbush. 'On the Effects in Cosmic-Ray Intensity Observed During the Recent Magnetic Storm'. In: *Phys. Rev.* 51 (12 June 1937), pp. 1108–1109. DOI: `10.1103/PhysRev.51.1108.3`. URL: `https://link.aps.org/doi/10.1103/PhysRev.51.1108.3`.

[69] J. Todd Hoeksema. 'The large-scale structure of the heliospheric current sheet during the Ulysses epoch'. In: *Space Science Reviews* 72.1-2 (Apr. 1995), pp. 137–148. ISSN: 1572-9672. DOI: `10.1007/bf00768770`. URL: `http://dx.doi.org/10.1007/BF00768770`.

[70] Xudong Sun et al. 'On Poplar Magnetic Field Reversal And Surface Flux Transport During Solar Cycle 24'. In: *The Astrophysical Journal* 798.2 (Jan. 2015), p. 114. ISSN: 1538-4357. DOI: `10.1088/0004-637x/798/2/114`. URL: `http://dx.doi.org/10.1088/0004-637X/798/2/114`.

[71] E.N. Parker. 'The passage of energetic charged particles through interplanetary space'. In: *Planetary and Space Science* 13.1 (1965), pp. 9–49. ISSN: 0032-0633. DOI: `https://doi.org/10.1016/0032-0633(65)90131-5`. URL: `http://www.sciencedirect.com/science/article/pii/0032063365901315`.

[72] L. J. Gleeson and W. I. Axford. 'Cosmic Rays in the Interplanetary Medium'. In: *The Astrophysical Journal* 149 (Sept. 1967), p. L115. DOI: `10.1086/180070`. URL: `http://adsabs.harvard.edu/abs/1967ApJ...149L.115G`.

[73] J. R. Jokipii. 'Cosmic-Ray Propagation. I. Charged Particles in a Random Magnetic Field'. In: *The Astrophysical Journal* 146 (1966), pp. 480–487.

[74] Marius S. Potgieter. 'Solar Modulation of Cosmic Rays'. In: *Living Reviews in Solar Physics* 10 (2013). ISSN: 1614-4961. DOI: `10.12942/lrsp-2013-3`. URL: `http://dx.doi.org/10.12942/lrsp-2013-3`.

[75] Andreas Salchi. *Nonlinear Cosmic Ray Diffusion Theories.* Vol. 362. Astrophysics and Space Science Library. Springer, Berlin, Heidelberg, 2009.

[76] John W. Bieber, W. H. Matthaeus and Andreas Shalchi. 'Nonlinear guiding center theory of perpendicular diffusion: General properties and comparison with observation'. In: *Geophysical Research Letters* 31.L10805 (2004). URL: `doi.org/10.1029/2004GL020007`.

[77] W. H. Matthaeus et al. 'Nonlinear Collisionless Perpendicular Diffusion of Charged Particles'. In: *The Astrophysical Journal* 590.1 (May 2003), pp. L53–L56. DOI: `10.1086/376613`.

[78] J. R. Jokipii and E. H. Levy. 'Effects of Particle Drifts on the Solar Modulation of Galactic Cosmic Rays'. In: *The Astrophysical Journal* 213L (1977), pp. 85–88.

[79] C. Pei et al. 'Three-Dimensional Wavy Heliospheric Current Sheet Drifts'. In: *The Astrophysical Journal* 744 (2012), pp. 170–175.

[80] R. A. Burger, H. Moraal and G. M. Webb. 'Drift Theory of Charged Particles in Electric and Magnetic Fields'. In: *Astrophysics and Space Science* 116 (1985), pp. 107–129.

[81] R. A. Burger, H. Moraal and M. S. Potgieter. 'On the Inclusion of a Wavy Neutral Sheet in Two-Dimensional Drift Models'. In: *Proceedings of the 20th International Cosmic Ray Conference Moscow.* Vol. 3. 1987, pp. 283–286.

[82] M. S. Potgieter and H. Moraal. 'A Drift Model For The Modulation of Galactic Cosmic Rays'. In: *The Astrophysical Journal* 294 (1985), pp. 425–440.

[83] J. R. Jokipii and J. M. Davila. 'Effects of Particle Drift on the Transport of Cosmic Rays. IV. More Realistic Diffusion Coefficients'. In: *The Astrophysical Journal* 248 (1981), pp. 1156–1161.

[84] R. A. Burger et al. 'A Fisk-Parker Hybrid Heliospheric Magnetic Field with a Solar-Cycle Dependence'. In: *The Astrophysical Journal* 674 (2008), pp. 511–519.

[85] C. Pei et al. 'A general time-dependent stochastic method for solving Parker's transport equation in spherical coordinates'. In: *Journal of Geophysical Research* 115 (2010).

[86] J. Kóta and J. R. Jokipii. 'Effects of Drifts on the Transport of Cosmic Rays. VI. A Three-Dimensional Model Including Diffusion'. In: *The Astrophysical Journal* 265 (1983), pp. 573–581.

[87] R. A. Burger and M. S. Potgieter. 'The Calculation of Neutral Sheet Drift in Two-Dimensional Cosmic-Ray Modulation Models'. In: *The Astrophysical Journal* 339 (1989), pp. 501–511.

[88] C. Pei et al. 'Cosmic ray diffusion tensor throughout the heliosphere'. In: *Journal of Geophysical Research* 115 (2010).

[89] G. P. Zank, W. H. Matthaeus and J. W. Bieber. 'The radial and latitudinal dependence of the cosmic ray diffusion tensor in the heliosphere'. In: *Journal of Geophysical Research* 103.A2 (1998), pp. 2085–2097.

[90] J. R. Jokipii and David A. Kopriva. 'Effects of Particle Drift on the Transport of Cosmic Rays. III. Numerical Models of Galactic Cosmic-Ray Modulation'. In: *The Astrophysical Journal* 234 (1979), pp. 386–392.

[91] Miguel Reis Orcinha. 'Solar modulation studies and proton-electron separation with the AMS/RICH detector'. MA thesis. Instituto Superior Técnico, 2014.

[92] Rolf Kappl. 'SOLARPROP: Charge-sign dependent solar modulation for everyone'. In: *Computer Physics Communications* 207 (2016), pp. 386–399. ISSN: 0010-4655. DOI: `https://doi.org/10.1016/j.cpc.2016.05.025`. URL: `http://www.sciencedirect.com/science/article/pii/s001046551630159x`.

[93] AMS-02 Collaboration. *AMS-02 The Alpha Magnetic Spectrometer Experiment.* 2014.

[94] M. Aguilar, J. Alcaraz, J. Allaby et al. 'The Alpha Magnetic Spectrometer (AMS) on the International Space Station: Part I - results from the test flight on the space shuttle'. In: *Physics Reports* 366.6 (2002), pp. 331–405.

[95] Samuel Ting. 'Status of the AMS Experiment'. In: 22^{nd} *European Cosmic Ray Symposium.* 2010.

[96] J. Chang et al. 'The DArk Matter Particle Explorer mission'. In: *Astroparticle Physics* 95 (2017), pp. 6–24. ISSN: 0927-6505. DOI: `https://doi.org/10.1016/j.astropartphys.2017.08.005`. URL: `https://www.sciencedirect.com/science/article/pii/S0927650517300841`.

[97] *Cosmic Ray Energetics And Mass - CREAM for the ISS (ISS-CREAM).* 36th International Cosmic Ray Conference - ICRC2019. 2019.

[98] *The CALorimetric Electron Telescope (CALET) on the International Space Station.* 36th International Cosmic Ray Conference - ICRC2019. 2019.

[99] Boris Shwartz Claus Grupen. *Particle Detectors.* Vol. 26. CAMBRIDGE MONOGRAPHS ON PARTICLE PHYSICS , NUCLEAR PHYSICS AND COSMOLOGY. Cambridge University Press, 2008.

[100] Donald J. Williams. 'Charged Particles Trapped In The Earth's Magnetic Field'. In: ed. by H.E. Landsberg and J. van Mieghem. Vol. 15. Advances in Geophysics. Elsevier, 1971, pp. 137–218. DOI: `https://doi.org/10.1016/S0065-2687(08)60302-7`. URL: `https://www.sciencedirect.com/science/article/pii/S0065268708603027`.

[101] M. Kaan Öztürk. 'Trajectories of charged particles trapped in Earth's magnetic field'. In: *American Journal of Physics* 80.5 (2012), pp. 420–428. DOI: `10.1119/1.3684537`. eprint: `https://doi.org/10.1119/1.3684537`. URL: `https://doi.org/10.1119/1.3684537`.

[102] S. M. Krimigis. 'Alpha Particles Trapped in the Earth's Magnetic Field'. In: *Particles and Fields in the Magnetosphere.* Ed. by B. M. McCormac. Dordrecht: Springer Netherlands, 1970, pp. 364–379. ISBN: 978-94-010-3284-1.

[103] F. Barão et al. 'Evaluation of the AMS trigger rate'. Presentation done at Kennedy Space Center offline meeting on trigger rates, geomagnetic efficiency and CRsimD framework. Feb. 2011.

[104] C. C. Finlay et al. 'International Geomagnetic Reference Field: the eleventh generation'. In: *Geophysical Journal International* 183.3 (Dec. 2010), pp. 1216–1230. ISSN: 0956-540X. DOI: `10.1111/j.1365-246X.2010.04804.x`. eprint: `https://academic.oup.com/gji/article-pdf/183/3/1216/1785065/183-3-1216.pdf`. URL: `https://doi.org/10.1111/j.1365-246X.2010.04804.x`.

[105] Erwan Thébault et al. ‘International Geomagnetic Reference Field: the 12th generation’. In: *Earth, Planets and Space* 67.1 (May 2015), p. 79. ISSN: 1880-5981. DOI: `10.1186/s40623-015-0228-9`. URL: `https://doi.org/10.1186/s40623-015-0228-9`.

[106] P. Alken et al. ‘International Geomagnetic Reference Field: the thirteenth generation’. In: *Earth, Planets and Space* 73.1 (Feb. 2021), p. 49. ISSN: 1880-5981. DOI: `10.1186/s40623-020-01288-x`. URL: `https://doi.org/10.1186/s40623-020-01288-x`.

[107] F. Barão and L. Derome. ‘AMS rate evaluation from new physical triggers’. Presentation on acceptance, rates and livetime. Apr. 2011.

[108] M. Aguilar et al. ‘Observation of Fine Time Structures in the Cosmic Proton and Helium Fluxes with the Alpha Magnetic Spectrometer on the International Space Station’. In: *Phys. Rev. Lett.* 121 (5 July 2018), p. 051101. DOI: `10.1103/PhysRevLett.121.051101`. URL: `https://link.aps.org/doi/10.1103/PhysRevLett.121.051101`.

[109] Glen Cowan. *Statistical Data Analysis.* Oxford: Clarendon Press, 1998.

[110] Diego Casadei. ‘Estimating the selection efficiency’. In: *Journal of Instrumentation* 7.08 (Aug. 2012), P08021–P08021. DOI: `10.1088/1748-0221/7/08/p08021`. URL: `https://doi.org/10.1088%2F1748-0221%2F7%2F08%2Fp08021`.

[111] Glen Cowan. ‘Error analysis for efficiency’. Note on the modelling of efficiency estimation and its uncertainty. 2008. URL: `http://www.pp.rhul.ac.uk/~cowan/atlas/efferr.pdf`.

[112] Glen Cowan. ‘A Survey Of Unfolding Methods For Particle Physics’. In: *Proceedings for the Advanced Statistical Techniques in Particle Physics Workshop (2002) of The Institute for Particle Physics Phenomenology.* 2002, pp. 248–257. URL: `https://www.ippp.dur.ac.uk/Workshops/02/statistics/proceedings/cowan.pdf`.

[113] S Schmitt. ‘TUnfold, an algorithm for correcting migration effects in high energy physics’. In: *Journal of Instrumentation* 7.10 (Oct. 2012), T10003–T10003. DOI: `10.1088/1748-0221/7/10/t10003`. URL: `https://doi.org/10.1088/1748-0221/7/10/t10003`.

[114] Volker Blobel. ‘Unfolding Methods in Particle Physics’. In: *Proceedings of the PHYSTAT 2011 Workshop on Statistical Issues Related to Discovery Claims in Search Experiments and Unfolding, CERN, Geneva, Switzerland, 17-20 January 2011.* Jan. 2011, pp. 240–251. DOI: `"10.5170/CERN-2011-006.240"`. URL: `http://cds.cern.ch/record/2203257`.

[115] G. D’Agostini. ‘A multidimensional unfolding method based on Bayes’ theorem’. In: *Nuclear Instruments and Methods in Physics Research Section A: Accelerators, Spectrometers, Detectors and Associated Equipment* 362.2 (1995), pp. 487–498. ISSN: 0168-9002. DOI: `https://doi.org/10.1016/0168-9002(95)00274-X`. URL: `https://www.sciencedirect.com/science/article/pii/016890029500274X`.

[116] M. Aguilar et al. ‘Periodicities in the Daily Proton Fluxes from 2011 to 2019 Measured by the Alpha Magnetic Spectrometer on the International Space Station from 1 to 100 GV’. In: *Phys. Rev. Lett.* 127 (27 Dec. 2021), p. 271102. DOI: `10.1103/PhysRevLett.127.271102`. URL: `https://link.aps.org/doi/10.1103/PhysRevLett.127.271102`.

[117] T. Ullrich and Z. Xu. *Treatment of Errors in Efficiency Calculations.* 2007. DOI: `10.48550/ARXIV.PHYSICS/0701199`. URL: `https://arxiv.org/abs/physics/0701199`.

[118] ‘Hello Solar Cycle 25’. In: *News around National Oceanic and Atmospheric Administration* (Sept. 2020). URL: `https://www.weather.gov/news/201509-solar-cycle`.

[119] Wim van Drongelen. 'Chapter 6 - Continuous, Discrete, and Fast Fourier Transform'. In: *Signal Processing for Neuroscientists (Second Edition)*. Ed. by Wim van Drongelen. Second Edition. Academic Press, 2018, pp. 103–118. ISBN: 978-0-12-810482-8. DOI: `https://doi.org/10.1016/B978-0-12-810482-8.00006-0`. URL: `https://www.sciencedirect.com/science/article/pii/B9780128104828000060`.

[120] Alan V. Oppenheim, Ronald W. Schafer and John R. Buck. *Discrete-time signal processing*. Publisher Upper Saddle River, N.J. : Prentice Hall, 1999. ISBN: 0137549202.

[121] Chris Chatfield and Haipeng Xing. *The Analysis of Time Series: An Introduction with R*. 7th ed. Chapman & Hall/CRC Texts in Statistical Science. Chapman & Hall, 2019.

[122] Vaughan, S. 'A simple test for periodic signals in red noise'. In: *A&A* 431.1 (2005), pp. 391–403. DOI: `10.1051/0004-6361:20041453`. URL: `https://doi.org/10.1051/0004-6361:20041453`.

[123] J. Timmer and M. Koenig. 'On generating power law noise.' In: *Astronomy and Astrophysics* 300 (Aug. 1995), p. 707.

[124] Matteo Frigo and Steven G. Johnson. 'The Design and Implementation of FFTW3'. In: *Proceedings of the IEEE* 93.2 (2005). Special issue on "Program Generation, Optimization, and Platform Adaptation", pp. 216–231.

[125] Christopher Torrence and Gilbert P. Compo. 'A Practical Guide to Wavelet Analysis'. In: *Bulletin of the American Meteorological Society* 79.1 (1998), pp. 61–78. DOI: `10.1175/1520-0477(1998)079<0061:APGTWA>2.0.CO;2`. URL: `https://journals.ametsoc.org/view/journals/bams/79/1/1520-0477_1998_079_0061_apgtwa_2_0_co_2.xml`.

[126] National Oceanic Space Weather Prediction Center (SWPC) and Atmospheric Administration (NOAA). *Geostationary Operational Environmental Satellites (GOES) Space Environment Monitor (SEM) X-rays data - Solar Events*. 2022. URL: `http://satdat.ngdc.noaa.gov/sem/goes/data/new_full/` (visited on 10/05/2022).

[127] *Heliophysics: Space Storms and Radiation: Causes and Effects*. Ed. by Carolus J. Schrijver. Ed. by George L. Siscoe. Cambridge University Press, 2010. ISBN: 9780521760515.

[128] Myles R. Allen and Leonard A. Smith. 'Monte Carlo SSA: Detecting irregular oscillations in the Presence of Colored Noise'. In: *Journal of Climate* 9.12 (1996), pp. 3373–3404. URL: `https://journals.ametsoc.org/view/journals/clim/9/12/1520-0442_1996_009_3373_mcsdio_2_0_co_2.xml`.

[129] Dennis L. Hartmann. *Objective Analysis - Course Notes*. Course notes for Objective Analysis. Department of Atmospheric Sciences, University of Washington, 2014. Chap. 6a and 6b. URL: `https://atmos.washington.edu/~dennis/552_Notes_6b.pdf`.

[130] D. L. Gilman, F. J. Fuglister and J. M. Mitchell. 'On the Power Spectrum of "Red Noise"'. In: *Journal of Atmospheric Sciences* 20.2 (1963), pp. 182–184. DOI: `10.1175/1520-0469(1963)020<0182:OTPSON>2.0.CO;2`. URL: `https://journals.ametsoc.org/view/journals/atsc/20/2/1520-0469_1963_020_0182_otpson_2_0_co_2.xml`.

[131] M. R. Allen. 'Interactions between the atmosphere and oceans on time-scales of weeks and years.' PhD Thesis. University of Oxford, 1992.

[132] Chris Bretherton. *Lecture 11: White and red noise*. Lecture notes for Computational Methods for Data Analysis. Department of Atmospheric Sciences, University of Washington, 2014. URL: `https://atmos.washington.edu/~breth/classes/AM582/lect/lect8-notes.pdf`.

[133] M. E. Wiedenbeck et al. 'Time Dependence of Solar Modulation throughout Solar Cycle 23 as Inferred from ACE Measurements of Cosmic-Ray Energy Spectra'. In: *Proceedings of the 31st International Cosmic Ray Conference*. 2009.

[134] Nicola Tomassetti et al. ‘Testing diffusion of cosmic rays in the heliosphere with proton and helium data from AMS’. In: *Phys. Rev. Lett.* 121.25 (2018), p. 251104. DOI: `10.1103/PhysRevLett.121.251104`. arXiv: `1811.08909 [astro-ph.HE]`.

[135] Nicola Tomassetti et al. ‘Numerical modeling of cosmic-ray transport in the heliosphere and interpretation of the proton-to-helium ratio in Solar Cycle 24’. In: *Adv. Space Res.* 64.12 (2019), pp. 2477–2489. DOI: `10.1016/j.asr.2019.06.025`. arXiv: `1906.11477 [astro-ph.HE]`.

[136] M. Martucci et al. ‘Proton Fluxes Measured by the PAMELA Experiment from the Minimum to the Maximum Solar Activity for Solar Cycle 24’. In: *The Astrophysical Journal* 854.1 (Feb. 2018), p. L2. ISSN: 2041-8213. DOI: `10.3847/2041-8213/aaa9b2`. URL: `http://dx.doi.org/10.3847/2041-8213/aaa9b2`.

[137] K. Abe et al. ‘Measurement of the cosmic-ray low-energy antiproton spectrum with the first BESS-Polar Antarctic flight’. In: *Physics Letters B* 670.2 (2008), pp. 103–108. ISSN: 0370-2693. DOI: `https://doi.org/10.1016/j.physletb.2008.10.053`. URL: `http://www.sciencedirect.com/science/article/pii/s0370269308013270`.

[138] K. Abe et al. ‘Measurement of the Cosmic-Ray Antiproton Spectrum at Solar Minimum with a Long-Duration Balloon Flight over Antarctica’. In: *Phys. Rev. Lett.* 108 (5 Jan. 2012), p. 051102. DOI: `10.1103/PhysRevLett.108.051102`. URL: `https://link.aps.org/doi/10.1103/PhysRevLett.108.051102`.

[139] P. Kühl, R. Gómez-Herrero and B. Heber. ‘Annual Cosmic Ray Spectra from 250 MeV up to 1.6 GeV from 1995 – 2014 Measured with the Electron Proton Helium Instrument onboard SOHO’. In: *Solar Physics* 291.3 (Mar. 2016), pp. 965–974. ISSN: 1573-093X. DOI: `10.1007/s11207-016-0879-0`. URL: `https://doi.org/10.1007/s11207-016-0879-0`.

[140] H. Mavromichalaki et al. ‘Applications and usage of the real-time Neutron Monitor Database’. In: *Advances in Space Research* 47.12 (2011). Recent Advances in Space Weather Monitoring, Modelling, and Forecasting - 2, pp. 2210–2222. ISSN: 0273-1177. DOI: `https://doi.org/10.1016/j.asr.2010.02.019`. URL: `http://www.sciencedirect.com/science/article/pii/s0273117710001249`.

[141] *NMDB: real-time database for high resolution neutron monitor measurements.* Apr. 2018. URL: `http://www01.nmdb.eu/`.

[142] L. J. Gleeson and W. I Axford. ‘Solar Modulation of Galactic Cosmic Rays’. In: *The Astrophysical Journal* 154 (1968), pp. 1011–1026.

[143] L. J. Gleeson and I. H. Urch. ‘A Study of the Force-Field Equation for the Propagation of Galactic Cosmic Rays’. In: *Astrophysics and Space Science* 25 (1973), pp. 387–404.

[144] W. R. Webber and P. R. Higbie. ‘Galactic propagation of cosmic ray nuclei in a model with an increasing diffusion coefficient at low rigidities: A comparison of the new interstellar spectra with Voyage data in the outer heliosphere’. In: *Journal of Geophysical Research* 114 (2009).

[145] Ilya G. Usoskin, Galina A. Brazilevskaya and Gennady A. Kovaltsov. ‘Solar modulation parameter for cosmic rays since 1936 reconstructed from ground-based neutro monitors and ionization chambers’. In: *Journal of Geophysical Research* 116 (2011).

[146] D. Maurin et al. ‘Neutron monitors and muon detectors for solar modulation studies: Interstellar flux, yield function, and assessment of critical parameters in count rate calculations’. In: *Advances in Space Research* 55.1 (2015), pp. 363–389. ISSN: 0273-1177. DOI: `10.1016/j.asr.2014.06.021`. URL: `https://www.sciencedirect.com/science/article/pii/S0273117714003834`.

[147] A. Ghelfi et al. 'Neutron monitors and muon detectors for solar modulation studies: 2. phi time series'. In: *Advances in Space Research* 60.4 (2017). Solar Energetic Particles, Solar Modulation and Space Radiation: New Opportunities in the AMS-02 Era, pp. 833–847. ISSN: 0273-1177. DOI: `10.1016/j.asr.2016.06.027`. URL: `https://www.sciencedirect.com/science/article/pii/S0273117716303428`.

[148] Crispin W Gardiner et al. *Handbook of stochastic methods*. Vol. 3. springer Berlin, 1985.

[149] A. Kopp et al. 'A stochastic differential equation code for multidimensional Fokker–Planck type problems'. In: *Computer Physics Communications* 183.3 (2012), pp. 530–542. ISSN: 0010-4655. DOI: `https://doi.org/10.1016/j.cpc.2011.11.014`. URL: `https://www.sciencedirect.com/science/article/pii/S0010465511003766`.

[150] R. Du Toit Strauss and Frederic Effenberger. 'A Hitch-hiker's Guide to Stochastic Differential Equations'. In: *Space Science Reviews* 212.1 (Oct. 2017), pp. 151–192. ISSN: 1572-9672. DOI: `10.1007/s11214-017-0351-y`. URL: `https://doi.org/10.1007/s11214-017-0351-y`.

[151] Don Stephen Lemons. *An Introduction to Stochastic Processes in Physics*. The John Hopkins University Press, 2002. ISBN: 0-8018-6866-1.

[152] Yoshihiko Yamada, Shohei Yanagita and Tatsuo Yoshida. 'A stochastic view of the solar modulation phenomena of cosmic rays'. In: *Geophysical Research Letters* 25.13 (1998), pp. 2353–2356. DOI: `https://doi.org/10.1029/98GL51869`. eprint: `https://agupubs.onlinelibrary.wiley.com/doi/pdf/10.1029/98GL51869`. URL: `https://agupubs.onlinelibrary.wiley.com/doi/abs/10.1029/98GL51869`.

[153] Nicola Tomassetti et al. 'Evidence for a Time Lag in Solar Modulation of Galactic Cosmic Rays'. In: *The Astrophysical Journal* 849.2 (Nov. 2017), p. L32. ISSN: 2041-8213. DOI: `10.3847/2041-8213/aa9373`. URL: `http://dx.doi.org/10.3847/2041-8213/aa9373`.

[154] Miguel Orcinha et al. 'Observation of a time lag in solar modulation of cosmic rays in the heliosphere'. In: *J. Phys. Conf. Ser.* 1181.1 (2019). Ed. by Anatoly Lagutin, Igor Moskalenko and Mikhail Panasyuk, p. 012013. DOI: `10.1088/1742-6596/1181/1/012013`. arXiv: `1810.10530 [astro-ph.HE]`.

[155] M.S. Potgieter. 'The charge-sign dependent effect in the solar modulation of cosmic rays'. In: *Advances in Space Research* 53.10 (2014). Cosmic Ray Origins: Viktor Hess Centennial Anniversary, pp. 1415–1425. ISSN: 0273-1177. DOI: `https://doi.org/10.1016/j.asr.2013.04.015`. URL: `http://www.sciencedirect.com/science/article/pii/s0273117713002275`.

[156] V. Bindi et al. 'Overview of galactic cosmic ray solar modulation in the AMS-02 era'. In: *Advances in Space Research* 60.4 (2017). solar energetic particles, solar modulation and space radiation: new opportunities in the ams-02 era, pp. 865–878. ISSN: 0273-1177. DOI: `https://doi.org/10.1016/j.asr.2017.05.025`. URL: `http://www.sciencedirect.com/science/article/pii/s0273117717303708`.

[157] J.F. Valdés-Galicia and L.X. González. 'Solar modulation of low energy galactic cosmic rays in the near-earth space environment'. In: *Advances in Space Research* 57.6 (2016). Space and Geophysical Research related to Latin America - Part I, pp. 1294–1306. ISSN: 0273-1177. DOI: `https://doi.org/10.1016/j.asr.2015.11.009`. URL: `http://www.sciencedirect.com/science/article/pii/s0273117715007954`.

[158] E. C. Stone et al. 'Voyager 1 Observes Low-Energy Galactic Cosmic Rays in a Region Depleted of Heliospheric Ions'. In: *Science* 341.6142 (June 2013), pp. 150–153. ISSN: 1095-9203. DOI: `10.1126/science.1236408`. URL: `http://dx.doi.org/10.1126/science.1236408`.

[159] A. C. Cummings et al. 'GALACTIC COSMIC RAYS IN THE LOCAL INTERSTELLAR MEDIUM:VOYAGER 1OBSERVATIONS AND MODEL RESULTS'. In: *The Astrophysical Journal* 831.1 (Oct. 2016), p. 18. ISSN: 1538-4357. DOI: `10.3847/0004-637x/831/1/18`. URL: `http://dx.doi.org/10.3847/0004-637X/831/1/18`.

[160] O. Adriani et al. 'TIME DEPENDENCE OF THE PROTON FLUX MEASURED BY PAMELA DURING THE 2006 JULY-2009 DECEMBER SOLAR MINIMUM'. In: *The Astrophysical Journal* 765.2 (Feb. 2013), p. 91. ISSN: 1538-4357. DOI: `10.1088/0004-637x/765/2/91`. URL: `http://dx.doi.org/10.1088/0004-637X/765/2/91`.

[161] O. Adriani et al. 'Time Dependence of the Electron and Positron Components of the Cosmic Radiation Measured by the PAMELA Experiment between July 2006 and December 2015'. In: *Phys. Rev. Lett.* 116 (24 June 2016), p. 241105. DOI: `10.1103/PhysRevLett.116.241105`. URL: `https://link.aps.org/doi/10.1103/PhysRevLett.116.241105`.

[162] M. Garcia-Munoz et al. 'Cosmic-ray propagation in the Galaxy and in the heliosphere - The path-length distribution at low energy'. In: *The Astrophysical JournalSupplement Series* 64 (May 1987), p. 269. ISSN: 1538-4365. DOI: `10.1086/191197`. URL: `http://dx.doi.org/10.1086/191197`.

[163] B. Heber et al. 'MODULATION OF GALACTIC COSMIC RAY PROTONS AND ELECTRONS DURING AN UNUSUAL SOLAR MINIMUM'. In: *The Astrophysical Journal* 699.2 (June 2009), pp. 1956–1963. ISSN: 1538-4357. DOI: `10.1088/0004-637x/699/2/1956`. URL: `http://dx.doi.org/10.1088/0004-637X/699/2/1956`.

[164] P. Bobik et al. 'systematic investigation of solar modulation of galactic protons for solar cycle 23 using a monte carlo approach with particle drift effects and latitudinal dependence'. In: *The Astrophysical Journal* 745.2 (Jan. 2012), p. 132. ISSN: 1538-4357. DOI: `10.1088/0004-637x/745/2/132`. URL: `http://dx.doi.org/10.1088/0004-637X/745/2/132`.

[165] J. Giacalone and J. R. Jokipii. 'The Transport of Cosmic Rays across a Turbulent Magnetic Field'. In: *The Astrophysical Journal* 520.1 (July 1999), pp. 204–214. ISSN: 1538-4357. DOI: `10.1086/307452`. URL: `http://dx.doi.org/10.1086/307452`.

[166] J.L. Raath et al. 'The effects of magnetic field modifications on the solar modulation of cosmic rays with a SDE-based model'. In: *Advances in Space Research* 57.9 (2016), pp. 1965–1977. ISSN: 0273-1177. DOI: `https://doi.org/10.1016/j.asr.2016.01.017`. URL: `http://www.sciencedirect.com/science/article/pii/s0273117716000557`.

[167] R. D. Strauss et al. 'Modelling heliospheric current sheet drift in stochastic cosmic ray transport models'. In: *Astrophysics and Space Science* 339.2 (Feb. 2012), pp. 223–236. ISSN: 1572-946X. DOI: `10.1007/s10509-012-1003-z`. URL: `http://dx.doi.org/10.1007/s10509-012-1003-z`.

[168] K. Alanko-Huotari et al. 'Stochastic simulation of cosmic ray modulation including a wavy heliospheric current sheet'. In: *Journal of Geophysical Research: Space Physics* 112.A8 (Aug. 2007), n/a–n/a. ISSN: 0148-0227. DOI: `10.1029/2007ja012280`. URL: `http://dx.doi.org/10.1029/2007JA012280`.

[169] U. W. Langner. 'Modulation of cosmic ray protons in the heliosheath'. In: *Journal of Geophysical Research* 108.A10 (2003). ISSN: 0148-0227. DOI: `10.1029/2003ja009934`. URL: `http://dx.doi.org/10.1029/2003JA009934`.

[170] U. W. Langner. 'Solar wind termination shock and heliosheath effects on the modulation of protons and antiprotons'. In: *Journal of Geophysical Research* 109.A1 (2004). ISSN: 0148-0227. DOI: `10.1029/2003ja010158`. URL: `http://dx.doi.org/10.1029/2003JA010158`.

[171] Nicola Tomassetti. 'cosmic-ray protons, nuclei, electrons, and antiparticles under a two-halo scenario of diffusive propagation'. In: *Phys. Rev. D* 92 (8 Oct. 2015), p. 081301. DOI: `10.1103/PhysRevD.92.081301`. URL: `https://link.aps.org/doi/10.1103/PhysRevD.92.081301`.

[172] Jie Feng, Nicola Tomassetti and Alberto Oliva. 'Bayesian analysis of spatial-dependent cosmic-ray propagation: Astrophysical background of antiprotons and positrons'. In: *Phys. Rev. D* 94 (12 Dec. 2016), p. 123007. DOI: `10.1103/PhysRevD.94.123007`. URL: `https://link.aps.org/doi/10.1103/PhysRevD.94.123007`.

[173] S. E. S. Ferreira and M. S. Potgieter. 'Long-Term Cosmic-Ray Modulation in the Heliosphere'. In: *The Astrophysical Journal* 603.2 (Mar. 2004), pp. 744–752. ISSN: 1538-4357. DOI: `10.1086/381649`. URL: `http://dx.doi.org/10.1086/381649`.

[174] F. Plunian, G. R. Sarson and R. Stepanov. 'Deciphering solar turbulence from sunspots records'. In: *Monthly Notices of the Royal Astronomical Society: Letters* 400.1 (Nov. 2009), pp. L47–L51. ISSN: 1745-3933. DOI: `10.1111/j.1745-3933.2009.00760.x`. URL: `http://dx.doi.org/10.1111/j.1745-3933.2009.00760.x`.

[175] M.J. Boschini et al. 'Propagation of cosmic rays in heliosphere: The HelMod model'. In: *Advances in Space Research* 62.10 (2018). Origins of Cosmic Rays, pp. 2859–2879. ISSN: 0273-1177. DOI: `https://doi.org/10.1016/j.asr.2017.04.017`. URL: `http://www.sciencedirect.com/science/article/pii/s0273117717302971`.

[176] H. Mavromichalaki and B. Petropoulos. 'Time-lag of cosmic-ray intensity'. In: *Astrophysics and Space Science* 106.1 (1984), pp. 61–71. ISSN: 1572-946X. DOI: `10.1007/bf00653915`. URL: `http://dx.doi.org/10.1007/BF00653915`.

[177] Badruddin, M. Singh and Y. P. Singh. 'Modulation loops, time lag and relationship between cosmic ray intensity and tilt of the heliospheric current sheet'. In: *Astronomy & Astrophysics* 466.2 (Feb. 2007), pp. 697–704. ISSN: 1432-0746. DOI: `10.1051/0004-6361:20066549`. URL: `http://dx.doi.org/10.1051/0004-6361:20066549`.

[178] P. Lantos. 'Predictions of Galactic Cosmic Ray Intensity Deduced from that of Sunspot Number'. In: *Solar Physics* 229.2 (July 2005), pp. 373–386. ISSN: 1573-093X. DOI: `10.1007/s11207-005-5565-6`. URL: `http://dx.doi.org/10.1007/s11207-005-5565-6`.

[179] R.A. Nymmik. 'time lag of galactic cosmic ray modulation: conformity to general regularities and influence on particle energy spectra'. In: *Advances in Space Research* 26.11 (2000), pp. 1875–1878. ISSN: 0273-1177. DOI: `https://doi.org/10.1016/S0273-1177(99)01242-9`. URL: `http://www.sciencedirect.com/science/article/pii/s0273117799012429`.

[180] V. K. Mishra and A. P. Mishra. 'Study of solar activity and cosmic ray modulation during solar cycle 24 in comparison to previous solar cycle'. In: *Indian Journal of Physics* 90.12 (July 2016), pp. 1333–1339. ISSN: 0974-9845. DOI: `10.1007/s12648-016-0895-9`. URL: `http://dx.doi.org/10.1007/s12648-016-0895-9`.

[181] Partha Chowdhury, K. Kudela and Y.-J. Moon. 'A Study of Heliospheric Modulation and Periodicities of Galactic Cosmic Rays During Cycle 24'. In: *Solar Physics* 291.2 (Jan. 2016), pp. 581–602. ISSN: 1573-093X. DOI: `10.1007/s11207-015-0832-7`. URL: `http://dx.doi.org/10.1007/s11207-015-0832-7`.

[182] John Clem and Paul Evenson. 'Balloon-borne observations of the galactic positron fraction during solar minimum negative polarity'. In: *Journal of Geophysical Research: Space Physics* 114.A10 (Oct. 2009), n/a–n/a. ISSN: 0148-0227. DOI: `10.1029/2009ja014225`. URL: `http://dx.doi.org/10.1029/2009JA014225`.

[183] O. P. M. Aslam and Badruddin. 'Study of Cosmic-Ray Modulation During the Recent Unusual Minimum and Mini-Maximum of Solar Cycle 24'. In: *Solar Physics* 290.8 (Aug. 2015), pp. 2333–2353. ISSN: 1573-093X. DOI: `10.1007/s11207-015-0753-5`. URL: `https://doi.org/10.1007/s11207-015-0753-5`.

[184] Rene Brun et al. *root-project/root: v6.18/02*. Version v6-18-02. July 2019. DOI: `10.5281/zenodo.3895860`. URL: `https://doi.org/10.5281/zenodo.3895860`.

[185] F. James and M. Roos. 'Minuit: A System for Function Minimization and Analysis of the Parameter Errors and Correlations'. In: *Comput. Phys. Commun.* 10 (1975), pp. 343–367. DOI: `10.1016/0010-4655(75)90039-9`.

[186] Volker Blobel. 'Smoothing or Fitting without a parametrization'. Lecture for Block Vorlesung Statistical and numerical methods in High Energy Physics. University of Hamburg, Germany, Mar. 2005.

[187] Jerome H. Friedman. 'Data Analysis Techniques for High Energy Particle Physics'. Collection of lectures presented at the CERN School of Computing, Godoysund, Norway, August 11-24, 1974. Godoysund, Norway, Sept. 1974.

[188] Corinna Harmening and Hans Neuner. 'Choosing the Optimal Number of B-spline Control Points (Part 1: Methodology and Approximation of Curves)'. In: *Journal of Applied Geodesy* 10.3 (2016), pp. 139–157. DOI: `doi:10.1515/jag-2016-0003`. URL: `https://doi.org/10.1515/jag-2016-0003`.

[189] Carl de Boor. 'On calculating with B-splines'. In: *Journal of Approximation Theory* 6.1 (1972), pp. 50–62. ISSN: 0021-9045. DOI: `https://doi.org/10.1016/0021-9045(72)90080-9`. URL: `https://www.sciencedirect.com/science/article/pii/0021904572900809`.

[190] Johannes Bureick, Hamza Alkhatib and Ingo Neumann. 'Robust Spatial Approximation of Laser Scanner Point Clouds by Means of Free-form Curve Approaches in Deformation Analysis'. In: *Journal of Applied Geodesy* 10.1 (2016), pp. 27–35. DOI: `doi:10.1515/jag-2015-0020`. URL: `https://doi.org/10.1515/jag-2015-0020`.

[191] Michael Joseph Price. 'Penalized b-splines and their application with an in depth look at the bivariate tensor product penalized b-spline'. PhD thesis. Iowa State University, 2018. URL: `https://dr.lib.iastate.edu/server/api/core/bitstreams/a6adb839-f6d1-4e45-92d2-9dac9fe725de/content`.

[192] Petre Stoica and Yngve Selen. 'Model-order selection: a review of information criterion rules'. In: *IEEE Signal Processing Magazine* 21.4 (2004), pp. 36–47. DOI: `10.1109/MSP.2004.1311138`.

[193] Jetsada Laipaporn and Phattrawan Tongkumchum. 'A Survey Of Unfolding Methods For Particle Physics'. In: *Proceedings for International Conference On Applied Statistics ICAS 2018, 24-26 October 2018*. Oct. 2018, pp. 248–257. URL: `https://www.researchgate.net/profile/J-Laipaporn/publication/333916540_The_Use_of_Information_Criteria_for_Selecting_Number_of_Knots_in_Natural_Cubic_Spline_Volatility_Estimation/links/5d0c6184299bf1547c716593/The-Use-of-Information-Criteria-for-Selecting-Number-of-Knots-in-Natural-Cubic-Spline-Volatility-Estimation.pdf`.

[194] G.W. Stewart. *Afternotes on Numerical Analysis*. Other Titles in Applied Mathematics. Society for Industrial and Applied Mathematics, 1996. ISBN: 9781611971491. URL: `https://books.google.pt/books?id=VEHBOUOAL-EC`.

[195] Charles R. Harris et al. 'Array programming with NumPy'. In: *Nature* 585.7825 (Sept. 2020), pp. 357–362. DOI: `10.1038/s41586-020-2649-2`. URL: `https://doi.org/10.1038/s41586-020-2649-2`.

[196] Pauli Virtanen et al. 'SciPy 1.0: Fundamental Algorithms for Scientific Computing in Python'. In: *Nature Methods* 17 (2020), pp. 261–272. DOI: `10.1038/s41592-019-0686-2`.

[197] The pandas development team. *pandas-dev/pandas: Pandas*. Version latest. Feb. 2020. DOI: `10.5281/zenodo.3509134`. URL: `https://doi.org/10.5281/zenodo.3509134`.

[198] Wes McKinney. 'Data Structures for Statistical Computing in Python'. In: *Proceedings of the 9th Python in Science Conference*. Ed. by Stéfan van der Walt and Jarrod Millman. 2010, pp. 56–61. DOI: `10.25080/Majora-92bf1922-00a`.

[199] Edgar Gabriel et al. 'Open MPI: Goals, Concept, and Design of a Next Generation MPI Implementation'. In: *Proceedings, 11th European PVM/MPI Users' Group Meeting*. Budapest, Hungary, Sept. 2004, pp. 97–104.

[200] John L. Gustafson. 'Reevaluating Amdahl's Law'. In: *Commun. ACM* 31.5 (May 1988), pp. 532–533. ISSN: 0001-0782. DOI: `10.1145/42411.42415`. URL: `http://doi.acm.org/10.1145/42411.42415`.

[201] Gene M. Amdahl. 'Validity of the Single Processor Approach to Achieving Large Scale Computing Capabilities'. In: *Proceedings of the April 18-20, 1967, Spring Joint Computer Conference*. AFIPS '67 (Spring). Atlantic City, New Jersey: ACM, 1967, pp. 483–485. DOI: `10.1145/1465482.1465560`. URL: `http://doi.acm.org/10.1145/1465482.1465560`.